

FINAL REPORT

Development of a Micro-Fabricated Total-Field Magnetometer

SERDP Project MR-1512

MARCH 2011

Mark Prouty
Geometrics, Inc.

This document has been cleared for public release



Report Documentation Page				Form Approved OMB No. 0704-0188	
Public reporting burden for the collection of information is estimated to average 1 hour per response, including the time for reviewing instructions, searching existing data sources, gathering and maintaining the data needed, and completing and reviewing the collection of information. Send comments regarding this burden estimate or any other aspect of this collection of information, including suggestions for reducing this burden, to Washington Headquarters Services, Directorate for Information Operations and Reports, 1215 Jefferson Davis Highway, Suite 1204, Arlington VA 22202-4302. Respondents should be aware that notwithstanding any other provision of law, no person shall be subject to a penalty for failing to comply with a collection of information if it does not display a currently valid OMB control number.					
1. REPORT DATE MAR 2011		2. REPORT TYPE N/A		3. DATES COVERED -	
4. TITLE AND SUBTITLE Development of a Micro-Fabricated Total-Field Magnetometer				5a. CONTRACT NUMBER	
				5b. GRANT NUMBER	
				5c. PROGRAM ELEMENT NUMBER	
6. AUTHOR(S)				5d. PROJECT NUMBER	
				5e. TASK NUMBER	
				5f. WORK UNIT NUMBER	
7. PERFORMING ORGANIZATION NAME(S) AND ADDRESS(ES) Geometrics, Inc.				8. PERFORMING ORGANIZATION REPORT NUMBER	
9. SPONSORING/MONITORING AGENCY NAME(S) AND ADDRESS(ES)				10. SPONSOR/MONITOR'S ACRONYM(S)	
				11. SPONSOR/MONITOR'S REPORT NUMBER(S)	
12. DISTRIBUTION/AVAILABILITY STATEMENT Approved for public release, distribution unlimited					
13. SUPPLEMENTARY NOTES The original document contains color images.					
14. ABSTRACT					
15. SUBJECT TERMS					
16. SECURITY CLASSIFICATION OF:			17. LIMITATION OF ABSTRACT SAR	18. NUMBER OF PAGES 175	19a. NAME OF RESPONSIBLE PERSON
a. REPORT unclassified	b. ABSTRACT unclassified	c. THIS PAGE unclassified			

This report was prepared under contract to the Department of Defense Strategic Environmental Research and Development Program (SERDP). The publication of this report does not indicate endorsement by the Department of Defense, nor should the contents be construed as reflecting the official policy or position of the Department of Defense. Reference herein to any specific commercial product, process, or service by trade name, trademark, manufacturer, or otherwise, does not necessarily constitute or imply its endorsement, recommendation, or favoring by the Department of Defense.

REPORT DOCUMENTATION PAGE					<i>Form Approved OMB No. 0704-0188</i>							
The public reporting burden for this collection of information is estimated to average 1 hour per response, including the time for reviewing instructions, searching existing data sources, gathering and maintaining the data needed, and completing and reviewing the collection of information. Send comments regarding this burden estimate or any other aspect of this collection of information, including suggestions for reducing the burden, to the Department of Defense, Executive Services and Communications Directorate (0704-0188). Respondents should be aware that notwithstanding any other provision of law, no person shall be subject to any penalty for failing to comply with a collection of information if it does not display a currently valid OMB control number.												
PLEASE DO NOT RETURN YOUR FORM TO THE ABOVE ORGANIZATION.												
1. REPORT DATE (DD-MM-YYYY) 15-03-2011		2. REPORT TYPE Final Report			3. DATES COVERED (From - To) 5/2006 - 12/2010							
4. TITLE AND SUBTITLE Development of a micro-fabricated total-field magnetometer				5a. CONTRACT NUMBER W912HQ-06-C-0043								
				5b. GRANT NUMBER								
				5c. PROGRAM ELEMENT NUMBER								
6. AUTHOR(S) Mark Prouty				5d. PROJECT NUMBER MM-1512								
				5e. TASK NUMBER								
				5f. WORK UNIT NUMBER								
7. PERFORMING ORGANIZATION NAME(S) AND ADDRESS(ES) Geometrics, Inc 2190 Fortune Drive San Jose, CA 95131					8. PERFORMING ORGANIZATION REPORT NUMBER							
9. SPONSORING/MONITORING AGENCY NAME(S) AND ADDRESS(ES) SERDP 901 N Stuart St. Arlington, VA 22203					10. SPONSOR/MONITOR'S ACRONYM(S)							
					11. SPONSOR/MONITOR'S REPORT NUMBER(S)							
12. DISTRIBUTION/AVAILABILITY STATEMENT Approved for public release; distribution is unlimited												
13. SUPPLEMENTARY NOTES												
14. ABSTRACT Magnetometers are one of the basic instruments used for the detection and discrimination of unexploded ordnance (UXO). Cesium vapor sensors are the systems of choice due to their high sensitivity and total-field measurement, which is independent of sensor orientation. However, existing cesium vapor sensors are extremely large and consume a lot of power. In this work, we developed laser diode technology, used MEMs techniques to miniaturize the components of the cesium magnetometer, and investigated many interrogation schemes to characterize their performance. Specifically, the technical objective of this work was to investigate a high sensitivity, total field magnetometer of extremely low power, small size, and capable of being mass-produced for low cost. We have reduced the power consumption of a complete cesium sensor by a factor of 10, and demonstrated further size and power reductions in a laboratory environment												
15. SUBJECT TERMS Magnetometer, atomic magnetometer, cesium, unexploded ordnance												
16. SECURITY CLASSIFICATION OF: <table border="1" style="width: 100%; border-collapse: collapse; font-size: x-small;"> <tr> <td style="width: 33%;">a. REPORT</td> <td style="width: 33%;">b. ABSTRACT</td> <td style="width: 33%;">c. THIS PAGE</td> </tr> <tr> <td style="text-align: center;">U</td> <td style="text-align: center;">U</td> <td style="text-align: center;">U</td> </tr> </table>			a. REPORT	b. ABSTRACT	c. THIS PAGE	U	U	U	17. LIMITATION OF ABSTRACT <div style="text-align: center;">None</div>		18. NUMBER OF PAGES <div style="text-align: center;">162</div>	
a. REPORT	b. ABSTRACT	c. THIS PAGE										
U	U	U										
					19a. NAME OF RESPONSIBLE PERSON Mark Prout							
					19b. TELEPHONE NUMBER (Include area code) 408-954-0522							

Front Matter

Table Of Contents

Front Matter	ii
<i>Table Of Contents</i>	ii
<i>List of Acronyms</i>	iv
<i>List of Figures and Tables</i>	v
<i>Acknowledgments</i>	xi
Executive Summary	1
Objective	1
Tasks and Results	1
Laser Diode Light Sources	2
Cell Manufacturing Methods	3
Signal Extraction Techniques	3
Physics Package Integration	4
Electronics Design	4
Laboratory and Field Testing	5
Summary	5
Objective	6
Background	10
Materials and Methods	11
Results and Accomplishments	13
VCSEL light source development	14
Task 1.1: Fabricate first-generation VCSELs	14
Task 1.2: Investigation of VCSEL noise	19
Task 1.3: Determine whether VCSEL performance is adequate	22
Task 1.4: Fabricate second-generation VCSELs	22
Task 1.5: Develop photodiodes for integration with the physics package	24
Task 1.6: Develop micro-optics for the physics package	27
Cell Fabrication	27
Task 2.1 Fabrication of laboratory equipment for cell filing	29
Task 2.2 Determine cost and performance of cell filling methods	35
Task 2.3 Demonstration of wafer-level filling techniques	38
Signal Extraction and Detection Techniques	41
Introduction	41
Task 3.1a Frequency-modulated Non-linear Magneto-Optic Rotation	42
Task 3.1b Mx Implementation	43
Task 3.1c Bell-Bloom Implementation	45
Task 3.2 Demonstration of self-oscillation	50
Task 3.3 Measurement of performance	53
Task 3.4 Determine final electronics requirements	57
Task 3.5 Demonstrate self-oscillating FM-NMOR device in chip-scale device	60
Task 3.6 Heading error reduction	61
Physics Package Integration	100
Task 4.1: Design and thermal modeling of cell structure	100
Task 4.2: Non-magnetic heater design	102
Task 4.3: Fabrication of cell support structures	104
Task 4.4: Fabrication of prototype physics package	107
Electronics Design	112
Summary	112

Task 5.1 Breadboard demonstration of VCSEL wavelength control.....	113
Task 5.2 Breadboard demonstration of cell temperature control.....	116
Task 5.3 Breadboard demonstration of signal extraction circuit	117
Implementation.....	119
Task 5.4 Go / no-go determine if electronics will meet size and power requirements	119
Task 5.5 Complete fabrication of electronics subsystem.....	119
Task 5.6 Methodology for Circuit Size Reduction	120
Task 5.7 Drive Electronics Design	128
Task 5.8 Frequency Measuring Electronics Design.....	129
Task 5.9 Final Electronics Design	130
Testing	156
Task 6.1 Laboratory testing	156
Task 6.2 Field testing	157
Concluding Summary	159
Appendices	162
Appendix A: List of Technical Publications	162

List of Acronyms

ADC – Analog to Digital Converter
CAD – Computer-Aided Design
CCD – Charge-Coupled Device
CSAM – Chip Scale Atomic Magnetometer
CSAC – Chip Scale Atomic Clock
CPT – Coherent Population Trapping
CPU – Central Processing Unit
Cs – Cesium
DAC – Digital to Analog Converter
DARPA – Defense Advanced Research Projects Agency
DBR – Distributed Bragg Reflector
ELS – Energy Level Shift
EM – Electromagnetic
FFBB – Full-Frequency Bell-Bloom
FFT – Fast Fourier Transform
FIR – Finite Impulse Response
FM-NMOR – Frequency Modulated Nonlinear Magneto-Optical Rotation
FPGA – Field-Programmable Gate Array
HE – Heading Error
HFBB – Half-Frequency Bell-Bloom
IIR – Infinite Impulse Response
ITO – Indium Tin Oxide
LSB – Least-Significant Bit
LTP – Laser transition probabilities
MEMS – Microfabricated Electromechanical System
MFTFM – Micro-Fabricated Total Field Magnetometer
MSB – Most-Significant Bit
MTADS – Multi Sensor Towed Array Detection System
M_x – Magnetic moment in the x-direction
M_z – Magnetic moment in the z-direction
ND – Neutral Density
NIST – National Institute of Standards and Technology
nm – nanometer
nT – nano-Tesla
Pa – Pascal
Physics Package – The physical structure of the cell, laser diode, and light source.
pT – pico-Tesla
QAM – Quadrature Amplitude Modulation
QWP – Quarter-Wave Plate
RF – Radio Frequency
RFTP – Radio frequency transition probabilities
RIN – Relative Intensity Noise
STOLS – Surface Towed Ordnance Locator System
TEC – Thermo-Electric Cooler
UV – Ultraviolet
UXO – Unexploded Ordnance
VCO – Voltage-Controlled Oscillator
VCSEL – Vertical-Cavity Surface-Emitting Laser

List of Figures and Tables

Figure 1. Basic structure of an atomic magnetometer	2
Figure 2. Cost vs yearly production quantity of sensors.	6
Figure 3. Array of current generation sensors for land surveying application. Smaller sensor systems would greatly reduce the size and complexity of such platforms.	8
Figure 4. Handheld array made possible by the sensors developed in this project	9
Figure 5. Block diagram of Geometrics Cs magnetometer	10
Figure 6. Block diagram of sensor using CPT	11
Figure 7. (a) Schematic cross section of VCSEL and (b) list of semiconductor epitaxial layers grown on the GaAs wafer, showing composition, thickness, and doping type.	14
Figure 8. Reflection spectrum of an 894-nm VCSEL wafer.	15
Figure 9. (a) Cavity resonance wavelength versus radial position on the GaAs wafer. (b) Picture of a 3-inch-diameter GaAs wafer, with dotted lines showing the annular region that meets the wavelength requirement.	16
Figure 10. Optical microscope image of a VCSEL biased at 2-mA forward current	17
Figure 11. (a) VCSEL output power and diode voltage versus forward current. (b) VCSEL emission spectrum at a drive current of 2mA	18
Figure 12. (a) Microscope image of typical VCSEL chip containing 4 VCSELs. (b) Electrical schematic showing the common-cathode connection shared by the 4 VCSELs on the chip.	18
Figure 13. (a) Picture of VCSEL chip mounted on a TO-39 header without a lid. (b) Close-up view of the VCSEL chip showing wire bond connections to the VCSEL chip	19
Figure 14 Schematic diagram of VCSEL intensity noise measurement setup	20
Figure 15. Measurement of 894-nm VCSEL intensity noise from 1 Hz to 100 kHz, using an FFT spectrum analyzer (SRS SR785).	21
Figure 16. Measurement of 894-nm VCSEL intensity noise from 10 to 500 kHz, using a swept-frequency spectrum analyzer (HP 8562A). The spike near 250kHz is due to noise on the current driver for the laser, not the laser itself.	22
Figure 17. (a) VCSEL output power and diode voltage versus forward current. (b) VCSEL emission spectrum at a drive current of 3mA	23
Figure 18. (a) New 0.5-mm-square VCSEL chip mounted on micro-heater substrate. (b) Tuning of VCSEL wavelength versus electrical drive power applied to the micro-heater.	24
Figure 19 Four photodiode chip design types: A, B, C, D. The active photodiode area is shown in red, and the top-side metal pads are shown in yellow. Top side metal bond pads are labeled “A” for anode and “C” for cathode.	25
Figure 20. Unit cell of “Silicon2” mask set, containing 10 photodiode chips, numbered 0 to 9.	25
Figure 21. Microscope photographs of all four chip types. The die numbers are (a) I1N1, (b) I1M4, (c) I1M7, (d) I1M9. In the die number regions, the characters I and 1 appear blank and the character 7 appears as a smaller dot relative to the other characters.	26
Figure 22. (a) Dark current (blue) and white-light-illuminated current (red) from photodiode die number I4N0 (type A) of part OD-1737 wafer 116-2A. (b) Picture of the measured chip, sitting on a gold platen that electrically connects the (back side) cathode to the right-hand probe (out of focus).	26
Figure 23. Photograph of optics used in physics package. Quarter wave plate (upper right), polarizer (lower right), neutral density filter (lower left), and lens (upper left).	27

Figure 24. Wafer level manufacturing of Cs cells. Cells could be manufactured inexpensively in large volumes.....	28
Figure 25. Cell fabrication process for azide-based deposition.....	29
Figure 26. Thin-film azide deposition system constructed at NIST for wafer-level alkali cell fabrication.....	29
Figure 27. (a) Scanning electron micrograph of the CsN_3 films deposited with thermal evaporation. (b) A quantitative elemental analysis shows the presence of nitrogen in the films. (c) X-ray diffraction measurements suggest the film becomes more amorphous after deposition.	31
Figure 28. (a) Photograph of a 2×2 Cs cell arrays fabricated with the azide deposition method described above. (b) Optical absorption spectrum of a cell containing approximately 200 Torr of N_2 buffer gas. (c) Optical absorption spectrum of a cell containing approximately 1000 Torr of N_2 buffer gas.....	32
Figure 29 Arrays of cells showing feasibility of large volume production	33
Figure 30 Effect of UV irradiation time, showing increasing buffer gas pressure (wider line width).....	33
Figure 31 Line width variation before and after temperature soak.	34
Figure 32 Buffer gas pressure calculated from the line width before and after the temperature soaking.....	34
Figure 33 Change in line width during temperature soaking.	35
Figure 34 (a) Optical absorption resonance of a microfabricated cell based on UV-photodissociation of CsN_3 . (a) A micrograph of the cell.....	39
Figure 35. CPT resonance measured in a cell fabricated with UV-photodissociation of CsN_3	39
Figure 36. X-ray diffraction spectra from (a) bulk CsN_3 , as obtained after heating in the crucible to the deposition temperature but no evaporation, (b) deposited thin-film sample and (c) second thin-film sample deposited under a different crucible heating schedule.	40
Figure 37. Transition linewidth ($1/\pi T_2$), as a function of the buffer gas pressure for an alkali vapor cell of volume 1 mm^3 . This plot assumes that the cell temperature is adjusted to produce 50 % absorption, and therefore the approximately maximize the S/N of the instrument.	41
Figure 38. (a) Sensitivity as a function of optical power for a MEMS cell of volume 1 mm^3 , containing a buffer gas of 10 Torr Ne. (b) Atomic energy level structure showing broadening of the excited state hyperfine structure due to the presence of a high-pressure buffer gas.	43
Figure 39. Mx excitation of alkali atom spin precession.....	44
Figure 40. Sensitivity measured with the Mx excitation technique in a MEMS alkali vapor cell. The measurement demonstrates that sensitivities in the range of $1 \text{ pT}/\sqrt{\text{Hz}}$ are possible in highly miniaturized alkali vapor cells fabricated by MEMS processing techniques.	44
Figure 41. Block diagram of electronics required to operate a chip-scale atomic magnetometer in the Mx configuration.	45
Figure 42. Bell-Bloom excitation of Larmor precession in an alkali vapor cell. In this method, the frequency of the light is modulated by changing the injection current of the laser. The frequency modulation tunes the circularly-polarized laser beam on and off the resonance synchronously with the Larmor precession, which pumps the atoms into a precessing polarized state.	46

Figure 43. Bell-Bloom excitation methods. (a) The spin precession can be excited by modulating the laser wavelength at the full Larmor frequency and detuning the average laser wavelength from the line center. (b) Alternatively, the precession can be excited by modulating the laser wavelength at one-half the Larmor frequency and tuning the laser wavelength to the center of the optical transition.....	46
Figure 44. Apparatus for measuring the sensitivity of the magnetometer in the Bell-Bloom configuration.....	47
Figure 45. (a) Dispersive Larmor resonance (lock-in output) for the Bell-Bloom configuration with a modulation frequency of 37 kHz. (b) Noise spectrum from the lock-in output with the magnetic field tuned to the center of the resonance in (a). Noise below 100Hz is primarily due to limitations in the experimental test method.....	48
Figure 46. Electronics implementation for the full-frequency Bell-Bloom excitation method.....	49
Figure 47. Modes of operation and waveforms for FM-NMOR magnetometer	52
Figure 48 Performance of FM-NMOR magnetometer	52
Figure 49 Noise performance and cell used for FM-NMOR measurements.....	53
Figure 50. The chip-scale atomic magnetometer used in the Mx measurements. (a) Schematic of the magnetic sensor. The components are: 1—VCSEL, 2—polyimide spacer, 3—optics package including (from bottom to top) a neutral-density filter, polarizer, a quartz quarter waveplate, and a neutral-density filter, 4—ITO heater, 5—87Rb vapor cell with RF coils above and below it, and 6—ITO heater and photodiode assembly. (b) Photograph of the magnetic sensor. Note the gold wire bonds providing the electrical connections from the baseplate to the device	54
Figure 51 The response of the magnetometer is plotted as a function of frequency when a chirped 2.4 nT modulation is applied to the 5500 nT static field. Inset: The in-phase lock-in amplifier output as a function of magnetic field where the frequency of the applied RF field is 38.5 kHz.....	54
Figure 52 Noise density of the lock-in signal converted to units of magnetic field. The lock-in time constant is 0.1 ms with a filter roll-off 6 dB / octave. The ambient field is 5500 nT.	55
Figure 53 VCSEL response to square-wave modulation of the current. The top trace is the waveform fed into the laser current source, the middle trace shows the response of the VCSEL to this waveform at 40 kHz, and the bottom is the response at 87.5 kHz (the rate used for HFBB at earth's field). The response was measured by finding a region where the cell transmission was linear with respect to the VCSEL current at low frequency.....	55
Figure 54 FFBB magnetometer performance vs. cell temperature and light intensity in a 80 kHz magnetic field. Shown is the magnetic field sensitivity (a), the lock-in noise (b), the amplitude of the dispersive magnetic resonance signal (c), and the ratio of the magnetic resonance amplitude and the optical absorption depth (d). The dashed grey line in the noise plot gives the estimated photon shot noise from the off-resonance photodiode signal. The input light power given in these plots was measured before the light beam entered the magnetic shield, which is substantially larger than the amount of light inside the vapor cell	56
Figure 55 HFBB performance vs. modulation amplitude for several modulation waveforms in a 175 kHz magnetic field. The square- waveforms are of the form in Figure 53 and are designated as SQRXX, where XX is the percentage of the period spent on resonance. The horizontal grey lines in the plots show the values obtained for the best sensitivity point for FFBB sine wave modulation.....	56

Figure 56 HFBB (dashed lines, open points) and Mx (solid lines and points) performance vs. cell temperature and light intensity in a 80 kHz magnetic field. Shown is the magnetic field sensitivity (a), lock-in noise (b), magnetic resonance width (c), amplitude (d), slope (e), and the ratio of the magnetic resonance amplitude and optical absorption depth (f). The dashed grey line in the noise plot gives the estimated photon shot noise from the off-resonance photodiode signal.....	57
Figure 59 Response of the diode laser frequency to square-wave current modulation. Red traces indicate the modulation current waveform, while the black lines indicate the laser frequency response, as measured by the transmission of the laser through the atomic absorption profile. (a) A square-wave current modulation produces a distorted frequency waveform. (b) Adjusting the current waveform can produce a much more square frequency waveform, which should result in lower noise.	59
Figure 60 Sensitivity comparison of the FFBB scheme and the HFBB-SW scheme. An increased sensitivity is observed under most operating conditions.	59
Figure 61. A chip-scale atomic magnetometer constructed at NIST. This device can operate in either Mx or Bell-Bloom modes and has a measured sensitivity of up to 5 pT/rtHz.	60
Figure 62 Commercial magnetometer using a split polarizer method of reducing heading error ..	61
Figure 63 Two methods of using multiple directions of light to average heading error	61
Figure 64 Diagram of all energy levels of Cs.....	63
Figure 65. Ground state relaxation constant for Cs-N ₂ collisions as a function of buffer gas pressure (T=65 C):.....	69
Figure 66. Ground state relaxation constant for Cs-Cs spin exchange collisions as a function of Cs cell temperature	70
Figure 67. Ground state relaxation constant for Cs atoms-wall collisions for our small MEMS cell as a function of buffer gas pressure	70
Figure 68. Optical line width-because of pressure broadening as a function of buffer gas pressure	71
Figure 69. Exited state relaxation constant for Cs-buffer gas quenching effect as a function of buffer gas pressure.....	71
Figure 70 Excited state populations.....	73
Figure 71. Dimensions of cesium cell for an MFAM sensor.	75
Figure 72. The number of polarized atoms as a function of the buffer gas pressure for the cesium cell with a=2cm, b=1.2cm and c=0.45 cm.....	77
Figure 73. Change of Npol for different values of a,b,c when the cell volume is constant (1.08 cm ³).	78
Figure 74. The spatial distribution of the polarized atoms Npol(x,y=0,z=0) in the direction of x (along the longest side of the cell).	79
Figure 75. This plot shows the transient behavior of polarized atoms for all diffusion modes and for the first seven leading modes. Buffer gas pressure p=100 Torr.	80
Figure 76. Absorption of the laser beam tuned to D1 cesium line in the case of buffer gas (nitrogen) pressure p=30 Torr. Both hyperfine components are resolved.....	81
Figure 77. Absorption of the laser beam tuned to D1 cesium line in the case of buffer gas (nitrogen) pressure p=100 Torr. Both hyperfine components are resolved.....	81
Figure 78. Absorption of the laser beam tuned to D1 cesium line in the case of buffer gas (nitrogen) pressure p=300 Torr. Spectral width of absorption spectra is high and hyperfine components are barely resolved.	82

Figure 79. Change of absorption rate for $F=4$, $m=3$ to excited states transition as a function of the buffer gas pressure.....	83
Figure 80. Variation of RF line width (error signal width) as a function of buffer gas pressure. RF line width value is presented in relative units of RF line width for $p=500$ Torr.	84
Figure 81. Ratio p_2/p_1 of the populations of two ground states $F=4$, $m=3$ (population p_2) and $F=4$, $m=4$ (population p_1) as a function of pressure.....	85
Figure 82. Ratio p_2/p_1 of the populations of two ground states $F=4$, $m=3$ (population p_2) and $F=4$, $m=4$ (population p_1) as a function of pressure, relative to the value of p_2/p_1 at a pressure of 500 Torr.....	85
Figure 83. Offset in magnetic field reading (heading error) as a function of angle for various optical geometries.....	87
Figure 84. Beam geometries used to minimize heading error and dead zones.....	88
Figure 85. Generating multiple beams from a single laser source.	89
Figure 86. Calculating properties of refracted laser beams	90
Figure 87. Photograph of cross section of laser intensity from VCSEL	91
Figure 88. Graph of cross section of laser intensity from VCSEL.....	91
Figure 89. Populations of various energy levels.....	93
Figure 90. Change in the populations as a function of changing angle of the sensor.	94
Figure 91. Simulation of RF resonance.....	95
Figure 92. Results of heading error calculation.....	95
Figure 93 RF resonance shifts for different energy levels.....	96
Figure 94 Equations used for calculating combined RF resonance from individual states.....	97
Figure 95 Using three beams to obtain heading error curves of different phases.	98
Figure 96 Combining individual heading errors into a signal free from heading error.....	98
Figure 97 Sensitivity of heading error with variation in sensor parameters.....	99
Figure 98. Simplified schematic diagram of a magnetometer physics package.....	100
Figure 99. Top view of Mag1 heater mask layout. The heater chip size is 8-mm square. The heating element lies within the 2-mm square (colored red) where the cesium cell sits. The central part of the heater chip is suspended over a 6-mm air hole (shown in blue) that provides thermal isolation of the heated cesium cell.....	101
Figure 100. Thermal conductivities of various materials used in the cell support structure. The heater power required to maintain a temperature difference of 70K (cell at 95°C and ambient at 25°C) is shown in the right-most column for each material.....	102
Figure 101. Pairs of traces, situated one above the other, that carry equal currents in opposite directions are used to cancel the magnetic field contributions at large distances from the traces.....	103
Figure 102. Cross-sectional drawing of two counter-conducting traces that run from $x_1=-1$ mm to $x_2=+1$ mm. The magnetic field calculated in the plane $x=0$ is shown in false color (3dB change in magnitude per color step). The black line segments show the magnetic vector field directions	103
Figure 103. Portions of input and output data (text) files from MagTrace1 computer program.....	104
Figure 104. (a) Microfabricated Pt heater (inner 1.2-mm ring) and temperature sensor (outer ring). (b) Measured Pt sensor resistance versus temperature.....	105

Figure 105. (a) Temperature versus heater power for a single heater/support platform suspended over a 6-mm air hole. (b) Picture of cesium cell sitting on the heater/support structure.	106
Figure 106. (a) Schematic diagram showing major components of the magnetometer physics package. (b) Photograph of the first delivered magnetometer physics package.	107
Figure 107. (a) Picture of a cesium cell sitting on a microfabricated 8-mm-square glass heater/support structure, which is bonded to a 25-mm-square carrier circuit board (b).	108
Figure 108. (a) Cross sectional view of the physics package 3-D CAD model. (b) Exploded view of the physics package 3-D CAD model.	108
Figure 109. Photograph of the first delivered physics package prototype.	109
Figure 110. Photographs of the illuminated VCSEL without (a) and with (b) a collimating lens. The electrical connections to the physics package were made with 34-AWG twisted pair wires. The wires were soldered to the edge of each circuit board as shown in Figure 111(a). The circuit board solder pads were positioned on a 0.5-mm pitch, which required a special V-groove clamping fixture to holder the wires on a precise 0.5-mm pitch for soldering to the circuit board, as shown in Figure 111(b).	110
Figure 111. Photographs of twisted pair 34-AWG wires after (a) and before (b) soldering to the VCSEL circuit board. A special V-groove clamp was used to hold the wires on a precise 0.5-mm pitch for soldering	110
Figure 112. Summary of electrical connections to the first prototype physics package.	111
Figure 113. General electronics block diagram	112
Figure 114 Modulation of the laser frequency	113
Figure 115 Photodiode output	113
Figure 116 FFT of photodiode output	114
Figure 117 Waveform after first demodulator	114
Figure 118 FFT of demodulator output	115
Figure 119 Signal after second demodulator	115
Figure 120 FFT of signal after second demodulator	116
Figure 121. Mz magnetometer electronics block diagram	117
Figure 122. Complete electronics system mounted on a cart for testing. Components are as follows: 1) Signal buffers, 2) External counter assembly, 3) H1 synthesizer, 4) photo preamplifier, 5) DAC board, 6) Processor board, 7) regulators and protection circuits, 8) heater power amplifiers, 9) logging system. Only items 3-8 are needed in the final system. Items 1,2 and 9 are for testing.	120
Figure 123. Block diagram of the electronics of a magnetometer.....	121
Figure 124. The operation of the magnetometer consists of many independent feedback loops. Each must be analyzed for its particular requirements.....	122
Figure 125. General block diagram for the Larmor feedback loop	123
Figure 126. Comparison of FIR and IIR filters.	124
Figure 127. Noise shaping block diagram.	125
Figure 128. Shaped noise spectrum.	126
Figure 129. Increasing resolution of an analog signal using integrators attached to the DAC. ..	127
Figure 130. Using several slower-speed but lower-power DACS to create a higher bandwidth signal using a multiplexer.....	127

Figure 131. Increasing dynamic range of a DAC by adding the DC component of the signal using analog means.	128
Figure 132. Board-Level Block Diagram.	129
Figure 133. Laser servo block diagram.	136
Figure 134. Laser heater waveforms.	137
Figure 135. Absorption signal as wavelength is varied.	137
Figure 136. Power Supply Schematic.	140
Figure 137. Communications and I/O.	141
Figure 138. Main motherboard block diagram.	142
Figure 139. CPU Schematic.	143
Figure 140. Counter Schematic.	144
Figure 141. Larmor CPU schematic.	145
Figure 142. Larmor VCO schematic.	146
Figure 143. Local DACs schematic.	147
Figure 144. H1 control schematic.	148
Figure 145. Voltage reference schematic.	149
Figure 146. Photo preamplifier schematic.	150
Figure 147. Top-level sensor driver board schematic.	151
Figure 148. Laser servo schematic.	152
Figure 149. Laser driver amplifier schematics.	153
Figure 150. Heater amplifier schematics.	154
Figure 151. Temperature sensing circuit.	155
Figure 152. Magnetometer signals gathered in an uncontrolled environment in the laboratory.	156
Figure 153. Spectral response of magnetometer with a reference sensor.	157
Figure 154. Electronics system mounted on a cart for field testing.	157
Figure 155. Photographs of the test system.	158
Figure 156. Time series data taken with an automobile passing by at a distance of 10m.	158
Figure 157. Field data over a small survey grid. Three representative lines are shown.	159

Acknowledgments

This material is based upon work supported by the US Army Corps of Engineers, Humphreys Engineering Center Support Activity under Contract No. W912HQ-06-C-0043. Any opinions, findings and conclusions or recommendations expressed in this material are those of the authors and do not necessarily reflect the views of the US Army Corps of Engineers.

Executive Summary

Objective

Magnetometers are one of the basic instruments used for the detection and discrimination of unexploded ordnance (UXO). Cesium vapor atomic magnetometers are commonly used since their readings are independent of the orientation of the sensor, which eliminates the noise problems due to rotation or even vibration of other types of sensors. In order to better discriminate UXO from clutter or scrap, a high spatial density of readings is desirable. In order to efficiently make such measurements, and to position such measurements accurately, arrays of sensing elements would be highly desirable. However, existing cesium vapor sensors are extremely large and consume a lot of power.

In this work, we developed laser diode technology and used MEMs techniques to miniaturize the components and reduce the power consumption of the cesium magnetometer. Specifically, the technical objective of this work was to investigate a high sensitivity, total field magnetometer of extremely low power, small size, and capable of being mass-produced for low cost. Achievements were as follows:

- Showed prototypes with sensor power less than 100 mW, excluding readout electronics.
- Built sensor physics package size less than 1.0 cc (excluding electronics)
- Built electronics occupying approximately 15 square in, including counter.
- Showed potential production cost of about \$200 per sensor in large quantities
- Demonstrated sensitivity of 5 - 15 pT / root-Hz.

During this project, we have developed a roadmap towards commercialization of this technology. A near-term system will be manufactured in prototype quantities 2010, and be in commercial production in 2011.

- Power less than 3 W, including readout electronics and physics package
- Sensor physics package size approximately 25 cc (excluding electronics)
- Electronics occupying approximately 15 square inches
- Price and sensitivity (10pT / rt-Hz) similar to existing sensors

Tasks and Results

The structure of an atomic magnetometer consists of the elements shown in Figure 1. Our work involved the following tasks:

1. Optimize the design and performance of the laser diode light source.
2. Optimize the production techniques for filling miniature cells with the proper amounts of cesium and buffer gas.
3. Optimize the interrogation techniques for extracting the magnetometer reading from the device.
4. Design and optimize the structure of the complete sensor (known as the physics package).
5. Design the electronics subsystem to implement the temperature control, laser frequency control and signal extraction methodology.
6. Test devices in the Earth's environment using a complete electronics system.

All of the tasks above were accomplished with outstanding results. We have shown excellent performance with a complete magnetometer system, consisting of electronics required to operate the sensor, as well as a 1 cubic inch physics package, mostly consisting of framework for the actual sensing portion, which is 0.1 cc. This technology will make a significant commercial impact. A brief summary of the work on each task is shown below.

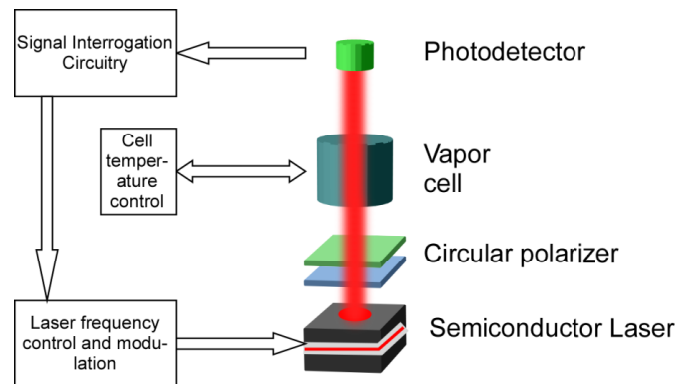


Figure 1. Basic structure of an atomic magnetometer

Laser Diode Light Sources

Task history:

1.1 Fabrication of 12 devices	10/2006
1.2 Investigation of intensity and polarization noise	02/2007
1.3 Determine whether performance is adequate to meet sensitivity goals	03/2007
1.4 Fabricate 12 second-generation devices	06/2007
1.5 Process development for integration with physics package	08/2007
1.6 Micro-optics process development	10/2007

Currently available atomic magnetometers typically use cesium-vapor lamps as their light source. These cesium lamps are fairly large and consume a lot of power (over 5 watts), most of which is dissipated as heat. Laser diodes may be made small and low power (under 1 mW), but efforts must be taken to bring them to the proper wavelength. Vertical-Cavity Surface-Emitting Lasers (VCSELs) are the technology of choice for this application for several reasons: very low power consumption (under 2 mW), round output laser beam emitted perpendicular to the semiconductor wafer surface, single wavelength operation, and potential for low-cost production (\$20 - \$50 each).

In operation, the wavelength of the VCSEL device is controlled by varying the temperature of the device. However, the manufactured room temperature wavelength must lie in the range 891 to 893 nm so that the VCSEL can be tuned exactly to the 894.35nm D1 line of Cs by heating it to between 50 and 90C. The VCSEL wavelength can be tuned with temperature at a rate of +0.06nm/K.

Two runs of devices were fabricated in this project, and the technology was transferred to a commercial vendor. Commercial devices are now being produced.

Cell Manufacturing Methods

Task history:

2.1 Fabrication of laboratory equipment for cell filling	11/2006
2.2 Determine cost and performance of cell filling methods	02/2007
2.3 Demonstration of wafer-level filling techniques	05/2007
2.4 Integration with micro-optics assembly	10/2007
2.5 Demonstration of functioning devices	3/2008

The first step in creating a MEMS cell is to etch holes into silicon wafers. We used a straightforward deep ion etching technique. The holes are 1mm square, and the wafer is 1mm thick. Next, a Pyrex glass wafer is anodically bonded to one side of the silicon wafer. This, too, is a straightforward process, and is well-demonstrated by earlier work.

Next, Cs and a buffer gas must be deposited into the cell. There are several ways of doing this. Most are based upon some means of directly introducing cesium and a buffer gas into the cell. Finally, a second glass wafer is bonded onto the top of the hole sealing the alkali atoms inside the cell.

In this project, we developed a low cost method of filling the cells, one that can be easily extended to filling wafers of cells in parallel. We have developed a technique of filling the cells with a cesium azide (CsN_3) compound, which, under UV illumination, dissociates into cesium metal and the desired nitrogen buffer gas. This, then, supplies both the buffer gas and the Cs in one step. We have shown the feasibility of filling arrays of cells by filling 5x5 arrays in a silicon wafer.

Signal Extraction Techniques

Task history:

3.1 Investigation of self-oscillating FM-NMOR on table-top apparatus	10/2006
3.2 Demonstration of self-oscillation	02/2007
3.3 Measurement of performance	02/2007
3.4 Determine final electronics requirements	07/2007
3.5 Demonstrate self-oscillating FM-NMOR device in chip-scale device	11/2007
3.6 Heading error reduction	04/2010

There are several methods to extract a magnetometer signal from the Cs cell. They differ with respect to the complexity of the required structure as well as performance considerations such as sensitivity, dead zones, and heading errors. In each technique, the laser light pumps the cells into a polarized state where the spins of the atoms (which are precessing about the magnetic field) are aligned in phase with each other. Some form of modulation is used to interrogate the resonance

of the Cs atoms and extract the frequency of resonance. This frequency is proportional to the magnetic field. Some techniques are summarized here:

Mx Magnetometer

The Geometrics G-858 uses this method of signal extraction. This method uses a coil of wire to modulate the population. The electronics are simple, but it requires careful alignment between the coil axis and the optical axis. This method has both equatorial and polar dead zones.

Mz Magnetometer

This method uses the same coil structure as the Mx method, but the details of the modulation are different. The electronics are more complex, but it does not require careful alignment between the coil axis and the optical axis. In addition, this method has only an equatorial dead zone.

Bell-Bloom

In the Bell-Bloom method, the modulation is applied to the light itself. This results in a good performance magnetometer with only a polar dead zone and a very simple device structure.

Physics Package Integration

Task history:

4.1 Design and thermal modeling of cell structure	02/2007
4.2 Non-magnetic heater design	06/2007
4.3 Fabrication of prototype structures	10/2007
4.4 Fabrication of 1 cc physics package	02/2008
4.5 Fabrication of prototype	03/2009

The complete physics package design requires the following major considerations:

- Thermal control of the cell and VCSEL. The cell is operated at 50-100 degrees C. The VCSEL may be either heated or cooled to bring the light output to the proper wavelength. Resistive heating may be used, if the current leads are carefully designed to minimize magnetic fields.
- Thermal insulation is required to keep the two components at the proper temperature, and to minimize the amount of power lost in heating the cell.
- Required optical elements, such as polarizers, lenses, and a photodiode need to be laminated to the structure. The point here is to make the manufacturing process efficient and capable of being done with a wafer-full of devices.

Electronics Design

Task history:

5.1 Breadboard demonstration of VCSEL wavelength control	02/2007
5.2 Breadboard demonstration of cell temperature control	05/2007

5.3 Breadboard demonstration of signal extraction circuit	11/2007
5.4 Go / no-go determine if electronics will meet size and power requirements	11/2007
5.5 Complete fabrication of electronics subsystem	12/2008
5.6 Methodology for circuit size reduction	05/2009
5.7 Drive electronics design	09/2009
5.8 Frequency measuring electronics design	12/2009
5.9 Final electronics design	08/2010

All of the electronics have been built and were optimized using prototype physics packages. The performance measurements made by NIST estimate the performance obtainable using ideal electronics. For example, their lab equipment is not able to track actual changing fields – noise is measured with a constant magnetic field. Real world electronics generally trade off some performance for the sake of simplicity and do not generally obtain the theoretical level of performance. We have been able to quantify the requirements for the electronics system, and characterize the obtainable performance for various levels of complexity in the electronics. A final electronics design was completed

Laboratory and Field Testing

Task history:

6.1 Laboratory testing	12/2008
6.2 Field testing in San Jose	03/2009

We completed a test in the laboratory of our electronics system and physics package. Noise levels obtained were about 60 pT per root Hz. This is a factor of 5-10 worse than is theoretically achievable with this physics package with perfect electronics. A noise estimate of 6 pT per rt Hz was achieved in the laboratory at NIST as part of this project. With further optimization, we feel we can improve the achieved performance. However, even at 60 pT performance, the system is quite good for UXO exploration. Existing systems used in the field achieve about 10 pT sensitivity, but the noise levels of the Earth's field variation, background geology, and clutter are about 10 or more times higher.

Summary

In the first year of this project, we had good indications that this project was achievable. All of the high risk issues in this project had been addressed by that time. VCSELs were tested, a promising cell filling methodology was identified, and several interrogation methods were identified. In the second year, we focused on real-world scenarios, building physics packages, laser diodes, and measuring and optimizing the performance to determine a final design. In the third year, we continued to explore the rather complicated design space, and we now understand the effect on cost and performance of the various components in order to implement an optimal design. We built two generations of prototypes which prove the capabilities of miniature sensors. Finally, we re-designed the electronics for a new generation of improvements in size and performance.

Objective

In this project, a team from Geometrics, Sandia National Laboratories (Sandia), and the National Institute of Standards and Technology (NIST) developed micro fabricated total field magnetometers (MFTFM). The size of the sensor itself is less than 1 cc, compared to existing sensors of about 250cc. In addition, the power consumption, including electronics, has been reduced to about 2W, compared to 20 W for existing sensors. The electronics required to run the sensors was also reduced in size. The sensitivity of these sensors is near 10pT / rt Hz, very similar to the performance of existing Cs sensors for UXO work. Finally, such sensors will be manufacturable at greatly reduced cost over existing sensors. Current sensors cost about \$5000 each – it is expected the sensors could be made in volume for as little as \$200 each. See Figure 2.

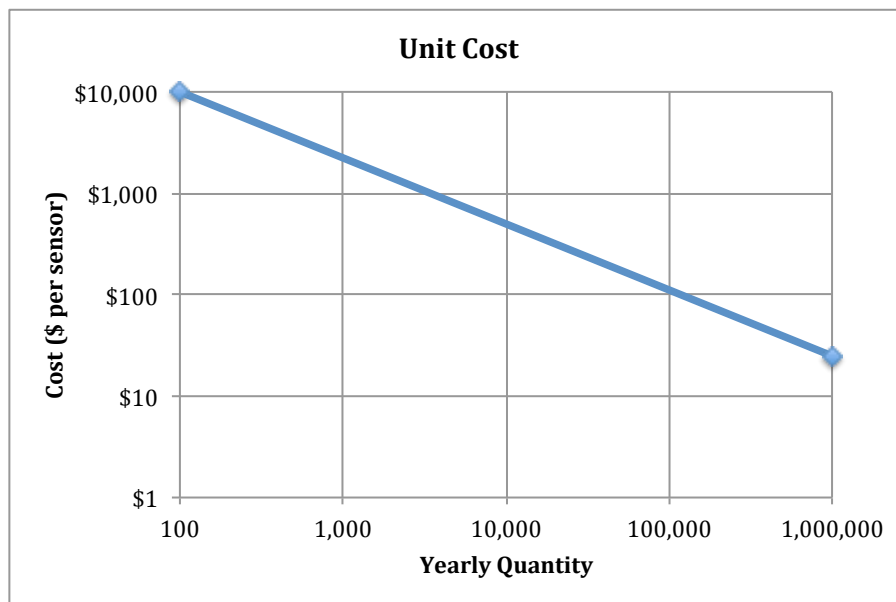


Figure 2. Cost vs yearly production quantity of sensors.

Magnetometers are one of the basic devices used to search for Unexploded Ordnance (UXO). Their advantage over other sensors is their ability to detect deep, ferrous objects. Their sensitivity to deep objects is achieved by the fact that the applied field is generated by the earth itself, and, therefore, does not diminish in strength away from the detector. Other technologies, such as EM detectors, usually have their own on-board transmitters, and the signal due to an object is reduced both by the reduction in transmitter strength with distance, as well as the reduction in signal strength from the object with distance from the sensor. Only the latter causes a signal reduction for magnetometers.

One major problem in remediation of UXO from former military sites is that of differentiating between scrap objects that could be left in the ground and hazardous objects that must be removed. The extremely high cost of remediating sites may be vastly reduced by discriminating the scrap from the UXO. Much progress has been made towards this goal by identifying magnetic signatures of UXO. The general technique is to use an optimization method

to find a dipole source that best fits the readings measured over the target.¹ This technique works well when data points are accurately positioned, and when the target anomalies are separated sufficiently so as not to have overlapping signatures. For highly contaminated sites, however, a large problem exists. One of the keys to improved discrimination algorithms on overlapping objects is having more closely sampled, accurately-positioned data.

Recent work has been done to analyze higher order moments of the field from the target in order to improve discrimination.² This requires obtaining a greater density of information near and around the targets.^{3 4} Greater density of information may be obtained by traveling slower and more thoroughly over the area being surveyed. However, with this method, it is difficult to accurately position the data measurements, and the positioning errors have limited the accuracy of the data analysis. In addition, this greatly increases the cost of the survey by increasing the number of traverses. Increasing the number of sensors employed on a given pass of the instrument will increase the sample density without reducing survey speed. In addition, in an array the relative positions of the sensors are accurately known, and the data gathered is therefore of much higher quality.⁵ Existing magnetometer systems, however, are large, bulky, and expensive (see Figure 3). Only a few array systems are currently in use (such as MTADS and STOLS), and their cost is extremely high.

What is needed, then, is a new generation of small, inexpensive, low power, and lightweight sensors in order to keep survey speeds high while increasing the sampling density. This new technology will make arrays of dozens of sensing elements practical. Data could even be gathered in two-dimensional arrays with possibly hundreds of elements, providing still greater sampling density and positional accuracy. Therefore, this research increases the value of a large amount of on-going work on new platforms and data processing techniques. With these sensors, we feel entirely new approaches for real-time signal processing are also feasible.

For greatest productivity, airborne platforms are of great interest in the Wide Area Assessment phase of the UXO cleanup problem. Several helicopter platforms, including ones made by the Naval Research Laboratory, Battelle, and Sky Research, have shown great potential for rapid surveying of suitable sites. This has increased interest in Unmanned Aerial Vehicle platforms for carrying sensors across survey sites. Such vehicles offer the potential for high productivity, greater safety, and significantly lower cost over manned helicopter survey methods. MFTFM sensors would greatly increase the practicality of UAV platforms. Their smaller size causes less interference with the aerodynamics of the flight platform, and their lower power requirement greatly reduces the battery size or fuel consumption, obviously of key concern for small airborne platforms.

¹ H. H. Nelson, T. W. Altshuler, E. M. Rosen, J. R. McDonald, B. Barrow, and N. Khadr, "Magnetic modeling of UXO And UXO-like targets and comparison with signatures measured by MTADS," in Proc. UXO Forum Anaheim, CA, May 1998, pp. 282-291.

² D. Leiblich, "The Physics of Scrap Discrimination: Non-Dipole Magnetic Fields," UXO Poster 238, SERDP-ESTCP- Technical Symposium and Workshop, Washington DC, 2004.

³ H. Nelson, "High-Quality, Multi-Sensor Overlapping Signature Data Sets," UXO Poster 215, SERDP-ESTCP- Technical Symposium and Workshop, Washington DC, 2004.

⁴ R. Jones, "Standardized Analysis for UXO Demonstration Sites," UXO Poster 220, SERDP-ESTCP- Technical Symposium and Workshop, Washington DC, 2004.

⁵ S. Billings, L. Pasion, J. Foley, "Advanced magnetic analysis for PIG discrimination at the former Lowery bombing and gunnery range." UXO Forum 2004.

Even in a single or dual sensor mode of operation, the MFTFM will be a great advantage. Current magnetometers are bulky, cumbersome devices. The total system weight, including spare battery packs, is about 30 kg. The sensors must be held away from the operator, which requires a long staff, and due to the weight of the sensor and the long lever-arm, a counterweight. This greatly reduces the productivity of a field surveyor. A system built around an MFTFM, in contrast, would weigh only a few kg, allowing for far greater productivity.



Figure 3. Array of current generation sensors for land surveying application. Smaller sensor systems would greatly reduce the size and complexity of such platforms.

Another advantage of the MFTFM is that they could be used to develop small hand-held magnetic gradiometers. These devices are often used to re-acquire targets after the initial field sweep by the data logging system.⁶ Current generation hand-held systems are made with fluxgate technologies. Fluxgates have lower sensitivity than Cs magnetometers, yet they continue to be used in small wands simply because the total field sensors are far too bulky and heavy. A new generation of wand-based magnetic gradiometers would greatly facilitate the extraction process by providing the sensitivity of a Cs magnetometer with the convenience and low cost of a fluxgate wand.

Extremely small and low cost sensors could also be weaved into a blanket or mat, or built into a portable array, as shown in Figure 4. Such an array system could be laid over a target to interrogate the signal in detail. This could provide a more accurate picture of the subsurface, without the need for first scanning the sensor, and then positioning and mapping the readings on a PC. Such a system could be used even during the re-acquisition phase, first, to accurately determine the location of a target, and secondly, after excavation to make sure no other items remain nearby. This technique might also provide the documentation necessary to show the

⁶ C. Youmans, "In-Field Analog Instrument Methodology for Validation of Anomalies," UXO Forum 2004.

object was cleared, without the requirement for performing a final survey over an area to prove that no other anomalies remain.

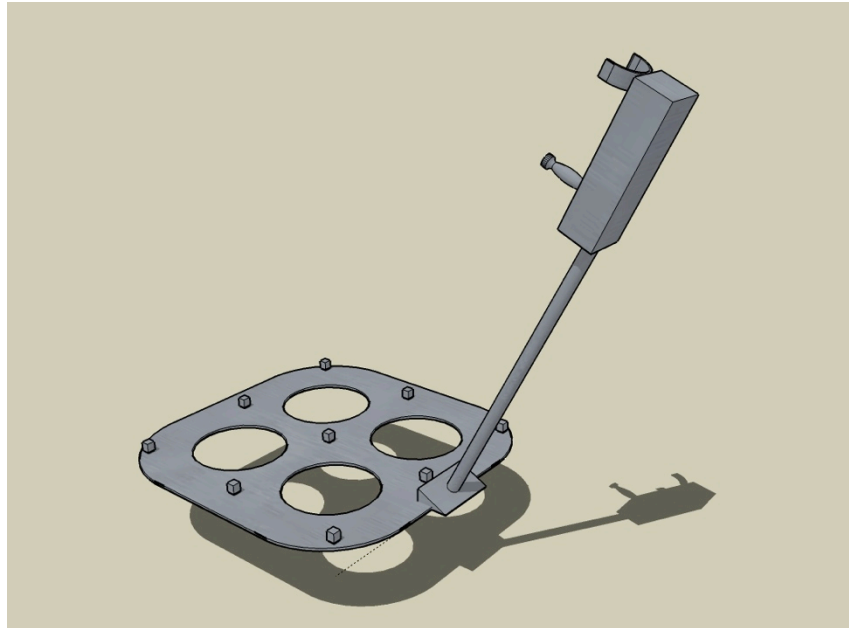


Figure 4. Handheld array made possible by the sensors developed in this project

Another drawback of existing total field sensors, which we have shown in this work may be eliminated, is the fact that they have dead zones. A dead zone is a position of the sensor relative to the vector of the earth's magnetic field where the sensor does not produce a signal. Careful field techniques may overcome this limitation, but at a cost of lower productivity. The sensor must be held rigidly in a fixed position, and the user may not 'probe' into bushes or change orientation since the signal may "drop out." This reduces productivity, and further requires additional time and cost in removing vegetation before traversing the site with bulky fixed-orientation platforms.

Another area of intense interest is that of combined sensor platforms. EM devices are being actively developed that can give multi-component information about the targets. Still, magnetometers have a significant advantage in sensitivity. A combined approach is often desired, but less often used due to the cost involved. The goal of many groups is to have a common platform with both magnetometer sensors and EM sensing devices.⁷ A great limitation in the practicality of combined systems is the sheer bulk of such a system. The MFTFM technology would reduce the size of a magnetometer array to be a very small addition to the size of the EM system. Thus, a magnetometer sensor array could be much more easily integrated into the EM platform, allowing for surveying with both techniques simultaneously.

⁷ R. Siegel, "Tradeoffs in Interleaving Total Field Magnetometer and EM61 Data for a Co-Located Dual-Mode Man-Portable Application," UXO Poster 239, SERDP-ESTCP- Technical Symposium and Workshop, Washington DC, 2004

Background

In order to make a highly sensitive measurement of the magnetic field, one needs to exploit a physical property that is strongly dependent upon the magnetic field, and weakly dependent upon other parameters. The frequencies of atomic spectral lines meet these two objectives. They are very stable, depending upon physical constants and properties of the element in question, and certain lines have a frequency which is dependent upon the magnetic field. In addition, frequency is an easy property to measure digitally. Thus, highly accurate measurements may be made of the magnetic field using the frequencies of atomic spectral lines.

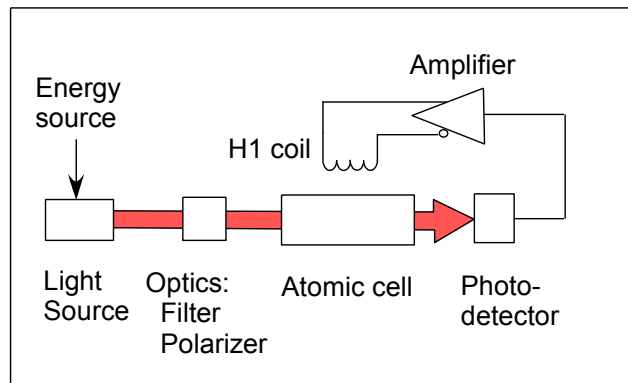


Figure 5. Block diagram of Geometrics Cs magnetometer

The details of exactly how this is done provides for a rich variety of methods of producing a magnetometer signal, with inherent tradeoffs in performance, stability, reliability, cost, complexity, sensitivity, and so on.

Geometrics commercial Cs sensors operate on the principle of optical pumping. The principle is shown in Figure 5. Light passes through the cell with a certain polarization. The Cs atoms in the cell will absorb this light, rising to a higher energy state, then re-radiate and fall back randomly to a lower energy state. Some of the lower states will not absorb light of the input polarization, and hence, atoms will gather in this state, since the other states are absorbing energy. Now, suppose energy is supplied into the Cs cell from the H1 coil, at a frequency corresponding to the energy difference between two m levels. This RF energy re-populates states that can absorb the light energy, and the photodiode output is reduced. The frequency of the RF energy required to dim the photodiode signal is the output of the magnetometer.

New ways of interrogating a Cs cell have come from recent research directed towards atomic clocks. The principles of atomic magnetometers and atomic clocks are closely related. The major difference is in which spectral lines are chosen as a reference for the measurement. Some lines have a frequency dependent upon a magnetic field – those are used for magnetometers. Other lines do not depend upon the magnetic field – those lines are used for clocks.

Other principles have recently been introduced for operating atomic clocks. One such principle is Coherent Population Trapping (CPT).⁸ The advantage of this method is that the RF energy required to move the atoms between two ground states is not supplied directly to the atomic cell, via an H1 coil (for magnetometers) or a microwave cavity (for atomic clocks).⁹ Instead, the RF energy is used to modulate the light source directly, producing two sidebands, one at each of the two ground states of interest. Figure 6 shows the difference schematically.

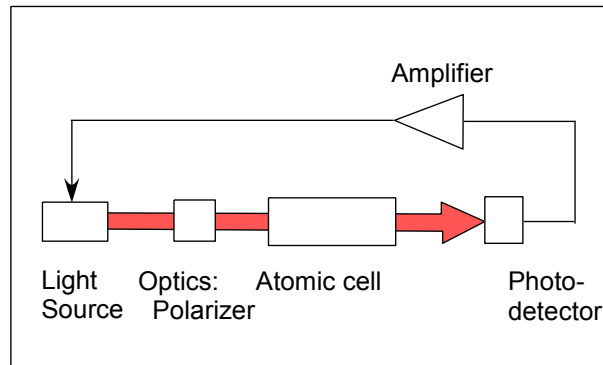


Figure 6. Block diagram of sensor using CPT

The discovery of the CPT method, and its elimination of the electromagnetic feedback enabled recent research directed towards miniaturizing atomic clocks. It is impossible to miniaturize the microwave cavity, since its size is related to its resonant frequency of operation. In addition, the advancement of laser diode technology makes possible the use of CPT in a small device. Because of these developments, DARPA began funding several groups who have made great progress in developing a chip-scale atomic clock (CSAC).¹⁰

Due to the close relationship between atomic clocks and atomic magnetometers, the techniques developed in the CSAC projects can be used to miniaturize atomic magnetometers. In fact, a magnetometer based upon this technology was announced by NIST in 2004.¹¹ The magnetometer device built by NIST operates on the CPT principle. However, that device was relatively noisy: 40 pT per root Hz was obtained. The goal of this work was to investigate the operation of the magnetometer using other techniques, which produced a noise level of better than 10 pT per root Hz.

Materials and Methods

Prior to the inception of this work, the feasibility of miniaturizing atomic magnetometers was clearly established. First, several CSAC projects actually built prototype clocks, with very

⁸ J. Vanier, M.W. Levine, D. Janssen, M.J. Delaney, "The Coherent Population Trapping Passive Frequency Standard," IEEE Transaction on Instrumentation and Measurement, Vol 52, No 2, April 2003, pp. 258 – 262.

⁹ J. Vanier, M.W. Levine, D. Janssen, M.J. Delaney, "On the Use of Intensity Optical Pumping and Coherent Population Trapping Techniques in the Implementation of Atomic Frequency Standards," IEEE Transaction on Instrumentation and Measurement, Vol 52, No 3, June 2003, pp. 822 – 831.

¹⁰ www.darpa.mil/csac

¹¹ P. D. D. Schwindt, S. Knappe, V. Shah, L. Hollberg, J. Kitching, L. Liew and J. Moreland, "Chip-scale atomic magnetometer," Appl. Phys. Lett. 85, 6409, 2004

similar structures to those required in our work. Secondly, NIST had previously operated their CSAC structure as a magnetometer, obtaining encouraging results even with a system optimized for use as a clock. In this project we aim to optimize the design of the magnetometer, with the goal of designing a physical structure, interrogation method, and manufacturing process which will enable the commercial success of these sensors. For that, a reasonable performance is required, as well as a reasonable production cost. The production cost must take into account the capital expenses of the production equipment, as well as the yield of the processes and the complexity of the structure. These are the basic issues that are being addressed in this project.

Our method is to build upon the CSAC work, taking it to the next level, as well as designing, measuring, and optimizing the ways in which magnetometers differ from clocks. In some ways, magnetometers are easier to make than clocks – for example, long term stability and drift is typically not a concern. However, the magnetic fields generated by the device itself, coming from internal operating currents or from magnetic materials used in the device, are of major concern with magnetometer sensors. In addition, the required noise properties of the light source used in the sensor differ for clocks and magnetometers. Most importantly, the information bandwidth of a magnetometer is much higher than a clock. Users are interested in a wide bandwidth of information from the magnetometer, which means that narrow band filters may not be used internally to limit the noise. This complicates the electronics requirements.

These issues are being addressed by theory, design, direct measurement, and experimentation. The three partners in this project are well suited for this work, and are able to efficiently try different approaches and measure the results, comparing the work with the theory to make sure that the measurements are correct, the physical structures behave as expected, and the principles are understood. Some of the properties of the laser light sources for magnetometry optimization were not known, and these were measured. In addition, we have used VCSELs to replace the discharge lamps in Geometrics existing sensors, making measurement of the performance of the laser diode light sources in bench-top devices.

Other work addresses the production efficiency of these devices. This includes the method of filling the Cs cells, for example. Previous work has shown the feasibility of filling the cells individually, by direct introduction of the Cs material into the cells, basically one-by-one. In this work, we have explored a novel method of filling the cells much more quickly and inexpensively.

Results and Accomplishments

Task 1: Develop laser diode light source

1.1 Fabrication of 12 devices	10/2006
1.2 Investigation of intensity and polarization noise	02/2007
1.3 Determine whether performance is adequate to meet sensitivity goals	03/2007
1.4 Fabricate 12 second-generation devices	06/2007
1.5 Process development for integration with physics package	08/2007
1.6 Micro-optics process development	10/2007

Task 2: Development of cell fabrication methods

2.1 Fabrication of laboratory equipment	11/2006
2.2 Determine cost and performance of cell filling methods (go/no-go)	02/2007
2.3 Demonstration of wafer-level filling techniques	05/2007
2.4 Integration with micro-optics assembly	10/2007
2.5 Demonstration of functioning devices	03/2008

Task 3: Magnetic signal extraction methodologies

3.1 Investigate self-oscillating FM-NMOR	10/2006
3.2 Demonstration of self-oscillation	02/2007
3.3 Measurement of performance (go / no-go)	03/2007
3.4 Determine final electronics requirements	07/2007
3.5 Demonstrate self-oscillating FM-NMOR device in chip-scale device	11/2007
3.6 Heading error reduction	04/2010

Task 4: Physics package design and integration

4.1 Design and thermal modeling of cell structure	02/2007
4.2 Non-magnetic heater design	06/2007
4.3 Fabrication of prototype structures	10/2007
4.4 Fabrication of 1 cc physics package	02/2008
4.5 Fabrication of prototype	03/2009

Task 5: Electronics Development

5.1 Breadboard demonstration of VCSEL wavelength control	12/2006
5.2 Breadboard demonstration of cell temperature control	05/2007
5.3 Breadboard demonstration of signal extraction circuit	11/2007
5.4 Go / no-go determine if electronics will meet requirements	11/2007
5.5 Complete fabrication of electronics subsystem	12/2008
5.6 Methodology for circuit size reduction	05/2009
5.7 Drive electronics design	09/2009
5.8 Frequency measuring electronics design	12/2009
5.9 Final electronics design	08/2010

Task 6: Field Testing

6.1 Laboratory testing	12/2008
6.2 Field testing in San Jose	03/2009

VCSEL light source development

Task 1.1: Fabricate first-generation VCSELs

The first milestone, due at the end of month 5 (October 2006), required the fabrication and delivery of 10 prototype 894-nm VCSELs for use in initial magnetometer experiments. This milestone was accomplished on time. This section describes details of the fabrication of these generation 1 VCSELs.

A cross-sectional schematic view of our 894-nm VCSEL device structure is shown in Figure 7(a). Current passes vertically through the p-i-n diode structure and electron-hole recombination, accompanied by photon emission, occurs in the quantum wells. The VCSEL device fabrication starts with epitaxial growth of many precise layers of compound-semiconductor materials, by metal-organic vapor-phase epitaxy (MOVPE). As shown schematically in Figure 7(a), the VCSEL consists of three parts: a lower distributed Bragg reflector (DBR) mirror, a 1-wavelength-thick active optical cavity containing 5 InGaAs quantum wells, and a top DBR mirror. A detailed list of the epitaxial layers that were grown on a GaAs substrate wafer are shown in Figure 6(b). The top and bottom DBR mirrors consist of 21 and 36 DBR periods, respectively. Each DBR period consists of two quarter-wavelength-thick layers, one high-index ($n=3.47$) $\text{Al}_{0.16}\text{Ga}_{0.84}\text{As}$ layer and one low-index ($n=3.02$) $\text{Al}_{0.92}\text{Ga}_{0.08}\text{As}$ layer. The top DBR is doped p-type, the cavity is unintentionally doped, and the bottom DBR is doped n-type.

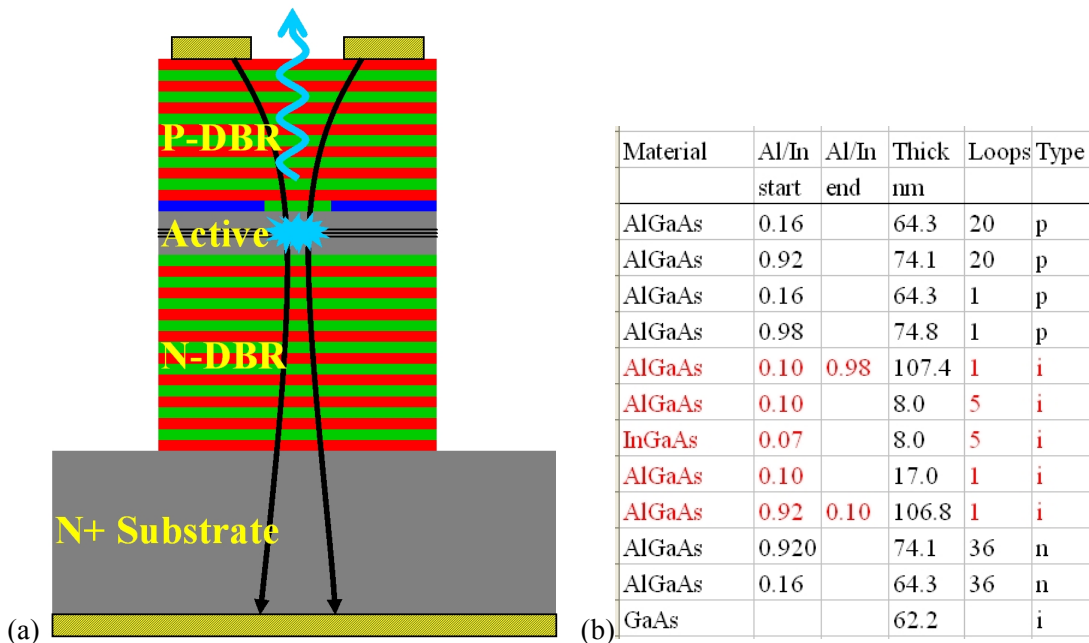


Figure 7. (a) Schematic cross section of VCSEL and (b) list of semiconductor epitaxial layers grown on the GaAs wafer, showing composition, thickness, and doping type.

After the epitaxial structure is grown on the GaAs wafer, we measure the optical reflection versus wavelength, as shown in Figure 8, in order to determine the approximate laser wavelength. The reflection spectrum in Figure 8 shows a cavity resonance dip at 894.6nm. The resonance dip varies with radial position on the wafer as shown in Figure 9(a). The VCSEL wavelength must match exactly the cesium D1 transition at 894.35nm (in air) within a typical 20-K-wide operating temperature range. This requirement translates into a 1.2nm range of acceptable cavity resonance wavelengths such that the operating VCSEL output wavelength can be tuned with temperature (at a rate of 0.06nm/K) to hit the cesium D1 wavelength within the operating temperature range. Hence, we generally obtain an annular band, indicated by the red dashed lines in Figure 9(b), of the wafer surface area inside of which the correct range of VCSEL operating wavelengths will be achieved. The stringent wavelength requirement reduces our yield to approximately 10% of the wafer area. Fortunately, because the VCSEL is so small, it is possible to obtain over 10,000 VCSELs on a single wafer, so there are still plenty that meet the wavelength constraint.

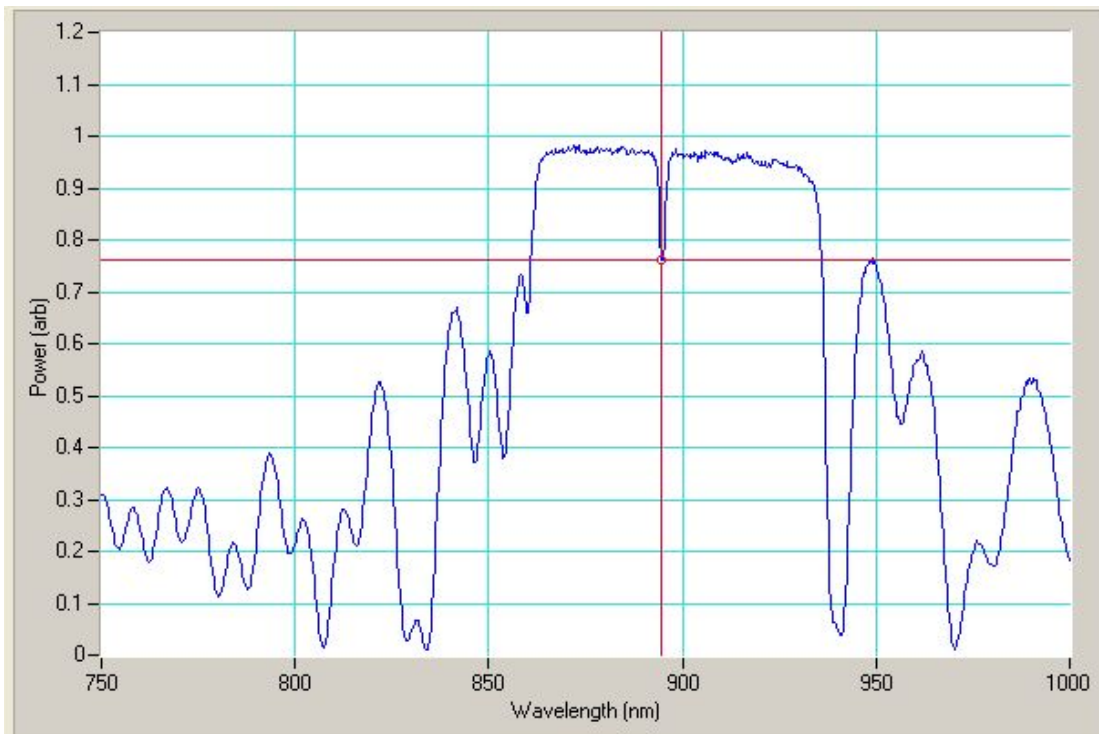


Figure 8. Reflection spectrum of an 894-nm VCSEL wafer.

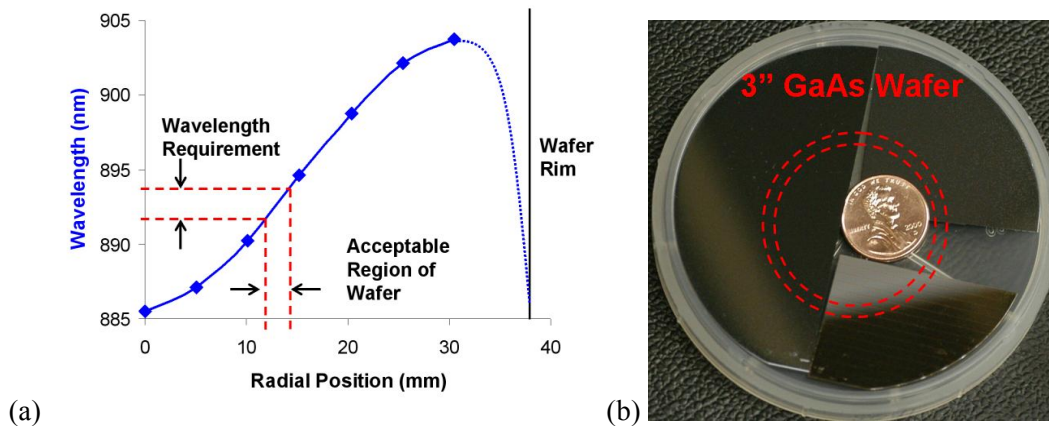


Figure 9. (a) Cavity resonance wavelength versus radial position on the GaAs wafer. (b) Picture of a 3-inch-diameter GaAs wafer, with dotted lines showing the annular region that meets the wavelength requirement

We now describe the VCSEL fabrication process, referring back to the cross-sectional schematic diagram shown in Figure 7(a) and ahead to the top view of a completed VCSEL shown in Figure 10. First, the top metal anode ring (Ti,Pt,Au) is deposited to make electrical contact to the p-type DBR, leaving a circular opening for light to emerge from the top of the semiconductor wafer. Second, the aperture and top metal are protected by a photoresist disk, and we etch through the semiconductor DBR layers using a Cl-based reactive ion etch process to create the semiconductor mesa shown in Figure 7(a). Next, a bottom metal cathode ring (Ge,Au,Ni,Au) is deposited around the base of the mesa to make electrical contact to the n-type DBR below the active region. The wafer is then baked in a furnace at 420C for approximately 30 minutes, in a wet steam atmosphere, which converts the $\text{Al}_{0.98}\text{Ga}_{0.02}\text{As}$ layer immediately above the active region into electrically insulating aluminum oxide, as shown by the blue layers in Figure 6(a). The selective oxidation of $\text{Al}_{0.98}\text{Ga}_{0.02}\text{As}$ proceeds from the edge of the mesa toward the center at a rate of approximately 0.5 microns per minute. The mesa diameter is approximately 33 microns, so that a 30-minute oxidation leaves a 3-micron disk of un-oxidized semiconductor in the center of the mesa. The electrically insulating aluminum oxide forces current to travel through the 3-micron circle at the center of the mesa, and hence the laser emission comes from this region, as shown by the picture of an operating VCSEL in Figure 9. Finally, we pattern photoresist and reflow it at 200C to form polymer bridges that ramp gently from the top of the mesa down to the substrate surface on which the wire bond pads will be deposited. The photoresist bridges appear in Figure 10 as the dark regions that extend radially in the +y and -y directions from the VCSEL mesa. Finally, bond pad metal is deposited to create the 80-micron-diameter anode bond pad below the VCSEL mesa, flanked on the left and right by cathode (ground) bond pads. If the substrate is doped n-type, as shown in Figure 6(a), then an insulating layer of silicon nitride is deposited before the bond pad metal is applied, so that the bond pads are electrically isolated from the substrate. However, before the bond pad metal is deposited, openings must be etched in the silicon nitride film on top of the anode and cathode metal rings, so that the bond pads are electrically connected to the VCSEL mesa.

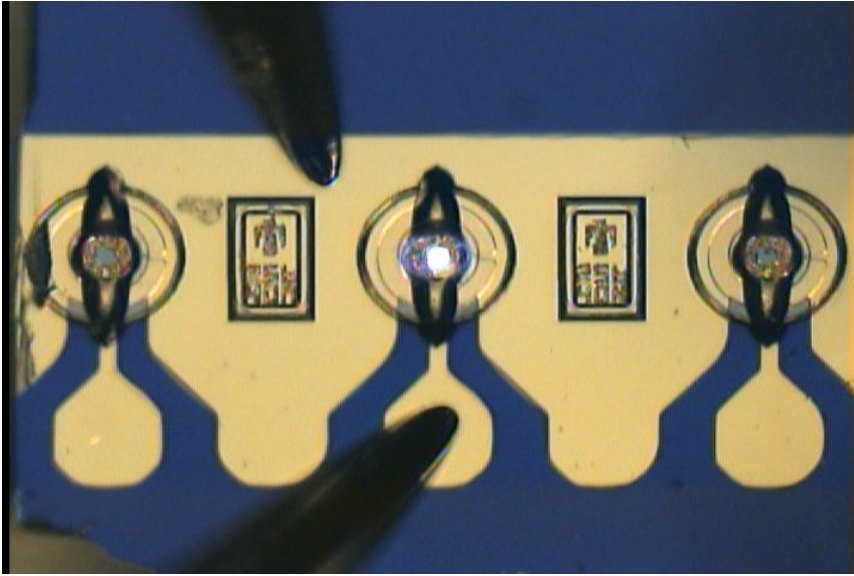


Figure 10. Optical microscope image of a VCSEL biased at 2-mA forward current

Each step of the microfabrication process described in the previous paragraph requires a separate photolithography step. Specifically, 4-inch-square photolithography masks are required for the following steps: anode metal deposition and liftoff, top mesa etch, cathode metal deposition and liftoff, lower mesa etch, silicon nitride etch, photoresist bridge definition, and bond pad metal evaporation and liftoff. For the generation 1 VCSELs that were initially fabricated for this project, we re-used an existing VCSEL mask set. However, we have started the design of a new VCSEL mask set that is better optimized for the needs of this magnetometer project.

After the oxidation step is completed, the VCSEL can be operated at a probe station, as shown by the electrical probe needles in Figure 10. The VCSEL is initially tested at this stage in the process, and is tested again before and after subsequent high-risk process steps. The first standard test that we perform is to measure output optical power and VCSEL diode voltage versus forward current, as shown by the PI and VI plots in Figure 11(a). As shown in Figure 11(a), the VCSEL threshold current is 1.2mA, above which the output power increases with a slope efficiency of 0.61mW/mA. The diode voltage at threshold is 1.65V, yielding a minimum power consumption for this laser of $P_{th} = V \cdot I = 1.65V \cdot 1.2mA = 1.98 \text{ mW}$. The second standard measurement we record is the optical emission spectrum. The optical emission spectrum shown in Figure 11 (b) was measured at a forward bias current of 2.0mA and shows single-frequency operation at a wavelength of 891.65nm at room temperature (25C). Higher-order transverse modes appear at shorter wavelengths than the fundamental mode, and Figure 11 (b) shows a side-mode suppression ratio of 27dB at 2.0mA drive current. For oxide aperture diameters in the range 4 to 5 microns, the side mode suppression ratio will typically decrease as the operating current is increased. A 3-micron-aperture VCSEL might maintain a side-mode

suppression ratio above 25dB over the entire range of drive currents. A 4-micron-aperture VCSEL typically only achieves a side-mode suppression ratio above 10dB for drive currents less than about 2.0mA.

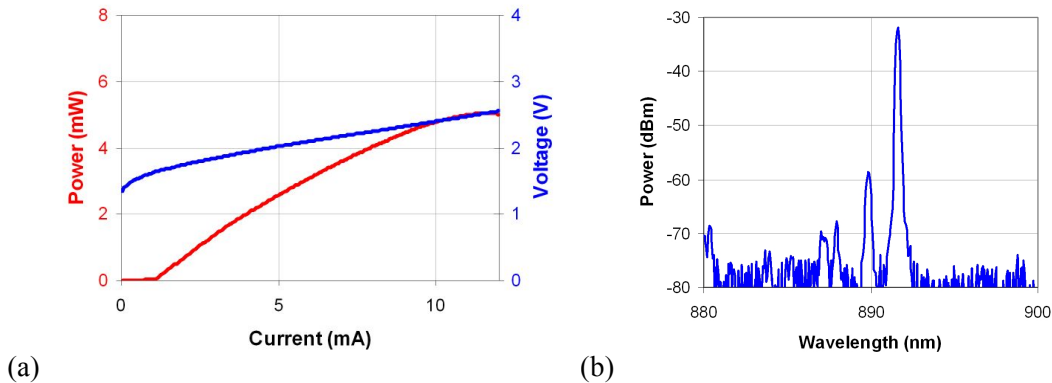


Figure 11. (a) VCSEL output power and diode voltage versus forward current. (b) VCSEL emission spectrum at a drive current of 2mA

Figure 12(a) shows a typically VCSEL device chip that was delivered to NIST for integration and testing with prototype miniature magnetometers. The chip contains 4 VCSELs that are nominally identical and electrically connected such that they share a common cathode connection as shown in Figure 12(b). The chip is approximately 1.25-mm long, 0.50-mm wide, and 0.25mm thick. The anode bond pads (labeled A1, A2, A3, A4) are each 80 microns in diameter. The VCSELs are arranged on a 0.25-mm pitch along the x-axis. While all 4 VCSELs on the chip are nominally identical, the radial variation of wavelength on this particular wafer results in a wavelength that varies versus x position at a rate of +1.2nm/mm. Thus, the left and right VCSELs on this particular chip are separated by 0.75mm in position and hence 0.9nm in wavelength.

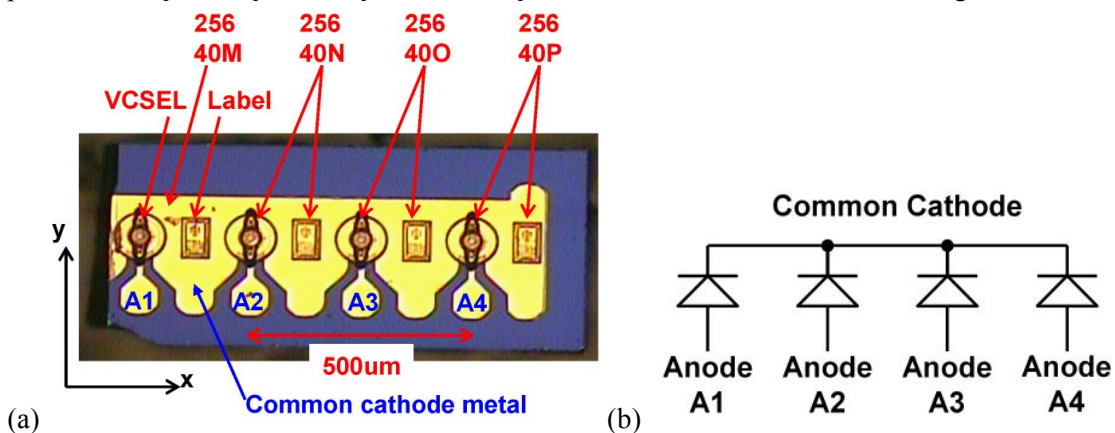


Figure 12. (a) Microscope image of typical VCSEL chip containing 4 VCSELs. (b) Electrical schematic showing the common-cathode connection shared by the 4 VCSELs on the chip.

Finally, we packaged 6 VCSEL chips into TO-39 headers, as shown in Figure 13(a), and delivered them to Geometrics so they could get experience driving VCSELs safely, temperature tuning them and wavelength locking them to the cesium D1 line. Each TO-39 header has 3 pins: 1 connected to the case and 2 that are electrically isolated. The left (L) isolated pin is connected to the anode of one VCSEL and the right (R) isolated pin is connected to the anode of a second VCSEL on the chip. The common cathode is connected to the TO-39 case metal. Thus, 2 VCSELs are electrically connected on each TO-39 header. We put lids (with a single central hole for light output) on the TO-39 headers in order to protect the VCSEL chips and wire bonds from damage due to handling.

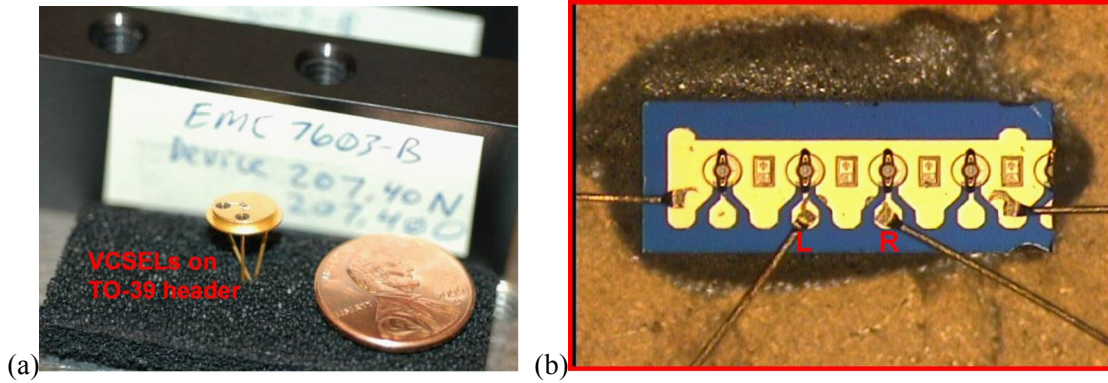


Figure 13. (a) Picture of VCSEL chip mounted on a TO-39 header without a lid. (b) Close-up view of the VCSEL chip showing wire bond connections to the VCSEL chip

Task 1.2: Investigation of VCSEL noise

Completed in February 2007. We investigated the VCSEL noise below 400 kHz because it directly impacts the signal-to-noise ratio and hence the sensitivity of the magnetometer.

Laser diode noise is typically quantified as relative intensity noise (RIN), which is conveniently expressed in terms of measured detector photocurrent as

$$RIN = \frac{i_n^2}{I_{DC}^2},$$

where i_n is the photocurrent noise density (A/ $\sqrt{\text{Hz}}$) and I_{DC} is the DC photocurrent. For a shot-noise limited laser, the measured noise is $i_n^2 = 2qI_{DC}$, so $RIN = 2q/I_{DC}$, where q is the electron charge. As a specific example, a shot-noise limited laser that produces a photocurrent of 1mA yields a RIN of -155dB/Hz. Unfortunately, semiconductor lasers typically exhibit excess noise above the shot-noise level. Moreover, VCSELs are known to exhibit 1/f noise, which makes high-sensitivity measurements at frequencies lower than the 1/f corner frequency (typically 1 to 100 kHz) especially challenging. Our goal was to obtain a RIN level within 10 dB of shot noise over the range of frequencies from 70 to 350 kHz.

A schematic diagram of the experimental setup for measuring the optical intensity noise of our VCSELs over the frequency range from 0 to 500 kHz is shown in Figure 14. We employed a commercially available VCSEL driver (Thorlabs model LDC-200V), which is a low-noise current source that can deliver up to 20mA of output current. The VCSEL and a collimating lens were housed inside an oven to maintain a constant VCSEL temperature, which was typically set in the range 25°C to 60°C. More specifically, the VCSEL was embedded inside a 1-inch-cube of aluminum, that sat on a thermo-electric cooler (TEC) that was driven by a commercially available TEC driver (Thorlabs model TED-200). The temperature of the cube was monitored with a 10-kohm thermistor. The aluminum cube and TEC were both contained inside an aluminum sheet-metal box to reduce air currents. A small hole in the aluminum box allowed the VCSEL output beam to escape and be directed onto a high-sensitivity optical detector.

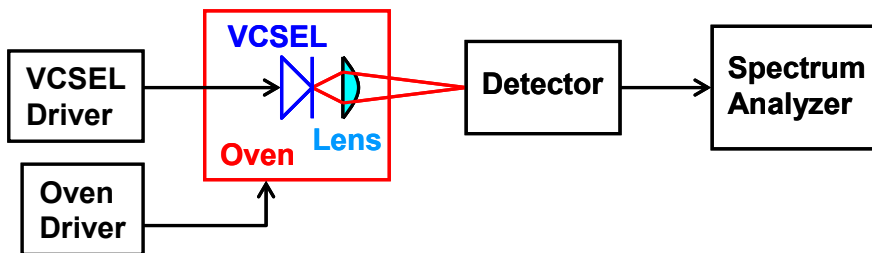


Figure 14 Schematic diagram of VCSEL intensity noise measurement setup

For RIN measurements below 100kHz, we employed a New Focus model 2001 optical detector, which has high-sensitivity and a 3-dB bandwidth of 200kHz. The output of the detector was measured using a low-frequency (up to 100kHz) spectrum analyzer (Stanford Research Systems model SR785 Dynamic Signal Analyzer). Actual RIN measurements of an 894-nm VCSEL from 1 Hz to 100 kHz are shown in Figure 15. The 1/f corner frequency shown in Figure 15 is 1 kHz, which is adequately below the typical frequency range (70 to 350 kHz) for magnetometer measurements.

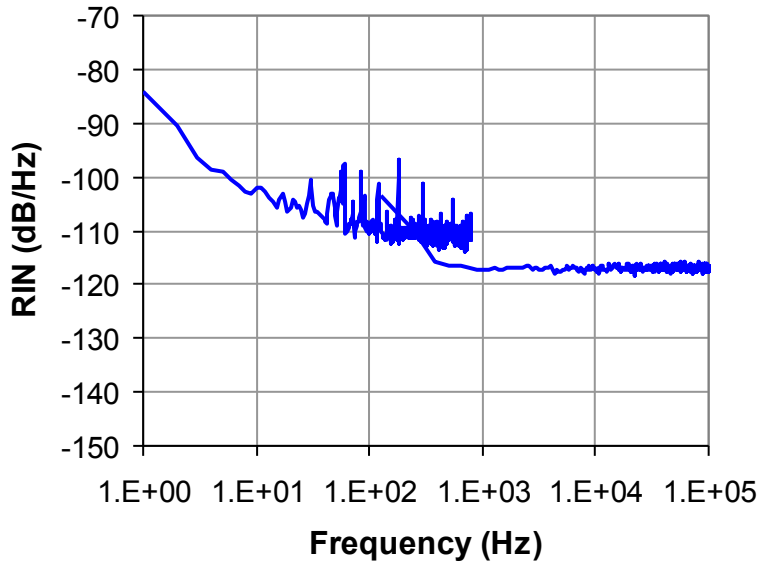


Figure 15. Measurement of 894-nm VCSEL intensity noise from 1 Hz to 100 kHz, using an FFT spectrum analyzer (SRS SR785).

For RIN measurements above 100 kHz, we employed a New Focus model 2051 optical detector set at gain $G = 1 \times 10^3$, which yielded a transimpedance of 626 kOhm and a 3-dB bandwidth of 700 kHz. The output of the detector was measured using a swept-frequency spectrum analyzer (Hewlett Packard model 8562A), with a resolution bandwidth setting of 3 kHz. Actual RIN measurements of an 894-nm VCSEL from 10 to 500 kHz are shown in Figure 16. For these measurements, the VCSEL was biased at 1.07 mA (for reference, the threshold current was 0.44 mA). The DC detector output voltage was 6.9 V, from which we infer a detected photocurrent of 11 uA that corresponds to a shot-noise level of -135 dB/Hz. At a detection frequency of 200 kHz, the measured noise power was -61 dBm within the 3 kHz resolution bandwidth of the spectrum analyzer. Thus, the RIN at 200 kHz was -125.6 dB/Hz ($RIN = (P_{RF}/B)/P_{DC}$, where P_{RF} is the radio frequency power detected within the resolution bandwidth B of the spectrum analyzer). With no optical power incident on the detector, the electronics noise floor was measured at -82 dBm on the spectrum analyzer, so we are assured that we measured laser noise at -61 dBm. Thus, our RIN was approximately 10 dB above the shot noise level. Moreover, we expect the RIN to decrease at higher laser output power levels.

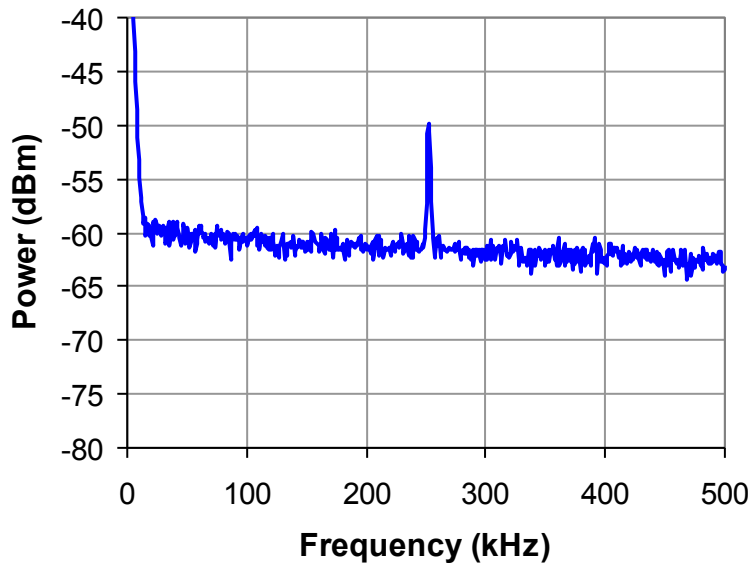


Figure 16. Measurement of 894-nm VCSEL intensity noise from 10 to 500 kHz, using a swept-frequency spectrum analyzer (HP 8562A). The spike near 250kHz is due to noise on the current driver for the laser, not the laser itself.

The measured level of laser noise is adequate for the goals of this project. However, we still want to reduce VCSEL noise in future device generations in order to improve magnetometer sensitivity and hence operating margin.

Task 1.3: Determine whether VCSEL performance is adequate

Go/No-Go completed in March 2007. We passed the go / no-go milestone that was set to determine whether the VCSEL noise performance was adequate to meet the magnetometer sensitivity goals.

In the 2007 publication by Schwindt, et al¹², a magnetometer sensitivity of 5 pT/Hz^{1/2} was reported, with a detected intensity noise 2.6 times the shot noise level. Our first-generation VCSEL noise power level was approximately 4 times higher, which implies a magnetometer sensitivity of 10 pT/Hz^{1/2}, which is adequate to meet the go / no-go milestone.

Task 1.4: Fabricate second-generation VCSELs

Completed in June 2007. A second generation of improved VCSELs was fabricated to meet this milestone. The main goal was to decrease the laser linewidth, which contributes additional noise

¹² P.D.D. Schwindt, B. Lindseth, S. Knappe, V. Shah, J. Kitching, and L.-A. Liew, "Chip-scale atomic magnetometer with improved sensitivity by use of the Mx technique," Appl. Phys. Lett. 90, 081102 (2007)

due to FM to AM conversion via the atomic line shape (transmission versus frequency). A second goal was to decrease the VCSEL foot-print to 0.5-mm square, in order to fit onto the micro-heater element used to thermally tune the VCSEL to the cesium resonance wavelength.

The epitaxial structure used was similar to the first generation design, but we increased the laser cavity Q, shifted the peak optical-gain wavelength, and used a non-conducting GaAs substrate, typically used for high bandwidth ($>1\text{GHz}$) VCSELs. Measured performance of a typical VCSEL is shown in Figure 17. The threshold current of this VCSEL (emc8216a,258,35n) was 1.0 mA, and the optical emission spectrum at 3.0 mA showed a side-mode suppression ratio greater than 30 dB. Separate measurements of optical output versus temperature showed that minimum threshold current was attained at an ambient temperature of 70°C , which is near the intended operating temperature, since the VCSEL is heated in the physics package in order to tune and lock its wavelength to the 894.6-nm (in vacuum) cesium D1 resonance.

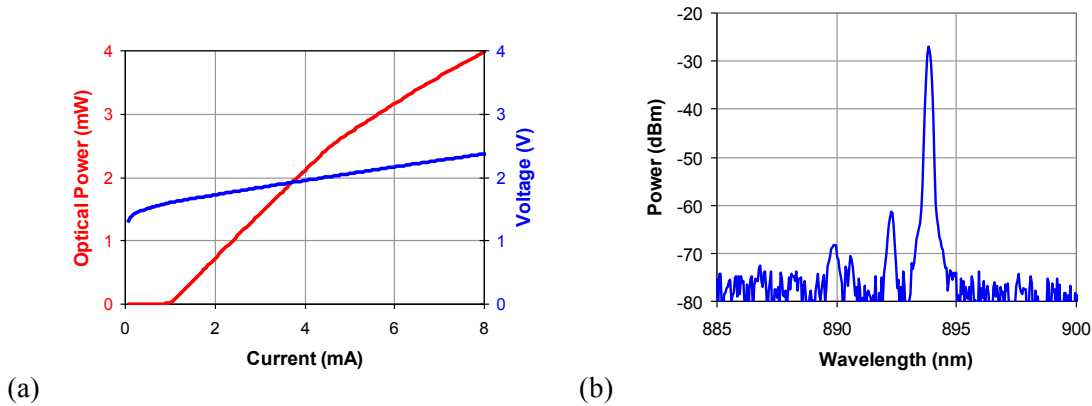


Figure 17. (a) VCSEL output power and diode voltage versus forward current. (b) VCSEL emission spectrum at a drive current of 3mA

Figure 18 (a) shows a new VCSEL chip mounted on a glass micro-heater chip. The VCSEL chip measures $0.5 \times 0.5 \times 0.25$ mm. The glass micro-heater chip measures $4 \times 4 \times 0.15$ mm. We have measured a VCSEL wavelength tuning rate of 0.066 nm per mW of power applied to the micro-heater, as shown in Figure 18(b). Thus, if 40 mW of power is available to drive the micro-heater, any VCSEL whose wavelength falls within a 2.6 nm range can be tuned to the cesium resonance wavelength by means of thermal tuning alone.

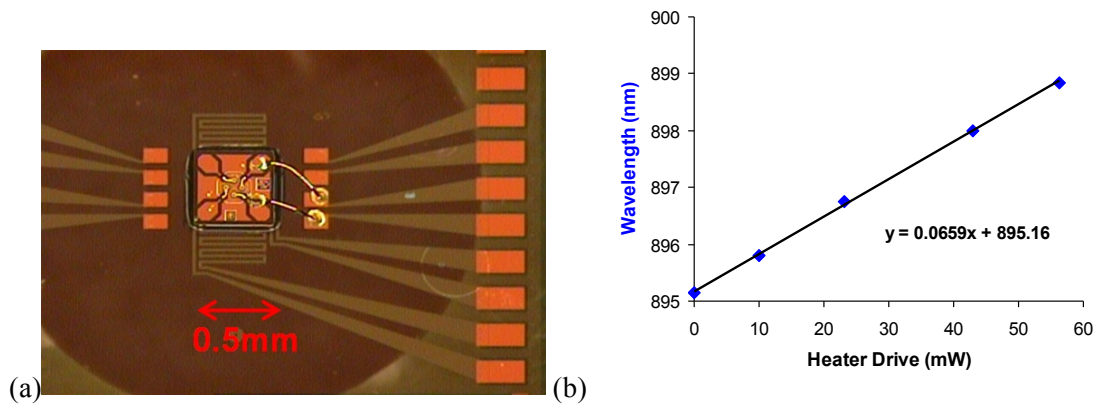


Figure 18. (a) New 0.5-mm-square VCSEL chip mounted on micro-heater substrate. (b) Tuning of VCSEL wavelength versus electrical drive power applied to the micro-heater.

Task 1.5: Develop photodiodes for integration with the physics package

Completed in June 2007. Custom silicon photodiodes were designed and fabricated to produce low-capacitance (small areas) photodiodes suitable for operation at 350 kHz at relatively high transimpedance amplifier gain values (greater than 10 kOhm).

The custom photodiode design and fabrication cost was shared with another project that required small (250um by 500um) photodiode chip dimensions. The photodiode wafer was thinned to 150um so that the chips would be slightly less thick (150um) than wide (250um). Four types of photodiode chips were designed to meet the demands of various applications. Figure 19 shows the four chip design types, labeled **A**, **B**, **C**, **D**. All chips have blanket back side metal of Ti/Pt/Au available as a cathode connection, and the top side metal pads (anode and optional cathode) are also Ti/Pt/Au. The active photodiode area is anti-reflection coated, with a single quarter-wave layer. Photodiode chip type **A** provides the largest active area, measuring 200um by 300um, and a single top-side anode connection. Photodiode chip types **B**, **C**, and **D** provide both anode and cathode pads on the top side of the chip, and active areas measuring 200um, 100um, and 50um, respectively, by 200um. For the magnetometer project, we only planned to use photodiode chip types **A** and **B**.

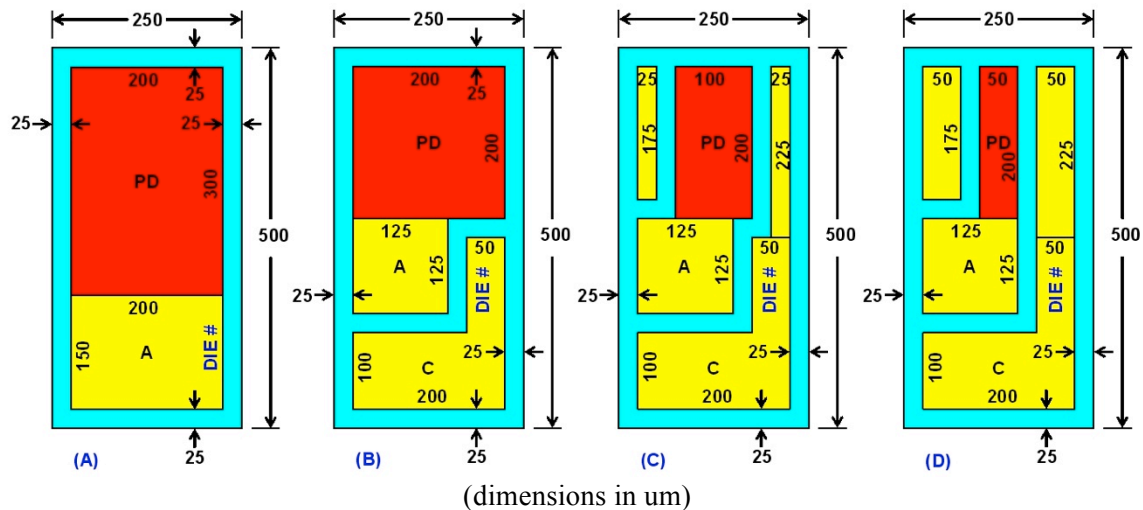


Figure 19 Four photodiode chip design types: A, B, C, D. The active photodiode area is shown in red, and the top-side metal pads are shown in yellow. Top side metal bond pads are labeled “A” for anode and “C” for cathode.

The photodiodes were fabricated by Opto-Diode Corporation from 4-inch-diameter silicon wafers. The “Silicon2” mask set was designed at Sandia with a repeating unit cell, shown in Figure 20, which consists of a single row of 10 photodiode chips, numbered 0 to 9. Chips 0, 1, 2, 3 are type A; chips 4,5,6 are type B; chips 7,8 are type C; and chip 9 is type D. The chips are designed to measure 250um by 500um, and they are arranged on a pitch of 13mil (330.2um) by 23mil (584.2um) so they can be diced on a saw that steps in mil units and has a kerf width of approximately 80um.

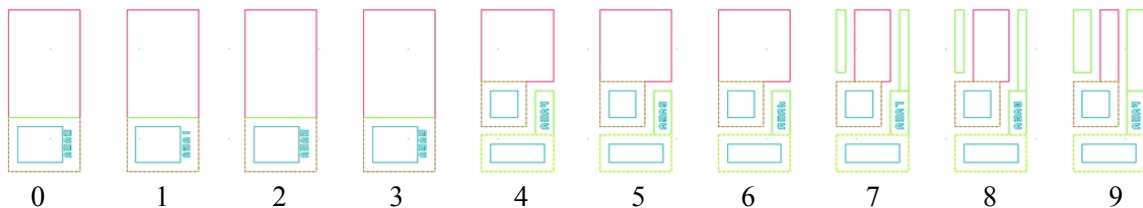


Figure 20. Unit cell of “Silicon2” mask set, containing 10 photodiode chips, numbered 0 to 9.

Each chip was fabricated with a 4-digit serial number of format RRCC that designates the row RR (A0, A1, ..., A9, B0, B1, ..., Z9) and column CC. According to this serial number format, the last digit is the chip number within each unit cell, and therefore corresponds to the chip design type. Unfortunately, the as-fabricated resolution was not sufficient to resolve the 25um tall digits in the serial numbers. However, we can reconstruct the serial number sequence by inspecting the entire wafer and noting that certain alpha-numeric characters usually produce a blank (I, 1), others produce only tiny (10um) dots (J, L, 7), while the remaining characters yield a full-size

(20 μ m) dot. Pictures of four fabricated chips from part OD-1737 wafer 116-2A are shown in Figure 21.

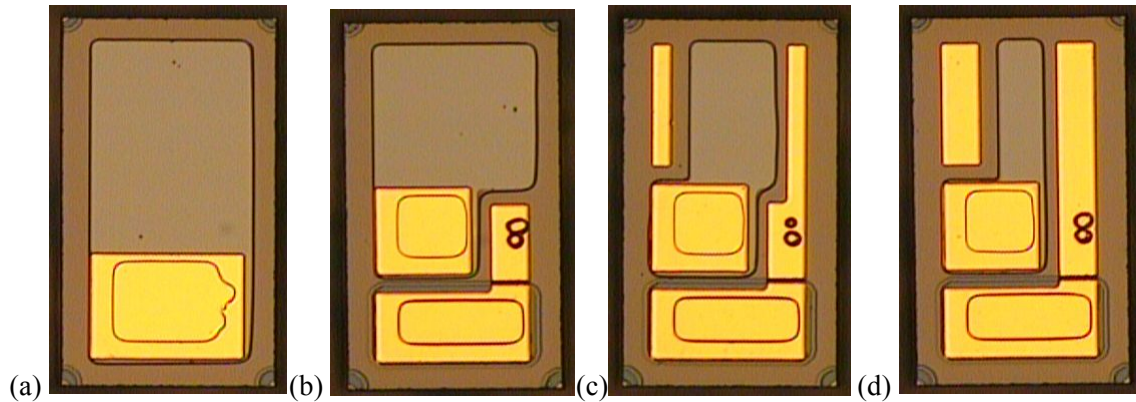
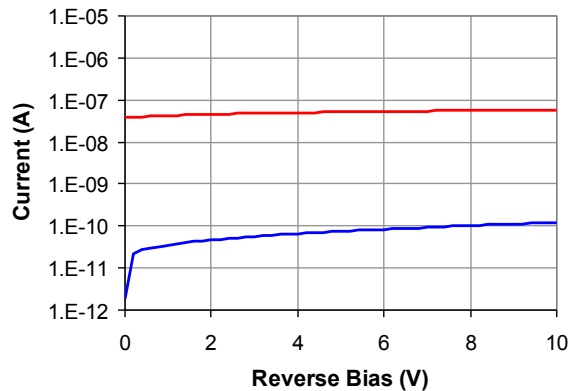
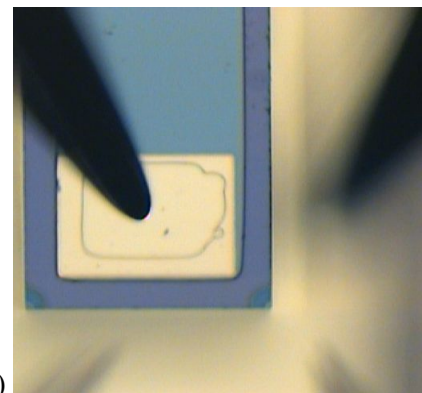


Figure 21. Microscope photographs of all four chip types. The die numbers are (a) I1N1, (b) I1M4, (c) I1M7, (d) I1M9. In the die number regions, the characters I and 1 appear blank and the character 7 appears as a smaller dot relative to the other characters.

Figure 22(a) shows the measured dark current versus reverse bias voltage of die number 14N0 (type A photodiode) of part OD-1737 wafer 116-2A. The dark current was 47pA at a reverse bias voltage of 2V. Figure 22 (b) shows the actual photodiode chip on a probe station, immediately after the measurements were taken.



(a)



(b)

Figure 22. (a) Dark current (blue) and white-light-illuminated current (red) from photodiode die number I4N0 (type A) of part OD-1737 wafer 116-2A. (b) Picture of the measured chip, sitting on a gold platen that electrically connects the (back side) cathode to the right-hand probe (out of focus).

Task 1.6: Develop micro-optics for the physics package

Completed in September 2007. Sandia purchased optical components and performed further fabrication steps as required to enable their integration into a prototype magnetometer physics package.

Figure 23 shows the optics that are used in the magnetometer physics package: lens, polarizer, quarter wave-plate (QWP), and neutral density (ND) filter. The lens (Thorlabs model A414-B) has a focal length of 3.3mm and a diameter of 4.5mm. This lens is placed one focal length away from the VCSEL in order to collimate the beam. The collimated beam diameter (at $1/e^2$ intensity points) is calculated to be 1.3mm, assuming a VCSEL beam divergence (half angle at $1/e^2$ intensity radius) of 0.2 radians (11.5 degrees). The polarizer (Thorlabs model LPVIS100) was purchased with a diameter of 25 mm and diced into 3-mm squares, as shown in Figure 23. The quarter wave plate (CVI model QWPO-895-15-4) was purchased with a diameter of 38 mm and diced into 3-mm squares. The neutral density filter (Thorlabs model NE220B) was purchased with a diameter of 25 mm and diced into 3-mm squares.

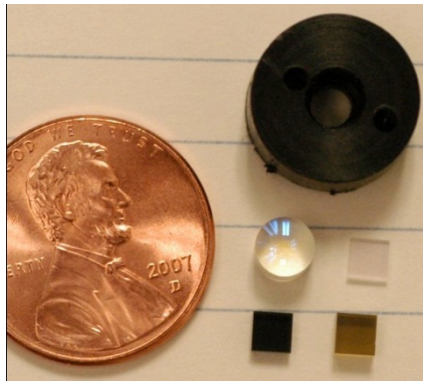


Figure 23. Photograph of optics used in physics package. Quarter wave plate (upper right), polarizer (lower right), neutral density filter (lower left), and lens (upper left).

The main deficiency of the micro-optics described above is that they were all approximately 2 mm thick, so the stack of 4 optics added up to a minimum 8-mm optical path length between the VCSEL and the cesium cell. We note that all of these optical elements, with the exception of the lens, can in principle be made less than 0.1 mm thick.

Cell Fabrication

The alkali vapor cell is a key component in any atomic magnetometer. In traditional atomic magnetometers, the cell is fabricated using glass-blowing techniques and filled by distilling metallic alkali metal into the cell. Recently, micromachining processes were developed, which enable the fabrication of very small vapor cells. In addition to small size, these fabrication processes potentially allow large numbers of cells to be fabricated with the same process sequence, which may result in considerably reduced fabrication costs in a commercial setting.

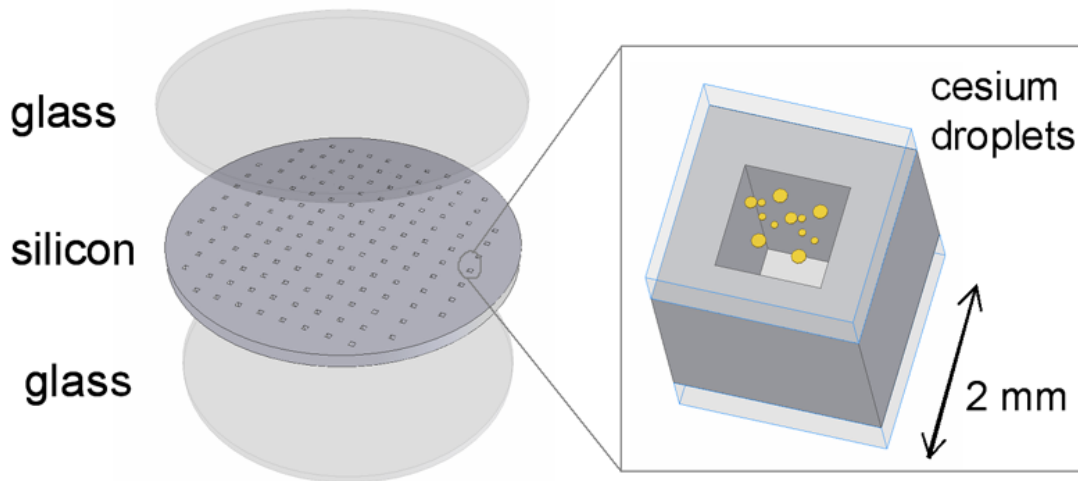


Figure 24. Wafer level manufacturing of Cs cells. Cells could be manufactured inexpensively in large volumes.

With the cell fabrication techniques developed so far, the part of the cell fabrication process in which the alkali atoms are introduced into the cell has been difficult to carry out in arrays. These techniques are based on direct deposition of alkali metals into the cell preform with a pipette¹³, the reaction of stable compounds inside the cell¹⁴ and the use of an atomic beam¹⁵. In all of these techniques, the alkali material is introduced into the cell preforms one by one with a dispenser of some kind. While the use of array-like dispensers may allow many cells to be filled simultaneously, we believe an approach based on evaporated thin films may be more successful in a commercial setting. The goal of this task, therefore, is to develop a method for fabricating large number of alkali vapor cells in wafers based on the deposition and subsequent UV dissociation of alkali azide materials.

The basic procedure we are following is shown in Figure 25. An array of holes of cross-section $\sim 1 \text{ mm}^2$ is etched in a Si wafer 1 mm thick. A glass wafer is then bonded on one side using anodic bonding. A thin film of CsN_3 is then deposited into the bottom of the cell preforms. The preforms are then transferred to a high vacuum system, which is evacuated before a second glass wafer is bonded to the top of the preform structure sealing the cells. The wafer is then removed from the vacuum system and exposed to UV light to dissociate the CsN_3 into Cs metal and N_2 . The released N_2 acts as a buffer gas, preventing collisions of the alkali atoms with the cell walls. The pressure of the N_2 in the cell can be controlled by adjusting the UV exposure time.

¹³ L. A. Liew, S. Knappe, J. Moreland, H. Robinson, L. Hollberg, and J. Kitching, "Microfabricated alkali atom vapor cells," *Appl. Phys. Lett.*, vol. 84, pp. 2694-2696, 2004.

¹⁴ L. A. Liew, S. Knappe, J. Moreland, H. Robinson, L. Hollberg, and J. Kitching, "Microfabricated alkali atom vapor cells," *Appl. Phys. Lett.*, vol. 84, pp. 2694-2696, 2004.

¹⁵ S. Knappe, V. Gerginov, P. D. D. Schwindt, V. Shah, H. G. Robinson, L. Hollberg, and J. Kitching, "Atomic vapor cells for chip-scale atomic clocks with improved long-term frequency stability," *Opt. Lett.*, vol. 30, pp. 2351-2353, 2005.

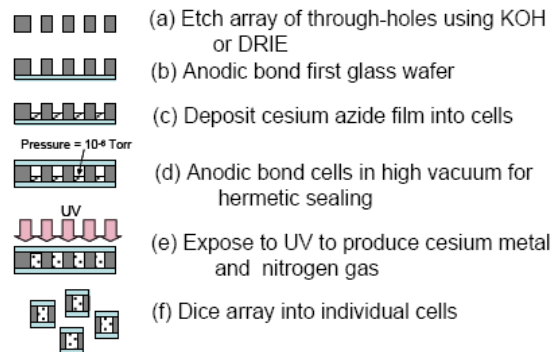


Figure 25. Cell fabrication process for azide-based deposition.

Task 2.1 Fabrication of laboratory equipment for cell filing

We have constructed a thin-film deposition apparatus for depositing CsN_3 into the cell preforms. A schematic and photograph of the apparatus is shown in Figure 26. Thermal evaporation of CsN_3 is not as straightforward as it is with single-element materials such as metals. CsN_3 is thermodynamically unstable and undergoes phase changes when heated. In addition there is tendency toward the material exploding inside the chamber if not heated in a carefully controlled manner. Several parameters of the deposition process were investigated including the heating and cooling rates and evaporation temperature. Although the deposition process is still not well understood, usable CsN_3 films are now routinely deposited in the system.

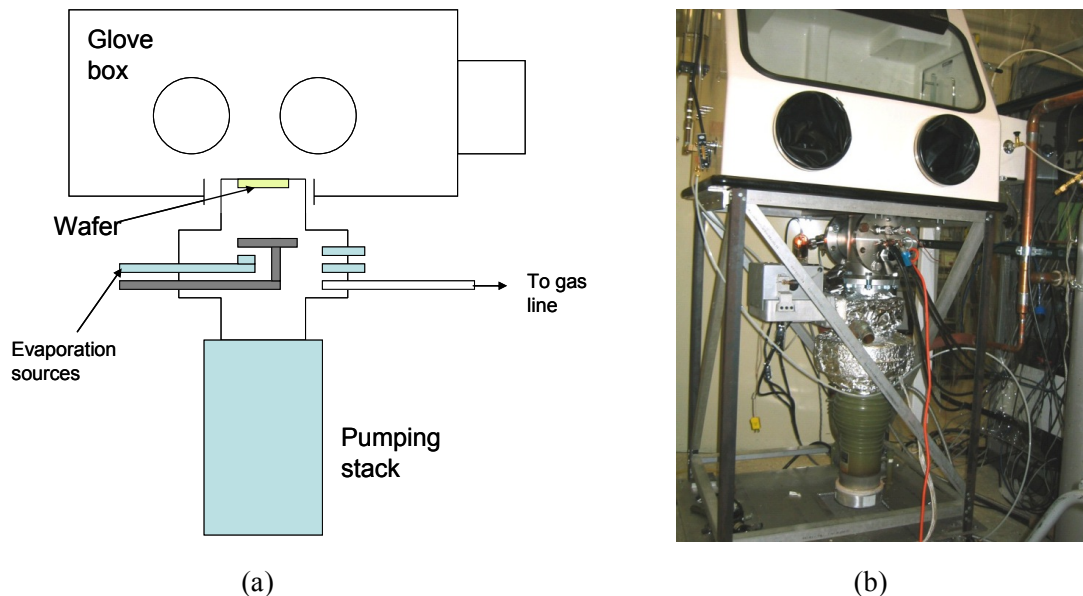


Figure 26. Thin-film azide deposition system constructed at NIST for wafer-level alkali cell fabrication.

The procedure for filling the cells is described in detail in reference ¹⁶. We summarize those results here. Since CsN_3 is highly hygroscopic, a custom vacuum evaporator was constructed that was coupled to a nitrogen glove box such that the deposited films could be stored under inert conditions after deposition. Solid crystals of CsN_3 , obtained commercially, were ground into a fine powder and placed in an alumina crucible heated by tungsten basket filaments. An aluminum foil shadow mask was placed over the preform cavities. After the chamber was pumped to a base pressure of 1.33×10^{-4} Pa (1×10^{-6} Torr), the CsN_3 was heated in stages at a rate of $2^\circ\text{C}/\text{min}$, held at 250°C for several hours, heated to the melting point of 310°C , and held at this temperature for several minutes.

The temperature was then increased to $325 - 360^\circ\text{C}$ and the shutter opened once a stable temperature and pressure were reached. Deposition rates varied from 0.1 to a few nanometers per second, with a pressure of 1.33×10^{-3} Pa (1×10^{-5} Torr). Typical thicknesses deposited were between 100 to 500 nm as measured by the crystal sensor, although the occurrence of splattering and other instabilities makes the measured thickness somewhat variable. Due to the relative lack of thermophysical data on CsN_3 , and also because CsN_3 is an ionic compound, the deposition process is slow, unstable, and not well understood. In general, direct thermal evaporation of compounds is difficult (or impossible, depending on the system in question) because of the tendency of the compound to break down into the constituent species due to the different vapor pressure of each species. Previous researchers have found that dissociation of CsN_3 in vacuum was negligible for temperatures up to 400°C ; nevertheless, we found a strong tendency for CsN_3 self-heating to occur, leading to rapid decomposition or explosion within the vacuum chamber. Thus, once melted, the CsN_3 is unstable and the exact nature of the deposition process is unknown due to simultaneous competing thermodynamic processes. We have observed that deposition of these films occurs through a combination of slow controlled vacuum evaporation and uncontrolled “splattering” of the evaporant, leading to highly nonuniform films that contain, at least partially, CsN_3 . Various combinations of thermal cycling, soaks at intermediate temperatures for various lengths of time, and adjusting the heating/cooling rates were found to stabilize the deposition process and reduce the likelihood of sudden or large fluctuations in temperature and pressure, to yield functional films.

¹⁶ L.-A. Liew, J. Moreland, and V. Gerginov, "Wafer-level fabrication and filling of cesium-vapor cells for chip-scale atomic devices," proceedings of Eurosensors, Göteborg, Sweden, 2007.

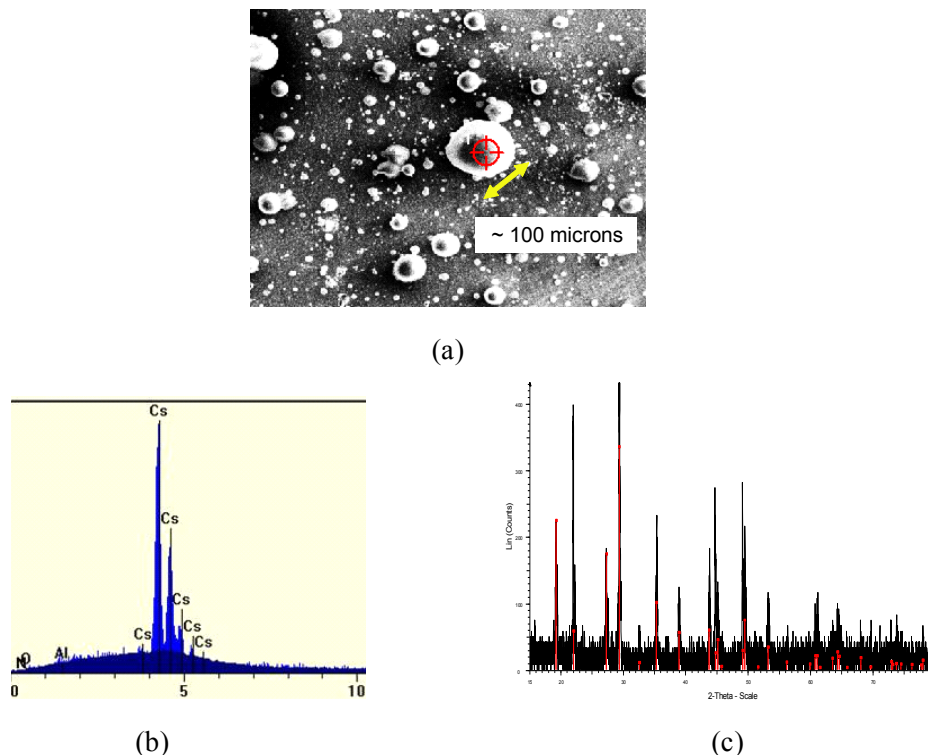


Figure 27. (a) Scanning electron micrograph of the CsN_3 films deposited with thermal evaporation. (b) A quantitative elemental analysis shows the presence of nitrogen in the films. (c) X-ray diffraction measurements suggest the film becomes more amorphous after deposition.

The deposited films are non-uniform and consist of big agglomerates that range in size from a few micrometers to a hundred micrometers in diameter, as shown in Figure 27(a). Energy dispersive spectroscopy indicated the presence of nitrogen in the films, as expected. Oxygen was also detected but its presence is inconclusive, possibly indicating a partial decomposition of the evaporant during deposition and producing cesium oxide, or else the oxygen detected could be that present in the aluminum substrate on which the films were deposited for EDS analysis (Figure 27 (b)). Following CsN_3 deposition, the preform was placed in a custom vacuum anodic bonding chamber, baked overnight under vacuum, and then subsequently anodically bonded to another Pyrex piece at a temperature of 300 °C, voltage of 1000 V, and chamber pressure of 2.6×10^{-4} Pa (2×10^{-6} Torr), thus enclosing a high vacuum inside the cell cavities. The sealed cell array was then exposed under a UV lamp of wavelength 254 nm and intensity of 2.3 mW/cm^2 , over various lengths of time ranging from 8 hours to over 100 hours (depending on the thickness and nature of the deposited film). Finally, the array was diced into individual cells. The N_2 gas produced from the reaction serves as a buffer gas to prevent collisions between the atoms and cell walls, and its pressure is proportional to the amount of azide dissociated. Because the residual azide is a thin film, the cell windows are relatively clean and optically transparent, more so than

in our previous work in which the presence of bulk oxides or salts partially attenuated the laser light during cell testing or device operation.

This technique was used to fabricate small arrays of alkali vapor cells, demonstrating the fundamental capability of this process for array fabrication. Photographs of a small array, as well as optical absorption spectra confirming the presence of alkali atoms and a buffer gas, are shown in Figure 28. A larger array of cells is shown in Figure 29.

With our experimental set up, we found that the vacuum bonding of the glass covers on the cells is considerably more challenging. Longer bond times are required, which has yielded some poorer quality and some chemical reactions of the cesium azide films at the elevated temperatures of the bonding process. In addition, the bonding process generates some O₂ within the cells, oxidizing some of the Cs. We found that depositing a larger amount of azide into the cell initially solves this problem. It may be necessary to remove the oxygen trapped in the cell later by pumping it out and sealing the hole with a thick file deposition.

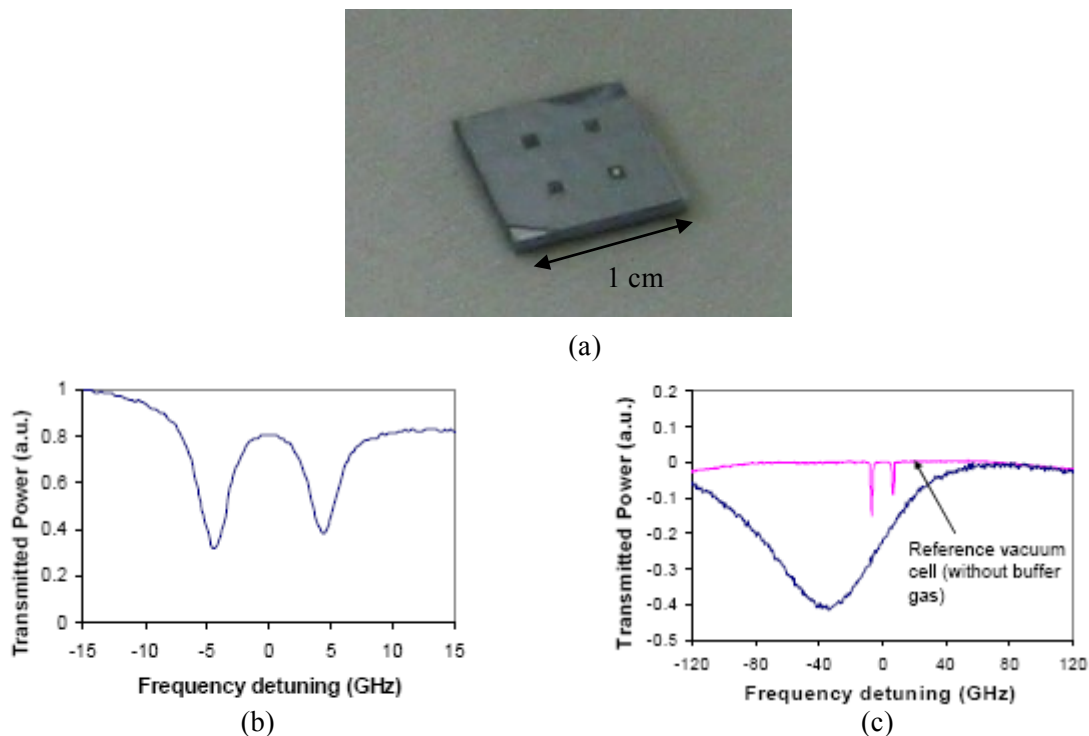


Figure 28. (a) Photograph of a 2X2Cs cell arrays fabricated with the azide deposition method described above. (b) Optical absorption spectrum of a cell containing approximately 200 Torr of N₂ buffer gas. (c) Optical absorption spectrum of a cell containing approximately 1000 Torr of N₂ buffer gas.

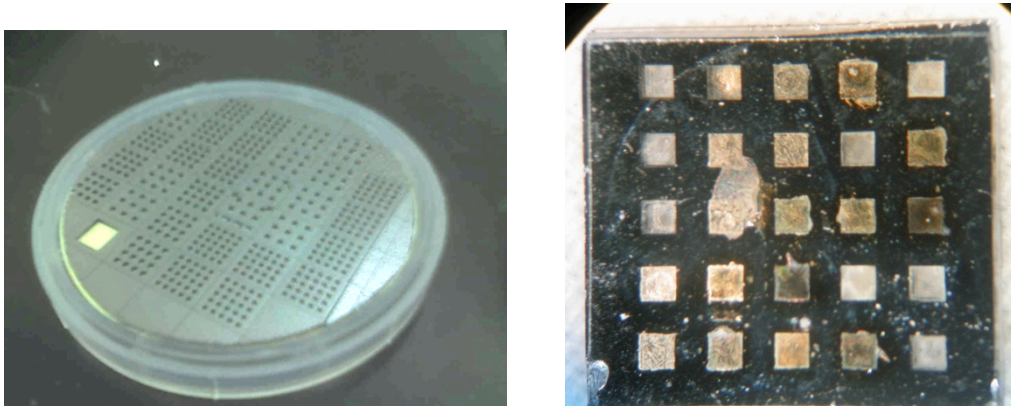


Figure 29 Arrays of cells showing feasibility of large volume production

The effect of UV irradiation time has been investigated. We show in Figure 30 the effect of increased irradiation time. Longer times cause more azide to dissociate, increasing the buffer gas pressure (and amount of cesium, which condenses on the cell walls). The buffer gas pressure determines the line widths -- higher buffer gas pressure creates broader lines. Since buffer gas pressure is one parameter we wish to adjust for optimal magnetometer performance, it is important to show we can do that with the method.

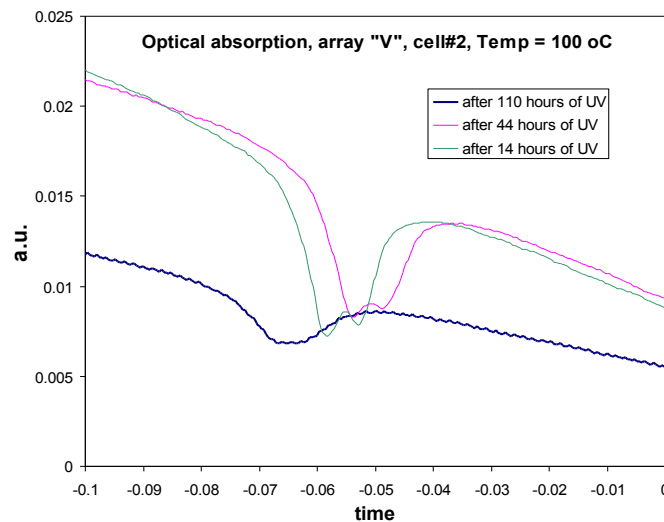


Figure 30 Effect of UV irradiation time, showing increasing buffer gas pressure (wider line width)

In addition, we have found that the buffer gas pressure is consistent across cells in a single array. In our experiments, the buffer gas pressure did vary from one array to another, depending upon

the initial thin-film deposition of the azide into the cells. This, then, must be carefully controlled in production – with our methods, we were not as able to carefully control this process.

The gas composition stability was investigated by heating the cells for several weeks and measuring the optical absorption characteristics during that time. We made many such measurements and various temperature and with many cell. Figure 31 shows an example of the results. Good stability was obtained.

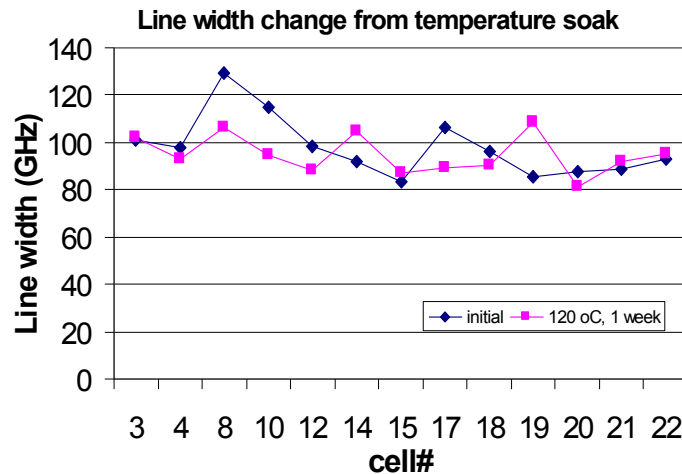


Figure 31 Line width variation before and after temperature soak.

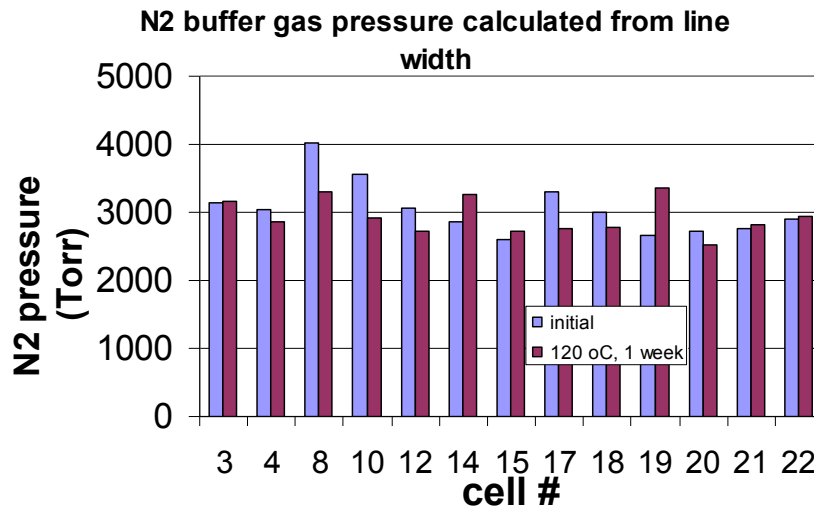


Figure 32 Buffer gas pressure calculated from the line width before and after the temperature soaking

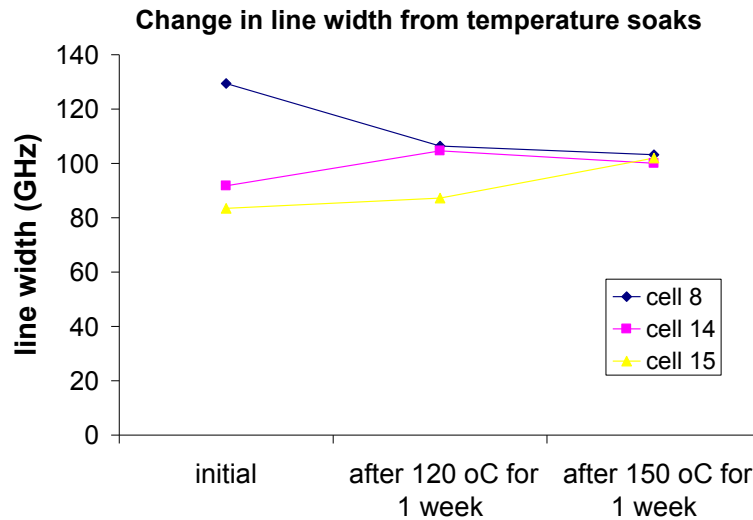


Figure 33 Change in line width during temperature soaking.

We conclude, therefore, that the basic wafer-level cell fabrication process has been characterized and that cells can be fabricated in a satisfactory manner in arrays. We had some repeatability issues with our experimental setups. We feel, however, that with improved production equipment, the process could be made repeatable, ensuring accurate and stable buffer gas pressures.

Task 2.2 Determine cost and performance of cell filling methods

Several methods of fabricating alkali vapor cells have been developed in our lab (and elsewhere) over the last few years. Most of these methods were developed for use in chip-scale atomic clocks; for these devices, it is critical that the contents of the cell, in particular the pressure of the buffer gas, remain stable over long time periods. The stability of the cell contents translates directly into frequency stability. However, atomic magnetometers are considerably less sensitive to changes in buffer gas pressure than atomic clocks. This is because the Larmor precession frequency on which the field measurement is based is largely insensitive to the pressure of the buffer gas contained in the cell with the alkali atoms.

There are two suitable cell filling methods. In each method, material is deposited into a cell “preform”, consisting of a piece of Si with a hole etched into it, and a glass wafer bonded onto one side. The first filling method is based on the deposition of alkali atoms directly into the cell preform using an alkali source inside a vacuum chamber. The alkali atoms are created through a chemical reaction of BaN_3 and AlCl , where Al represents the alkali species, in a glass ampoule with a very thin necked opening positioned above the cell opening. When the ampoule is heated, alkali atoms are created in the reaction, exit the ampoule through the opening and accumulate in the bottom of the cell. The ampoule is then moved out of the way and a second glass piece is bonded to the top of the preform, sealing the alkali atoms (along with a buffer gas) inside the cell.

In the second method, suitable at present only for Cs, a thin film of CsN₃ is evaporated into the preform via heating with an electron beam in a crucible. A second glass wafer is bonded into the top of the Si wafer in an evacuated environment. The cell is then exposed to UV light, which dissociates the CsN₃ into Cs and N₂; the pressure of N₂, and corresponding quantity of Cs, are controlled through the time the cell is exposed to the UV light.

The key advantage of the azide deposition technique over the ampoule technique is that a large number of cells could be filled simultaneously, thereby substantially reducing manufacturing costs. Since the amount of the material consumed in the fabrication is almost zero, the costs are determined almost completely by operator and equipment use time. Once the relevant equipment has been constructed and installed, we estimate the following processing time.

Capital Equipment

Equipment necessary for the azide deposition process is reasonably modest. The following table list the main components:

Item	Approximate Cost
Bench-top anodic bonder Hot Plate High-voltage power source Cables Sample holders and fixtures	\$2,000
Azide Evaporator Vacuum System Roughing pump Diffusion pump Liquid N ₂ trap Pneumatic valves and controller Rough pressure sensor and controller Ion gauge and controller Vacuum feedthroughs Chamber and flanges	\$20,000
Glove Box	\$15,000
Thermal evaporation system Thickness monitor Crystal sensor head Crystals Tungsten basket filaments Alumina crucibles High power current source for filaments Shutter and feedthrough Thermocouples Electrical and water feedthroughs	\$10,000
Miscellaneous parts and machining labor Attaching glove box to diff pump Building support frame for glove box and diff pump	\$2,000

Making fixture and sample holders Making and modifying feedthroughs in flanges Optional Parts Mass spectrometer Baffle boat RF cleaning	\$20,000
Vacuum Anodic Bonder Vacuum system Roughing pump Turbo pump and controller valves Pressure gauges (TC gauges, ion gauge) and controller Custom jar (baseplate and glass jar) Electrical and TC feedthroughs Frame/cart Flanges, connectors	\$15,000
Anodic bonding system High voltage power source High current power source for heaters Parts and labor for sample fixture and electrodes Thermocouples Cartridge heaters Solid-state relays Temperature controller Linear motion drives	\$10,000

Cost of production (small quantities)

A skilled technician could perform the following:

Mask fabrication – 1 hour (This is for these simple cell designs which are just holes in silicon. The more complicated the design, the longer the mask fabrication will take. For example, when making in-situ heaters, the masks took overnight)	*
Wafer prep and nitride/oxide deposition – 8 hours	**
Front and back side patterning – 6 hours	
Silicon etching – 8 to 12 hours	**
Post-etch clean and nitride/oxide strip – 6 to 8 hours	**
Preform fabrication (i.e. anodic bonding) – 2 to 6 hours	
Azide deposition – 8 to 24 hours	
Vacuum anodic bonding – 12 to 36 hours	*
UV Photolysis – 8 to 100 hours	*
Dicing – 2 to 4 hours	
Total time to make one wafer of cells: about 65 to 200 hours	

Notes:

1. Each wafer can contain 400 – 1000 cells depending on the cell size and spacing.
2. * processes for which the operator does not have to be present for the majority of the time
3. ** processes for which multiple wafers can be done together, and which may be done unattended.

Task 2.3 Demonstration of wafer-level filling techniques

We describe a modification to our original proposal for developing a capability for wafer-level fabrication of alkali vapor cells for chip-scale magnetometers. The new approach is to create wafers of vapor cells by deposition of CsN_3 into preforms followed by UV dissociation after sealing. In this method, a cell preform is created by etching a hole in a Si wafer and then bonding a glass wafer onto one side, sealing the cell at one end. CsN_3 is then deposited into the cell preform. At present the material is deposited in bulk form; we anticipate that evaporation of a film of CsN_3 material would also be possible. The preform, with the CsN_3 in place is placed into an evacuated chamber. Inside this chamber, the second glass wafer is bonded to the surface containing the remaining opening, sealing the CsN_3 material in the cell. The cell is then exposed to UV light from a mercury lamp. After some time, the CsN_3 dissociates into Cs metal and N_2 . By timing the UV exposure, the correct pressure of N_2 can be obtained to act as a buffer gas in the cell.

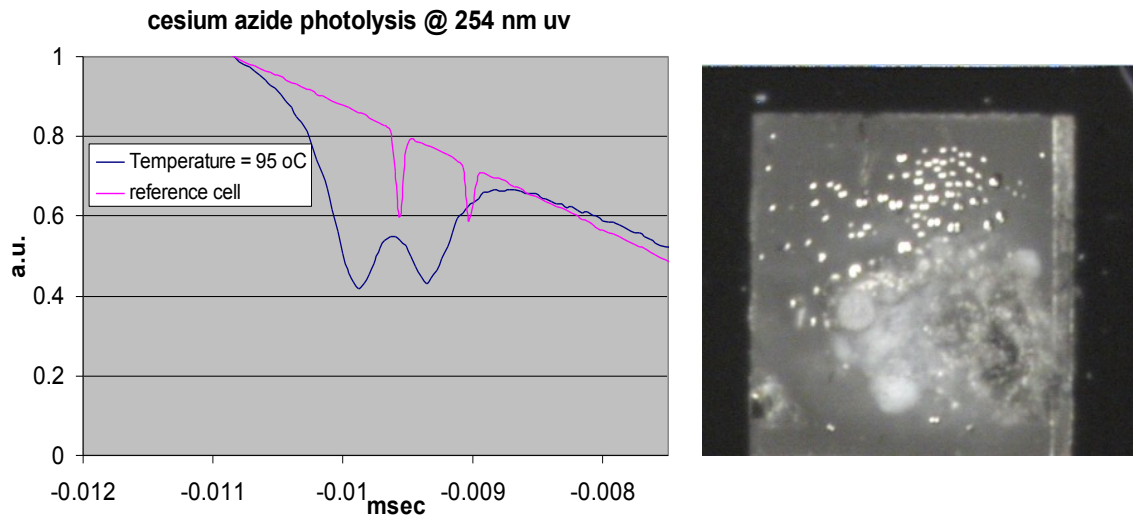


Figure 34 (a) Optical absorption resonance of a microfabricated cell based on UV-photodissociation of CsN_3 . (a) A micrograph of the cell.

We have demonstrated microfabrication of cells in this way with a pressure of buffer gas appropriate for use in a chip-scale atomic clock. The optical absorption resonance of one of these cells is shown in Figure 34(a). From the width and shift of the optical absorption lines, the pressure of the buffer gas can be determined to be ~ 100 Torr. A CPT resonance excited between the $m_F=0$ hyperfine-split atomic states is shown in Figure 35.

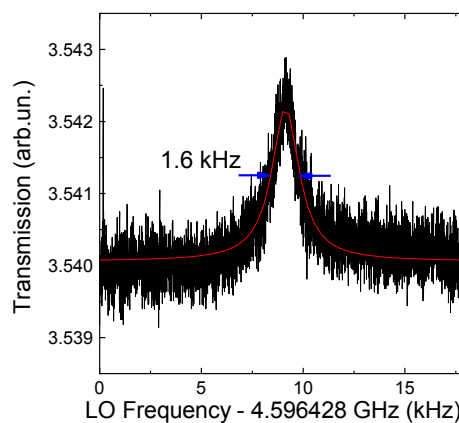


Figure 35. CPT resonance measured in a cell fabricated with UV-photodissociation of CsN_3 .

The advantages of this method over the original proposed cell filling scheme (with an array of ampoules containing the alkali metal) are that more conventional fabrication equipment (shadow-mask based deposition) is used and it is generally a less complicated process since there are no moving deposition parts. We therefore expect it to be more amenable to commercialization. The main disadvantage is that it may only be possible to make cells filled with Cs, since RbN_3 dissociates at too low a temperature. But we are evaluating this difficulty at present. In addition, one must be willing to have N_2 in the cell with Cs as a buffer gas; other buffer gases can be added, but N_2 is created in dissociation so it will be present. Finally, there may be slow changes in N_2 pressure over time as dissociation continues or reverses. While this presents some significant problems for use of such cells in atomic clocks, it should not limit their use in magnetometers.

Work was carried out to investigate the consistency of the Cesium azide coating process. Since Cesium azide is a highly volatile material, it was anticipated that small changes in the deposition parameters (evaporant temperature, heating rate, substrate temperature) might cause substantial changes in the quality of the coating. This was found indeed to be the case. Thin-film samples deposited under different conditions were tested using x-ray diffraction measurements, as shown in Figure 36. Figure 36 (a) shows the spectrum from a sample of CsN_3 that was heated to its evaporation temperature but now evaporated. The series of strong peaks shows that the material is in the BCT phase. Figure 36 (b) shows a spectrum from an evaporated sample. The missing peak at $2\theta = 27^\circ$ and the weaker peak strengths at other diffraction angles shows that the sample is polycrystalline but still BCT phase. This suggests the film is indeed CsN_3 . The final spectrum, Figure 36(c), shows a strong peak at $2\theta = 21^\circ$, indicating that the film has become a single crystal of Cs_7O during the evaporation. This experiment indicates the importance of the exact heating temperature schedule in preparing high-quality thin films.

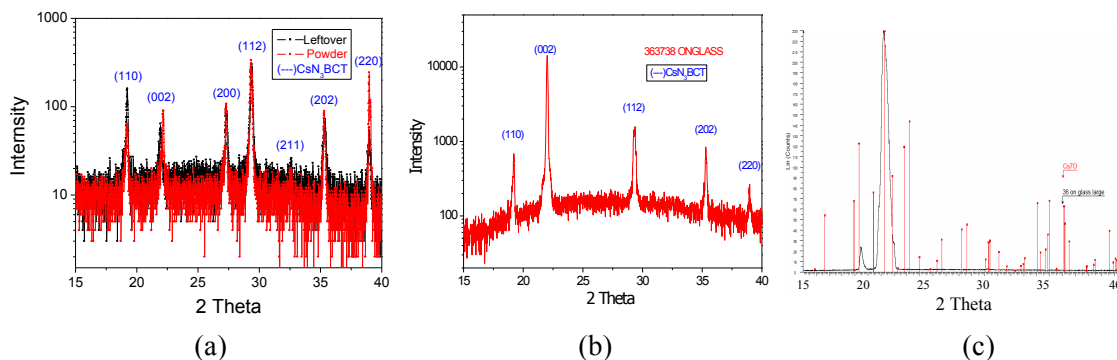


Figure 36. X-ray diffraction spectra from (a) bulk CsN_3 , as obtained after heating in the crucible to the deposition temperature but no evaporation, (b) deposited thin-film sample and (c) second thin-film sample deposited under a different crucible heating schedule.

Signal Extraction and Detection Techniques

Introduction

The sensitivity of most atomic magnetometers is given by the equation

$$\delta B_{\min} = \frac{h}{g\mu} \frac{1}{(S/N)T_2\sqrt{\tau}}, \quad (1)$$

where g is the ground-state Lande factor of the atom, S/N is the signal-to-noise ratio, T_2 is the spin relaxation time, τ is the measurement time, μ is the Bohr magneton and h is Planck's constant. The two parameters over which we have most control are S/N , the signal-to-noise ratio, and T_2 , the relaxation time. S/N can be controlled by varying the temperature of the cell, and hence the alkali atom density, and the optical power in the probe field. T_2 is determined by a variety of design parameters including the size of the alkali vapor cell, the pressure and composition of the buffer gas, and the cell temperature and the intensity of the applied optical field. For cells of size $\sim 1 \text{ mm}^3$, relaxation times in the range of 100 μs to 1 ms are typical, depending on the buffer gas pressure, leading to transition linewidths in the range of 1 kHz to 10 kHz. A plot of typical transition linewidths as a function of buffer gas pressure is shown in Figure 37.

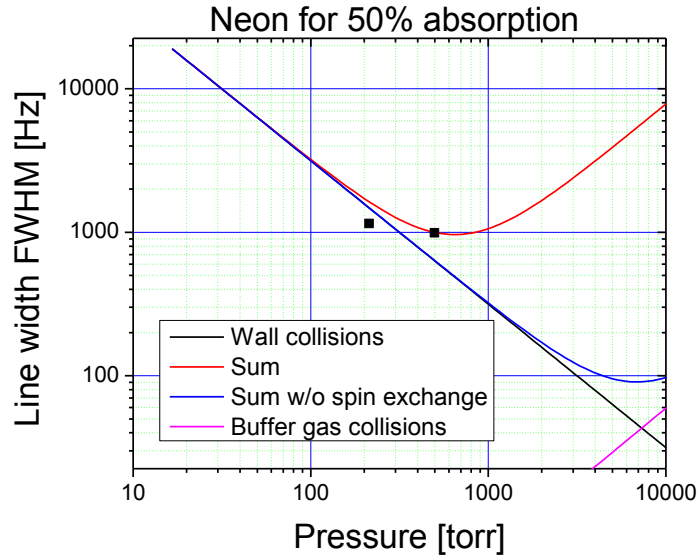


Figure 37. Transition linewidth ($1/\pi T_2$), as a function of the buffer gas pressure for an alkali vapor cell of volume 1 mm^3 . This plot assumes that the cell temperature is adjusted to produce 50 % absorption, and therefore the approximately maximize the S/N of the instrument.

In many experimental configurations, the S/N ratio is limited by photon shot noise of the probe beam. The random arrival times of the photons at the photodetector creates this fundamental noise source. For a probe beam with a total power of 100 μW , the signal-to-noise ratio is approximately $10^7 \sqrt{\text{Hz}}$, for a signal contrast of 100 %. Typically, the signal contrast is closer to 1 %, resulting in a S/N of $10^5 \sqrt{\text{Hz}}$. If the transition linewidth is 1 kHz ($T_2 = 3.3 \times 10^{-4} \text{ s}$, 142 nT

for ^{87}Rb), the sensitivity of an atomic magnetometer based on ^{133}Cs is approximately 4 pT/ $\sqrt{\text{Hz}}$. As will be shown below, sensitivities close to this level are obtained in highly compact devices.

As a result of these measurements, we have concluded that sensitivities in the pT/ $\sqrt{\text{Hz}}$ range are probably not feasible with the FM-NMOR technique, at least in cells containing a buffer gas. The main limitation is the short relaxation times in the small cells. We have therefore identified several other excitation techniques are compatible with the high buffer gas pressure and therefore that result in sensitivities in the pT/ $\sqrt{\text{Hz}}$ range; we describe these below.

Task 3.1a Frequency-modulated Non-linear Magneto-Optic Rotation

One method of exciting the atomic spin resonance is based on FM-modulated non-linear magneto-optic rotation (FM-NMOR)¹⁷. In this method, a linearly polarized laser beam is frequency-modulated on and off the resonance at the Larmor frequency, synchronously pumping the atoms into an aligned state, precessing about the static magnetic field. The atomic alignment in turn alters the polarization of the excitation field, which is detected with a polarization analyzer. The main advantage of this method, as compared to more conventional schemes that pump the atoms into a polarized state, is the absence of a fundamental heading error due to optical pumping.

Early measurements at NIST of this excitation technique on millimeter-scale alkali vapor cells containing a buffer gas uncovered a fundamental problem. For very small alkali vapor cells, a high buffer gas pressure is needed, to prevent collisions of the alkali atoms with the cell walls from causing excessively rapid decoherence, broad linewidths and low sensitivity. However, the high buffer-gas pressure broadens the optical transitions in the atom to the point where the excited state hyperfine structure is in fact no longer resolved. For ^{133}Cs , the excited state hyperfine splitting on the D1 line is 1.3 GHz and the broadening of the optical transition is approximately 20 MHz/Torr. In order for resonances of reasonable size to be excited via FM-NMOR, the excited-state hyperfine structure of the atomic transition must be resolved. We found experimentally that because of this broadening, it was not possible to operate the FM-NMOR magnetometer with a buffer gas pressure above ~ 10 Torr. At this low buffer gas pressure, the relaxation time was rather short ($< 100 \mu\text{s}$) and the best sensitivity obtained was about 1 nT/ $\sqrt{\text{Hz}}$, as shown in Figure 38.

¹⁷ D. Budker, D. F. Kimball, V. V. Yashchuk, and M. Zolotarev, "Nonlinear magneto-optical rotation with frequency-modulated light," *Phys. Rev. A*, vol. 65, pp. -, 2002

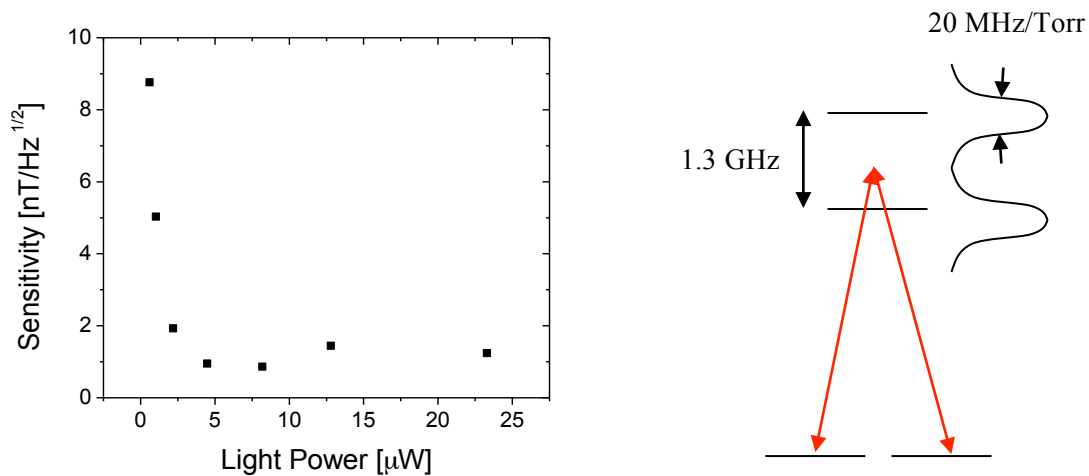


Figure 38. (a) Sensitivity as a function of optical power for a MEMS cell of volume 1 mm^3 , containing a buffer gas of 10 Torr Ne. (b) Atomic energy level structure showing broadening of the excited state hyperfine structure due to the presence of a high-pressure buffer gas.

As a result of these measurements, we have concluded that sensitivities in the $\text{pT}/\sqrt{\text{Hz}}$ range are probably not feasible with the FM-NMOR technique, at least in cells containing a buffer gas. The main limitation is the short relaxation times in the small cells. We have therefore identified several other excitation techniques are compatible with the high buffer gas pressure and therefore that result in sensitivities in the $\text{pT}/\sqrt{\text{Hz}}$ range; we describe these below.

Task 3.1b Mx Implementation

The current generation of commercial Cs magnetometers are based on the Mx excitation technique¹⁸. This technique is shown in Figure 39. The main advantage of this technique is that a large signal can be obtained, even when the buffer-gas pressure is high. As a result, the relaxation time can be made quite long (milliseconds) and the sensitivity of a magnetometer based on this approach can be in the range of a few $\text{pT}/\sqrt{\text{Hz}}$.

¹⁸ A. Bloom, "Principals of operation of the Rubidium vapor magnetometer," *Appl. Opt.*, vol. 1, pp. 61-68, 1962.

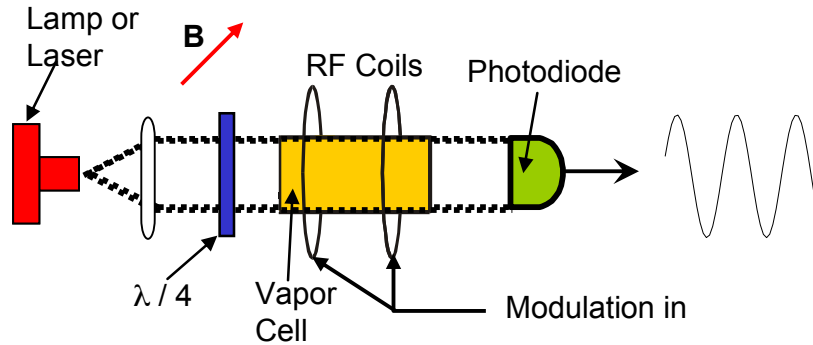


Figure 39. Mx excitation of alkali atom spin precession.

This sensitivity level was verified experimentally using a table-top apparatus, in which a light beam was sent through a MEMS alkali vapor cell of volume 2 mm^3 containing a buffer gas pressure of 810 Torr of a combination of N_2 and Ne. The cell demonstrated a linewidth of 635 Hz and a sensitivity of $6 \text{ pT}/\sqrt{\text{Hz}}$ was measured, as shown in Figure 40. This sensitivity level is a better by a factor of 8 than our previous CPT-based magnetometer¹⁹. We conclude from this measurement that a sensitivity in line with the goals of this project is feasible with the Mx excitation technique and a MEMS alkali vapor cell.

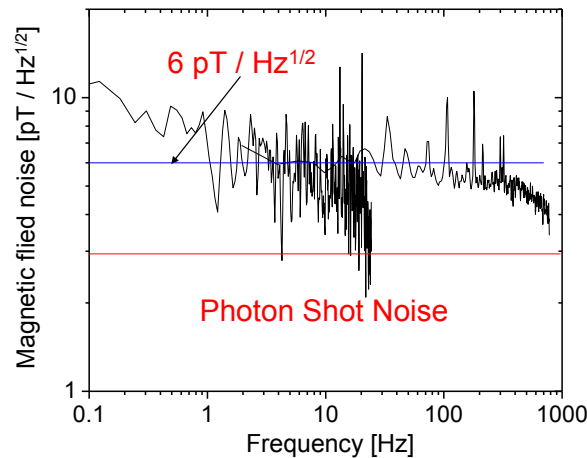


Figure 40. Sensitivity measured with the Mx excitation technique in a MEMS alkali vapor cell. The measurement demonstrates that sensitivities in the range of $1 \text{ pT}/\sqrt{\text{Hz}}$ are possible in highly miniaturized alkali vapor cells fabricated by MEMS processing techniques.

Although the sensitivity appears acceptable, we now face the difficulty that with the Mx excitation technique, a substantial heading error exists due to optical pumping. In addition, this excitation technique results in both equatorial and polar dead zones, and requires moderately

¹⁹ P. D. D. Schwindt, S. Knappe, V. Shah, L. Hollberg, J. Kitching, L. A. Liew, and J. Moreland, "Chip-scale atomic magnetometer," *Appl. Phys. Lett.*, vol. 85, pp. 6409-6411, 2004.

complex electronics to run. Nevertheless, we believe that these difficulties can be overcome by using two laser beams with orthogonal circular polarizations (see discussion below) and with moderate engineering of the control system. A schematic of one possible control system is shown in Figure 41.

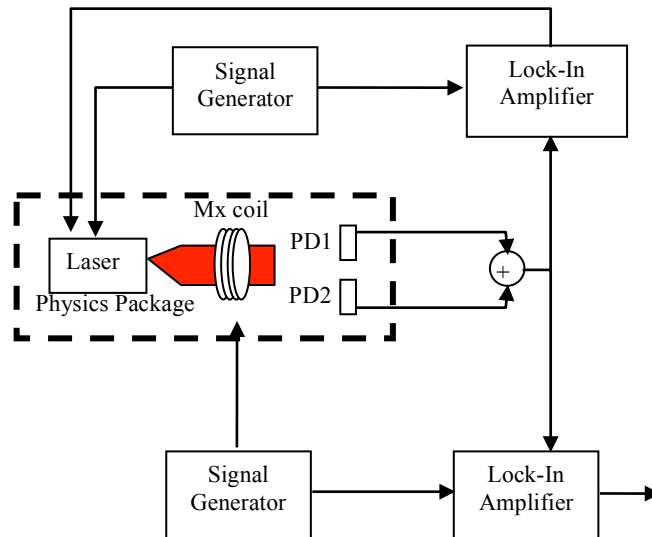


Figure 41. Block diagram of electronics required to operate a chip-scale atomic magnetometer in the Mx configuration.

Task 3.1c Bell-Bloom Implementation

A second alternative to the FM-NMOR technique is the Bell-Bloom excitation technique²⁰, shown schematically in Figure 42. In this excitation method, no oscillating magnetic field is applied to the atoms. Instead the frequency (or amplitude) of the optical pumping light field is modulated at the Larmor precession frequency. Atoms are therefore pumped into a coherently precession state by the synchronous optical pumping. The precession is read out by monitoring the intensity of the transmitted light using a photodiode. By comparing the phase of the component of the photodiode signal oscillating at the Larmor frequency with the phase of the original laser modulation, the resonance can be observed and the Larmor frequency determined.

²⁰ W. E. Bell and A. L. Bloom, "Optically driven spin precession," *Phys. Rev. Lett.*, vol. 6, pp. 280-283, 1961.

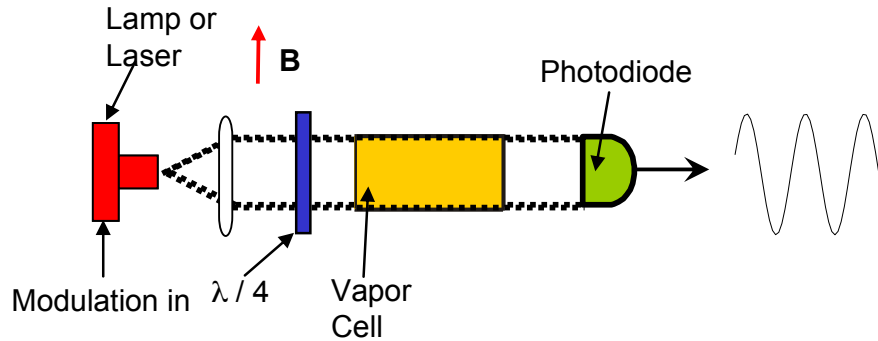


Figure 42. Bell-Bloom excitation of Larmor precession in an alkali vapor cell. In this method, the frequency of the light is modulated by changing the injection current of the laser. The frequency modulation tunes the circularly-polarized laser beam on and off the resonance synchronously with the Larmor precession, which pumps the atoms into a precessing polarized state.

The precession atomic polarization can be excited either by modulating the laser wavelength at the Larmor precession frequency or at one-half of this value, as shown in Figure 43. If modulation at the Larmor frequency is used, the laser wavelength is detuned somewhat from the center of the atomic absorption resonance. As a result, the optical pumping rate is at a maximum exactly once per cycle: this occurs when the laser is tuned exactly to the peak of the atomic absorption profile. If instead modulation at one-half the Larmor frequency is used, the laser is tuned to the center of the atomic absorption profile. Now the optical pumping rate is a maximum exactly twice per modulation cycle and therefore the atoms are again pumped at the Larmor frequency.



Figure 43. Bell-Bloom excitation methods. (a) The spin precession can be excited by modulating the laser wavelength at the full Larmor frequency and detuning the average laser wavelength from the line center. (b) Alternatively, the precession can be excited by modulating the laser wavelength at one-half the Larmor frequency and tuning the laser wavelength to the center of the optical transition.

The sensitivity of both types of Bell-Bloom magnetometer was found to be comparable to that of the Mx magnetometer and typically was in the range of 10-15 pT/√Hz for the full-frequency Bell-Bloom and 15-20 pT/√Hz for the half-frequency Bell-Bloom. The main limitation here is the slightly smaller value of S/N due to the fact that the optical pumping rate cannot be varied independently from the excitation strength. Further optimization appears possible, for example by adjusting more carefully the temperature of the alkali vapor cell.

Measurements of the noise of the magnetometer were measured in the following way; a schematic of the system is shown in Figure 44. The injection current of the laser is modulated with a sinusoidal signal from a signal generator at 37 kHz. The laser is detuned from the optical resonance of the atoms by about one-half an optical linewidth (approximately 10 GHz, for the buffer gas pressure used in this experiment). The amplitude of the laser current modulation is such that the peak-to-peak frequency deviation of the laser is 20 GHz. Because the laser frequency is being modulated on and off the optical resonance, a signal is observed on the CSAM photodiode at the modulation frequency. When the ambient magnetic field is swept near 8285 nT, the phase (and amplitude) of this output signal changes as the optical field is modulated additionally by the Larmor precession of the atoms. When sent to the input of a lock-in amplifier with the original modulation signal as the reference, a resonance is observed in the lock-in output as the magnetic field is scanned.

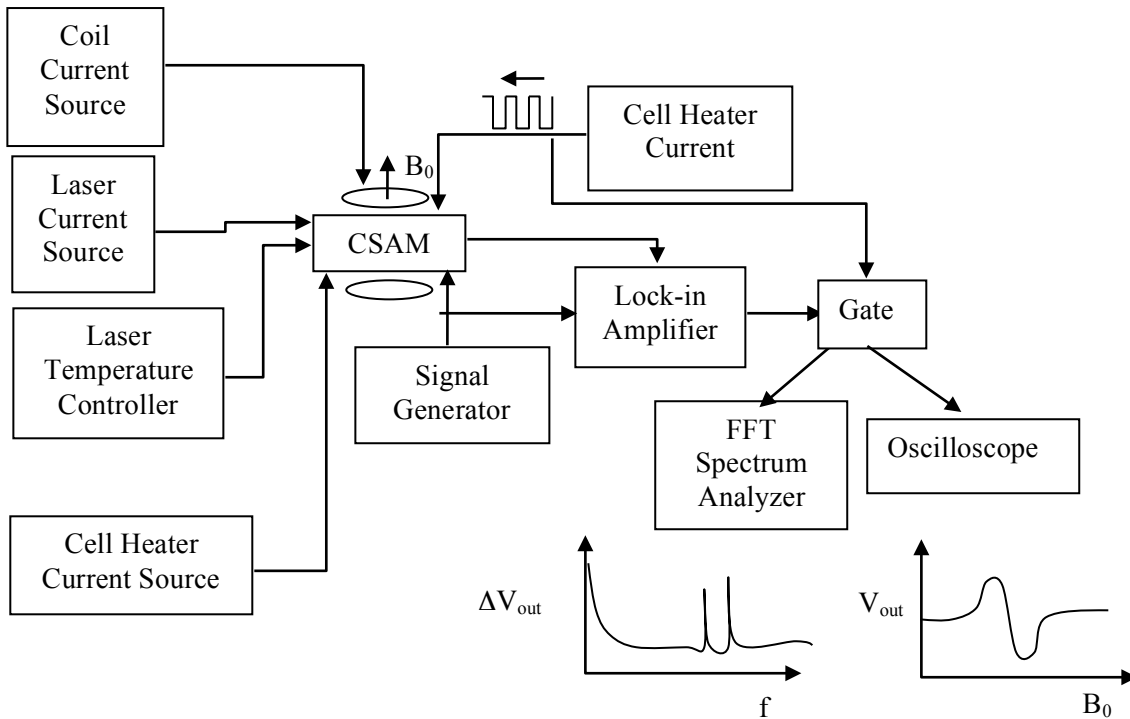


Figure 44. Apparatus for measuring the sensitivity of the magnetometer in the Bell-Bloom configuration.

The cell is heated to a temperature of approximately 135 °C with a pair of resistive heaters placed on either side of the cell. These resistive heaters generate a magnetic field that prevents a good measurement of the magnetometer sensitivity. To avoid this difficulty, the heaters are chopped on and off and the signal and noise is measured only when the heater current is off.

The dispersive resonance is shown in Figure 45(a). The width of the resonance is approximately 500 nT and the peak-to-peak voltage, for this particular setting of the pre-amplifier and lock-in amplifier gains, is 0.9 V. By fitting the slope of the resonance at its center, the voltage-to-magnetic field conversion factor is 3 mV/nT.

The magnetic field is then adjusted to a constant value corresponding to the center of the resonance. The voltage fluctuations at the lock-in output are measured with a FFT spectrum analyzer. These voltage fluctuations (in V/ $\sqrt{\text{Hz}}$) are converted into equivalent magnetic field fluctuations by the conversion factor above. The noise spectrum of the magnetometer (sensitivity) is shown in Figure 45(b).

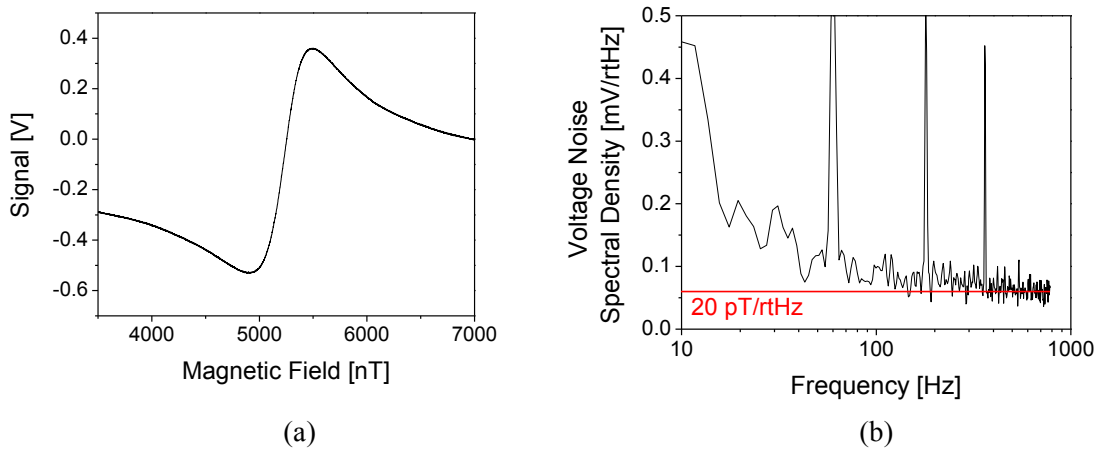


Figure 45. (a) Dispersive Larmor resonance (lock-in output) for the Bell-Bloom configuration with a modulation frequency of 37 kHz. (b) Noise spectrum from the lock-in output with the magnetic field tuned to the center of the resonance in (a). Noise below 100Hz is primarily due to limitations in the experimental test method.

The magnitude of the noise measured in the magnetometer can be understood in the following way. The total optical power detected by the resonance is approximately 95 μW . This results in a DC photocurrent out of the photodetector of $i_0 = 28 \mu\text{A}$. The shot noise (in $\text{A}/\sqrt{\text{Hz}}$) corresponding to this photocurrent is $\sqrt{2ei_0} = 3 \times 10^{-12} \text{A}/\sqrt{\text{Hz}}$. The signal is the amount by which the amplitude of the modulated component of the photocurrent changes over the resonance. This is about 1 % of the total DC photocurrent. The signal-to-noise ratio is therefore roughly $0.01\sqrt{i_0/2e} \sim 10^5 \sqrt{\text{Hz}}$. The estimated sensitivity from the linewidth and S/N is 5 pT/ $\sqrt{\text{Hz}}$, about a factor of 4 lower than what is measured in the experiment between 100 Hz and 1 kHz. This additional noise is probably due to noise on the laser intensity or frequency that is picked up by the detection system. The noise below 100 Hz is dominated by the effects of the chopping of the heater current.

The Bell-Bloom configuration offers several advantages compared with the Mx technique. The first is the absence of an equatorial dead zone, allowing a sensitive measurement of magnetic

field over a wider range of orientations. Secondly, no RF coils are needed in the device structure. This simplifies the device architecture from a MEMS fabrication viewpoint since fewer components are required. Third, since no oscillating magnetic field is needed to excite the resonance, there is less chance of individual components in a sensor array interfering with each other.

Comparing the operation of the two Bell-Bloom configurations (full-frequency vs. half-frequency), the half-frequency Bell-Bloom has two distinct advantages over the full-frequency Bell-Bloom. One is that the laser can be locked to the exact center of the optical absorption resonance, rather than to the side of the resonance. This not only makes the locking algorithm easier to implement but makes it less likely that the nominal laser wavelength will drift over time due to changes in the resonance shape or width. A second advantage is that there is less likelihood that spurious RF fields generated by the leads providing electrical current to the laser will interfere with the Bell-Bloom signal. The RF fields in the half-frequency Bell-Bloom method are of course at one-half the Larmor frequency and therefore will be out of resonance with the atomic spins. One possible control system implementation for this Bell-Bloom excitation technique is shown in Figure 46.

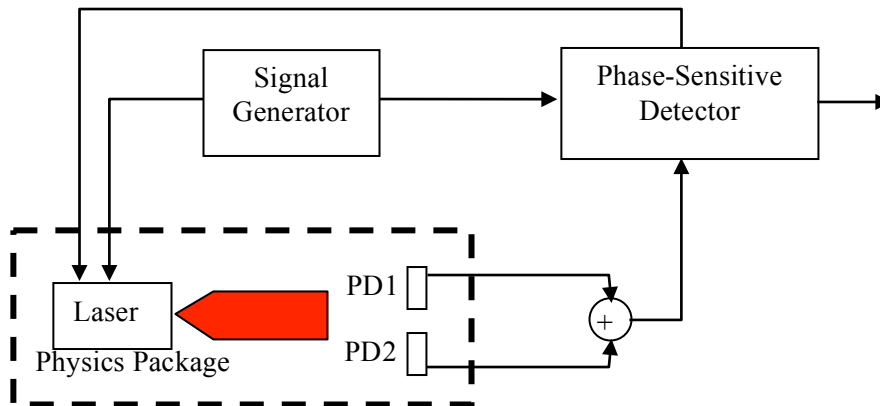


Figure 46. Electronics implementation for the full-frequency Bell-Bloom excitation method.

Given the comparable sensitivities of the three alternative excitation methods (Mx, full-frequency Bell-Bloom and half-frequency Bell-Bloom), we have identified the half-frequency Bell-Bloom method as the optimal method for this project. We plan therefore to proceed by implementing a MEMS design for this type of magnetometer. A summary of the advantages and disadvantages of each method is shown in Table 1.

Table 1 Summary of Tradeoffs

Method	Sensitivity	Dynamic Range	Dead Zones	Type	Implementation
CPT	10-100	100,000nT	None	Scalar	Small heading error, difficult signal processing
FMNMOR	50-100	100,000	Equatorial	Scalar	Very complicated

					optics
Mx	6pT	100,000	Polar and equatorial	Scalar	Wire coil needed, cross talk in arrays.
Full F Bell-Bloom	10-15 pT	100,000	Polar	Scalar	Extraneous resonances
Half F Bell-Bloom	15-20pT	100,000	Polar	Scalar	Easy

Task 3.2 Demonstration of self-oscillation

A self-oscillating magnetometer based on frequency-modulated non-linear magneto-optic rotation was constructed and tested at NIST. A schematic of our experimental apparatus is shown in Figure 47. We use a vertical cavity surface emitting laser (VCSEL) tuned to the D1 line to illuminate a vapor cell (diameter 3.5 cm) filled with isotopically enriched 87Rb. The beam from the VCSEL is collimated to a diameter of ~1.3 mm and is attenuated to ~62 uW. The interior of the cell is coated with an anti-relaxation paraffin layer, and the cell is placed inside a two-layer magnetic shield containing a solenoid that applies a magnetic field along the propagation direction of the light. The cell is placed between a linear polarizer and an analyzer oriented at 45 degrees with respect to each other to measure the polarization rotation caused by the atoms.

To excite the resonance, we modulate the VCSEL injection current at twice the Larmor frequency such that the peak-to-peak amplitude of the modulation of the laser frequency is 1.38 GHz, roughly three times the Doppler width of the optical resonance. When the laser frequency is on resonance, an atom in the laser beam is optically pumped by the linearly polarized light into an aligned state along the direction of the light's polarization. After the atom exits the laser beam, the atomic alignment precesses at the Larmor frequency due to the magnetic field. Because the state of atomic polarization is symmetric, the atomic alignment returns to the same state after half the Larmor precession period. Thus, with light modulated at twice the Larmor frequency, the atomic alignment is resonantly driven as the atom moves in and out of the laser beam. We probe the atomic alignment with the light by detecting a rotation of the light polarization at the output of the cell. Optical rotation occurs when the atomic alignment is at an angle to the light polarization, and the light is maximally rotated when both the light is on resonance and the atomic alignment is at a 45 degree angle relative to the light polarization. The FM-NMOR signal shows optical rotation in opposite directions depending on the sign of the angle between the atomic alignment and the laser polarization.

We operate the experiment in three modes: the unlocked mode, the analog self-oscillating mode, and digital self-oscillating mode (Figure 47). In the unlocked mode an external driving oscillator modulates the VCSEL current, and the FM-NMOR signal from the balanced receiver is sent to a lock-in amplifier with the original modulation as the reference. When frequency of the oscillator is swept about the FM-NMOR resonance frequency, a dispersive line shape is observed at the in-phase output of the lock-in amplifier. The measured sensitivity of the magnetometer in the unlocked mode is plotted in Figure 48 and is ~0.15 pT / rt Hz. at 1 Hz bandwidth. In the unlocked mode we manually tune the driving oscillator to the nominal FM-NMOR resonance to measure

the magnetic field. A magnetometer using lock-in detection that automatically acquires and locks to the FM-NMOR resonance would require the additional complication of a microprocessor, especially in light of the fact that there is another, lower amplitude FM-NMOR resonance when the VCSEL is driven at the Larmor frequency.

If the magnetometer is made to self-oscillate, its control system can be greatly simplified. To make FM-NMOR system self-oscillate, the output waveform from the balanced receiver needs to emulate the input waveform before it is fed back to the VCSEL. As shown in the Figure 47, the output waveform is not a simple replication of the input modulation, and in the analog self-oscillating mode we use a four-pole low-pass filter to attenuate all harmonics but the fundamental frequency. To tune the roll-off frequency of the low-pass filter and the phase shifter, we first run the magnetometer in the unlocked mode and send the output signal of the balanced receiver through the analog components. The roll-off frequency is set to 1.25 times the frequency of the driving oscillator, and the phase shift and gain are set such that the output of the analog components overlaps the output of the driving oscillator when viewed on an oscilloscope. Then the driving oscillator is removed and the analog output is connected to the VCSEL. The magnetic field is then determined by simply counting the frequency of the analog output. We observe self-oscillation in fields ranging from 35 nT to 35,000 nT, and the sensitivity of the magnetometer in the analog self-oscillating mode is shown in Figure 48 and is ~ 0.15 pt / rt Hz. at 1 Hz bandwidth in a 143 nT field.

We have determined that the FM-NMOR technique suffers from significant drawbacks with regard to magnetometers based on small vapor cells containing buffer gases. This is due to the requirement that the excited state hyperfine structure must be resolved in order to observe the FM-NMOR signal. The reason that the excited state hyperfine structure must be resolved is that the FM-NMOR technique relies on the generation of a coherent atomic state between the $m = +1$ and $m = -1$ Zeeman levels. This coherence can only be optically pumped efficiently when there is no incoherent absorption of light by these states. Since the FM-NMOR technique relies on linearly polarized light, such absorption channels will exist whenever light couples one of the hyperfine ground states to the upper excited state hyperfine level ($F=J+1/2$) on the D1 line. When the presence of a buffer gas broadens the excited state such that the hyperfine splitting of the state is not resolved, there is no way to excite the coherent while simultaneously preventing coupling to the $J+1/2$ level.

The condition that the hyperfine structure of the excited states being resolved is largely incompatible with magnetometers based on highly compact cells containing buffer gases. In order to attain a narrow transition linewidth in a small cell, a high buffer gas pressure must be used, to prevent more frequent collision of the alkali atoms with the walls of the cell. For a mm-scale cell, the optimum buffer gas pressure is about 1 atm. However, a buffer gas with this high pressure broadens the optical transitions far beyond the excited state hyperfine splitting and hence prevents the use of FM-NMOR. Table-top experiments carried out recently at NIST that with mm-scale vapor cell containing the maximum buffer gas allowed by the condition that the excited-state hyperfine structure be resolved (about 5 Torr, in 87Rb), the magnetometer sensitivity was limited to near 1 nT/ $\sqrt{\text{Hz}}$, far above the sensitivity goals of the project. This prompted us to investigate the other techniques, with much better sensitivity shown in the following sections

If microfabricated cells containing wall coatings were available, it should be possible to attain narrowed linewidths without using a buffer gas, and therefore without broadening the optical transition. However, at present microfabricated cells containing a wall coating have not been demonstrated and we believe there is significant risk associated with this concept.

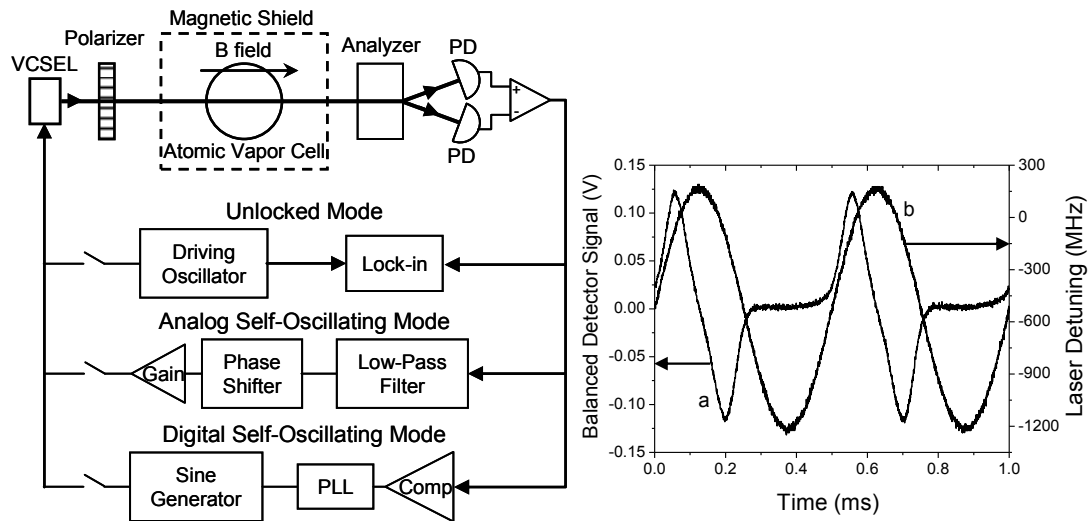


Figure 47. Modes of operation and waveforms for FM-NMOR magnetometer

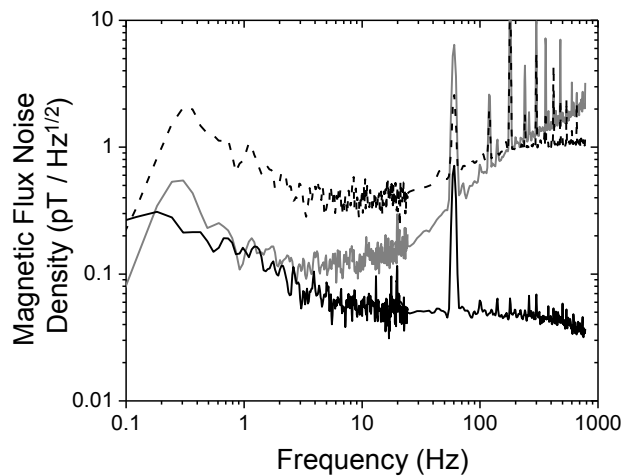


Figure 48 Performance of FM-NMOR magnetometer

Task 3.3 Measurement of performance

The performance of the FM-NMOR method was tested in millimeter-scale cells at several buffer gas pressures. The best measurements in these cells produced magnetometer sensitivities in the range of 1 nT/rtHz. Because of the large attenuation of the FM-NMOR signal at high buffer gas pressure, the buffer gas pressure had to be kept below about 20 Torr. At this pressure, the frequent collisions of the atoms with the walls of the cell produced rapid relaxation, which in turn resulted in degraded sensitivity.

Figure 49 shows the results for FM-NMOR in a small (3 mm diameter) wall coated alkali vapor cell. While the results are encouraging in terms of performance, the technical challenges involved in fabricating MEMS alkali vapor cells with wall coatings are considerable.

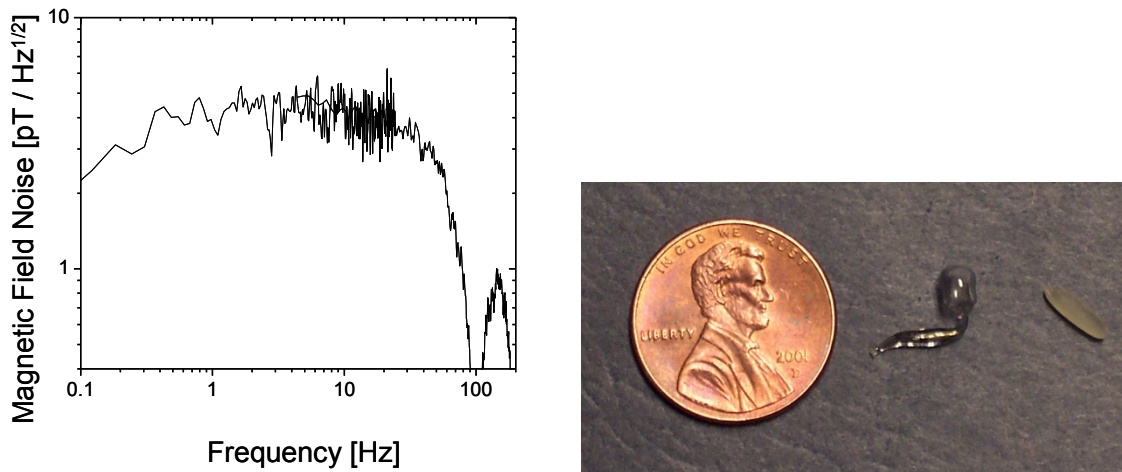


Figure 49 Noise performance and cell used for FM-NMOR measurements.

Since the FM-NMOR approach did not seem advantageous, we turned our attention to constructing a chip-scale Mx magnetometer. This was investigated simultaneously with the chip-scale Bell-Bloom magnetometer.

Performance results with Mx Magnetometer

We proceeded to make measurement using the Mx interrogation method, and achieved considerably better results. Figure 50 shows the device used in these measurements.

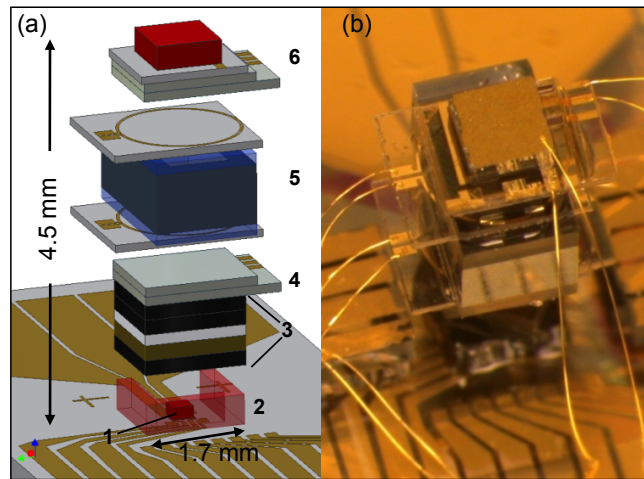


Figure 50. The chip-scale atomic magnetometer used in the M_x measurements. (a) Schematic of the magnetic sensor. The components are: 1—VCSEL, 2—polyimide spacer, 3—optics package including (from bottom to top) a neutral-density filter, polarizer, a quartz quarter waveplate, and a neutral-density filter, 4—ITO heater, 5— ^{87}Rb vapor cell with RF coils above and below it, and 6—ITO heater and photodiode assembly. (b) Photograph of the magnetic sensor. Note the gold wire bonds providing the electrical connections from the baseplate to the device

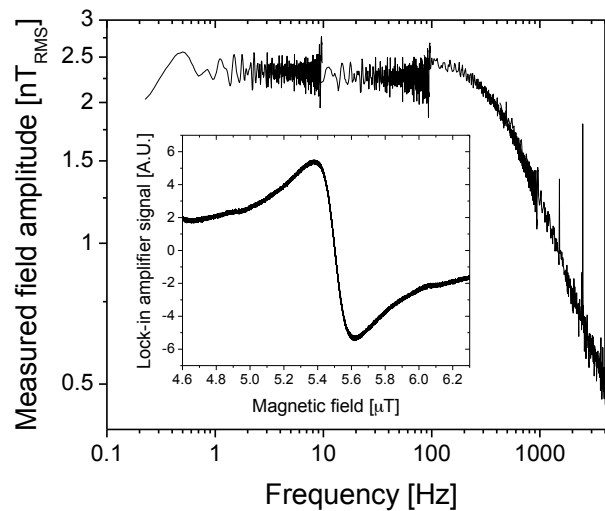


Figure 51 The response of the magnetometer is plotted as a function of frequency when a chirped 2.4 nT modulation is applied to the 5500 nT static field. Inset: The in-phase lock-in amplifier output as a function of magnetic field where the frequency of the applied RF field is 38.5 kHz.

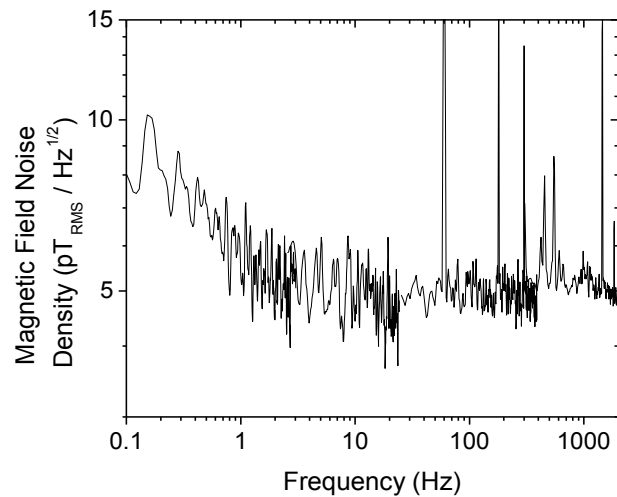


Figure 52 Noise density of the lock-in signal converted to units of magnetic field. The lock-in time constant is 0.1 ms with a filter roll-off 6 dB / octave. The ambient field is 5500 nT.

Bell-Bloom Results

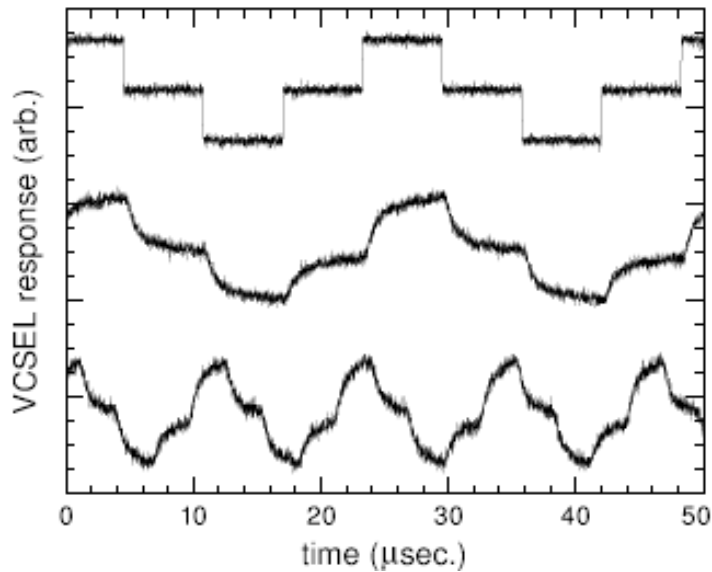


Figure 53 VCSEL response to square-wave modulation of the current. The top trace is the waveform fed into the laser current source, the middle trace shows the response of the VCSEL to this waveform at 40 kHz, and the bottom is the response at 87.5 kHz (the rate used for HFBB at earth's field). The response was measured by finding a region where the cell transmission was linear with respect to the VCSEL current at low frequency

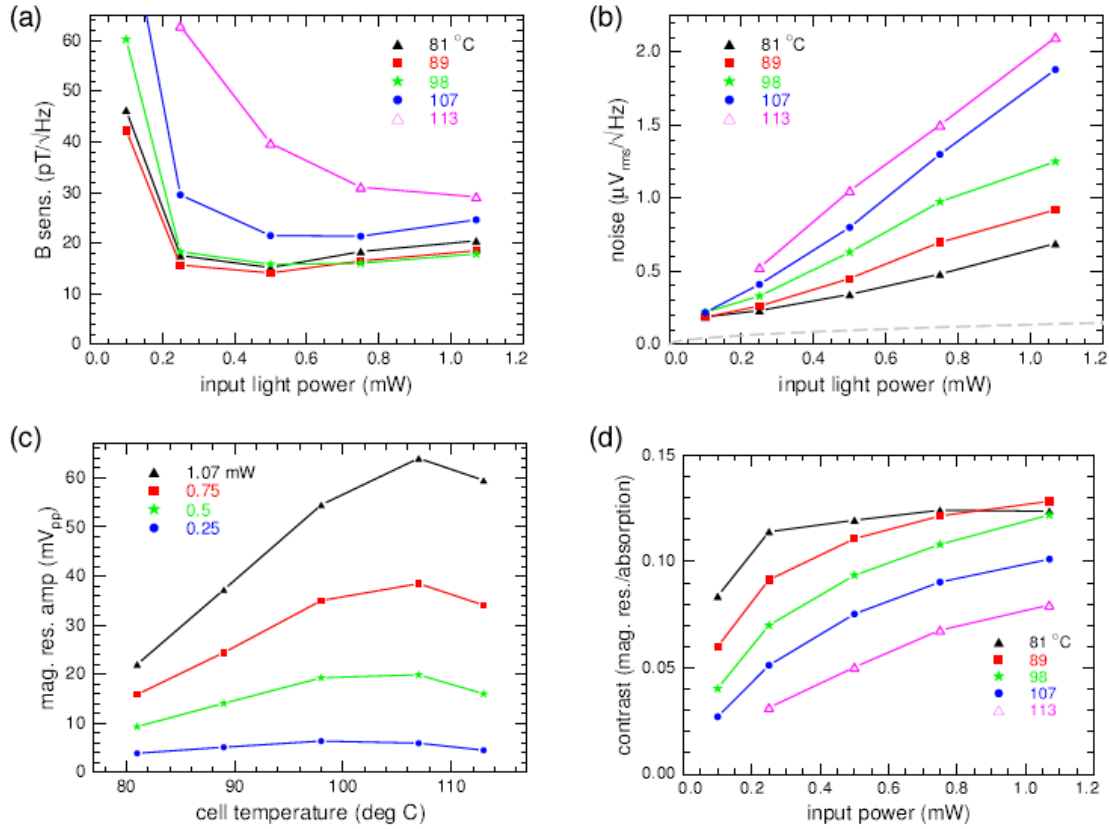


Figure 54 FFBB magnetometer performance vs. cell temperature and light intensity in a 80 kHz magnetic field. Shown is the magnetic field sensitivity (a), the lock-in noise (b), the amplitude of the dispersive magnetic resonance signal (c), and the ratio of the magnetic resonance amplitude and the optical absorption depth (d). The dashed grey line in the noise plot gives the estimated photon shot noise from the off-resonance photodiode signal. The input light power given in these plots was measured before the light beam entered the magnetic shield, which is substantially larger than the amount of light inside the vapor cell

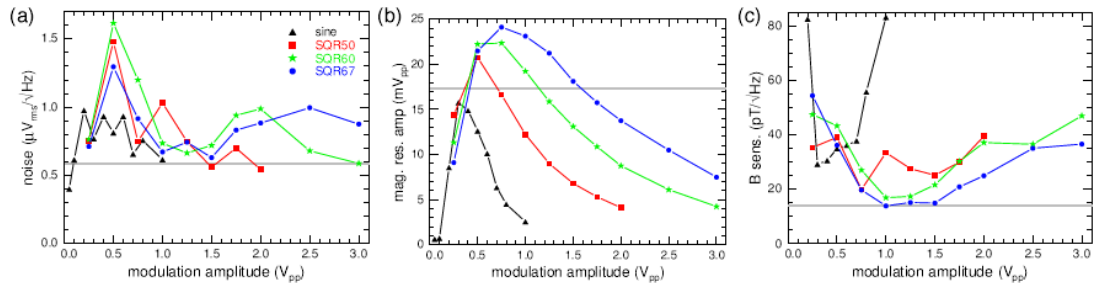


Figure 55 HFBB performance vs. modulation amplitude for several modulation waveforms in a 175 kHz magnetic field. The square-waveforms are of the form in Figure 53 and are designated as

SQRXX, where XX is the percentage of the period spent on resonance. The horizontal grey lines in the plots show the values obtained for the best sensitivity point for FFBB sine wave modulation

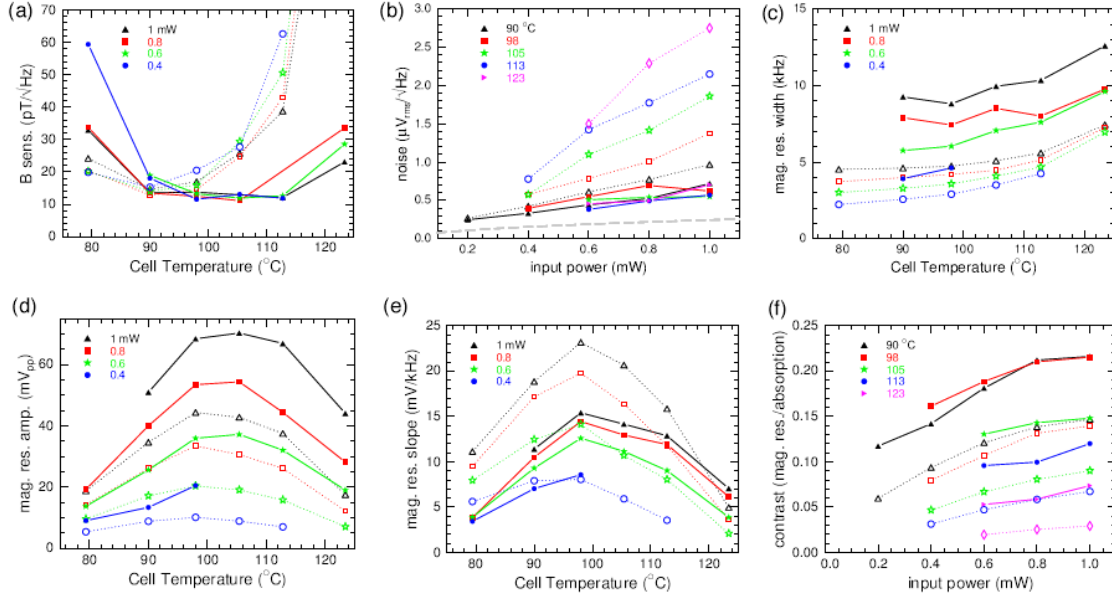


Figure 56 HFBB (dashed lines, open points) and Mx (solid lines and points) performance vs. cell temperature and light intensity in a 80 kHz magnetic field. Shown is the magnetic field sensitivity (a), lock-in noise (b), magnetic resonance width (c), amplitude (d), slope (e), and the ratio of the magnetic resonance amplitude and optical absorption depth (f). The dashed grey line in the noise plot gives the estimated photon shot noise from the off-resonance photodiode signal.

Task 3.4 Determine final electronics requirements

We characterized the half-frequency Bell-Bloom (HFBB) excitation scheme. In the HFBB scheme, the frequency of the laser is modulated at a frequency near one-half of the atomic Larmor frequency. The transmitted power detected at twice the modulation frequency is demodulated to establish the Larmor frequency and hence the magnetic field. Because the laser spends some time on the side of the atomic absorption resonance, the noise is expected to be higher than if the laser remained tuned to the top of the absorption line. This is because FM noise on the laser is converted into AM noise by the slope of the atomic absorption profile if the laser is tuned to the side of the profile, whereas the slope is essentially zero at the profile peak. Schematics of the FFBB and HFBB modulation schemes are shown in Figure 57(a) and (b). A plot of the noise for the HFBB and conventional Mx excitation is shown in Figure 58

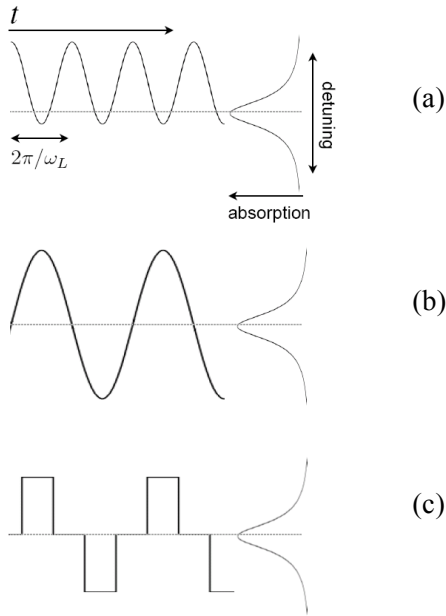


Figure 57 Bell-Bloom modulation schemes (a) Full-frequency Bell Bloom (FFBB), (b) Half-frequency Bell-Bloom (HFBB), (c) HFBB with square-wave modulation (HFBB-SW)

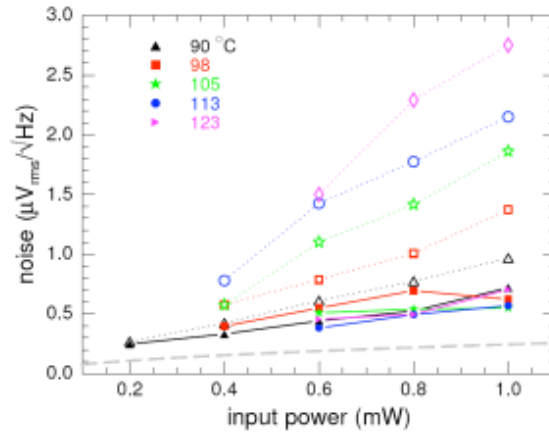


Figure 58 Noise measured after signal demodulation as a function of the optical power input to the cell. Solid data points are for the Mx configuration, while open data points are for the HFBB configuration. A clear increase in the noise is observed, particularly for higher cell temperatures when the slope of the absorption profile is larger. The grey dashed line indicates the estimated photon shot noise

In order to address this problem, we have investigated a modulation scheme in which the laser is modulated with a square-wave waveform, as shown in Figure 57(c). Since with this scheme, the laser spends almost no time on the side of the absorption profile, the noise due to FM-AM conversion should be considerably lower. We have discovered a minor difficulty with this idea: the laser FM modulation starts to roll off at about a few hundred kHz. As a result, when the laser is modulated with frequencies corresponding to the Larmor frequency of the earth's magnetic field (100 kHz and above), the modulation waveform is considerably distorted, as shown in Figure 59(a). Since with this frequency modulation waveform the laser spends more than the desired amount of time on the side of the absorption profile, less noise reduction is expected than if the laser frequency were a perfect square wave.

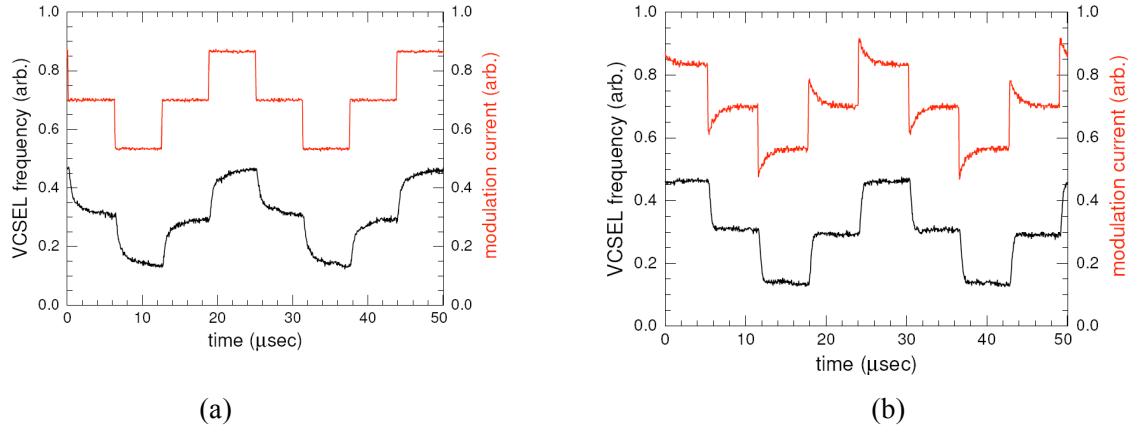


Figure 59 Response of the diode laser frequency to square-wave current modulation. Red traces indicate the modulation current waveform, while the black lines indicate the laser frequency response, as measured by the transmission of the laser through the atomic absorption profile. (a) A square-wave current modulation produces a distorted frequency waveform. (b) Adjusting the current waveform can produce a much more square frequency waveform, which should result in lower noise.

In order to correct this problem, the laser current waveform was adjusted to enhance the higher harmonic components, which are attenuated by the laser frequency response. The corrected frequency spectrum is shown in Figure 59(b).

This modified modulation waveform does produce an improved sensitivity. The sensitivity data are shown in Figure 60.

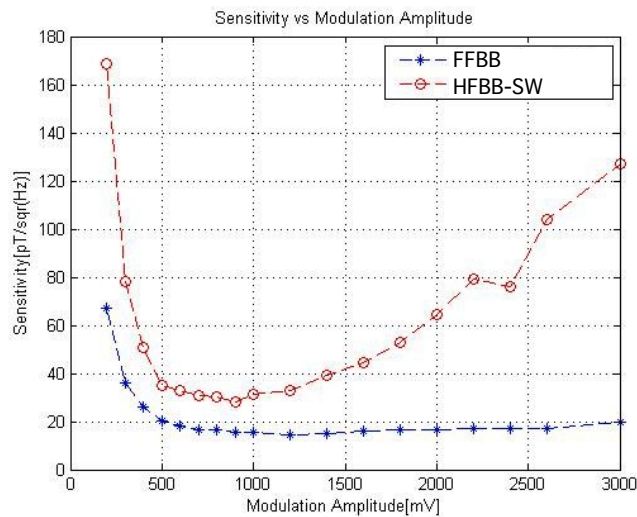


Figure 60 Sensitivity comparison of the FFBB scheme and the HFBB-SW scheme. An increased sensitivity is observed under most operating conditions.

Task 3.5 Demonstrate self-oscillating FM-NMOR device in chip-scale device

Two chip-scale atomic magnetic sensor prototypes were constructed at NIST during this project. The first device was a CPT magnetometer, which measured a magnetically sensitive hyperfine transition in ^{87}Rb , rather than the Larmor precession frequency directly. The alkali vapor cell in this magnetometer had a buffer gas pressure of only 240 Torr, in order that the ground-state hyperfine structure could be resolved. This CPT magnetometer had a sensitivity of 50 pT/ $\sqrt{\text{Hz}}$ at 10 Hz, had a volume of 12 mm³, and ran on ~ 200 mW of electrical power. This instrument required a high-frequency (3.4 GHz) local oscillator to probe the transition and moderately complex control electronics to operate.

The second chip-scale magnetometer was constructed to operate in the Mx mode. It had a similar structure to the first, but had a pair of microfabricated coils in a Helmholtz configuration in the device stack. These coils allowed the application of an RF field at the atomic Larmor frequency to be applied, as required in the Mx mode. In addition, this device could be operated in the Bell-Bloom modes if the laser injection current, rather than the coil current, was modulated. The cell in this magnetometer has a buffer gas pressure of 2000 Torr, which provided considerably longer relaxation times and correspondingly better sensitivity. The sensitivity was measured to be 5 pT/ $\sqrt{\text{Hz}}$ in the frequency range from 2 Hz to 1 kHz.

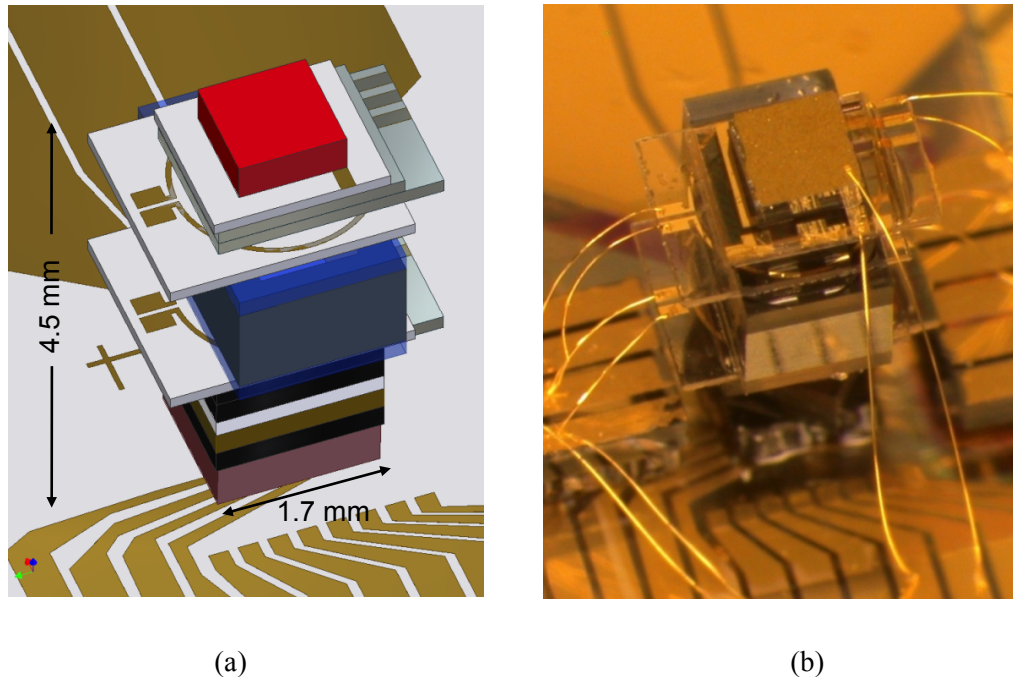


Figure 61. A chip-scale atomic magnetometer constructed at NIST. This device can operate in either Mx or Bell-Bloom modes and has a measured sensitivity of up to 5 pT/ $\sqrt{\text{Hz}}$.

Task 3.6 Heading error reduction

Introduction

Heading error is caused by fundamental quantum mechanical effects. Simple quantum mechanical models ignore the interactions that lead to heading error, and therefore cannot be used to analyze and optimize heading error. In this task, we have developed advanced models that allow us to simulate the heading error for a given sensor configuration.

In existing commercial systems, heading error is largely canceled out by averaging the signals from right- and left-circularly polarized light. These two polarizations have largely opposite heading errors, making this method quite effective. Figure 62 shows this principle.

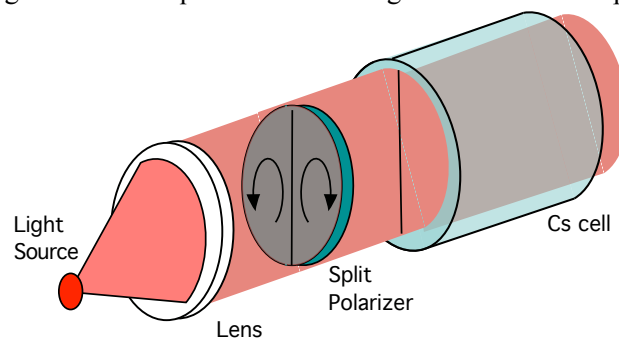


Figure 62 Commercial magnetometer using a split polarizer method of reducing heading error

In small laser-illuminated sensors, however, the situation is more complicated. First, since the laser light is narrow band, it does not stimulate as many transitions, and therefore the polarization averaging mentioned above is not as effective. Secondly, that method does not work at all for some of the interrogation methods we are considering in this work. Finally, split polarizers are complicate to make in a very small size.

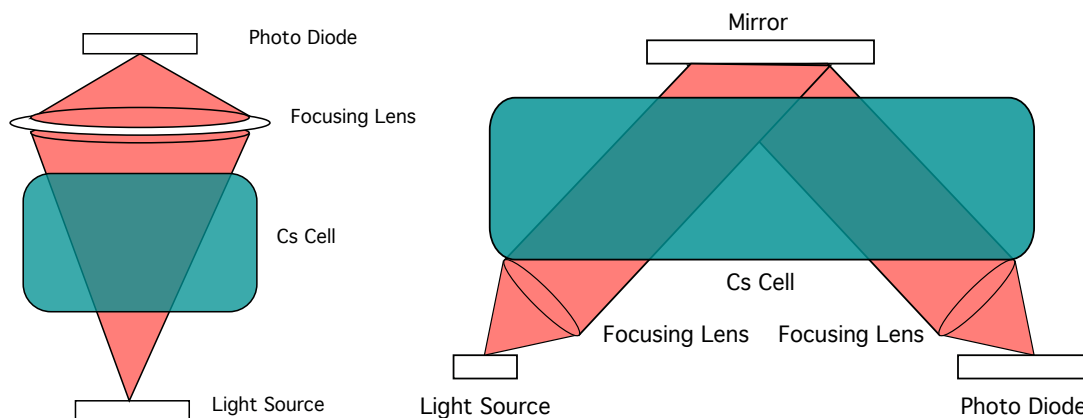


Figure 63 Two methods of using multiple directions of light to average heading error

Other methods, such as those shown in Figure 63 may be used in small sensors, however. Here the heading error is averaged by using many directions of the light path. Each will have a different heading error characteristic, and the bulk of the heading error may be averaged-out. The goal of our heading error analysis is to design and evaluate such optical paths to optimize the heading error reduction.

We completed an analysis allowing us to model the details of the quantum mechanics impacting the performance of the magnetometer. A simple model of an atom in a magnetometer consists of only two states – a ground state, which is further split into two sub-states due to the Zeeman effect, and an excited state. The RF resonance between the Zeeman levels may be described by a single Lorentzian function. In this simple system, heading error would not exist. Since it is the heading error we are interested in studying, this model is obviously not sufficient.

In fact, as shown in Figure 64 the atoms in a Cs magnetometer have 2 ground states and 2 excited levels, all of which are split due to the Zeeman effect. However, the frequency of this shift is not the same for all states. The signal we receive is an average of these frequencies, weighted by the populations of each energy level. The populations of the various levels changes with the sensor orientation – this is one of the causes of heading error. Thus, we have developed a much more detailed mathematical model of the populations of the states to study how the heading error may be balanced and eliminated.

Description

The density matrix is a quantum equivalent to the atomic or molecular density function $\rho(x,y,z,t)$ used in classical mechanics, which describes the number of particles/cc having certain physical parameters. In quantum mechanics the behavior of one atom can be described by a wave function obtained from Schrodinger equation. The density matrix derivation comes from the wave function formalism and is used to describe the quantum-mechanical behavior of a statistical ensemble of atoms interacting with themselves and with different forms of electromagnetic radiation. The density matrix is then used in statistical quantum mechanics (quantum thermodynamics) as an equivalent of the wave function used in the description of a single atom. The quantum-mechanical Liouville equation for the density matrix comes from the Schrodinger equation for individual wave functions.

Our model is based on the quantum-mechanical Liouville equation for the density matrix ρ :

$$E1 \quad \frac{d\rho}{dt} = -i\hbar(H\rho - \rho H)$$

where H is the quantum mechanical Hamilton operator describing the physics of the magnetometer. The magnetometer signal, $S(\rho)$, is a complicated function of the density matrix. However, having a solution for ρ means knowing the magnetometer signal.

**Double resonance in
Cesium D₁ transition hyperfine structure
1-laser light, 2-RF field (H1 drive)**

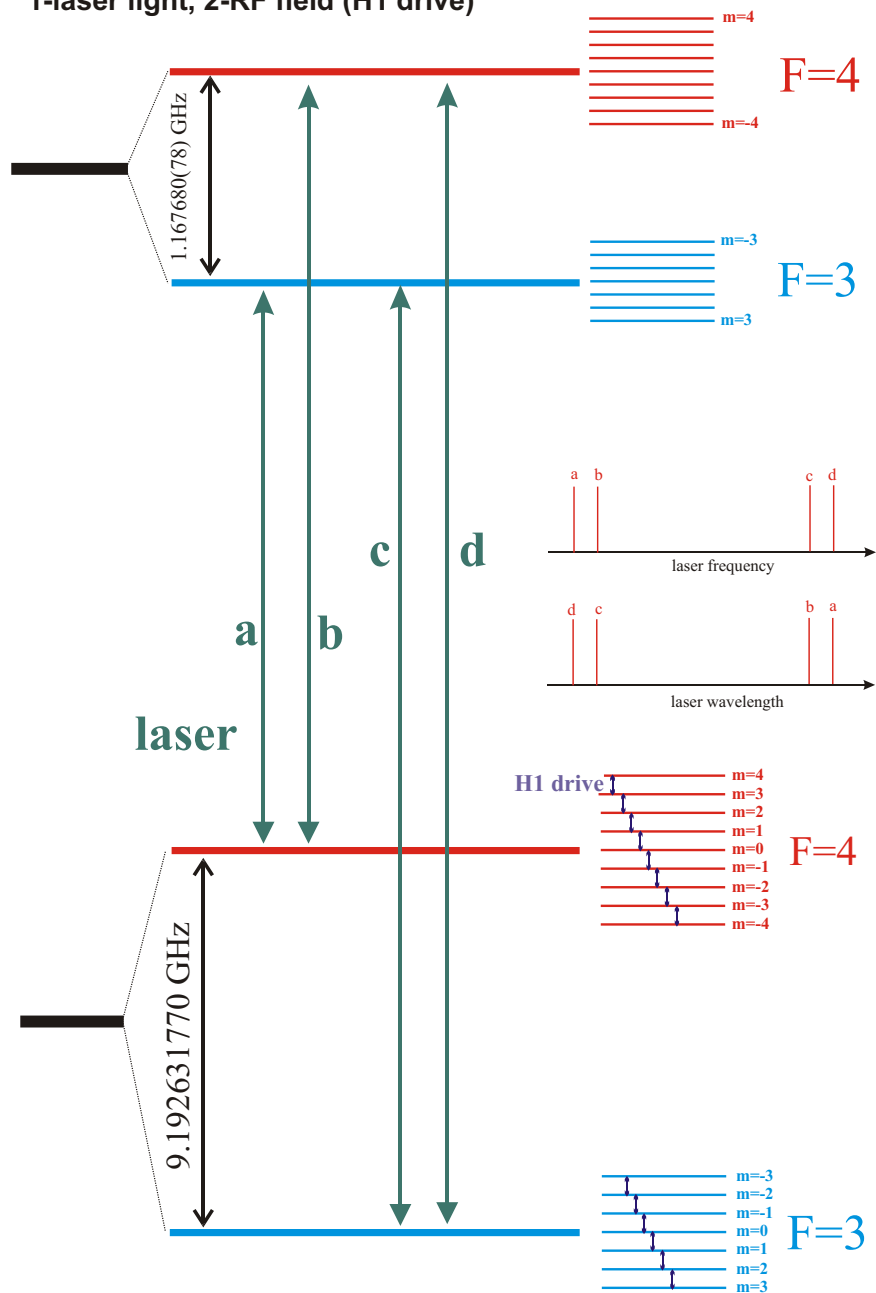


Figure 64 Diagram of all energy levels of Cs

The density matrix diagonal elements r_{ii} describe a quantum population of a certain energy level in the Cesium atom. Off-diagonal elements r_{ij} describe quantum coherences between the i-th and j-th energy levels. In our case we have four groups of hyper-fine structure sublevels: two group of levels of ground states (16=9+7 Zeeman levels) and two groups of levels of excited states (16=9+7 Zeeman levels). All told, we have 32 ground levels and 32 excited levels. The density matrix will have about 400 real number elements. The density matrix equation can be written in the form of a real number equation:

$$E2 \quad \frac{d\rho}{dt} = A\rho - B$$

where

$$A = \Delta + V_L + V_R + R$$

and

$$\Delta = \Delta_0 + \Delta_L + \Delta_{RF} + \Delta_R$$

where Δ_0 describes the atomic structure of cesium, Δ_L the energy levels shifts (ELS) caused by the laser light, Δ_{RF} ELS caused by the radio-frequency field and, Δ_R ELS caused by relaxation processes. V_L describes the atoms' interaction with the laser, V_R describes the atoms' interaction with the radio-frequency field, R is a relaxation matrix and $-B=A\rho_0$ describes the initial state of the density matrix

Approach to solution of equation E1 (E2).

Equation E1 or E2 in their full form, including the laser and radio frequency fields (optical-RF double resonance) is very complicated. The approach applied in the field of atomic magnetometry is to separate the effect of laser radiation on the atoms (optical pumping, or preparation of atomic polarization/magnetization) from the effect of the RF field (the magnetic resonance). According to this approach:

Step#1: Solution of E2 only for laser field. This is the step known as optical pumping:

$$E3 \quad \frac{d\rho_L}{dt} = A_L\rho_L - B_L$$

Step#2: solution of E2 only for RF field-magnetic resonance, using the initial density matrix $\rho_0=\rho_L$ taken as a solution of the density matrix obtained from step#1:

$$E4 \quad \frac{dr_{RF}}{dt} = A_{RF}r_{RF} - A_{RF}r_{OP}$$

To find a density matrix solution which takes into account the mutual influence of the laser and radio-frequency fields an iteration procedure can be applied. The density matrix obtained from step#2 can be considered as a initial density matrix for step#1. This loop is iterated until the procedure does not change the density matrix solution, $\rho_{RF..}$

In our magnetometer set up the laser field has only one optical frequency ω_L . In this case we can obtain a steady state solution density matrix ρ_L in the so called rotating frame in the form:

$$\text{E3-SS} \quad B_L = A_L \rho_L$$

where ρ_L can be considered as a vector and A_L as a matrix. We can find a solution of E3-SS in the form:

$$\text{S-E3-SS} \quad \rho_L = (A_L)^{-1} B_L$$

where $(A_L)^{-1}$ is a reciprocal matrix of A .

The same situation can be applied to equation E4 for a steady-state solution of the matrix ρ_{RF} :

$$\begin{aligned} \text{E4-SS} \quad B_{RF} &= A_{RF} \rho_{RF} \\ \text{S-E4-SS} \quad \rho_{RF} &= (A_{RF})^{-1} B_{RF} \end{aligned}$$

In our design, the RF field can be represented as:

$$B_{RF}(t) = B_{0,RF} \left[B_M \cos(\omega - \Delta\omega) t + B_M \cos(\omega + \Delta\omega) t + \cos(\omega t + \frac{\pi}{2}) \right]$$

The density matrix elements can be written in the form of a Fourier series:

$$\begin{aligned} \text{FS} \quad u_{ij} &= \text{Re} \rho_{RF,ij} = \sum_{n=0}^{\infty} u_{ij}^n \cos(n\Delta\omega t + \varphi_n) \\ v_{ij} &= \text{Im} \rho_{RF,ij} = \sum_{n=0}^{\infty} v_{ij}^n \sin(n\Delta\omega t + \varphi_n) \end{aligned}$$

and the set of differential equations E4 can be written as a matrix equation for Fourier components u_{ij}^n, v_{ij}^n .

To solve the density matrix equation we need to know the form and parameters of the matrices A_0, V_L, V_R , and R . For A_0 we need to know the value of all of the 64 atomic energy levels $E(L, I, J, F, M_F, B_0)$ for a certain value of the magnetic field B_0 (this is the magnetic field being measured by the magnetometer). For V_L we need to calculate 82 laser transition probabilities (LTP), describing optical transitions between ground and excited energy levels induced by laser light. To calculate these probabilities we also need to take into consideration the effect of excited state mixing caused by cesium atom collisions with buffer gas molecules. This mixing effect is described by a mixing matrix:

$$\text{MM} \quad M = \sum_{N=1}^{\infty} \frac{\tau^N \tau_c}{(\tau + \tau_c)^{N+1}} M_1^N$$

where M is a mixing matrix because of one Cs-buffer gas collision, τ is excited level lifetime, τ_c is mean time of the mixing collision.

For V_R we need to calculate 14 radio-frequency field transitions probabilities (RFTP), describing radio-frequency transitions between ground state Zeeman levels.

To calculate relaxation matrix R and ELS Δ_R we need to consider numerous atomic collision phenomena taking place in the cesium cell. The general form of the relaxation and energy shift matrix can be written in the form of a sum:

$$R = \sum_i \Gamma_i R_i, \quad \Delta_R = \sum_i \Delta_{R-i}$$

where Γ_i is the relaxation rate constant for the i -th relaxation phenomena and R_i is the relaxation matrix for the i -th relaxation process. Δ_{R-i} describes the ELS matrix for the i -th relaxation process.

Collisional processes:

1. Collisions between excited state cesium atoms and buffer gas molecules (nitrogen N_2):
 - a) pressure broadening relaxation: Γ_{PB} -rate and R_{PB} matrix. There is also energy shift effect described by Δ_{PB} matrix.
 - b) excited state quenching by buffer gas molecules (N_2): Γ_q -relaxation rate constant and R_q relaxation matrix. During this process all radiation energy of the excited state is transferred to the buffer gas molecule and excited state decays to the ground state without producing fluorescent light which can produce an additional unwanted effect of trapped radiation atomic polarization degradation.
2. Collisions between ground state cesium atoms and buffer gas molecules:
 - a) $Cs-N_2$ - relaxation because of spin-rotation interaction: Γ_S s-rate constant, R_S relaxation matrix. $\Gamma_S = \Gamma_{S-2} + \Gamma_{S-3}$, where Γ_{S-2} comes from binary (two-body) collisions and Γ_{S-3} comes from Van der Waals $Cs-N_2$ molecules formation- (three body collisions).
 - b) $Cs-N_2$ - relaxation because of cesium atoms hyperfine structure modulation during collisions: Γ_C -so called Calver rate and R_C relaxation matrix. There is also energy shift effect because of this phenomena: matrix Δ_C . $\Gamma_C = \Gamma_{C-2} + \Gamma_{C-3}$, where Γ_{C-2} comes from binary (two-body) collisions and Γ_{C-3} comes from Van der Waals $Cs-N_2$ molecules formation- (three body collisions). The same refers to Δ_C .
3. Collisions between ground state cesium atoms, $Cs-Cs$, This is a relaxation because of the electron spin exchange interaction: Γ_{SE} rate constant and R_{SE} relaxation matrix. There is also an energy shift effect because of this phenomena, represented as matrix Δ_{SE} . The relaxation effect because of Cs_2 and Cs_3 molecules was evaluated but was not found to be significant in our case.
4. Ground state collisions between cesium atoms and cell walls: diffusion relaxation rate Γ_{D-i} and matrix: R_{D-i} , where i depicts i -th diffusion mode. In practice we need to consider just two diffusion modes.

Other phenomena

5. Spontaneous decay of excited energy levels: Γ_E -rate and R_E matrix
6. Ground state relaxation and ELS because of magnetic field inhomogeneities: Γ_B (matrix R_B), Δ_B .

Finally we can write Δ_R and R matrixes as:

$$\Delta_R = \Delta_{PB} + \Delta_C + \Delta_{SE} + \Delta_B$$

$$R = \Gamma_E R_E + \Gamma_{PB} R_{PB} + \Gamma_q R_q + \Gamma_S R_S + \Gamma_C R_C + \Gamma_{SE} R_{SE} + \Gamma_{D-1} R_{D-1} + \Gamma_{D-2} R_{D-2} + \Gamma_B R_B$$

The effect of laser radiation trapping-(caused by re-absorption of laser radiation by atoms) can be included as a correction to Δ_L and V_L : $\delta\Delta_{RT}$ and δV_{RT} .

Steps we followed to solve the equation in the above framework:

1. 32 cesium energy level positions were calculated as a function of measured static magnetic field. Zeeman splitting calculated from Rabi-Breit formula.
2. Light and RF energy shifts $\Delta_L + \delta\Delta_{RT}$, Δ_{RF} -formulas obtained.
3. Laser transition probabilities (LTP) without excited states mixing calculated. Calculation of mixing matrix pending (about 80% of this task finished).
4. Radio-frequency field transitions probabilities (RFTP) calculated.
5. Full relaxation matrix R and ELS matrix Δ_L obtained from:
 - a. impact theory (Fourier transform of radiation auto-correlation function): $\Gamma_{PB} R_{PB}$, Δ_{PB} , $\Gamma_C R_C$, Δ_C ,
 - b. Bloch-Wangness-Redfield theory of relaxation: $\Gamma_q R_q$, $\Gamma_S R_S$, $\Gamma_{SE} R_{SE}$, $\Gamma_E R_E$, $\Gamma_B R_B$, Δ_B
 - i. diffusion equation for rectangular and cylindrical shape of cesium vapor cell: Γ_{D-i} , R_{D-i} for all possible diffusional modes.
6. Partial relaxation rates Γ_i and partial energy shifts Δ_i calculated for any buffer gas pressure and cell temperature.
7. Doppler-broadening effect calculated as a function of cell temperature.
8. The full general form of equation E1 and E2 found and written.
9. The formulas for all of the elements of matrix A_L and B_L found and written.
10. The formulas for all of the elements of matrix A_{RF} and B_{RF} found and written.
11. The set of equations for Fourier components u_{ij}^n , v_{ij}^n of ρ_{RF} (two levels) in the case of QAM modulation of RF field-found and written.
12. The formula for absorption coefficient (magnetometer signal) $S(\rho_{RF})$ -which is a function of density matrix elements ρ_{RF} - found and written.
13. Formulas for magnetic field value in three dimensions [$B_x(x,y,z)$, $B_y(x,y,z)$, $B_z(x,y,z)$] inside cylindrical solenoid (coil) found and written. Formulas are based on the elliptical Euler integrals and take into account the number of wire-loops of the solenoid, wire diameter and wire-loops position). The magnetic field from each separate wire-loop is calculated and the total field from solenoid obtained as a sum of magnetic fields from all of the wire-loops. Those formulas were used to find magnetic field gradients produced by H1 drive, to evaluate Γ_B (matrix R_B), Δ_B .

14. Solve equation E3-SS for to find density matrix ρ_L prepared for optical pumping.
Because of high complexity of the matrix equation it must be done in two steps. In the first step the equation will be solved only for atomic populations (diagonal elements of density matrix) in the form of so called rate equations. The obtained solution will help to decrease the number of excited states involved by replacing them with “effective excited states”. In the second step the equation E3-SS will be solved for diagonal and off-diagonal elements of ρ_L with fewer “effective” levels.
15. Solve equation E4-SS for full form of density matrix ρ_{RF} using results of equation of E3-SS.
16. Find the final form of density matrix ρ_{RF} by applying the iteration loop between equations E3-SS and E4-SS.
17. Find the magnetometer signal for different parameters of magnetometer physical set up, for example magnetometer position with respect to the measured magnetic field, H1 drive intensity, cesium cell temperature, buffer gas pressure, cesium cell shape and dimensions, laser intensity, laser frequency. Those results deliver information helpful in finding optimum parameters for magnetometer operation (specially in heading error elimination) and are used in solving equations with QAM modulations.
18. Using parameters described above solve set of equations for Fourier expansion FS for two level case with RF frequency modulations. This can give a magnetometric signal as a sum of all of the harmonics of modulation frequency :

$$S(Dw) = \sum_{i=0}^{\infty} S_n(nDw)$$

This solution is used to optimize H1 drive intensity, modulation depth, and modulation frequency. Analysis of the behavior second, third and fourth harmonics of the signal for different magnetometer parameters delivers information used to optimize the magnetometer performance.

19. Using information obtained from solution of density matrix described in point 5 find formulas and solve set equations for FS (Fourier expansion of ρ_{RF}) for all ground levels in case of RF QAM modulation. This solution will give the full magnetometric signal (all harmonics). Analysis of this solution for different magnetometer parameters will deliver necessary information to optimize magnetometer performance specially to find the best way to eliminate or strongly diminish heading error problem.

Simplifications found during the above process

1. Theoretical models of excited state mixing were found and were used for excited state mixing calculations. Excited state mixing is an effect of atomic collisions of cesium atoms with buffer gas. Atoms in excited state have different orbital angular momentum ($L=1$) than in ground state ($L=0$). During atomic collisions excited state L is randomized and the mixing effect between excited states occurs. Using established theoretical model it was found that for 1000 Torr of nitrogen buffer gas molecules in our MEMS magnetometer full excited state mixing occurs and 16 excited levels can be replaced by one excited state which significantly simplifies the theoretical model! The optical pumping equation was rewritten for the case of complete excited state mixing.

2. Analytical solution for atomic ground state populations based on equation S-E3-SS were found in ground level relaxation perturbation form. Because of linear form of equation S-E3-SS ground state relaxation contribution can be scaled by the strongest relaxation constant—in MEMS case (nitrogen pressure $p=1000$ Torr) excited to ground state relaxation (over 13 GHz). Because ground state relaxation is small compared to excited state relaxation only R , R^2 and R^3 , components from ground state relaxation are practically important in an analytical solution. Analytical formulas for ground state populations expressed by optical absorption coefficients $\{A_i, i=1..16\}$ stimulated emission coefficient $\{B_i, i=1..16\}$, excited to ground state relaxations $\{g_i, i=1..16\}$ and terms $R_{ij}R_{kl}$, R_{kl} , R_{ij} , R_{kl} , R_{mn} (ground state relaxation matrix) were found and are presently implemented to give numerical values of ground state populations. Finding analytical formulas for the population is very important because it significantly simplifies the ground state population analysis.

Results

The graphs below were obtained during using the above framework. Analysis of those graphs can, for example, help find the proper composition of buffer gasses. We obtained similar graphs for Kr as buffer gas and for mixture of Kr and N. We are looking for as small ground state relaxation as possible. Bigger pressure increases some relaxation coefficients but lowers the relaxation constant coming from Cs-wall collision. Kr can give as smaller ground state relaxation but there is no quenching from Kr and quenching is very important in lowering radiation-trapped atomic polarization degradation. This consideration shows why we should still look for optimum buffer gas composition

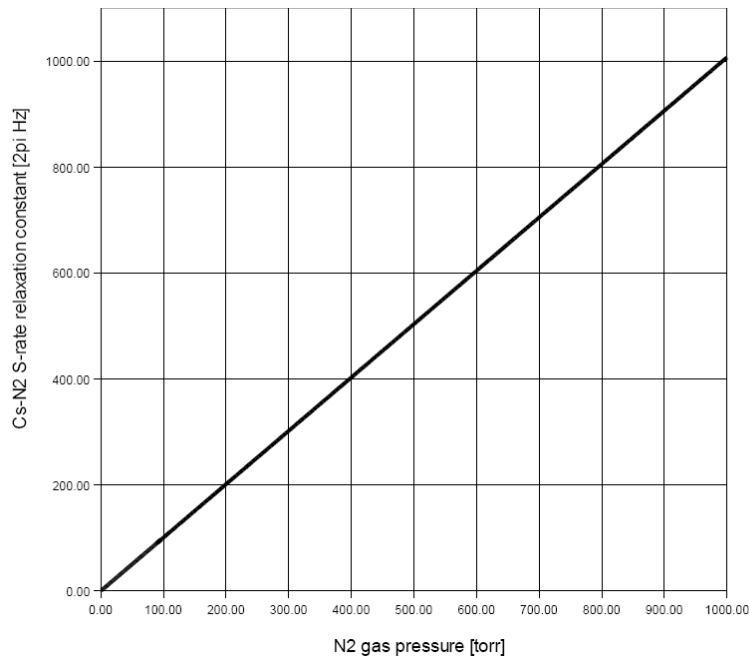


Figure 65. Ground state relaxation constant for Cs-N₂ collisions as a function of buffer gas pressure (T=65 C):

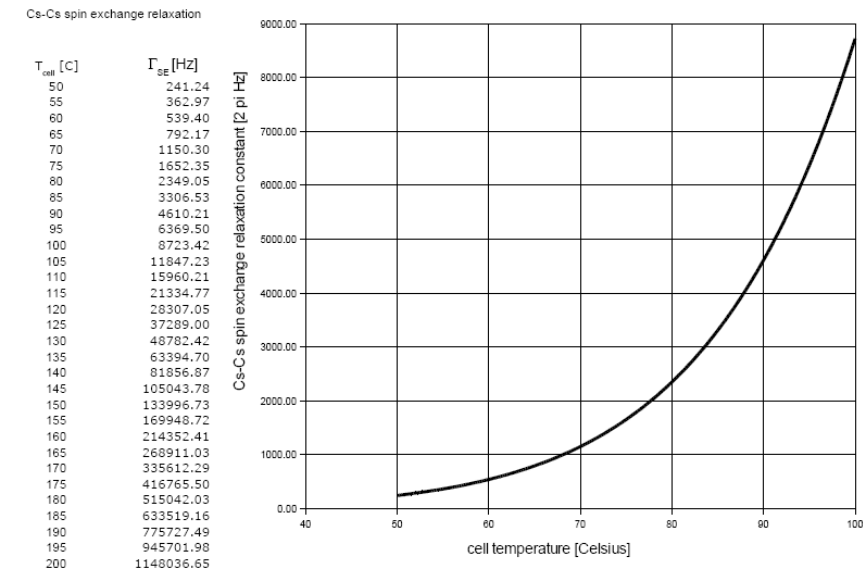


Figure 66. Ground state relaxation constant for Cs-Cs spin exchange collisions as a function of Cs cell temperature

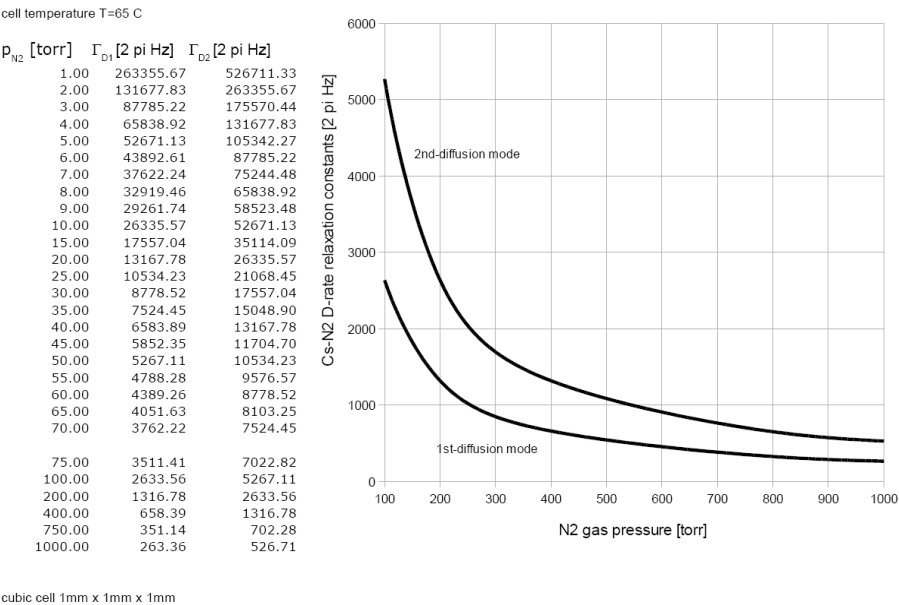


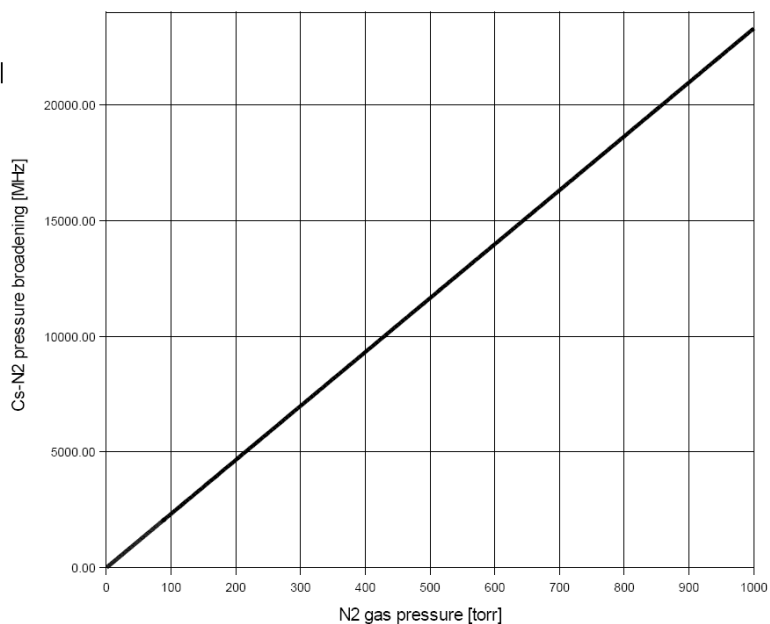
Figure 67. Ground state relaxation constant for Cs atoms-wall collisions for our small MEMS cell as a function of buffer gas pressure

:

cell temperature T=65 C

p_{N₂} [Torr] Γ₊ (N₂) [MHz]

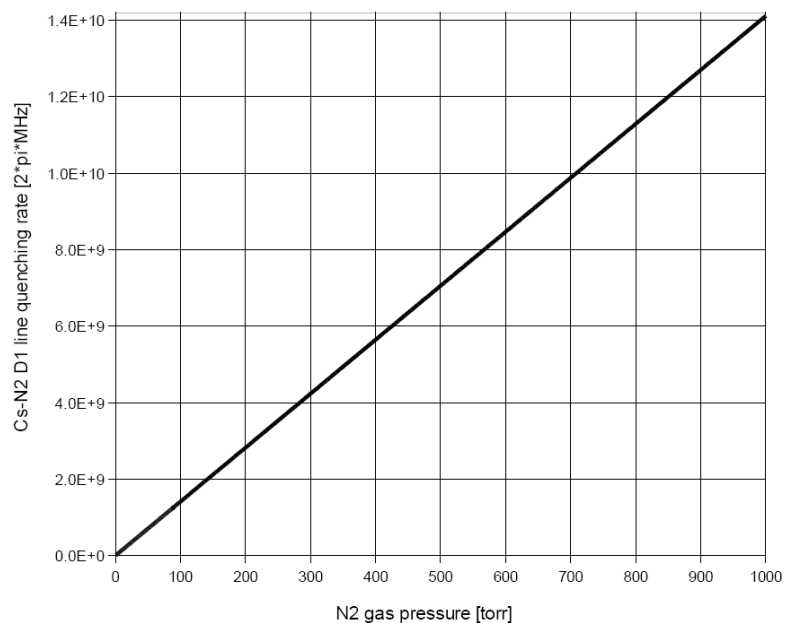
1	23.30
2	46.60
3	69.90
4	93.20
5	116.50
10	233.00
15	349.50
20	466.00
25	582.50
30	699.00
40	932.00
50	1165.00
60	1398.00
70	1631.00
80	1864.00
90	2097.00
100	2330.00
200	4659.99
300	6989.99
400	9319.99
500	11649.98
600	13979.98
700	16309.98
800	18639.97
900	20969.97
1000	23299.97

**Figure 68. Optical line width-because of pressure broadening as a function of buffer gas pressure**

cell temperature T=65 C

p_{N₂} [Torr] Q_{p1/2-s1/2} [2πHz]

1	1.411E+007
2	2.823E+007
3	4.234E+007
4	5.645E+007
5	7.057E+007
10	1.411E+008
15	2.117E+008
20	2.823E+008
25	3.528E+008
30	4.234E+008
40	5.645E+008
50	7.057E+008
60	8.468E+008
70	9.880E+008
80	1.129E+009
90	1.270E+009
100	1.411E+009
200	2.823E+009
300	4.234E+009
400	5.645E+009
500	7.057E+009
600	8.468E+009
700	9.880E+009
800	1.129E+010
900	1.270E+010
1000	1.411E+010

**Figure 69. Exited state relaxation constant for Cs-buffer gas quenching effect as a function of buffer gas pressure**

Results from optical pumping calculations

We calculated absorption coefficients for following parameters:

Sensor position $\alpha=0$ -only $\sigma+$ polarization, laser intensity $I=300 \mu\text{W}/\text{mm}^3$, cell temperature $T=65^\circ\text{C}$, buffer gas pressure $P=1000$ Torr, cell dimensions : rectangular cell $1\text{mm} \times 1\text{mm} \times 1\text{mm}$. Average excited -mixed state relaxation $\langle g_i \rangle = 884$ MHz

F	m	State #	Absorption coefficient A_i [kHz]
4	4	1	0
4	3	2	9
4	2	3	18.1
4	1	4	27.2
4	0	5	35.8
4	-1	6	44.6
4	-2	7	53.2
4	-3	8	61.6
4	-4	9	69.7
3	3	10	60.0
3	2	11	51.2
3	1	12	43.7
3	0	13	35.2
3	-1	14	26.5
3	-2	15	17.7
3	-3	16	8.9

Using analytical solution formulas for ground state population in the zero order approximation (no ground state relaxation effect) we obtain population on the form of:

$$S_i = L_i / (1 + L_1 + L_2 + \dots + L_{16})$$

When $L_i = (g_i + B_i) / A_i$. B_i -stimulated emission coefficient is very small compared to excited state relaxation g_i then:

$$L_i = g_i / A_i$$

Analyzing numerical values we can put g_i even: $g_1 \approx g_2 \approx \langle g_i \rangle$

Ratio of ground state population between levels i and k will be: $S_i / S_k = A_k / A_i$

Taking absorption coefficients A_i from above table we can evaluate ground state population ratios.

We can see that in case of very small ground state relaxation almost all ground state population will be in state #1

Numerical analysis of two level atom shows that for small values of g_i/A_i excited state population will be equal g_i/A_i

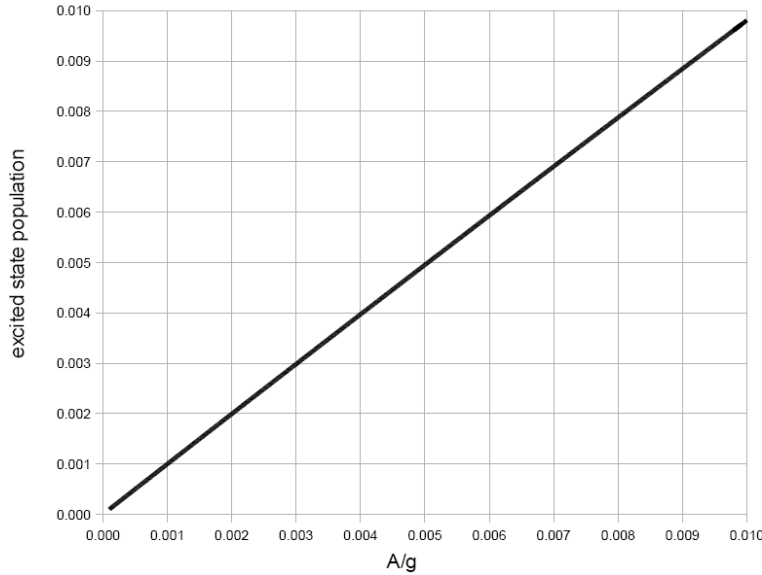


Figure 70 Excited state populations

This simple analysis shows that very few atoms will be in any of mixed excited states as a result of the optical pumping process.

This conclusion is very important because it says that we can use rate-equation approximation to calculate optical pumping effects. We don't need to take into account effects of excited-ground state optical coherences explicitly. Special optical coherences approximation can be used to calculate optical transitions coefficients (absorption and stimulated emission) . So optical coherences are eliminated from the density matrix equations. These results confirm that this simple rate-equation model for optical pumping is appropriate.

Analyzing the numerical values of ground state relaxation (about 10 times smaller than optical transition coefficients) we can introduce into our zeroth-order approximation model some effective additional absorption (ground state effective leak) for each level which roughly express ground state relaxation. This effective additional absorption for each level will have value of about $\Delta A_i = 0.5$ kHz. This will give us zero approximation of population ratios:

F	m	State #	Absorption coefficient A_i [kHz]	S_i/s_1
4	4	1	0.5	1
4	3	2	9.5	0.052
4	2	3	18.6	0.026
4	1	4	27.7	0.018
4	0	5	36.3	0.014

4	-1	6	45.1	0.011
4	-2	7	53.7	0
4	-3	8	62.1	0
4	-4	9	70.2	0.007
3	3	10	60.5	0
3	2	11	51.7	0
3	1	12	44.2	0
3	0	13	35.7	0
3	-1	14	27.0	0
3	-2	15	18.3	0
3	-3	16	9.4	0.053

We can deduce from this simple approximation that for σ^+ polarization we have practically one significantly populated level: $F=4, m=4$. For those sensor position we can use the simple two level approximation to calculate magnetometric signal.

3.6.2. Design Optimizations

We can now use the above framework to explore various designs of magnetometers theoretically. This allows us to learn much greater insight into the sensor operation, as well as more efficiently optimize the sensor design. There are a wide variety of methods that may be used to extract a signal containing the magnetic field information. We have explored many of these methods and identified their performance characteristics. This gives us the ability to choose amongst a variety of possible designs to achieve the optimal set of characteristics for a given application. Tradeoffs in performance and design complexity are summarized in Table 2.

Table 2. Summary of Tradeoffs.

Method	Sensitivity (pT)	Dynamic Range (nT)	Dead Zones	Type	Implementation
Coherent Population Trapping	10-100	100,000	None	Scalar	Small heading error, difficult signal processing
FMNMOR	50-100	100,000	Equatorial	Scalar	Very complicated optics
Mx	6	100,000	Polar and equatorial	Scalar	Wire coil needed, cross talk in arrays.
Full F Bell-Bloom	10-15	100,000	Polar	Scalar	Extraneous resonances
Half F Bell-Bloom	15-20	100,000	Polar	Scalar	Easy

3.6.3. Cell Dimensions and Buffer Gas Pressure

As an example of the design analysis we have performed, consider the issue of buffer gas pressure and cell dimensions. The cesium cell for a macroscopic MFAM sensor has dimensions of: $a=2$ centimeters (cm), $b=1.3$ cm, $c=0.45$ cm.

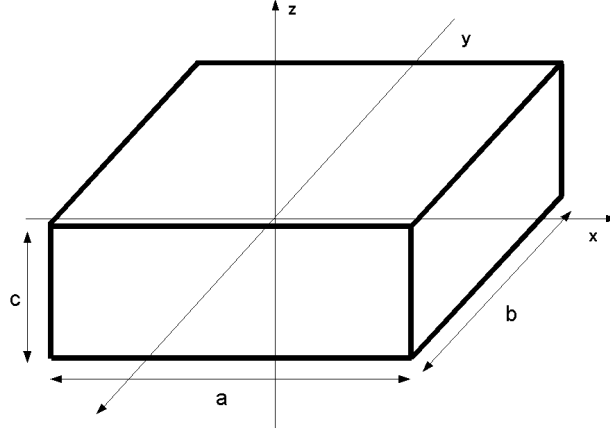


Figure 71. Dimensions of cesium cell for an MFAM sensor.

The rate of cesium atom collisions with the cell walls can be slowed by collisions with N_2 molecules in the buffer gas. Frequent cesium atom collisions with the buffer gas keep an atom far from the wall. This effect is described by a diffusion equation for polarized cesium atoms in the cell with a certain amount of buffer gas molecules:

$$\frac{\partial N_{pol}}{\partial t} = D \left[\frac{\partial^2 N_{pol}}{\partial x^2} + \frac{\partial^2 N_{pol}}{\partial y^2} + \frac{\partial^2 N_{pol}}{\partial z^2} \right] - \gamma N_{pol} + P \quad (1)$$

Where D is the Cs- N_2 diffusion coefficient, γ is the decay coefficient of Cs atom polarization and P is the rate of optical pumping which creates atomic polarization. When the atoms hit the wall, atomic polarization is destroyed, resulting in the boundary condition $N_{pol} = 0$ for $x = -a/2$, $x = a/2$, $y = -b/2$, $y = b/2$, $z = -c/2$, $z = c/2$.

The diffusion equation solution can be written in the form of the sum of the solutions for different diffusion modes (k, l, m):

$$N_{pol}(x, y, z, t) = N_{pol}^0 \sum_{k=0}^{\infty} \sum_{l=0}^{\infty} \sum_{m=0}^{\infty} \left[1 - e^{-(\Gamma_{k,l,m} + \gamma)t} \right] N_{pol}^{k,l,m}(x, y, z) \quad (2)$$

The steady state solution for certain diffusion mode (k, l, m) has a form of:

$$N_{pol}^{k,l,m}(x, y, z) = \frac{(-1)^{k+l+m}}{(2k+1)(2l+1)(2m+1)(\Gamma_{k,l,m} + \gamma)} \cos \left[(2k+1)\pi \frac{x}{a} \right] \cos \left[(2l+1)\pi \frac{y}{b} \right] \cos \left[(2m+1)\pi \frac{z}{c} \right] \quad (3)$$

where:

$$\Gamma_{k,l,m} = D_0 \pi^2 \frac{760}{p} \left(\frac{T}{273} \right)^{3/2} \left[\frac{(2k+1)^2}{a^2} + \frac{(2l+1)^2}{b^2} + \frac{(2m+1)^2}{c^2} \right] \quad (4)$$

represents the rate of collisions with the walls for different diffusion modes, D_0 is the diffusion coefficient in normal conditions (nitrogen pressure 760 Torr, and cell temperature $T=273$ degrees Kelvin [$^{\circ}\text{K}$]). It was found that diffusion can be described to a good approximation by considering only the first mode (0,0,0). Then $\Gamma_{0,0,0}$ can be considered as the number of cesium atom collisions with the wall per second. In a 1 mm cesium cell (sourced from Sandia) with a buffer gas pressure of 1000 Torr, then $\Gamma_{0,0,0}=250$ Hz and the signal was confirmed to be of good quality. For a slightly smaller cell with dimensions of: $a=2\text{cm}$, $b=1.2\text{cm}$ $c=0.45$ cm, we obtain $\Gamma_{0,0,0}=52\text{Hz}$ for buffer gas pressure of 100 Torr, which is 5 times less than that for a small cell, so even for low buffer gas pressure, the rate of collisions with walls is small enough to obtain good signal quality.

The total amount of polarized atoms integrated over the entire cell volume has the form:

$$N_{pol}(t) = N_{pol}^0 \sum_{k=0}^{\infty} \sum_{l=0}^{\infty} \sum_{m=0}^{\infty} N_{pol}^{k,l,m}(t) \quad (5)$$

where:

$$N_{pol}^{k,l,m}(t) = \left[1 - e^{-(\gamma + \Gamma_{k,l,m})t} \right] \frac{1}{[(2k+1)(2l+1)(2m+1)]^2} \frac{1}{[\Gamma_{k,l,m} + \gamma]} \quad (6)$$

And the steady state solution has the form:

$$N_{pol} = N_{pol}^0 \sum_{k=0}^{\infty} \sum_{l=0}^{\infty} \sum_{m=0}^{\infty} N_{pol}^{k,l,m} \quad (7)$$

$$N_{pol}^{k,l,m} = \frac{1}{[(2k+1)(2l+1)(2m+1)]^2} \frac{1}{[\Gamma_{k,l,m} + \gamma]} \quad (8)$$

Using equations (1) to (8) we can observe how the value of the magnetometric signal (which will be proportional to N_{pol}) will be influenced by the cesium cell shape and buffer gas pressure.

Figure 72 shows the number of polarized atoms as a function of the buffer gas pressure for the cesium cell with dimensions $a=2\text{cm}$, $b=1.2\text{cm}$ and $c=0.45$ cm. The signal at 500 Torr will be about two times the signal at 100 Torr. The amount of polarized atoms for $p=500$ Torr will be twice that for $p=100$ Torr. Higher buffer gas pressure involves more atoms in the total magnetometric signal and it decreases quantum shot noise and increases sensitivity.

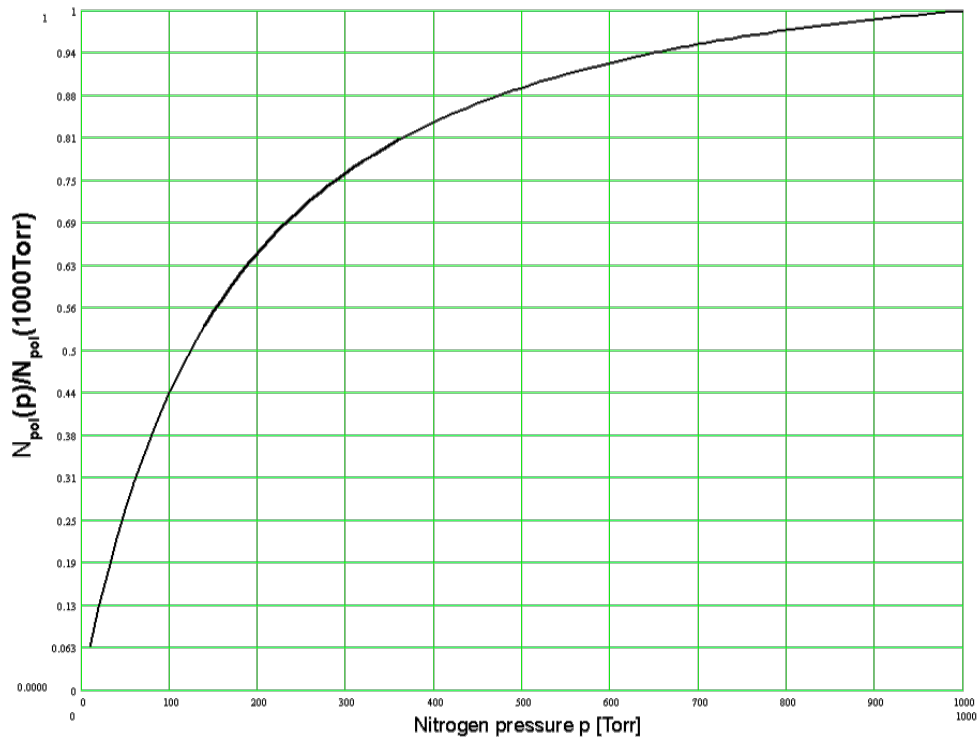


Figure 72. The number of polarized atoms as a function of the buffer gas pressure for the cesium cell with $a=2\text{cm}$, $b=1.2\text{cm}$ and $c=0.45\text{ cm}$.

For fixed cell volume $v=a*b*c$, fixed buffer gas pressure, and fixed temperature the maximum number of polarized atoms (minimum amount of atomic loss generated by collisions of cesium atoms with cell walls) is obtained with a cubic cell shape: $a=b=c$. However, because of competing cell design requirements, the cesium cell can't have a cubic shape and requires that $a \sim 2b$. The requirement for low power consumption limits the cell volume to about 1 cm^3 and at the same time limits the value of c . In Figure 73 we show the change of N_{pol} for different values of a, b, c when the cell volume is constant (1.08 cm^3). The graph shows the range of N_{pol} variation for two extreme values of a at a buffer gas pressure $p=100\text{ Torr}$.

The shape of the cell is mostly determined by other requirements and by low power consumption requirement. Values of a and b are determined by laser beam divergence and dimensions of available optical components. Values of c are then limited practically to the range 0.35mm to 0.55 mm . In this range the number of polarized atoms doesn't change dramatically so the chosen value of $c=0.45\text{ mm}$ is proper and should not dramatically decrease the signal value (sensitivity).

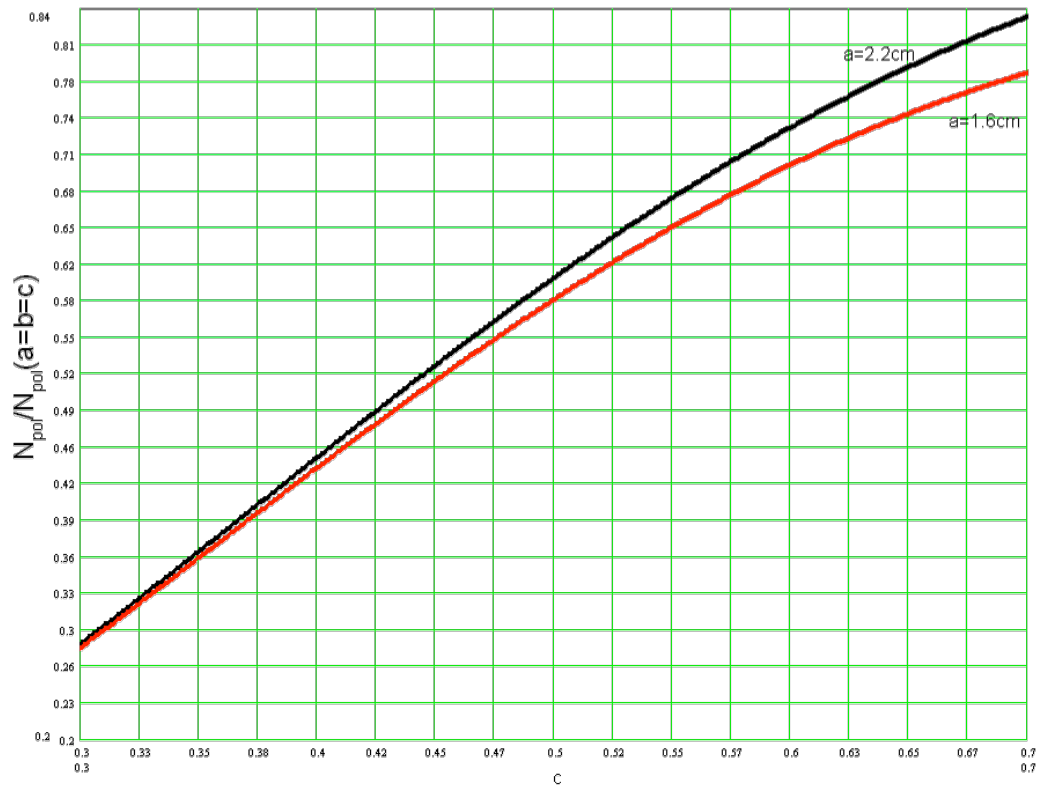


Figure 73. Change of N_{pol} for different values of a, b, c when the cell volume is constant (1.08 cm³).

Figure 74. The spatial distribution of the polarized atoms $N_{pol}(x, y=0, z=0)$ in the direction of x (along the longest side of the cell). shows the spatial distribution of the polarized atoms $N_{pol}(x, y=0, z=0)$ in the direction of x (along the longest side of the cell). The graph shows that the zone when the magnetometric signal (which is proportional to N_{pol}) starts to decrease to 50% of its maximum value, starts about 1 mm from the cell wall. In this case the buffer gas pressure was 100 Torr.

Even in the case of low buffer gas pressure, the region when there will be (effectively) no signal is less than one millimeter, which is small compared to the cell dimensions. So its reasonable in the optical design of the sensor to create a laser beam with large diameter to obtain a stronger signal (better sensitivity). A large laser beam will involve more atoms to produce the magnetometric signal and this effect decreases quantum shot noise coming from cesium atoms while improving sensitivity.

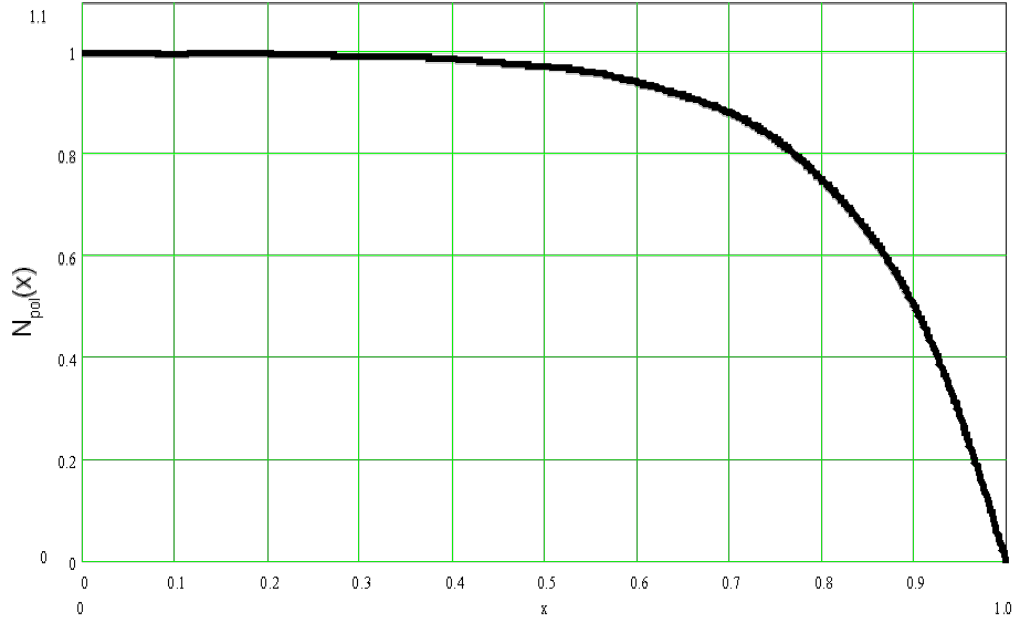


Figure 74. The spatial distribution of the polarized atoms $N_{\text{pol}}(x,y=0,z=0)$ in the direction of x (along the longest side of the cell).

3.6.4. Light Absorption and Atomic States of Most Interest

Figure 75 shows the transient behavior of polarized atoms for all diffusion modes and for the first seven leading diffusion modes at a buffer gas pressure of 100 Torr. Relaxation time for the first mode $1/\Gamma_{0,0,0}$ is about 20 ms. After times larger than $5/\Gamma_{0,0,0}$ we observe a steady state behavior of N_{pol} . The graph shows that almost 80% of the total value of N_{pol} (80% of the magnetometric signal) comes from the first diffusion mode (0,0,0) and about 95% of the total signal comes from three leading modes (0,0,0), (1,0,0) and (0,1,0).

This fact simplifies calculations when the collisions of cesium atoms with the wall have to be applied. It especially simplifies the density matrix equation used to calculate populations of electrons in ground states of cesium atoms. These calculations are used for the heading error evaluation. It was found that for a large range of buffer gas pressure ($p=40$ to 1000 Torr) the analysis presented above is accurate.

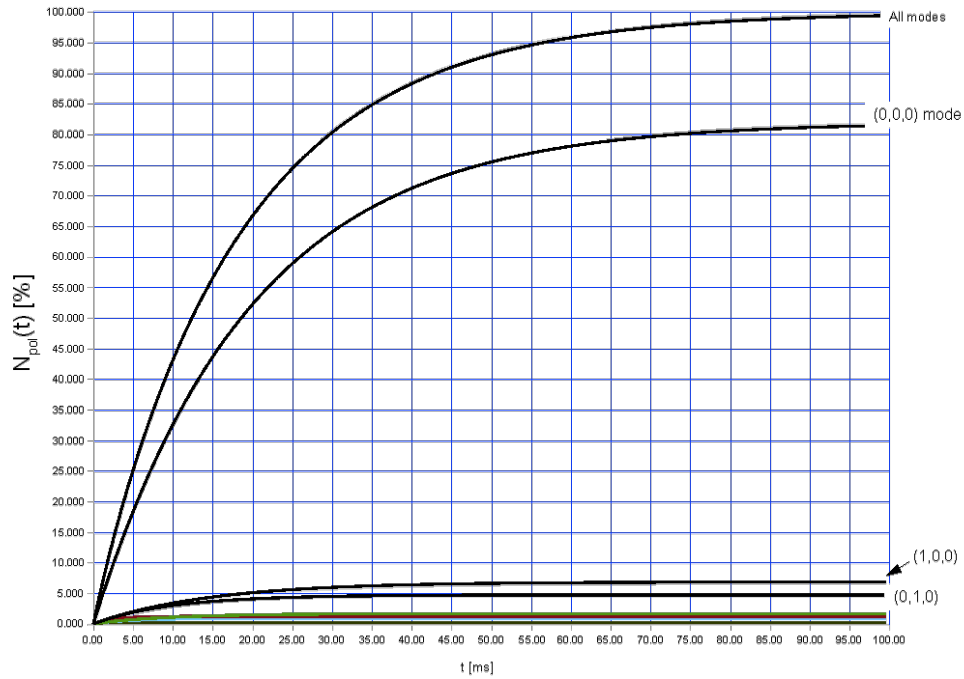


Figure 75. This plot shows the transient behavior of polarized atoms for all diffusion modes and for the first seven leading modes. Buffer gas pressure $p=100$ Torr.

When optically pumping with a narrow light source, one has to consider whether atoms will become trapped in states that do not interact with the light beam. In sensors that are pumped with a gas discharge lamp, this is not a problem, as all transitions are exposed to radiation of the correct frequency. However, this is not the case with a narrow-band laser light source. Figure 76 to Figure 78 show the absorption of a laser beam near the D1 cesium line for buffer gas pressures of 30, 100 and 300 Torr.

To obtain optical pumping for $F=3$ and $F=4$ hyperfine components at the 30 Torr pressure, two laser beams are required for practical operation. This fact leads to the conclusion that this buffer gas pressure is too low for magnetometric application. At 100 Torr pressure (Figure 76), the absorption in peaks with respect to the absorption value for 5.1 GHz is only 6 times higher. This means that it is possible to use one laser beam tuned between two hyperfine components to obtain effective optical pumping rate for $F=3$ and $F=4$ components (also see Figure 77). Therefore, for a buffer gas pressure $p=100$ Torr, one laser beam can be used for optical pumping. We take this buffer gas pressure value as a possible lower pressure in the cell (lower pressure limit). At 300 Torr (Figure 78) there is a very small difference between absorption in both hyperfine peaks and absorption for the laser light frequency of 5.1 GHz. Therefore, for buffer gas pressure $p=300$ Torr, one laser beam can be used for optical pumping. Because of the laser frequency locking technique used in our design we prefer to have the smallest possible difference between absorption in 5.1 GHz and in hyperfine peaks.

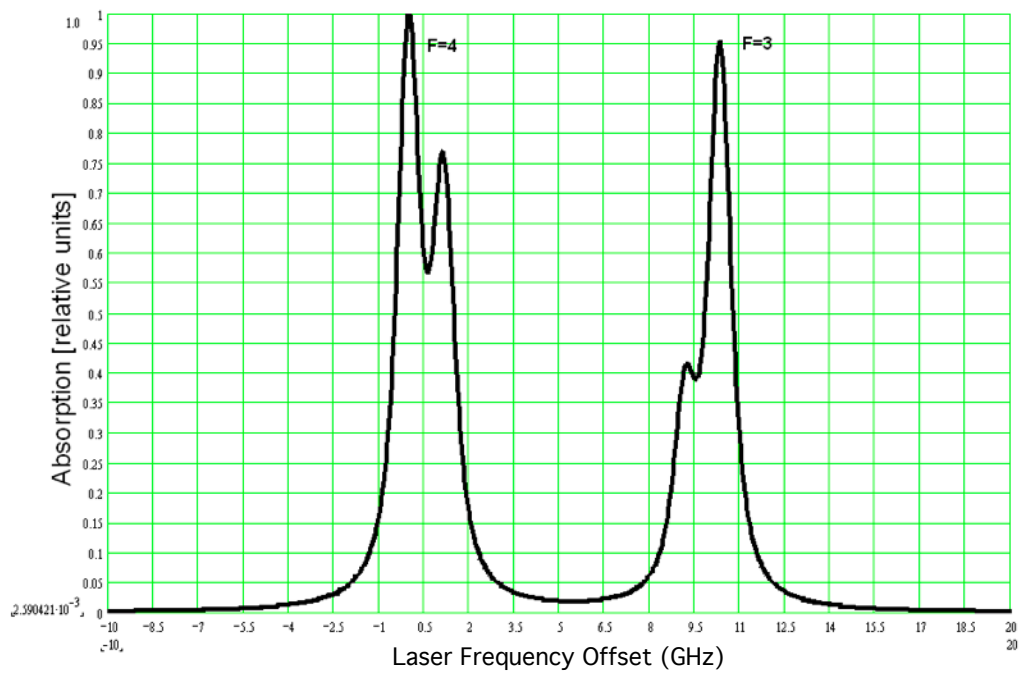


Figure 76. Absorption of the laser beam tuned to D1 cesium line in the case of buffer gas (nitrogen) pressure $p=30$ Torr. Both hyperfine components are resolved.

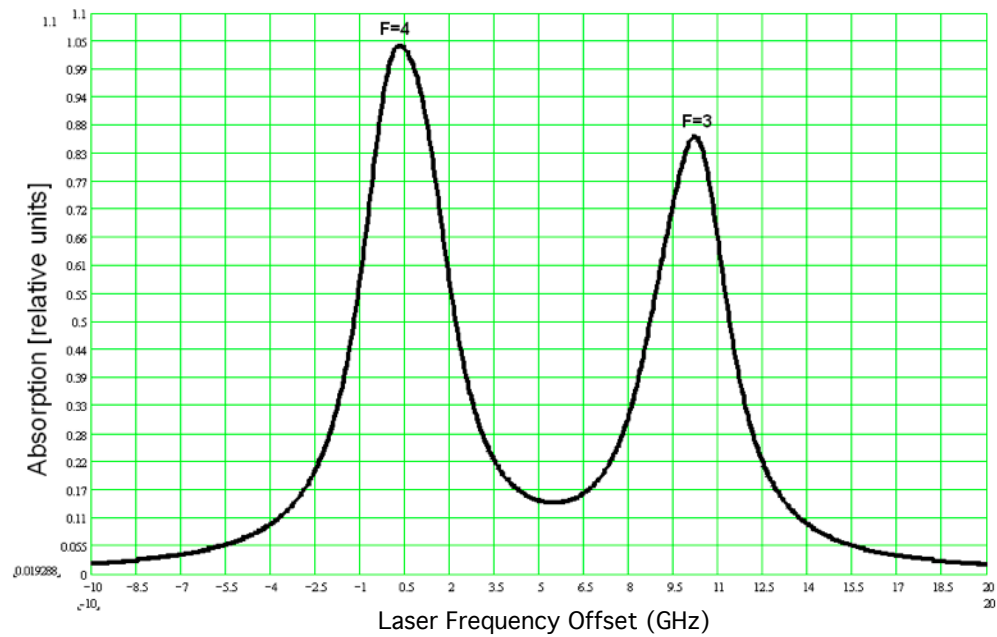


Figure 77. Absorption of the laser beam tuned to D1 cesium line in the case of buffer gas (nitrogen) pressure $p=100$ Torr. Both hyperfine components are resolved.

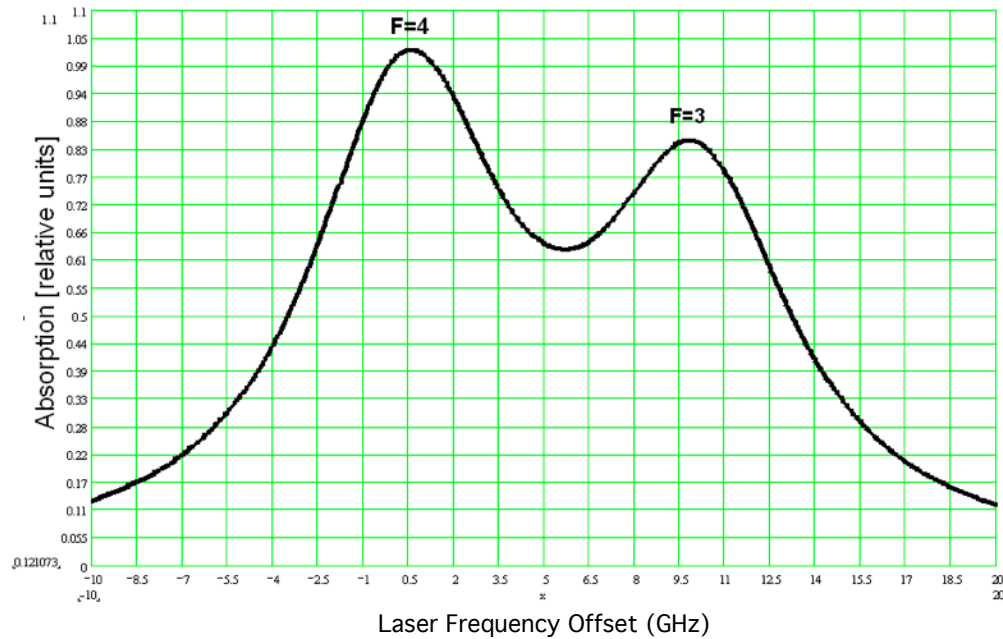


Figure 78. Absorption of the laser beam tuned to D1 cesium line in the case of buffer gas (nitrogen) pressure $p=300$ Torr. Spectral width of absorption spectra is high and hyperfine components are barely resolved.

Figure 79 shows the change of absorption rate for $F=4$, $m=3$ to excited states transition as a function of the buffer gas pressure. Laser frequency is tuned between $F=4$, $F=3$ hyperfine cesium lines (5.1 GHz), so one laser beam can be used to obtain optical pumping for $F=3$ and $F=4$ components. Absorption rate value determines effectiveness of optical pumping which creates atomic polarization of cesium atoms necessary to obtain magnetometric signal. Maximum value of this rate is about 380 Torr. The graph was obtained for 300 W/m^2 laser intensity.

From Figure 79, it is reasonable to establish an upper limit of the buffer gas pressure at roughly 500 Torr, which is significantly offset from the maximum value of the absorption rate (380 Torr). For higher pressures nothing interesting happens from a performance perspective, except the absorption rate, and therefore sensitivity, continues to drop.

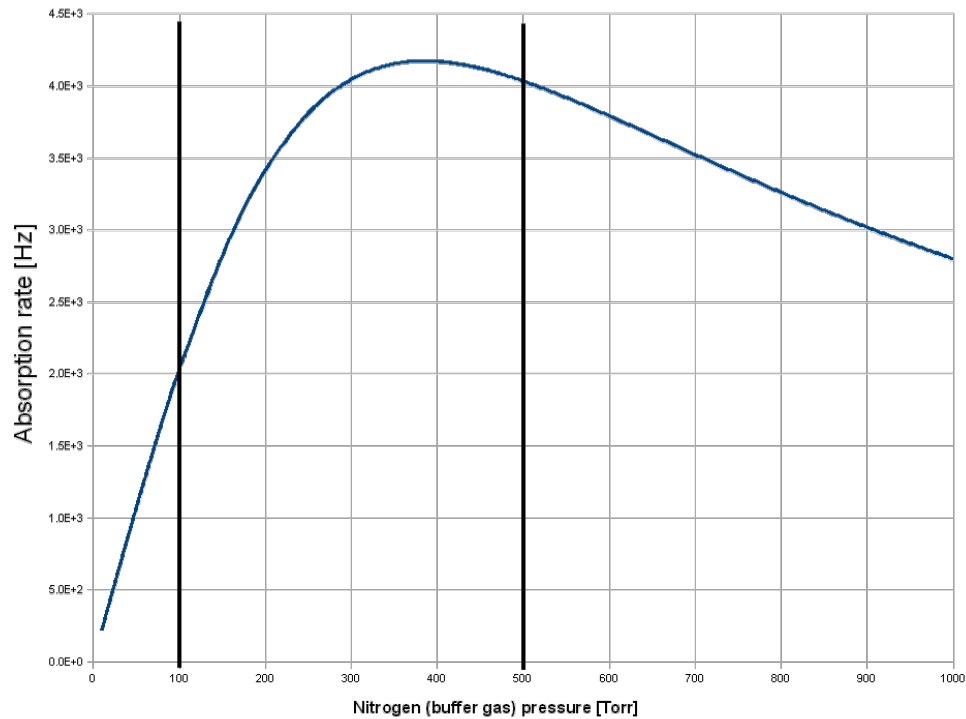


Figure 79. Change of absorption rate for $F=4$, $m=3$ to excited states transition as a function of the buffer gas pressure.

3.1.5. RF Line Width

Figure 80 shows the variation of RF line width (error signal width) as a function of buffer gas pressure. We can see that RF line width increases linearly with increasing value of buffer gas pressure. Therefore, lower buffer gas pressures are required to obtain a narrow RF line (error signal width). Generally speaking, a narrow EF line resonance enhances sensitivity. However, other effects demand higher buffer gas pressure, so we see the importance of accurately quantifying these effects to optimize the sensor performance.

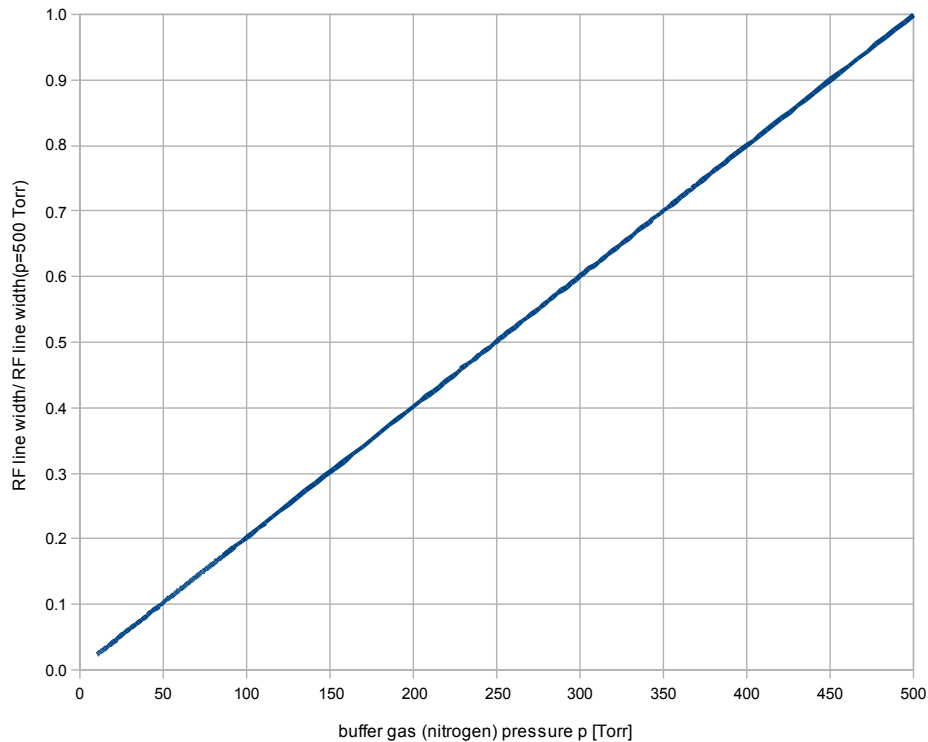


Figure 80. Variation of RF line width (error signal width) as a function of buffer gas pressure. RF line width value is presented in relative units of RF line width for $p=500$ Torr.

3.1.6. Heading Error

Total field magnetometers are designed to provide measurements that are nearly independent of sensor orientation with respect to the magnetic field vector. Changes in the readings due to orientation are called heading errors. These errors may be caused by the physical principles of the measurement, which can be reduced in the electronics design, or may be caused by impurities of ferrous materials in the construction of the sensor. Heading errors are particularly influenced by buffer gas pressure.

Figure 81 and Figure 82 present the ratio p_2/p_1 of the populations of two ground states $F=4$, $m=3$ (population p_2) and $F=4$, $m=4$ (population p_1). The calculations were obtained for the sensor position when only circular polarization of light is present. The ratio is proportional to the heading error. From this we can conclude that heading error will decrease with decreasing buffer gas pressure.

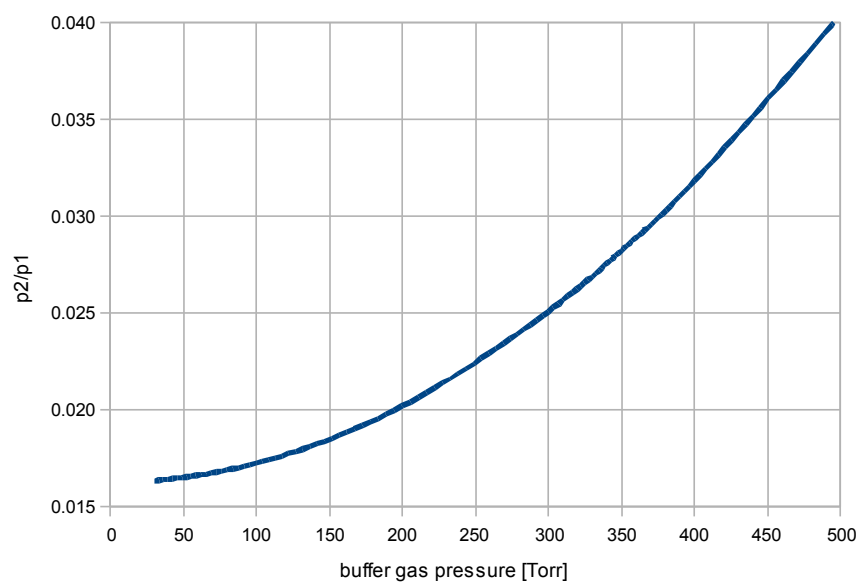


Figure 81. Ratio p_2/p_1 of the populations of two ground states $F=4$, $m=3$ (population p_2) and $F=4$, $m=4$ (population p_1) as a function of pressure.

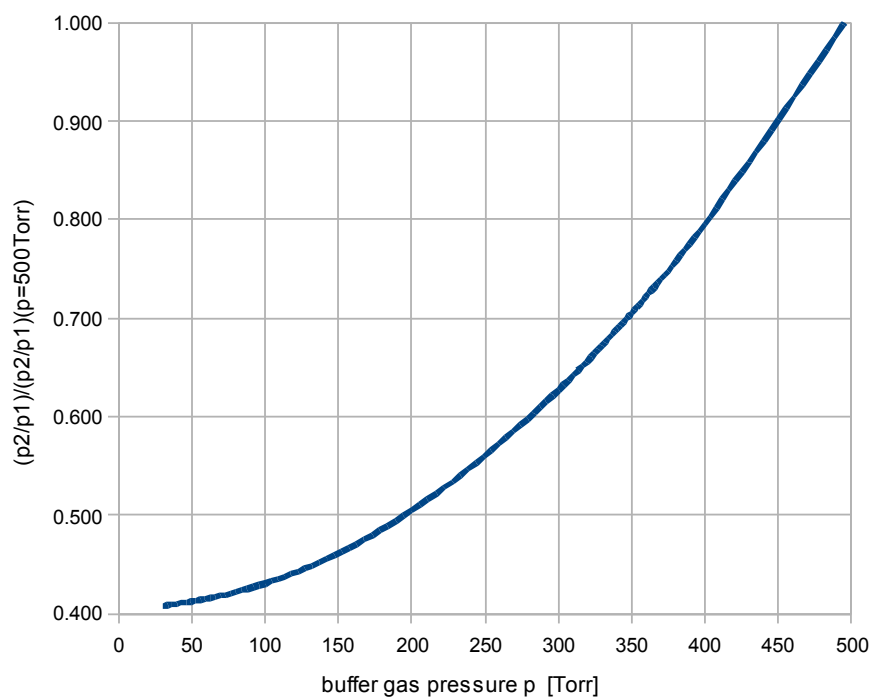


Figure 82. Ratio p_2/p_1 of the populations of two ground states $F=4$, $m=3$ (population p_2) and $F=4$, $m=4$ (population p_1) as a function of pressure, relative to the value of p_2/p_1 at a pressure of 500 Torr.

Summary of Design Tradeoffs

Figure 76 through Figure 79, concerning absorption, illustrate why we evaluated the buffer gas pressures between 100-500 Torr. As shown in Figure 76, 30 Torr is too low. From Figure 77, 100 Torr is usable. The absorption rate for 100 Torr is not very different from the absorption measured at 760 Torr, which was used in a 1 cubic mm cell whose performance has been well characterized.

In the range from 100 to 400 Torr we have an increasing optical pumping rate. There is no need to consider higher pressures because absorption decreases for higher pressures. Higher pressures serve to reduce the rate of collisions with the cell walls and are necessary for the 1 cubic mm cells we have used in earlier work. Here, we don't need high nitrogen pressure to dampen wall collisions because we have a large enough cell. Figure 82 indicates that we would like a higher pressure in the cell because we will have stronger signal when there is a higher optical pumping rate. Higher nitrogen pressure is also desirable because it is easier to lock the frequency of the laser to the correct value at higher pressures. For that, it is better to have a smaller change in absorption between the two peaks at $F=4$ and $F=3$ (Figure 78).

On the other hand, we prefer lower buffer gas pressure because we obtain a small RF line at lower nitrogen pressure (Figure 80) and a narrower RF line yields higher sensitivity. Also, for lower buffer gas pressure we have a smaller heading error. To find the tradeoff between all of these effects (to find the proper place between low 100 Torr and high 300-500 Torr) we ordered three cells at 100, 250, 500 Torr. This will help us to find the optimum pumping pressure by combining experimental findings with the previously identified theoretical considerations.

Our analysis demonstrates our capabilities to model the behavior of a magnetometer given a variety of design parameters. These results have been confirmed experimentally. We now have the ability to generate designs that tailor the performance of magnetic field sensors to particular applications.

Heading error shaping in two laser beam magnetometer.

It was found by numerical analysis that heading error in a two beam magnetometer can have the form of a sin function with a certain amplitude. This gives the possibility to eliminate heading error by subtracting a sin function generated by the electronics from the measured Larmor frequency (we know how to detect the sensor position from the analysis of higher harmonics of the error signal). This is possible with a small beam divergence. Significant beam divergence means a more complicated form of the heading error that is not so easily compensated. Figure 83 below shows heading error shape in a two beam magnetometer for different angle between the laser beams:

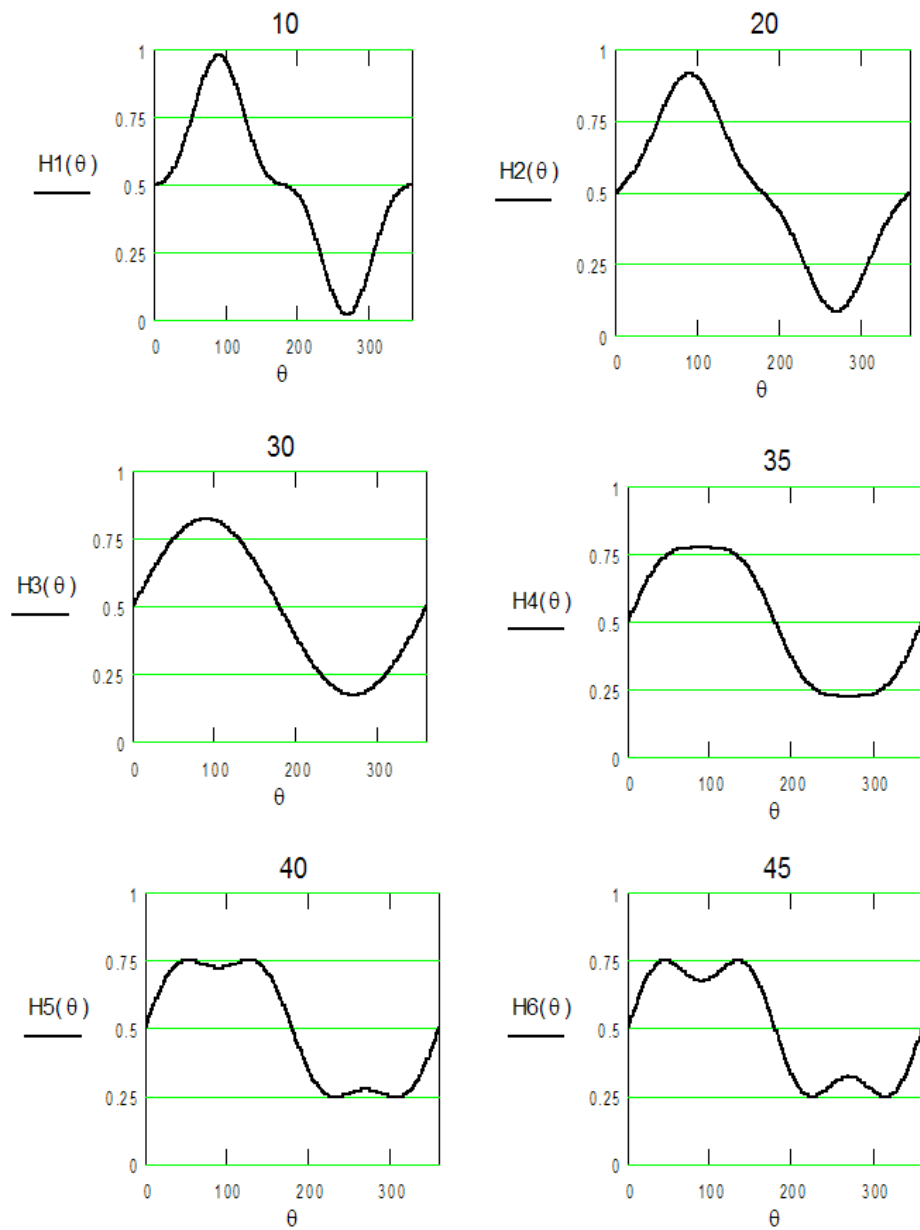


Figure 83. Offset in magnetic field reading (heading error) as a function of angle for various optical geometries.

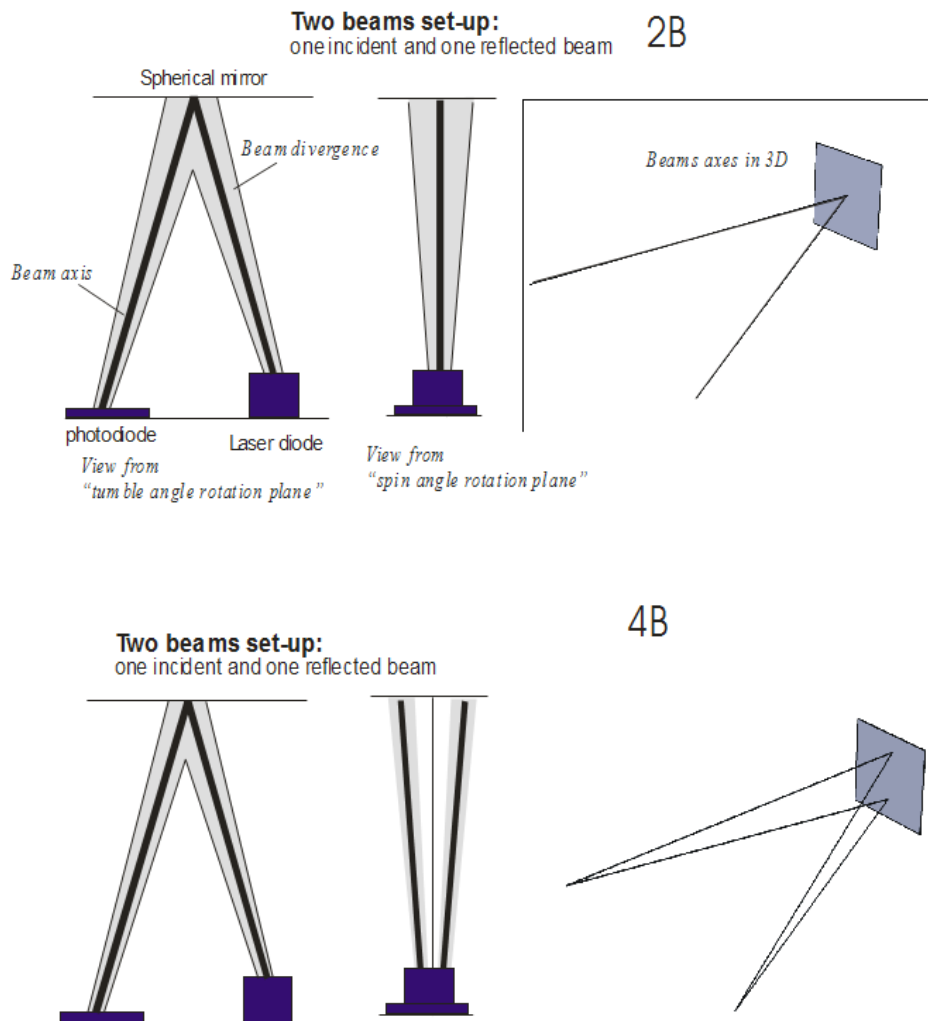


Figure 84. Beam geometries used to minimize heading error and dead zones

The existence of two beams also helps to eliminate the dead zone problem. The idea is that if one beam is in the dead zone the other beam is out of it and delivers the magnetometric signal. Figure 84 shows a configuration to remove dead zones and reduce heading error. Beam #1 passing the cell is the beam coming from the laser. This beam is reflected from the mirror and produces beam #2-reflected beam which passes the cell again and hits the photocell. The relatively large angle between those beams eliminates the dead zone in the tumble angle rotation. To eliminate dead zone in the spin angle rotation we used the beam's divergence, which gives laser beam distribution in the plane perpendicular to the plane created by the #1 and #2 beams. To improve amplitude of the signal in the spin angle dead zone it is not enough to have only divergent beams.

Each beam has most of its intensity concentrated in its center. To obtain relatively large amplitude of the signal in the spin angle rotation we need to generate two beams from beam #1. Those beams should be in the spin angle rotation plane. This will produce two reflected beams instead of just one.

A beam trace method and numerical calculations were performed to find different methods (optical elements) to obtain an “angular beam splitter” that splits one laser beam into two beams propagated at certain angle. It can be done by prisms or cylindrical lenses or by a system of prism and cylindrical lenses. Figure 85 shows examples of different solutions.

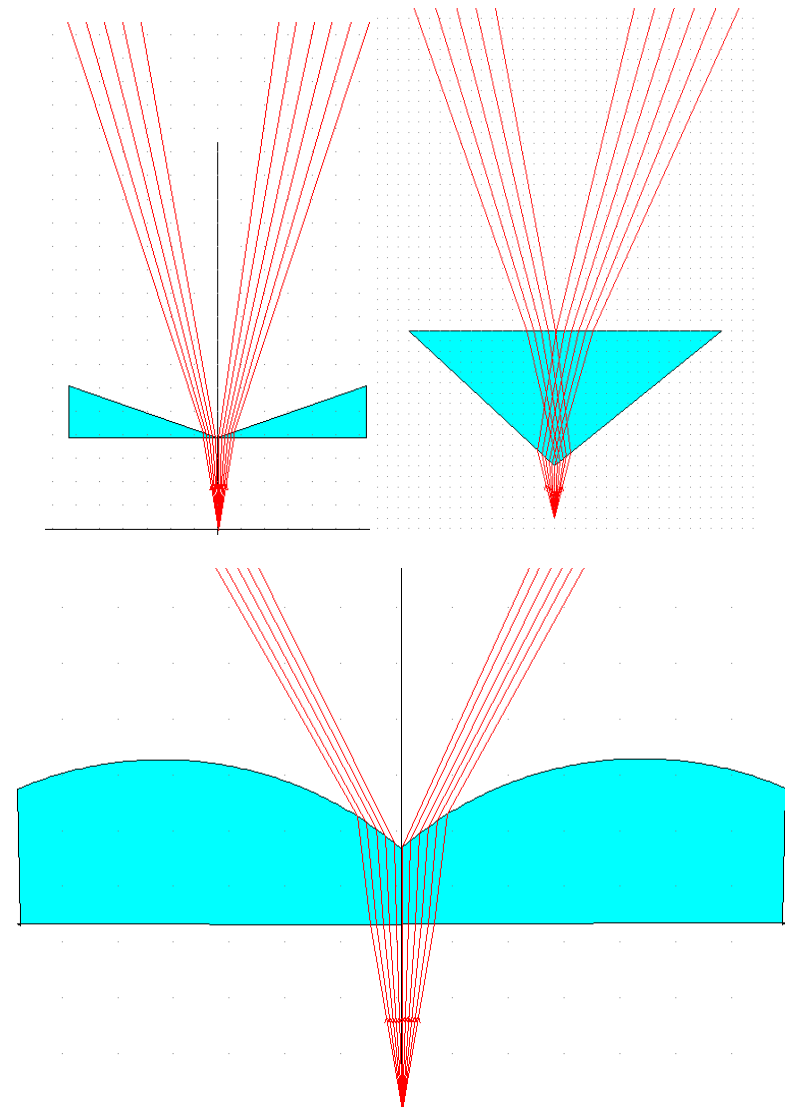
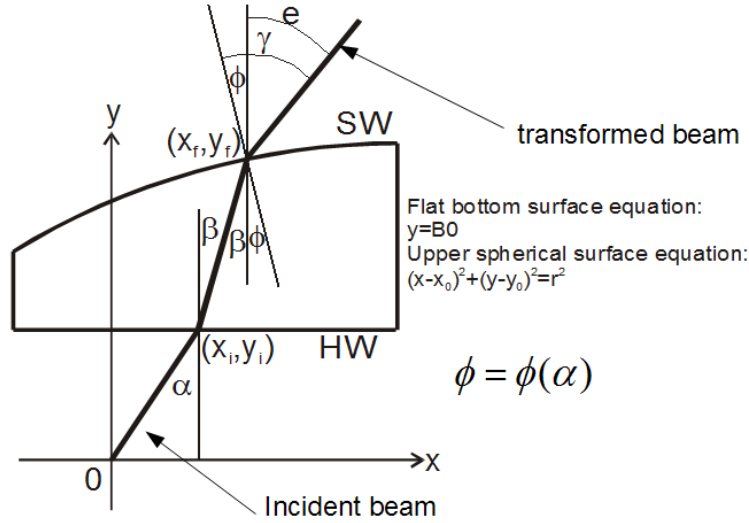


Figure 85. Generating multiple beams from a single laser source.

To design proper optical system for this task it is necessary to find the proper laser beam intensity distribution for the transformed beam. Figure 86 shows an example of the calculations:



$$a_t = \operatorname{tg} \left[90 - \arcsin \left(\frac{\sin(\alpha)}{n} \right) \right], b_t = B0 - a_t B0 \operatorname{tg}(\alpha) \rightarrow \text{First refracted beam eq is: } y = a_t x + b_t$$

Solution $\{x_f, y_f\}$ of the equation system: $\{y = a_t x + b_t, (x - x_0)^2 + (y - y_0)^2 = r^2\}$ is:

$$x_f = \frac{(x_0 - a_t b_t + a_t y_0) + \sqrt{(x_0 - a_t b_t + a_t y_0)^2 - (1 + a_t^2)(x_0^2 + b_t^2 - 2b_t y_0 + y_0^2 - r^2)}}{(1 + a_t^2)}$$

$$y_f = a_t \left[\frac{(x_0 - a_t b_t + a_t y_0) + \sqrt{(x_0 - a_t b_t + a_t y_0)^2 - (1 + a_t^2)(x_0^2 + b_t^2 - 2b_t y_0 + y_0^2 - r^2)}}{(1 + a_t^2)} \right] + b_t$$

$$\phi(\alpha, h, r) = \arctan g \left[\frac{x_f - x_0}{y_f - y_0} \right], \text{ where } h \text{ will be } B0 \text{ as a variable.}$$

$$e(\alpha, h, r) = \arcsin \left[n \sin \left(\arcsin \left(\frac{\sin(\alpha)}{n} \right) + \phi(\alpha, h, r) \right) \right] - \phi(\alpha, h, r)$$

Transformed beam intensity distribution $I(e)$ can be obtained as a parametric graph:

$$y\text{-axis: } I(\alpha) = I_0 \exp[-\alpha^2 / \delta^2]$$

$$x\text{-axis: } e(\alpha, h, r) = \arcsin \left[n \sin \left(\arcsin \left(\frac{\sin(\alpha)}{n} \right) + \phi(\alpha, h, r) \right) \right] - \phi(\alpha, h, r)$$

and the parameter is initial angle α .

Figure 86. Calculating properties of refracted laser beams

Accurately knowing the amount of light at each angles requires that we understand the distribution of light in our laser beam. In order to do this, we measured the intensity in the

following way. A set-up with a CCD camera was developed to check parameters of the laser beams. There will be couple of beams in the system and the power and the angular distribution of each beam has to be known for the proper system design. As an example of this activity the initial laser beam intensity distribution is shown in Figure 87.

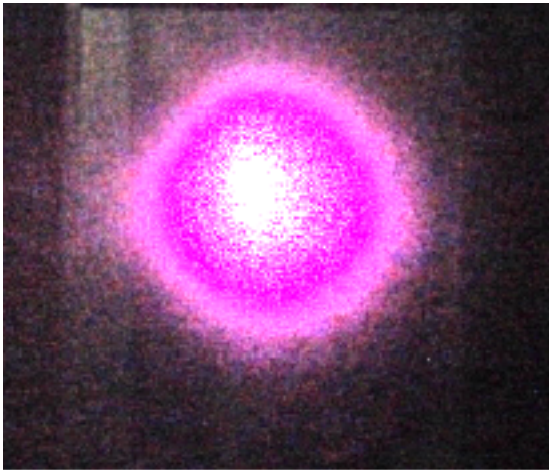


Figure 87. Photograph of cross section of laser intensity from VCSEL

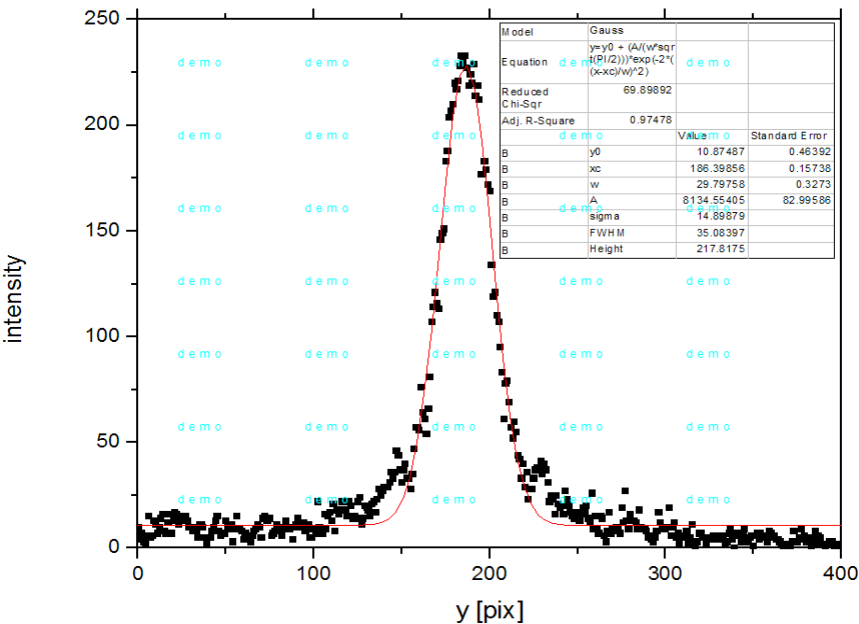


Figure 88. Graph of cross section of laser intensity from VCSEL

Population calculations

Figure 89 show the calculated populations of the many energy levels. On the left the laser is parallel to the magnetic field, while on the right, the laser is at an angle to the magnetic field.

The populations of the Cs are determined by the optical pumping process. For the laser beam parallel to the magnetic field, the state $F=4, m=4$ is very strongly populated because there is only sigma + light polarization and transfer from this level to excited level of m' can only be with this polarization $m'=m+1$, but this is impossible because the higher $m'=4$.

Therefore, this level is a trapping level and only ground level collisional relaxations cause a lower than 100% population of this level. Bar plot on the right shows that laser beam rotation results in sigma minus ($m'=m-1$) and pi ($m'=m$) transitions and state $F=4, m=4$ is losing its high population for lower ground levels.

Both of the cases shown create a net polarization and a magnetometer signal. However, the Larmor frequency is slightly different in each case, because of slight differences in the energy levels from the simplest model. This is one of the causes of heading error in a magnetometer. From the populations calculated here, we can calculate the heading error.

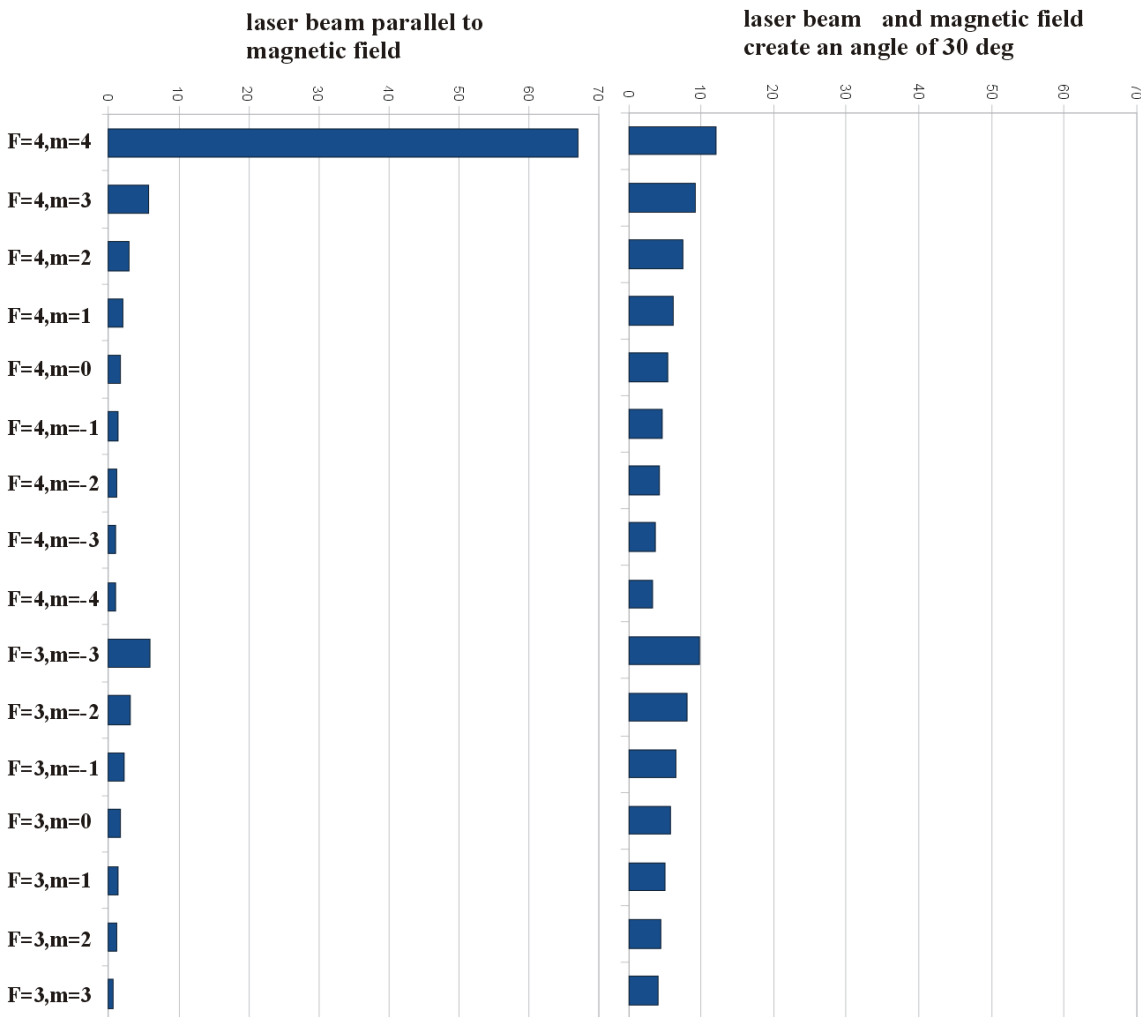


Figure 89. Populations of various energy levels.

Figure 90 illustrates the changing populations caused by the RF when we scan the RF frequency to obtain RF resonance between ground levels. This simulation shows a transfer of electrons from the level $F=4, m=4$ (for beam parallel to magnetic field) to lower ground levels. This modifies absorption coefficient and generates a change in the laser beam absorption, which causes a change in the laser beam intensity on the photodiode. Small window graph presents ground level population changes by RF field for the tumble angle 80 deg. when population are more even. We can see that some levels are losing population and some obtaining gaining population during the RF frequency sweep.

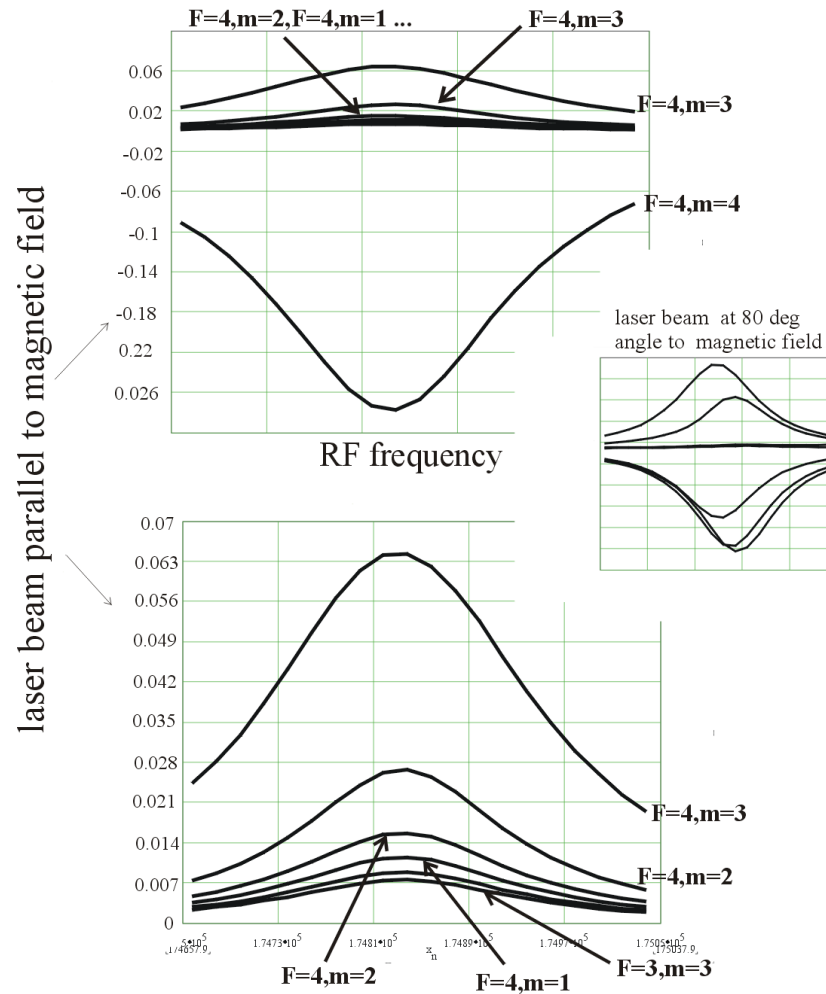


Figure 90. Change in the populations as a function of changing angle of the sensor.

Figure 91 shows the simulation of the change in the absorption coefficient during RF resonance. An increase in the absorption coefficient results in an increase in the laser beam absorption and a decrease of the laser intensity on the photodiode. This completes the simulation of all the processes occurring in the operation of the magnetometer. The properties of this resonance determine the noise level and the heading error of a particular design.

These processes are summarized as follows. First we have optical pumping which determines the ground level population (Figure 89). Then we can see that RF fields change these populations (Figure 90), and those changes generate absorption coefficient change (Figure 91) which produces the magnetometer signal. These figures show the sequence of processes producing change of the light intensity on the photodiode. Running the algorithms which reflect the sequence of those processes allows us to calculate heading error. An example is shown in Figure 92.

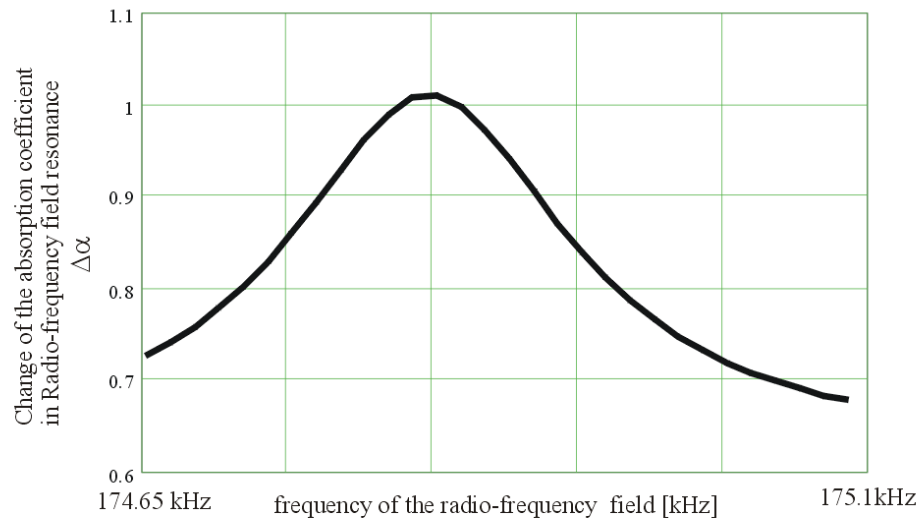


Figure 91. Simulation of RF resonance.

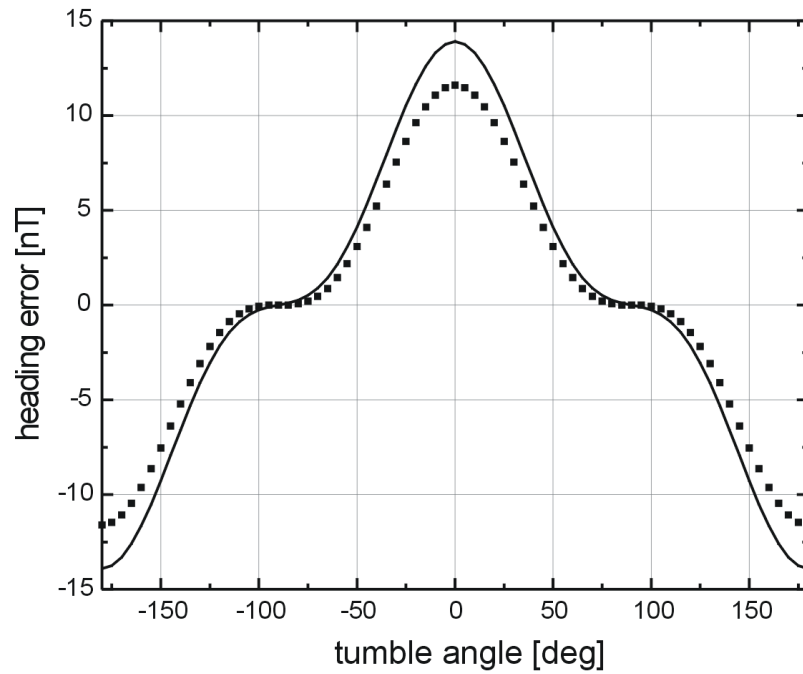


Figure 92. Results of heading error calculation

Minimizing Heading Error

Using the above framework, we can now design systems to minimize the heading error. When we rotated our sensor from $\theta=0$ (tu- tumble angle) to $\theta=90^\circ$ we observed a total heading error of about 40nT. The origin of the total heading error is visible on Figure 93. The total signal is modeled as the superposition of the signal (Lorentzian) from $F=4$ ground level manifold and $F=3$ ground level manifold. In the case of $\theta=0$ the signal from $F=4$ is dominating (75% of the total signal), $F=3$ gives about 25% of the total signal. For $\theta=90^\circ$ the contribution from both ground levels manifolds is almost equal (50%- $F=4$, 50%- $F=3$).

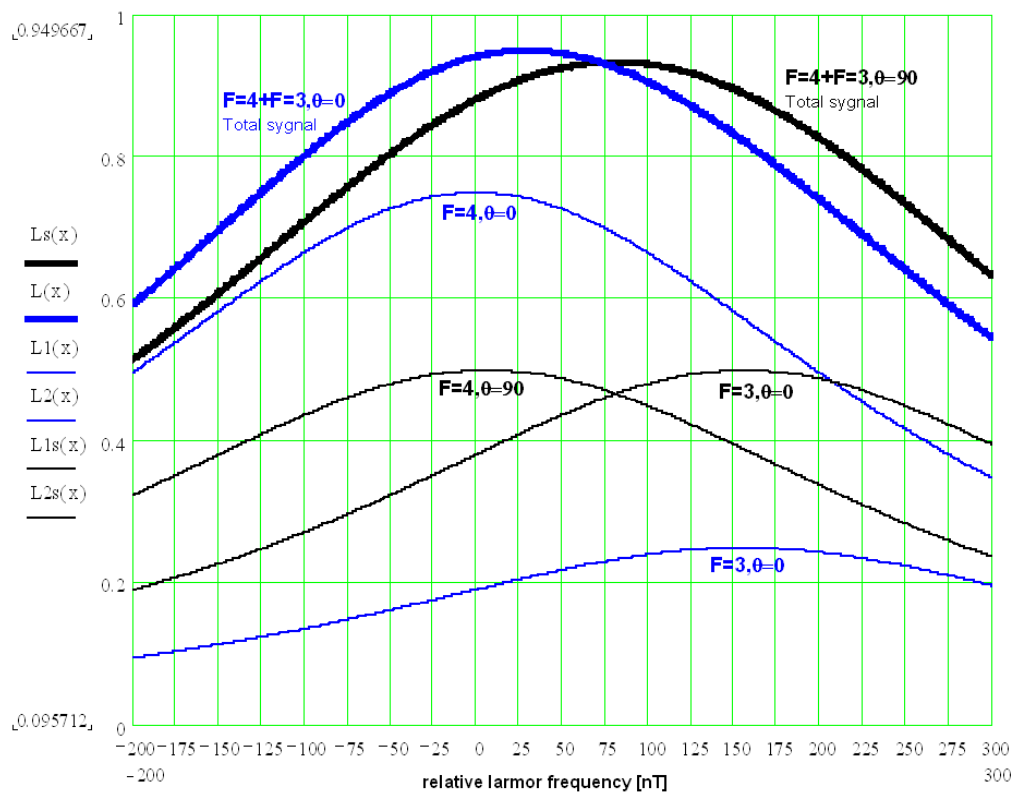


Figure 93 RF resonance shifts for different energy levels

Maximum position for (Larmor frequency) for $F=4$ and $F=3$ Lorentzians were calculated as an average Larmor frequencies over certain manifold ($F=4$ or $F=3$). The Larmor frequencies for all levels were calculated from Breit-Rabi formula (nonlinearity in Zeeman splitting) and they include light shifts for all of the ground level for $\theta=0$ and $\theta=90^\circ$. Equations are shown in Figure 94.

$$f4_{av} = \frac{1}{8} \sum_{\text{over } F=4} f_i$$

$$f_i = \nu(B)_i + LS_i - \nu(B)_{i-1} - LS_{i-1}$$

$$f3_{av} = \frac{1}{6} \sum_{\text{over } F=3} f_i$$

$$f_i = \nu(B)_i + LS_i - \nu(B)_{i-1} - LS_{i-1} - \text{Larmor frequency for } i \rightarrow i-1 \text{ RF transition}$$

$\nu(B)_i$ - atomic frequency cal. from Breit-Rabi formula

LS_i - light shift for i-th level

$f4_{av}$ - average larmor fr. for F=4 manifold

$f3_{av}$ - average larmor fr. for F=3 manifold

Figure 94 Equations used for calculating combined RF resonance from individual states.

Total heading error as visible on Figure 93 comes from the existence of the F=3 manifold which drags the maximum of the total signal (superposition of two Lorentian) in the direction of the larger values of the Larmor frequencies. During the sensor rotation a light shift causes small changes of the average Larmor frequencies and changes in the relative amplitudes from F=4 and F=3 manifold and the change of this amplitude is the main source of the total heading error.

Calculations showed that total heading error changes about 12% when we change the laser frequency from the F=3 absorption peak to the F=4 absorption peak. Total heading error for F=3 peak is about 40nT. So changing laser frequency from one absorption peak to another is not sufficient to eliminate the heading error.

Therefore, we cannot eliminate heading error using only one beam. We can compensate heading error which is generated using a known profile of heading error as a function of tumble angle; or we can flatten the heading error curve as a function of tumble angle using 3 laser beams. As shown in Figure 95, each beam which will have a heading error profile shifted in angle. We can detect the magnetometer signal from each beam separately and rescale the amplitude of each signal (or the slope of each error signal) using the second harmonic of the signal which carries information about signal amplitude. After rescaling all error signals to have the same slopes we can add error signals from 3 beams which will flatten the heading error profile as shown in Figure 96.

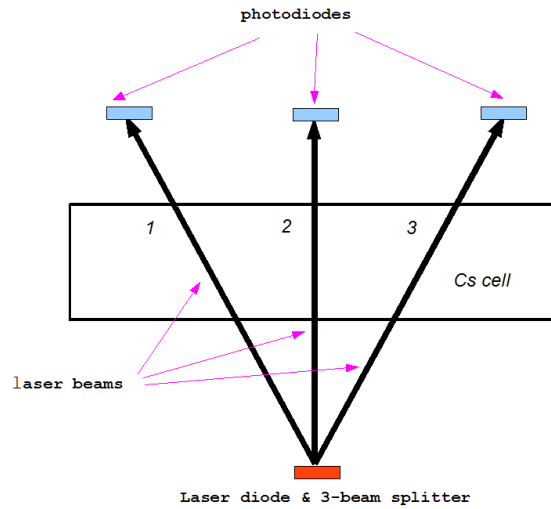


Figure 95 Using three beams to obtain heading error curves of different phases.

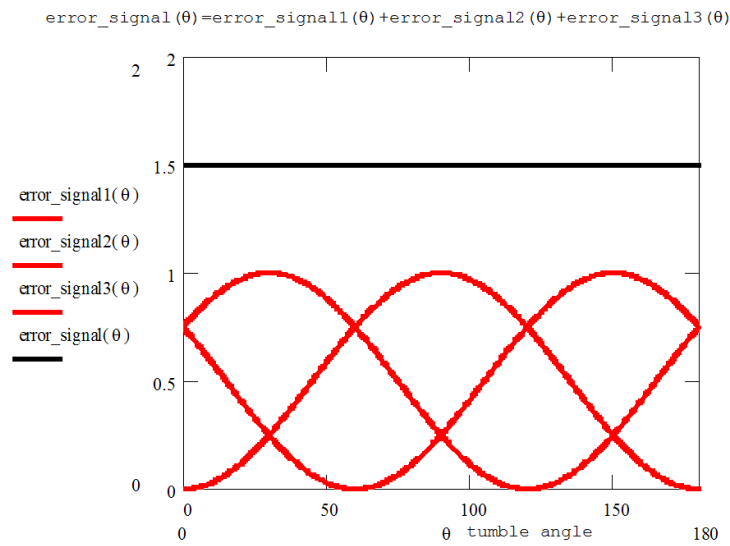


Figure 96 Combining individual heading errors into a signal free from heading error.

Consistency of heading error

When using magnetometer sensors in an array, where their signals are subtracted from each other, the absolute heading error of each sensor does not matter. In that application, if the heading error curves from all the sensors are matched, a heading error looks no different than an overall change in the background field reading. What is important in that application is whether or not heading errors are consistent enough from sensor to sensor. We can use our model to analyze how much the heading error will change with various inconsistencies in production of sensors.

Changes of total and light shift heading errors with changes of magnetometer parameters:

Central values of the parameters:

buffer gas pressure: $p_0=500$ Torr

laser intensity: $I_0=11$ $\mu\text{W}/\text{mm}^2$

laser frequency ν_0 : 9.77647177 GHz (F=3 absorption peak)

$p=p_0+dp$, $I=I_0+dI$, $\nu=\nu_0+d\nu$, $dhe=100*(he-he_0)/he_0$

dp [%]	dI [%]	dν [%]	dhe [%]
0	0	0	0
0	10	0	1.9
0	-10	0	-3.8
20	0	0	-3.7
-20	0	0	3.6
0	0	3	-3.5
0	0	-3	1.8

Figure 97 Sensitivity of heading error with variation in sensor parameters.

We can control very precisely the laser beam intensity and keep I-value from one physics package to another within $dI=\pm 1\%$ or even less. Buffer gas pressure p should not differ from cell to cell more than maximum $dp=\pm 10\%$. Laser intensity also is very stable from one sensor package to another. We lock the laser by modulating the laser frequency around the maximum of F=3 peak with an amplitude of 300MHZ which gives maximum changes of laser frequency $\pm 3\%$. This modulation, however, will be averaged in time and practically laser frequency should be stable to $d\nu=\pm 1\%$ or less.

The small variations in heading error with reasonable variations in sensor parameters are summarized in Figure 97. From the numbers indicated there we conclude that we can design sensors with small variations in heading error from sensor to sensor, and thus address the application of sensor arrays.

Physics Package Integration

Task 4.1: Design and thermal modeling of cell structure

Completed in January 2007. Our goal was to thermally isolate the cesium cell from the environment, by suspending it on a thin sheet of thermally insulating material, such that less than 100 mW was required to heat the cell to 95°C.

In order to understand the role of the cell support structure and heater, we show a schematic diagram of a simplified magnetometer physics package in Figure 98. The photodiode measures the optical power that is transmitted from the VCSEL through the cesium cell. The VCSEL wavelength must be tuned to the cesium resonance frequency (by heating the laser) in order for the light to interact with the gaseous cesium atoms. Additionally, the cell must be heated to approximately 95°C in order to obtain a sufficient vapor density of cesium atoms for approximately half of the optical power to be absorbed in the cesium cell. As shown in Figure 98, the physics package must also contain RF coils that are driven at the Larmor frequency, typically between 70 and 350 kHz in the Earth's magnetic field. Lenses may be required to collimate the diverging VCSEL output beam and to focus the beam that is transmitted through the cesium cell onto the photodiode. Two other optical components that are required are a linear polarizer and a quarter wave plate (QWP) to create a circular polarization state within cell, which optically pumps the cesium atoms into a spin-polarized state.

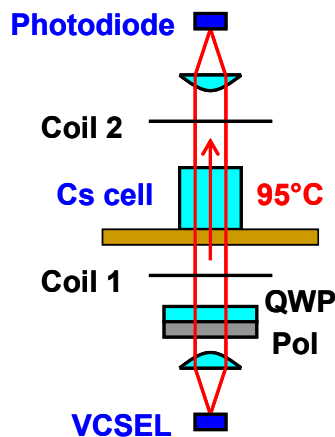


Figure 98. Simplified schematic diagram of a magnetometer physics package.

It was anticipated that heating the cesium cell to approximately 95°C would be the single biggest expense in our electrical power budget. Our goal was to thermally isolate the cell from the environment such that only 100 mW of electrical power heats the cell to 95°C. In order to meet this goal, we planned to support the cell on a thin sheet of thermally insulating material, such as polyimide or glass, as shown by the schematic drawing in Figure 99. The cesium cell was fabricated at NIST and had a cubic shape measuring approximately 2 mm on each side. The cesium cell sits at the center of the 8-mm square cell support sheet shown in Figure 99. The edges of the support sheet are supported by a rigid frame (printed circuit board), which is

assumed to be near ambient temperature (for example, 25°C in a room temperature environment). There are 3 main thermal loss paths from the cell to the environment: (1) conduction through the support and electrical conductors, (2) convection/conduction through the air surrounding the cell, and (3) radiation from the cell. In order to minimize the conduction through the support and electrical conductors, we want to minimize the cross section and maximize the length of each. The length of each conduction path is chosen to be 2mm, which is as long as can be reasonably fit inside a 10-mm cubic physics package. The thermal conductivity along each conduction path is $K = \sigma * H * W / L$, where σ is the material conductivity, H is the thickness, W is the width, and L is the length of the conduction path. Figure 100 shows thermal calculations for the Ti/Pt electrical traces drawn in Figure 99. Assuming 8 Ti/Pt electrical traces, each measuring 0.1-mm wide and 2-mm long, we calculate a 0.18 mW conductive heat loss through the electrical traces to maintain a 70K temperature differential from the cesium cell to the circuit board.

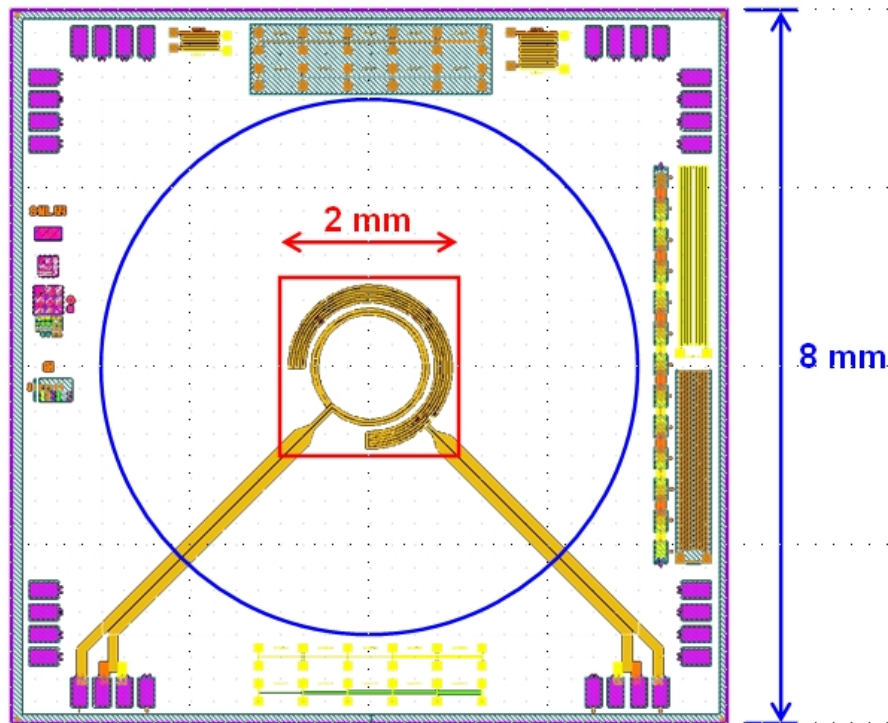


Figure 99. Top view of Mag1 heater mask layout. The heater chip size is 8-mm square. The heating element lies within the 2-mm square (colored red) where the cesium cell sits. The central part of the heater chip is suspended over a 6-mm air hole (shown in blue) that provides thermal isolation of the heated cesium cell.

Material	Conductivity W/(m*K)	Thickness (mm)	Width (mm)	Length (mm)	Number of Paths	Net cond (mW/K)	deltaT (K)	Power (mW)
Ti	17	0.00001	0.1	2	8	0.00007	70	0.005
Pt	69.1	0.00009	0.1	2	8	0.00249	70	0.174

Material	Conductivity W/(m*K)	Thickness (mm)	Radius1 (mm)	Radius2 (mm)	W/L $2\pi/\ln(r2/r1)$	Net cond (mW/K)	deltaT (K)	Power (mW)
Polyimide	0.12	0.025	1	3	5.719	0.01716	70	1.201
FR4	0.27	0.15	1	3	5.719	0.23163	70	16.214
Glass	1	0.15	1	3	5.719	0.85788	70	60.052

Figure 100. Thermal conductivities of various materials used in the cell support structure. The heater power required to maintain a temperature difference of 70K (cell at 95°C and ambient at 25°C) is shown in the right-most column for each material.

If the support sheet is left whole (without any cut-outs to remove thermally conducting material), then the thermal conductivity from an inner radius r_1 to an outer radius r_2 is $K = \sigma \cdot H \cdot (W/L)$, where $(W/L) = 2\pi / \ln(r_2/r_1)$. Assuming a 70K temperature difference between the cell and ambient, and a glass thermal conductivity of 1W/(m*K), we calculate a 60mW heat loss through the glass sheet, for the dimensions shown in Figure 99. Figure 100 shows the conductive heat loss calculations for various sheet materials (polyimide, FR4, and glass), assuming typical available thicknesses of each material.

Based on reported results of the DARPA chip-scale atomic clock project, radiation heat losses are expected to be approximately 4 mW, and convective heat losses are expected to be approximately 50 mW. Thus, the total heat loss is expected to be 114 mW, assuming the cell is supported on a 0.15-mm-thick glass support sheet without any cut-outs. Thinning the glass sheet from 0.15 to 0.05 mm would reduce the conductive loss from 60 to 20 mW, yielding a total heat loss of 74 mW, which is within our 100 mW budget. Using polymer support sheets, of either polyimide or FR4, would reduce conductive losses. However, the total heat loss is dominated by convective losses, which can only be eliminated by operating in a vacuum.

Task 4.2: Non-magnetic heater design

Completed in February 2007. In order to minimize magnetic fields created by the cell heater, the Ti/Pt heating traces (each 0.1µm thick and 20µm wide) were arranged in counter-conducting pairs, with one trace directly above the other, separated by an insulating layer (typically SiN) approximately 0.25µm thick. We wrote a C# computer program that applies the Biot-Savart law to determine the magnetic field that results from currents flowing through several metal traces.

We recall the Biot-Savart law

$$d\vec{B} = \frac{\mu_0}{4\pi} \frac{I d\vec{l} \times \hat{r}}{r^2},$$

which says that a current I flowing in a short wire segment of length $d\vec{l}$ produces a magnetic field contribution $d\vec{B}$ at distance r from the wire segment, where $\mu_0 / 4\pi = 1 \times 10^{-7} \text{ T}\cdot\text{m/A}$. The

direction of the magnetic field vector $d\vec{B}$ is determined by the cross product of the vector $d\vec{l}$ that points along the direction of current flow and the unit vector \hat{r} that points from the wire segment to the measurement location. The net magnetic field at any point (x,y,z) can be determined by summing the contributions from all current carrying wire segments.

Closely positioned pairs of traces, as shown in Figure 101, that conduct equal currents in opposite directions yield two magnetic field contributions that cancel each other (to first order) at large distances from the traces. To analyze the cancellation more exactly, we wrote a C# computer program that divides each metal trace into an integer number N (tsegs) of smaller trace segments, each of width dys, and sums the magnetic field contributions from all trace segments.

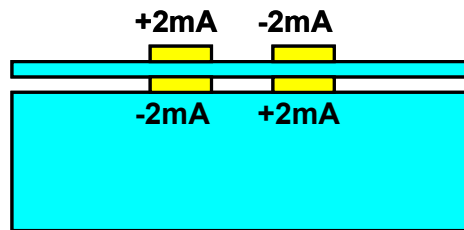


Figure 101. Pairs of traces, situated one above the other, that carry equal currents in opposite directions are used to cancel the magnetic field contributions at large distances from the traces.

For simplicity, we consider the geometry shown in Figure 102, where two traces run parallel to the x axis, and the current in each trace is either in the positive or negative x direction. These traces are each 20um wide and separated by 1um in the z direction (both their width and vertical separation are exaggerated in Figure 102 so the (red) traces can be seen). The graphical output of the C# code is shown in Figure 102. The false color indicates the magnetic field amplitude, where each color step represents a factor of 2 amplitude change (red represents the highest field amplitude = 19.899nT). The vector field directions are represented as black line segments on top of the false color display.

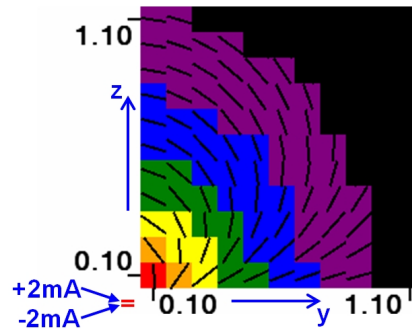


Figure 102. Cross-sectional drawing of two counter-conducting traces that run from $x_1=-1\text{mm}$ to $x_2=+1\text{mm}$. The magnetic field calculated in the plane $x=0$ is shown in false color (3dB change in magnitude per color step). The black line segments show the magnetic vector field directions

The numerical input data (text file) and output data (text file) are shown in Figure 103. Note that both traces are defined to be 20 μ m wide (10 segments each measuring 0.002mm wide), and that the upper trace is centered at (y,z)=(0,0). The lower trace is 1 μ m below the upper trace. For 2mA flowing in each heater trace, the magnetic field at (y,z)=(0.5mm,0.5mm), which is approximately the nearest point inside the cesium cell, is 0.769nT. For comparison, with just a single trace (no field cancellation), the magnetic field at the same position (y,z)=(0.5mm,0.5mm) is 461.9nT.

Input: 071220aa_mag_htr.txt

```
// 071220aa_mag_htr.txt
// test of MagTrace1 magnetic field calculation
// ver 1.0F 2-D measurement region, with field lines
// 2-trace config
// define measurement region (plane at x=xm)
```

xm	0	mm	
meas	y	z	comment
----	----	----	----
pt1	0.1	0.1	mm
pt2	1.1	1.1	mm
step	0.1	0.1	mm
scale	200	200	pixels/mm

```
// define current traces (field sources)
```

```
traces 2
```

trace	tcur	ys0	zs0	dys	tsegs	xs1	xs2
----	----	----	----	----	----	----	----
0	-2	0	-0.001	0.002	10	-1	1
1	2	0	0	0.002	10	-1	1

Output: 071220aa_mag_htr_out.txt

y mm	z mm	by nT	bz nT	bMag nT
0.5	0.5	-0.11	0.761	0.769

Figure 103. Portions of input and output data (text) files from MagTrace1 computer program.

Task 4.3: Fabrication of cell support structures

Go / no-go milestone completed in June 2007. We fabricated several versions of the cell heater and support platform, trying different substrate materials and mask layouts in order to minimize process difficulty and maximize yield. We passed the go / no-go milestone in June 2007 by demonstrating that we could heat 70K above ambient temperature using less than 100 mW of heater power.

The final mask version of the cell heater and support platform (mask set name Mag1) was shown previously in Figure 99. A cell heater fabricated on a 0.15-mm-thick pyrex glass substrate is shown in Figure 104(a). The heater consisted of two metal levels, each containing two loop traces, each trace measuring 20 μ m wide and separated by a 20 μ m gap. The measured heater resistance was 1.5 kOhm. The cell temperature sensor consisted of two metal levels, each containing six 270° arc traces, each trace measuring 14 μ m wide and separated by a 20 μ m gap.

The same Ti/Pt (10nm/90nm) metal deposition forms both the resistive heaters and RTD temperature sensors. As described above, two layers of near-identical metal trace patterns are employed such that equal and opposite currents flow in the top and bottom conductors, thereby canceling most of the generated magnetic fields at distances much larger than the separation of the two layers.

The cell is supported at the center of a 6-mm hole in the printed circuit board, on top of a 0.15-mm thick glass sheet that has patterned Ti/Pt heater and temperature sensor traces, arranged on two levels for magnetic field cancellation. A heater/support structure fabricated in April/May 2007 is shown in Figure 104 (a), where the inner 1.2-mm diameter “ring” is the heater element and the longer-path outer “ring” is the temperature sensor. Figure 104 (b) shows the measured temperature sensor resistance versus the temperature of the sensor. Although pure Pt is expected to yield a resistance increase with temperature of +0.39%/°C, the Ti/Pt traces that we employed exhibit a resistance increase with temperature of +0.25%/°C.

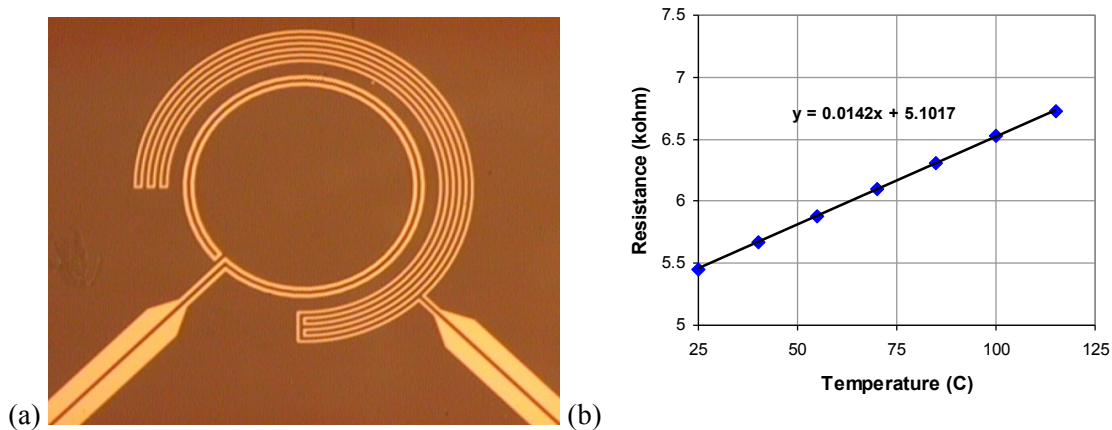


Figure 104. (a) Microfabricated Pt heater (inner 1.2-mm ring) and temperature sensor (outer ring). (b) Measured Pt sensor resistance versus temperature.

We measured the temperature versus heater drive power by mounting the heater/support glass over 6-mm air hole, as shown in Figure 105(b). Figure 105(a) shows the measured sensor temperature versus heater drive power. Driving the heater with 100 mW of input power yields a sensor temperature of 100°C (or 75K above ambient temperature), which is roughly consistent with our numerical calculations (described in a previous section). The demonstration of 70K temperature differential using less than 100 mW of heater power was sufficient to pass our go / no-go milestone.

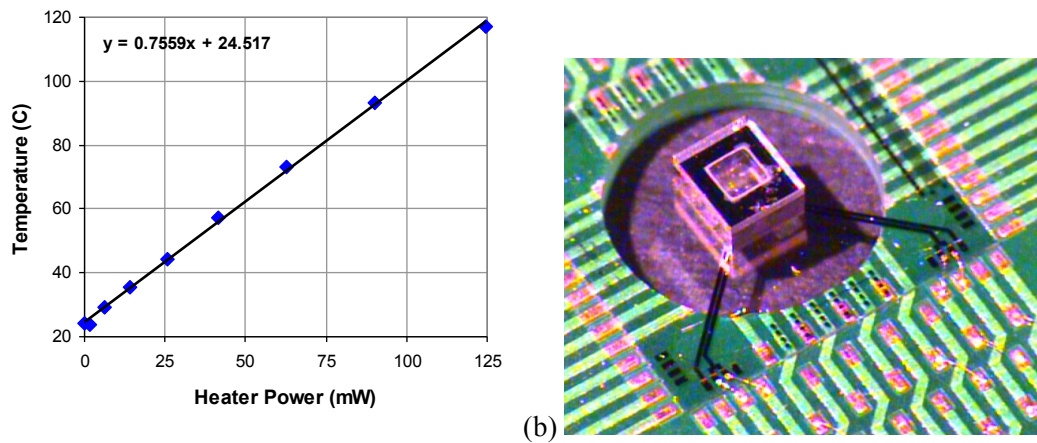


Figure 105. (a) Temperature versus heater power for a single heater/support platform suspended over a 6-mm air hole. (b) Picture of cesium cell sitting on the heater/support structure.

We also attempted fabrication of cell heater and support structures using polyimide and FR4 substrates. Unfortunately, the Ti/Pt metal did not adhere well enough to these polymer substrates to achieve high yield. Moreover, the FR4 substrate seemed to experience undesired dimensional changes at process temperatures above approximately 120°C. We believe that the polyimide fabrication process would work adequately if the thin (25um thick) polyimide sheet was permanently attached to a rigid frame throughout the fabrication process, rather than being free to curl due to mismatches in thermal expansion of various materials deposited on top of the polyimide sheet.

We mention that even with the glass substrates, our initial yield was poor (approximately 50%). The most prevalent problem was electrical short circuiting between the top and bottom metal levels needed to cancel magnetic fields. After much effort, we determined that the most important factor to achieve high yield is to ensure that the substrate is perfectly clean before the electrically insulating SiN layer is deposited over the bottom metal. Our hypothesis is that any particle on the substrate can obstruct the SiN from fully covering the bottom metal. If the particle detaches, it leaves an exposed hole in the insulating SiN layer. Then when the top metal is deposited, it pokes through the hole in the SiN layer and contacts the lower metal, creating an electrical short circuit.

We have developed a process to thin and re-polish the glass substrates after heater fabrication, reducing the thickness from 0.15 to 0.05 um, which achieves a 3-fold reduction in thermal conduction losses. However, in order to minimize risk, our first prototype physics package did not employ the thinned glass substrates.

Task 4.4: Fabrication of prototype physics package

Sandia finished assembling the first prototype physics package in November 2007 and delivered it to Geometrics for testing. A cross-sectional schematic view of the physics package is shown in Figure 106(a). The physics package contains the following components: cell heater/support structure, VCSEL heater/support structure, optics, magnetic coils, and the photodiode (listed from most to least challenging). We have fabricated and/or purchased all of these components and used them to assemble the first prototype physics package. A common 25-mm-square circuit board, shown in Figure 107(b) was designed to support all of the components that require electrical connections: VCSEL, cell heaters, photodiode. A single-loop magnetic coil of diameter 10 mm was patterned on the back side of each circuit board.

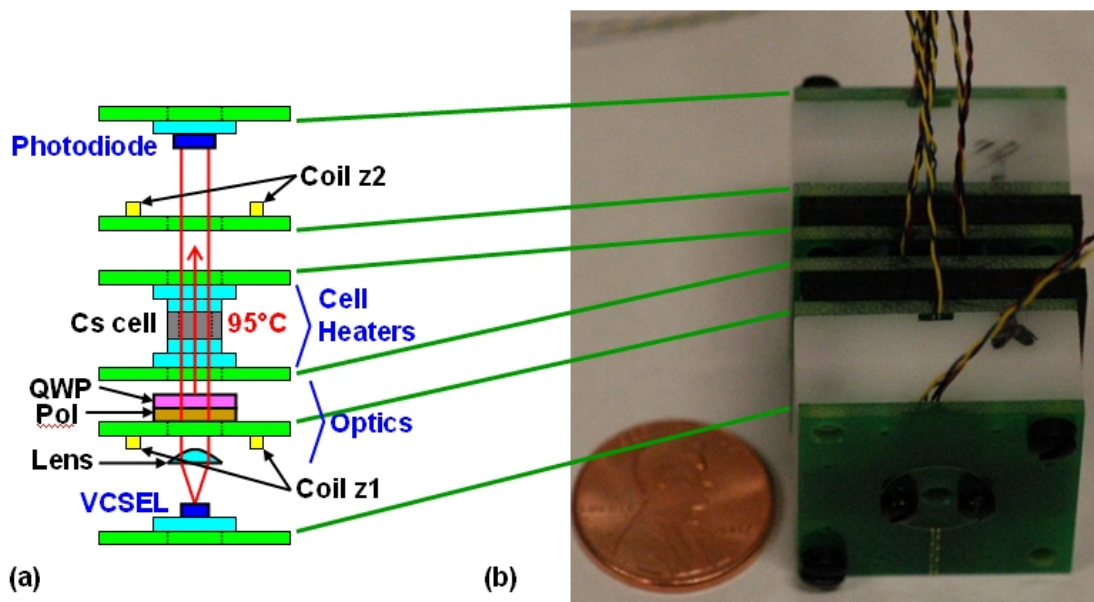


Figure 106. (a) Schematic diagram showing major components of the magnetometer physics package. (b) Photograph of the first delivered magnetometer physics package.

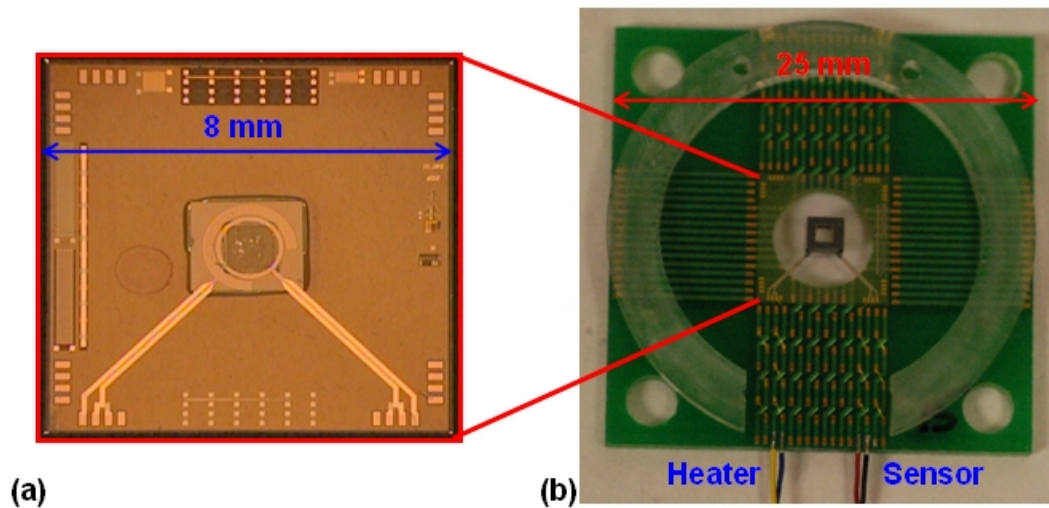


Figure 107. (a) Picture of a cesium cell sitting on a microfabricated 8-mm-square glass heater/support structure, which is bonded to a 25-mm-square carrier circuit board (b).

Figure 108(a) shows a cross-sectional view of the 3-D CAD model of the physics package. Figure 108 (b) shows an exploded view of the 3-D CAD model of the physics package. The vertical distance is dominated by optics. First, the VCSEL beam must propagate 3.3mm in order to diverge to the point of filling the 1-mm inner diameter of the cesium cell. Then the VCSEL must propagate through a polarizer and quarter wave plate. As shown in Figure 108(a), these optics are some of the largest components in the physics package.

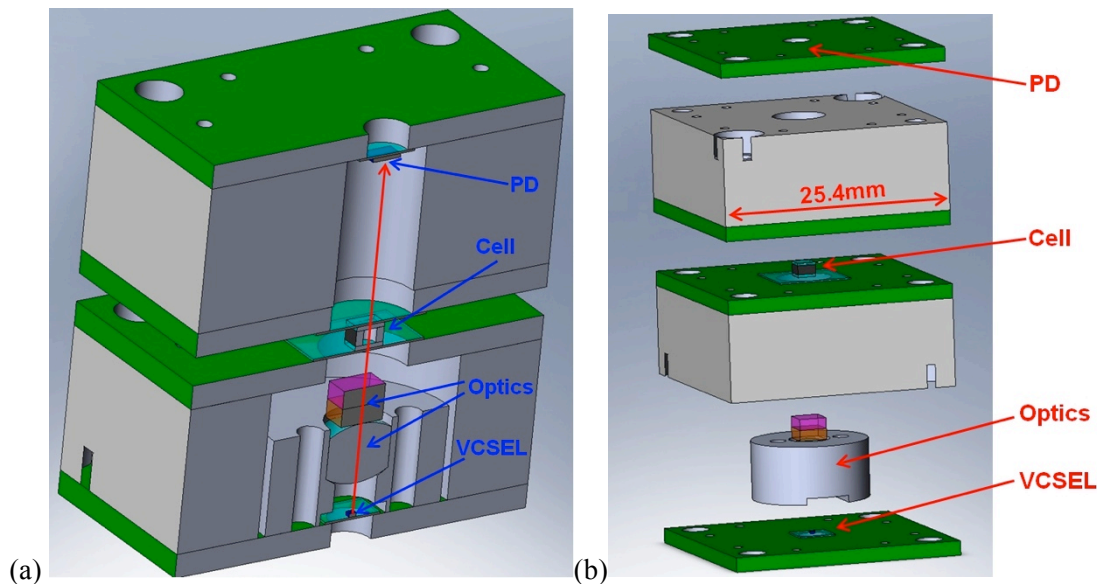


Figure 108. (a) Cross sectional view of the physics package 3-D CAD model. (b) Exploded view of the physics package 3-D CAD model.

Figure 109 shows a photograph of the first prototype magnetometer physics package that was delivered to Geometrics in November 2007. One of the goals of the first physics package was to determine the value of the collimating lens, by measuring the performance of a magnetometer with and without the lens. To this end, we have designed the lens to be removable. After the physics package has been tested and we experimentally determine which optical configuration works best, we will re-design the physics package to achieve a 2-fold reduction in linear dimension, and thus an 8-fold reduction in volume.

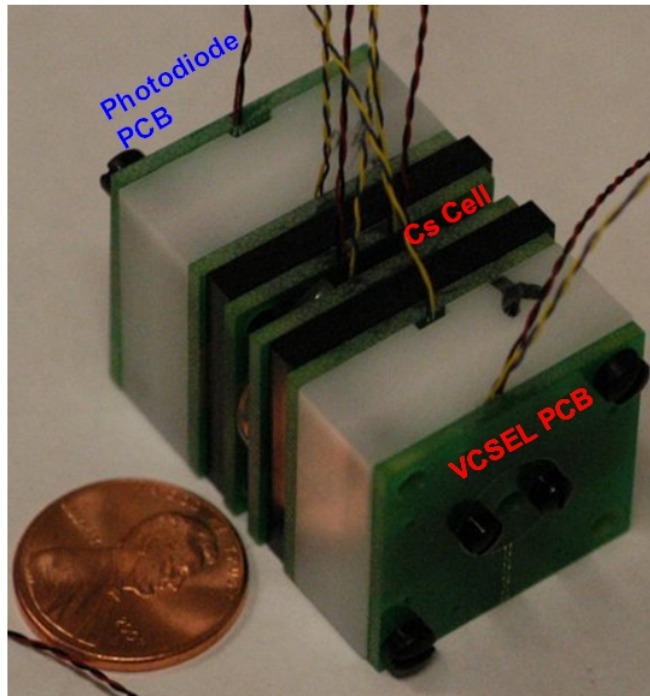


Figure 109. Photograph of the first delivered physics package prototype.

Figure 110 shows photographs of the illuminated VCSEL without (a) and with (b) the collimating lens installed. The lens (Thorlabs model A414-B) has a focal length of 3.3mm and a diameter of 4.5mm. This lens is placed one focal length away from the VCSEL in order to collimate the beam. The collimated beam diameter (at $1/e^2$ intensity points) is calculated to be 1.3mm, assuming a VCSEL beam divergence (half angle at $1/e^2$ intensity radius) of 0.2 radians (11.5 degrees). For a reference dimensional scale, we note that the white index card shown in Figure 110 has lines at 0.25" (6.35mm) intervals.

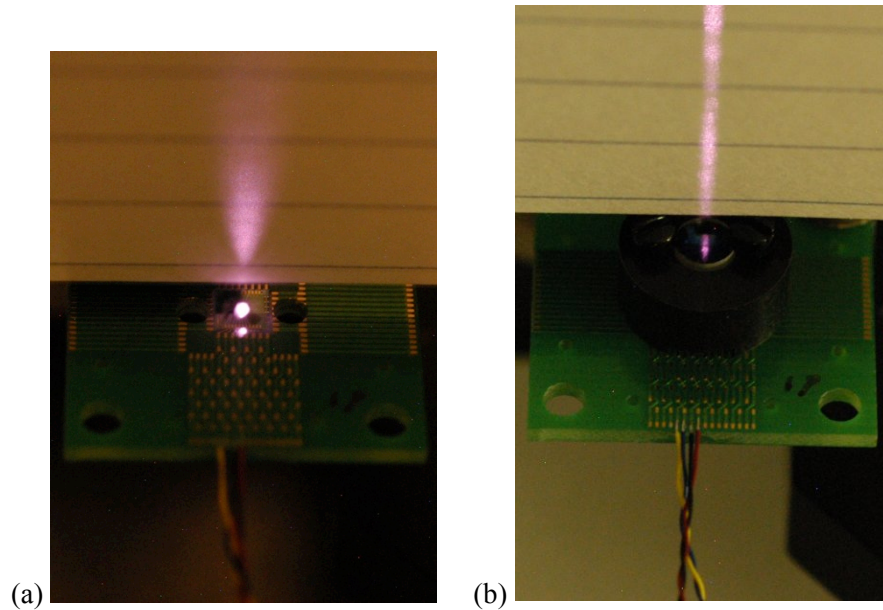


Figure 110. Photographs of the illuminated VCSEL without (a) and with (b) a collimating lens. The electrical connections to the physics package were made with 34-AWG twisted pair wires. The wires were soldered to the edge of each circuit board as shown in Figure 111(a). The circuit board solder pads were positioned on a 0.5-mm pitch, which required a special V-groove clamping fixture to hold the wires on a precise 0.5-mm pitch for soldering to the circuit board, as shown in Figure 111(b).

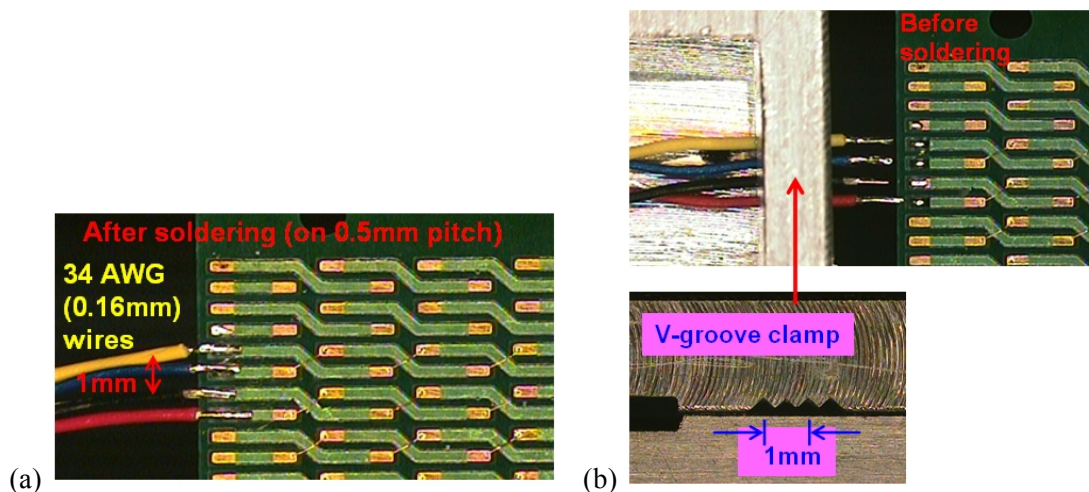


Figure 111. Photographs of twisted pair 34-AWG wires after (a) and before (b) soldering to the VCSEL circuit board. A special V-groove clamp was used to hold the wires on a precise 0.5-mm pitch for soldering

Figure 112 shows a list of the electrical connections that were made to the physics package with twisted pair wires. As of December 2007, this first physics package is undergoing testing at Geometrics. In January 2008, we hope to decide on modifications to incorporate into the design of the second physics package. In 2008, we plan to build at least two more physics packages, and possibly as many as four more physics packages, depending on available resources.

Pair	Label	Color	Connection	Load	Comment
1	V	Red/Black	VCSEL (red=anode)	1.5mA	1.7V, no ESD protection
2	Hv	Yellow/Blue	VCSEL heater	566ohms	approx 3mW input
3	C1	Yellow/Blue	Bottom coil Z1	1 loop	10mm diam, z=-7mm
4	H1	Yellow/Blue	Bottom cell heater	1.5kohm	approx 50mW input
5	S1	Red/Black	Bottom temp sensor	5.4kohm	dR/R=+0.25%/degreeC
6	S2	Red/Black	Top temp sensor	5.4kohm	dR/R=+0.25%/degreeC
7	H2	Yellow/Blue	Top cell heater	1.5kohm	approx 50mW input
8	C2	Yellow/Blue	Top coil Z2	1 loop	10mm diam, z=+7mm
9	D	Red/Black	Photodiode (red=anode)	20uA	21pF cap

Figure 112. Summary of electrical connections to the first prototype physics package.

Electronics Design

Summary

Excellent progress has been made in designing the electronics to drive the sensor. Figure 113 below shows a block diagram. A complete set of electronics has been designed and built. This design has been built in brassboard form, with adjustability for a greater range of operating conditions than will be necessary in the final design. However, this version of the circuitry will allow for us to make detailed measurements on the performance capabilities and requirements for the final system.

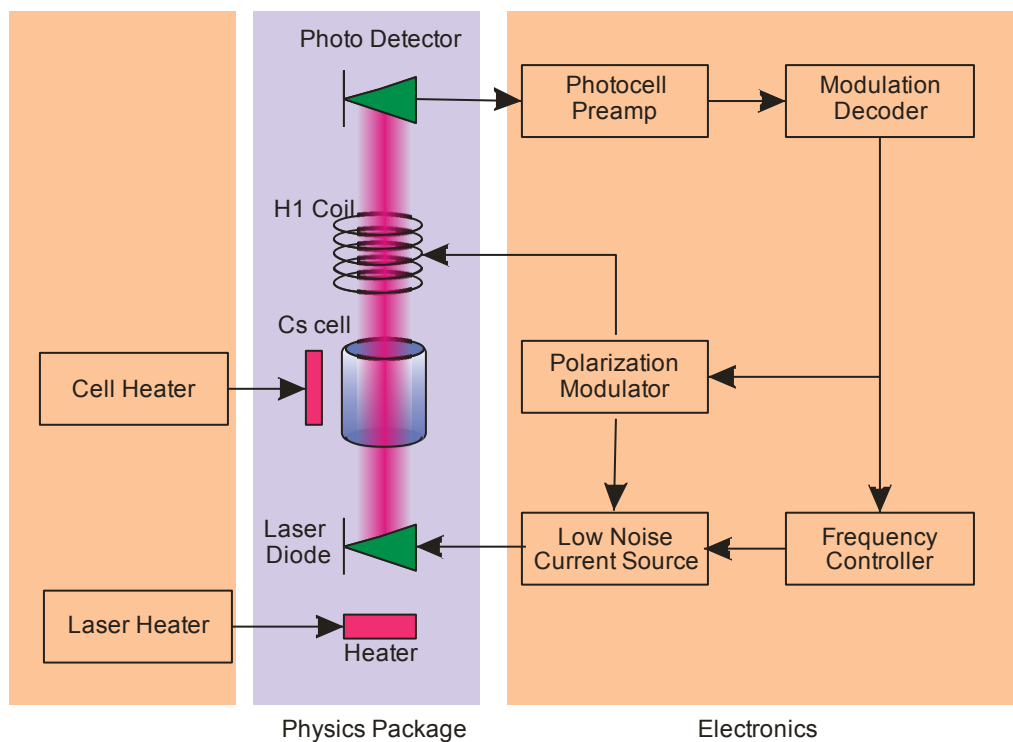


Figure 113. General electronics block diagram

Block diagram:

Figure 113 shows the required components of the entire electronic system. Individual components will be discussed below.

Task 5.1 Breadboard demonstration of VCSEL wavelength control

A very low noise current source is required to drive the VCSEL, without limiting the performance of the system by adding its own noise. The VCSEL temperature controls the operating wavelength. For a device this small, one major component of the temperature of the junction is the heat caused by the current flow through the device. Thus, a changing amplitude current drive results in a frequency variation of the output light. The current source is driven by a signal with the following components:

A DC component which is the average current necessary to operate at the correct wavelength. For best stability of the VCSEL itself, this current should be about 1 mA. Thus, the coarse VCSEL heater is adjusted so the a 1 mA current produces the correct wavelength.

A modulation component necessary to servo the wavelength to the correct value

A modulation component necessary for the signal interrogation method. For Bell-Bloom, the modulation is applied to the laser. For other modes of operation, the modulation may be applied to an H1 coil.

When the light from the laser is at exactly the correct wavelength, the cell will absorb approximately 50% of the light. If it is slightly mistuned, the cell will absorb less of the light. This fact is used in both types of magnetometers to keep the laser locked onto the line.

Laser Frequency Control Operation

To explain the operation, assume we are nearly but not perfectly on the line. Taking wavelength as volts, we modulate the laser as shown in Figure 114 :

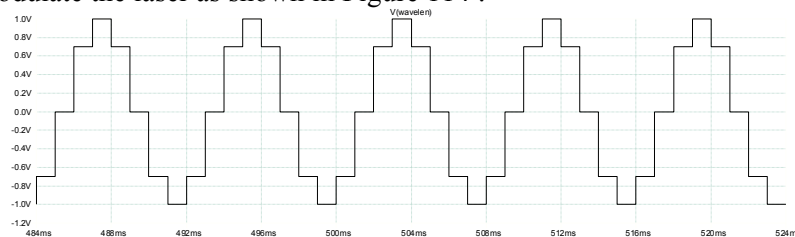


Figure 114 Modulation of the laser frequency

If we look on the “Brightness voltage” output from the sensor driver, we will see an AC waveform like this:

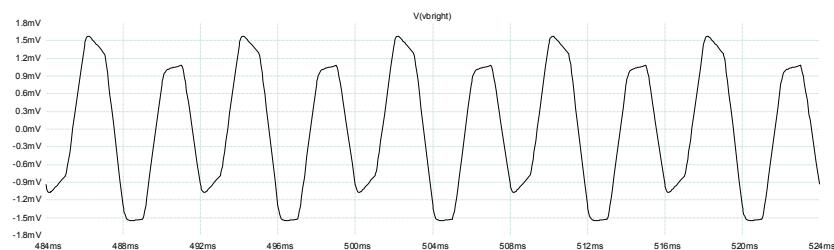


Figure 115 Photodiode output

This is centered around some DC level. Notice how there is more second harmonic than fundamental in this waveform. The fundamental is only about 0.5mV but the 2nd harmonic is about 2mV. If we were exactly on the line, there would be no fundamental at all. Figure 116 shows the signal in the frequency domain.

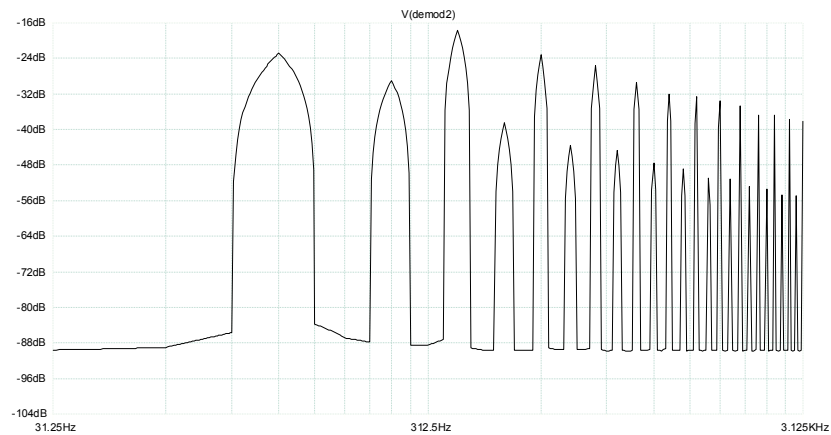


Figure 116 FFT of photodiode output

After we amplify and go through the first demodulator, the waveform will look like as shown in Figure 117:

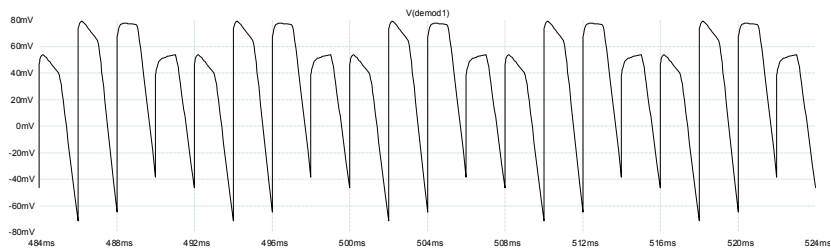


Figure 117 Waveform after first demodulator

Our “Phase” control isn't set perfectly here but it is close. Notice how the negative excursions of the 2nd harmonic have been folded up to be positive. This can be seen near 488mS on the graph.

Figure 118 shows this signal in the frequency domain.

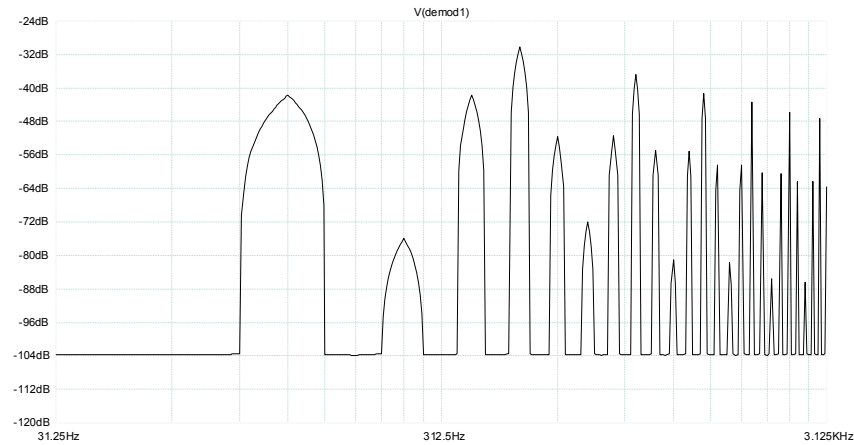


Figure 118 FFT of demodulator output

Notice that the 2nd harmonic is now 40dB below the fundamental. We have added a bunch of higher frequency components, but these are far from the signal frequency and are thus easy to filter out. Now we must remove the DC component, amplify by about 20dB and then go into the second demodulator and get the waveform shown in Figure 119, which is shown in the frequency domain in Figure 120.

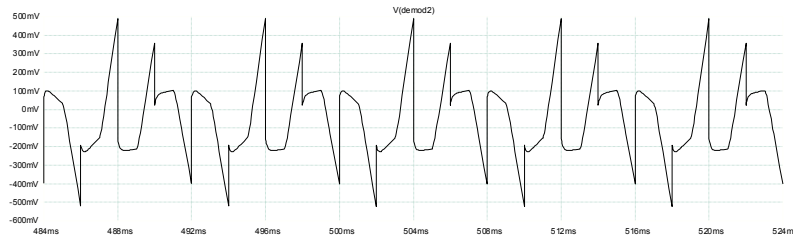


Figure 119 Signal after second demodulator

Notice that the average of this is just about -100mV. This means that the fundamental in the original signal has been made into a DC that is 20dB down. We started out with a harmonic that was bigger than the fundamental and ended up with a DC that was bigger than what is left of the 2nd harmonic. This means we have settled the control loop at the desired wavelength.

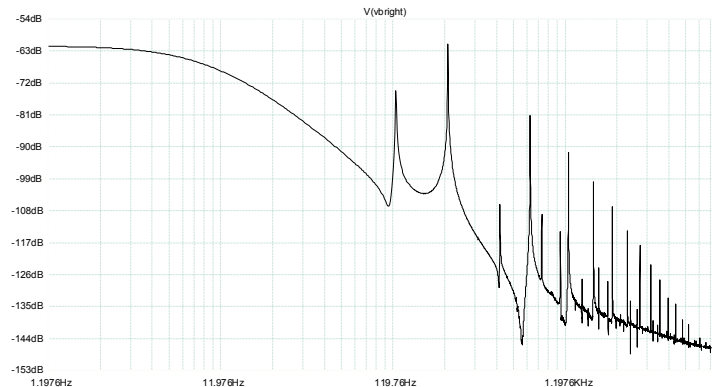


Figure 120 FFT of signal after second demodulator

Task 5.2 Breadboard demonstration of cell temperature control

A simple feedback loop is all that is necessary to control the cell temperature. A few considerations must be taken into account:

- 1) For low power operation, a low voltage, high current implementation is most efficient. However, this conflicts with the requirement of minimizing the magnetic fields. Hence, we operate at a higher voltage with less current, and must design an efficient power source for this circuit.
- 2) The temperature measuring components must be non-magnetic. We have used simple traces of metallization on glass plates as a thermal sensor. In addition, the optical absorption of the cell changes with temperature, and we can fine tune the temperature by measuring the absorption.
- 3) When the cell is at the right temperature it will absorb the right amount of light and the line width will be the right width. These two facts can be used to determine the exact cell temperature. We need to be within several degrees of the exact value to prevent a drift in the reading.
- 4) We still need some ability to detect the cell temperature because we need to get the cell above about 25C and below about 150C before we can lock the laser to be able to measure the cell temperature by absorption. We need to look at a way to solve this without significantly adding parts. One solution would be to make the heater out of something with a large temperature coefficient.
- 5) Once the system is up and running, the cell temperature servo can be engaged and the cell brought to the exact temperature.
- 6) The coolest part of the cell must not be the faces through which the light passes. Cs will condense on the coolest portions of the cell walls, and it is undesirable for droplets of Cs to occlude the light path.

Task 5.3 Breadboard demonstration of signal extraction circuit

The signal extraction circuitry is by far the most complex portion of the sensor design. In addition, there are still several possible options we are exploring. We have designed general circuitry allowing us to quantify the performance of each method. We are doing this because each approach has merits, and we may implement more than one method in various products to achieve different performance levels for different applications.

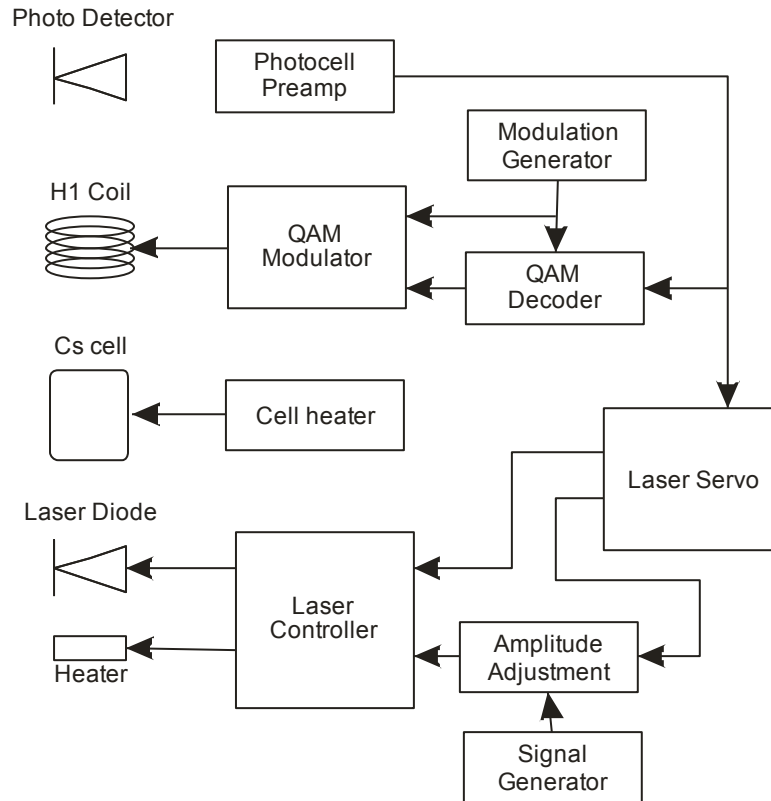


Figure 121. Mz magnetometer electronics block diagram

Circuit Operation

Figure 121 shows a Mz magnetometer using the new technology. Two main tasks must be done in this system. The laser must be tuned onto the correct line and the H1 coil must be driven. The description below explains in more detail.

If an AC magnetic field is applied to the sensor such that it has a component at right angles to the earth's field and has a frequency matching the Larmor frequency, the amount of light absorbed by the cell will increase. This AC field is called the **H1**.

A magnetometer can be made by modulating the **H1** drive frequency and observing the decrease in absorption at each extreme of the modulation cycle. The center frequency can then be adjusted until the decreases on either side become equal. This ensures that the center frequency of the modulated H1 drive is exactly at the Larmor frequency.

If the field changes, the correct "Larmor" frequency for the center of the sweep changes. A servo can act to constantly track the changes in the absorption and thus cause the magnetometer to track the changing magnetic field.

Although this would make a magnetometer that worked, it is not a very good design. Creating the frequency modulated H1 drive while also making a Larmor signal that has no modulation is far from easy. Limiting the field measurement to always enclose an integer number of cycles of the modulation removes the need for a modulation free Larmor but limits the options on modulation and measurement frequencies. Also merely making an FM modulated signal is not as easy as it sounds. Any asymmetry in the modulation will make an offset in the measured field value.

Quadrature Amplitude Modulation (QAM) allows the same error signal to be developed as one gets from the FM modulation without requiring the actual FM modulation. There are significant phase shifts from the modulation of the H1 drive to the demodulator's signal input. The demodulator must correct for these. This is done by delaying the demodulator's timing with respect to the modulation of the H1.

The simplest demodulator would simply apply a gain of +1 for half of a cycle and then -1 for the other half. This would work fairly well but it risks being very sensitive to noise or signals near odd harmonics of the modulation frequency. An analog filter can be used to provide a narrow band signal to the demodulator. In production this may be a good idea but during development this would require constant retuning as we experiment with different modulation frequencies.

The path we took was to sample the signal very rapidly and then to do all of the filtering in the digital domain. The filtering is done in two steps.

The signal is a repeating waveform. We break this waveform into 16 sections and generate an average value of the signal within that section. This is very like an analog commutating filter. A very simplified version of the code would look like this:

```
REPEAT FOREVER
  for I = 1 to 16
    DELAY CycleTime ./ 16
    NewValue = ReadADC
    Y(I) = Y(I) + (NewValue - Y(I)) * 0.1
  NEXT I
```


The actual code is far more complex than this because many conversions of the ADC are done before we advance to the next 16th of the cycle and the ratio of the two frequencies is not an integer. The 16 average voltage bins are weighted by $\sin(\omega t)$ and average into the second filter stage. This becomes the error signal output that goes to the VCO circuit ("Larmor Servo", in the block diagram).

Implementation

We must provide the laser with a very low noise current. Our design for the laser current controller is intended to allow Mx, Mz or Bell-Bloom modes of operation. Since VCSEL devices are extremely sensitive to static discharge and high voltages, it also provides high levels of protection to the laser diode. The safety circuit contains comparators that compare every voltage against its expected range. Any voltage being out of range trips the circuit and causes the connections to the laser to be shorted, protecting that device.

As a result of both the protection and generalization it is far more complex than we expect to use in production. We have implemented the operation circuitry in 4 shoebox-size electronics components. These will be used to characterize the performance of the physics package in terms of sensitivity and heading error, for a variety of signal interrogation methods. With this, we will determine the requirements for the final electronics design.

Task 5.4 Go / no-go determine if electronics will meet size and power requirements

During this project, we designed electronics circuitry consisting of three small circuit boards, totaling approximately 15 square inches and consuming about 2 watts. This is a significant improvement over the existing commercial sensors 20-watt power consumption and much larger size. This has met the goals set out for this project. Further improvements may later be made by using integrated circuit techniques to further reduce the size and power consumption of the circuitry.

Task 5.5 Complete fabrication of electronics subsystem

We have now built a complete electronics system, shown on a cart for field testing in Figure 122.

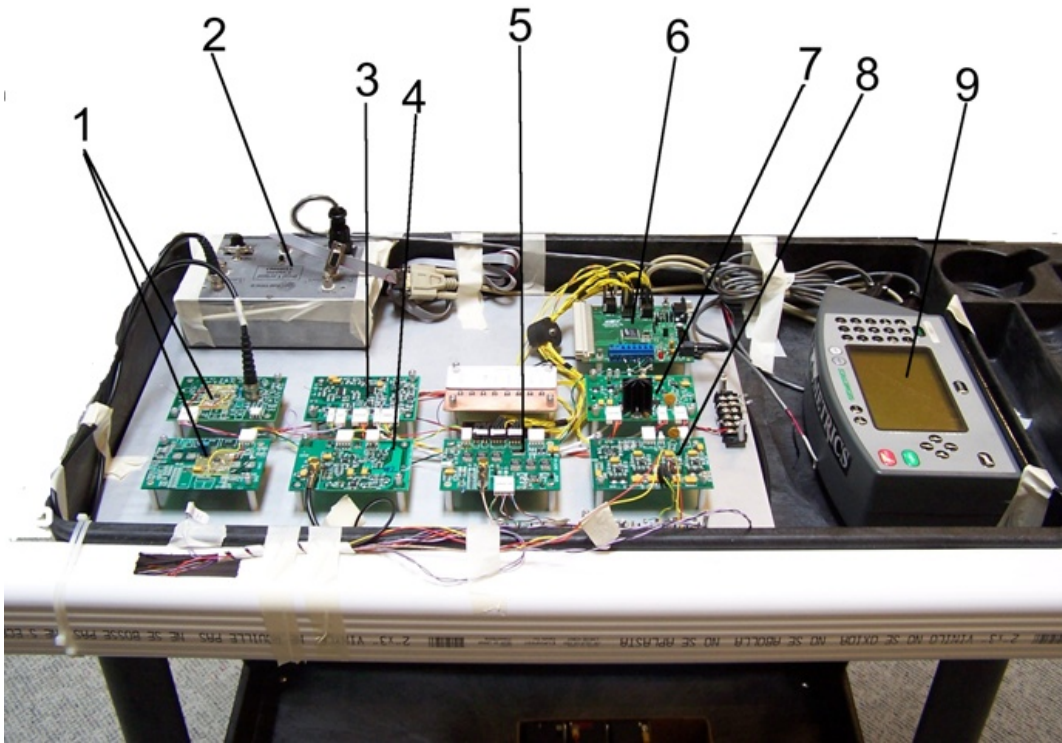


Figure 122. Complete electronics system mounted on a cart for testing. Components are as follows:
1) Signal buffers, 2) External counter assembly, 3) H1 synthesizer, 4) photo preamplifier, 5) DAC board, 6) Processor board, 7) regulators and protection circuits, 8) heater power amplifiers, 9) logging system. Only items 3-8 are needed in the final system. Items 1,2 and 9 are for testing.

Task 5.6 Methodology for Circuit Size Reduction

After the first pass design, we turned our attentions to improving the design in several ways. As shown in Figure 123, the electronics system consists of three elements:

1. The sensor electronics controls the operation of the physics package (the laser diode, Cs cell, heaters, modulation coils, and photodiode). This consists of the following elements:
 - a. VCSEL wavelength control
 - b. Cell heating control
 - c. Modulation and signal extraction

This block operates in a feedback loop with the physics package, as shown in the diagram. The output of this block is a signal whose frequency (the Larmor frequency) is proportional to the magnetic field strength.

2. The frequency measuring system measures the Larmor frequency, converting it to a usable digital output. This must be done to tremendous dynamic range. Even though we

often refer to this block as a “counter”, simply counting Larmor cycles for a given length of time does not provide nearly enough resolution. Techniques used to obtain the desired resolution and performance are 1) a high speed period measurement, 2) analog interpolation of that measurement, 3) oversampling, and 4) decimation, including sophisticated anti-alias filtering.

3. The data storage and user interface system presents the data to the user for analysis. This portion of the system is being developed with internal funding by Geometrics.

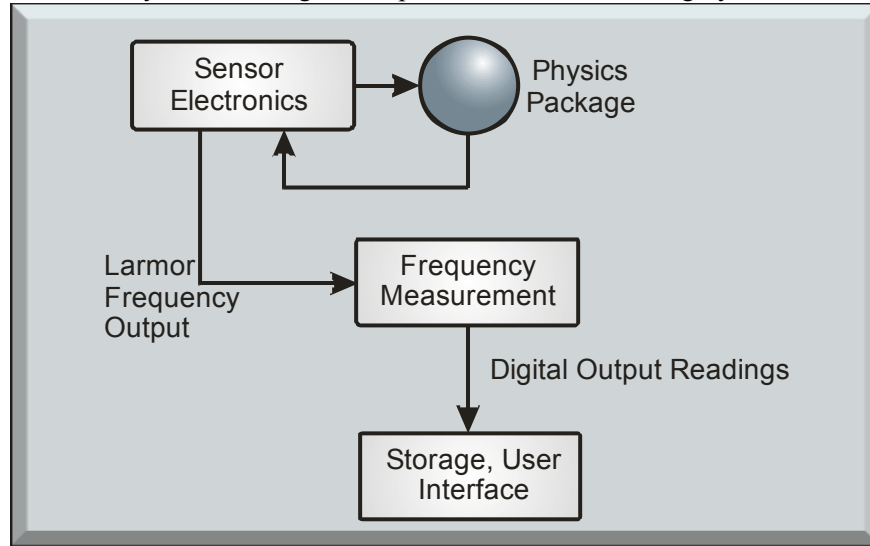


Figure 123. Block diagram of the electronics of a magnetometer

In prototype form, the sensor electronics and frequency measuring electronics utilize 4 separate shoe-box size components. In previous tasks, this was reduced to four 2x3 inch PC boards, with a power consumption of 5 watts. We later designed new circuitry for lower power consumption, and to allow for operation in arrays.

There are several approaches to extracting the Larmor signal and producing a digital readout. Basically, they span a continuum from all analog to mostly digital techniques. In addition, there are a variety of approaches to implementing the digital portion, from using several small microprocessors, to using a single large processor, or using a field programmable gate array (FPGA). We have analyzed the performance of each method, along with the design complexity.

We finally have used both digital and analog approaches in order to achieve the desired performance. An overall digital control of the system is essential, as there are many stages in the operation of this system, and the complexity and variety of the different modes of operation requires control by a microprocessor.

The required circuitry consists mainly of several feedback loops to control the operation of the sensor. This is shown in Figure 124. This section outlines some of the methods used to optimize the circuit design.

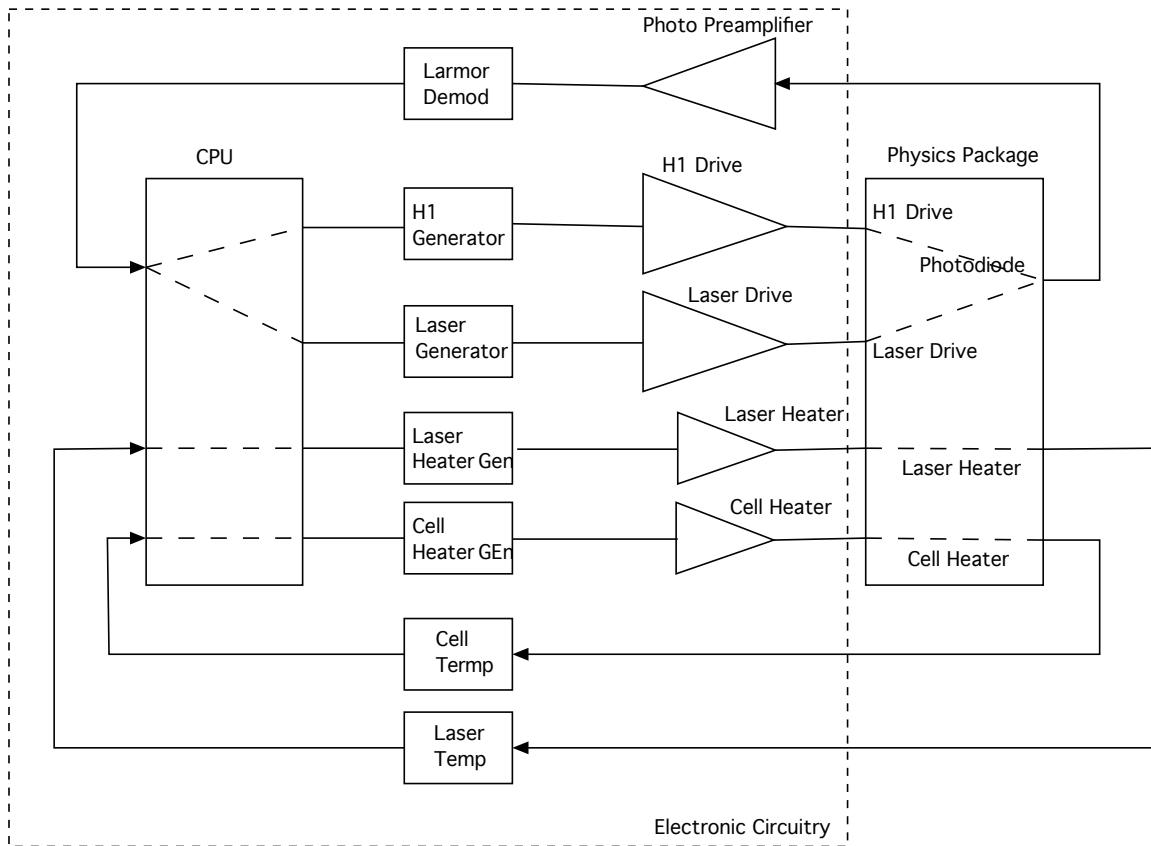


Figure 124. The operation of the magnetometer consists of many independent feedback loops. Each must be analyzed for its particular requirements.

Combined Digital / Analog methods

In this task, we carefully analyzed how to implement the many feedback loops that are required. Digital circuitry is advantageous in that it allows for a wide variety of control systems to be implemented, and allows for the system to run under different conditions. However, at the very fine level of control, both in terms of timing and in terms of accurate signal levels, digital electronics becomes too complex, too large, or consumes too much power. On the other hand, slow, coarse ADCs and DACs are inexpensive, are widely available as part of microcontrollers, and consume little power. Analog circuitry may be used in small blocks to obtain finer voltage resolution, and to allow for rapid feedback. Thus we have used a combination of digital and analog techniques to achieve our desired goals.

This effort is depicted in the block diagram shown in Figure 125. The elements of the feedback are as follows:

Modulation System. This system injects a modulation of some sort onto the signal passing through the cell. When de-modulated, this produces the error signal that indicates how the base frequency must be adjusted to track the Larmor resonance.

Digital Feedback System. This system is used to find the resonance, and allow the basic operation of the system to be programmed in software. This portion of the circuit also allows the CPU to be able to control the overall operation and track the stability of the system

Analog feedback system. This is used to track the resonance frequency at the finest resolution, beyond which the coarser digital system is able to operate. Once the system is near lock, this portion of the circuitry takes control, and fine tunes the operation of the circuit at a level the coarse nature of the digital circuitry would not allow.

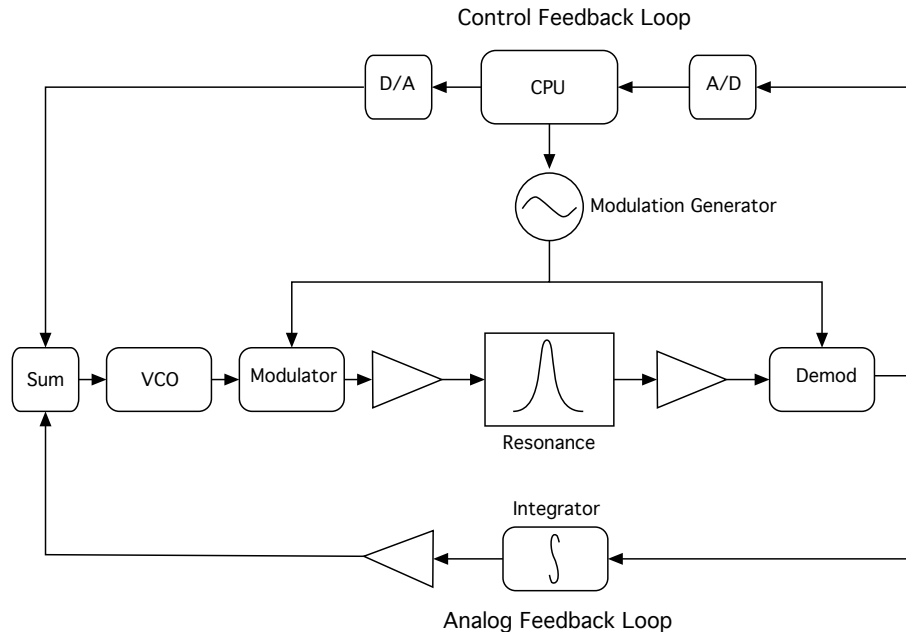


Figure 125. General block diagram for the Larmor feedback loop

Finite impulse response (FIR) filters

All filters are sensitive to information from the past. In the construction of digital filters, the designer has the option of making the filter's current output depend only on data from a finite period of time. This means that the system settles to a fixed operating point in a finite period of time. When low frequencies are important (such as when drift matters), we need the circuitry to have this property. An example of low pass filters is shown in Figure 126. The FIR filter settles to the steady state value after the impulse and after the step in a finite number of samples. The IIR only approaches the steady state exponentially. Analog filters are always of the IIR type.

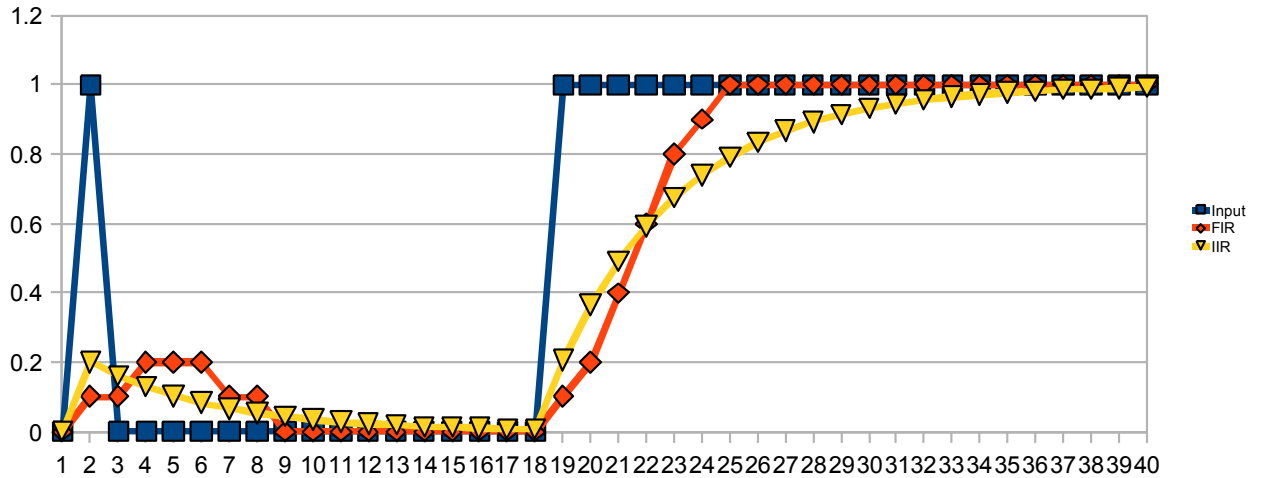


Figure 126. Comparison of FIR and IIR filters..

DAC update timing:

All of the DACs have their values determined by firmware, but their update timing is determined by hardware. The DAC update timing jitter must be held to a value small enough that the noise on the modulations of the H1 drive is less than 1pT per sqrt(Hz).

The fastest modulation we intend to use is on the order of 500Hz and the amplitude is on the order of 300nT. We can use this to set a limit on the jitter of the update rate.

$$500\text{Hz} * 2 * \pi * 300,000\text{pT} = 0.942 \times 10^9$$

Because the noise will be distributed over a 22kHz band, we can allow up to

$$\sqrt{22\text{kHz}} / 0.942\text{E}9 = 157 \text{ nanoseconds of jitter.}$$

Our jitter number is far less than this so the hardware timing is enough to ensure that the timing jitter will not become the determining factor in the noise performance of the system.

Noise shaping:

This concept is used many times throughout the design. When a continuous function is approximated by discrete steps some error is introduced. This is often referred to as “quantization

noise”. In the most direct approach, each point on the curve is rounded to the nearest step in the output voltage and this is the voltage that will be produced. This tends to lead to an evenly distributed noise that has an RMS amplitude of $1/\sqrt{12}$ th of the step size.

In the simple case, this noise is evenly distributed. This is undesirable for the magnetometer. It would be better if this noise was unevenly distributed such that most of it appeared at frequencies which do not impact the noise performance of the magnetometer. For this purpose we employ a method called “noise shaping”.

In the simplest form of noise shaping, the portion of the number that could not be represented on the output at one instant is remembered. This value is then added to the value to be represented at the next instant

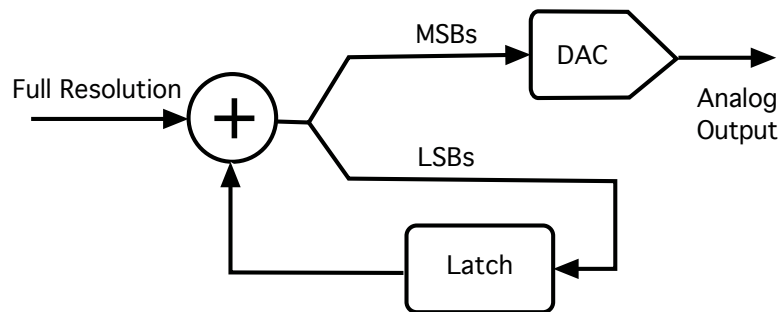


Figure 127. Noise shaping block diagram.

This local feedback process causes the noise spectrum to be shifted so that the bulk of the noise appears near Nyquist. With a perfect DAC, this would reduce the quantization noise in the frequencies that matter to be far lower than is required to obtain the desired performance.

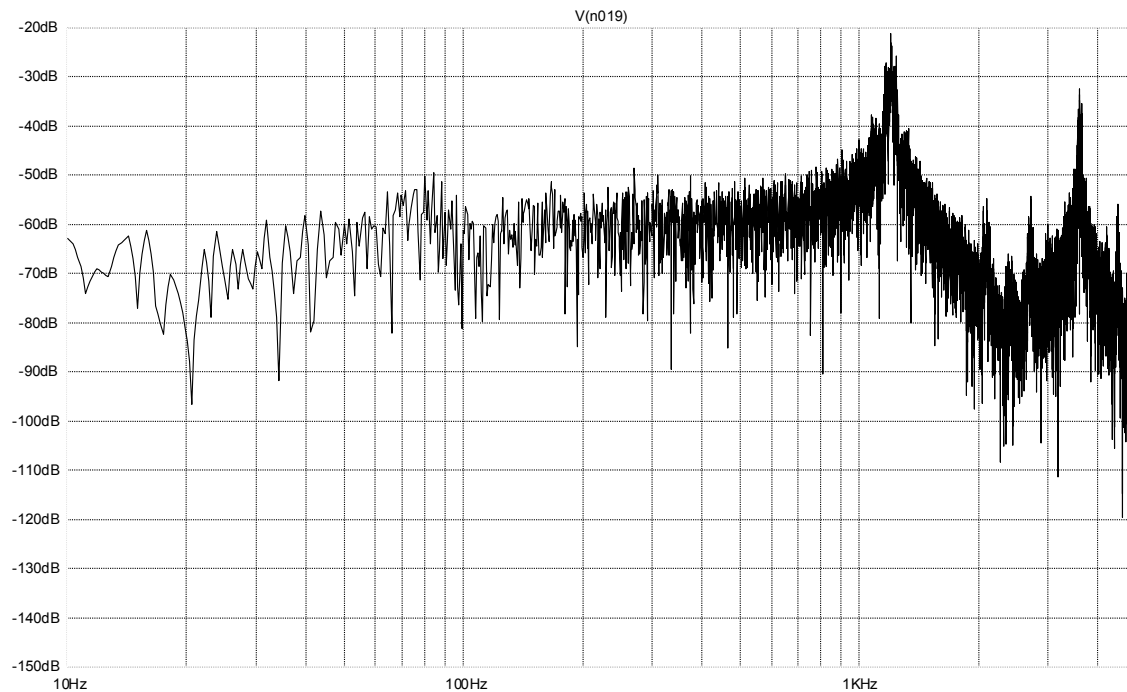


Figure 128. Shaped noise spectrum.

The real DACs, however are slightly imperfect. The steps are not of exactly equal amplitude. This would still introduced significant noise into the system if some method were not used to remove it. In the audio industry, a common method of suppressing such artifacts is a process known as dithering. A small high frequency signal is intentionally added to the signal to be represented so that the DAC always moves over a small group of output values near the desired output value. Typically, this would be a high frequency noise-like signal so that it doesn't itself create any strong artifacts. In the audio industry, the broad band of human hearing must be free of artifacts. In our case, a narrower band must be free from artifacts, allowing us to use a function that suppresses the artifacts in that band at the cost increasing them in a band that does not effect the performance of the system.

DAC Resolution

DAC resolution is obviously very important. In order to keep the system small and low power, we need to be creative in how we design our DACs. Three methods of obtaining a high resolution signal using simple DACs are shown here. In Figure 129, we show a method of sending a DAC signal into a couple of integrators to increase the resolution of the DAC. The quantization levels of the DAC output are smoothed over in the integration process, allowing for a continuum of signal voltages to be represented

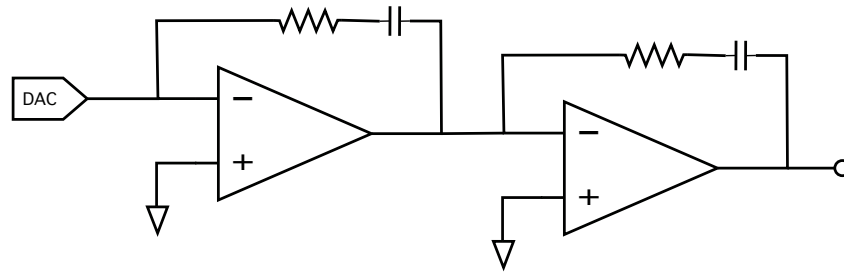


Figure 129. Increasing resolution of an analog signal using integrators attached to the DAC.

Figure 130 shows the process of obtaining a rapidly modulated signal using several low resolution DACs and a multiplexer. The DACs need to generate only the modulation envelop of the signal, albeit at different points in phase. Then the multiplexer simply switches the signal from one DAC to the other, generating a more complicated, higher frequency waveform than the slow DACs could do by themselves. In the example shown, the complicated waveform shown can be generated by the DACs holding their output voltage, and the multiplexer cycling amongst them. More complicated waveforms may be generated by slowly varying the outputs of the DACs.

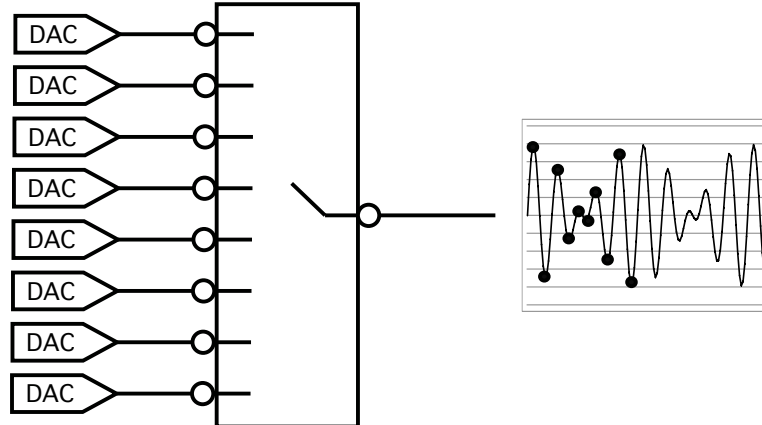


Figure 130. Using several slower-speed but lower-power DACs to create a higher bandwidth signal using a multiplexer.

Finally, a method of connecting a DAC to an analog filter circuit is shown in Figure 131. If we wish to have a small AC signal on a larger DC component, we would need a large number of bits if we used a conventional DAC. By using the circuit shown, however, we can use all the dynamic range of the DAC to generate an accurate AC signal, and have the analog circuitry filter the signal over a longer period of time to generate the DC offset. Thus, we are trading time resolution for voltage resolution for the low frequency components of the signal, while utilizing

the DAC to its fullest extent to generate an accurate AC signal using the entire dynamic range of the DAC.

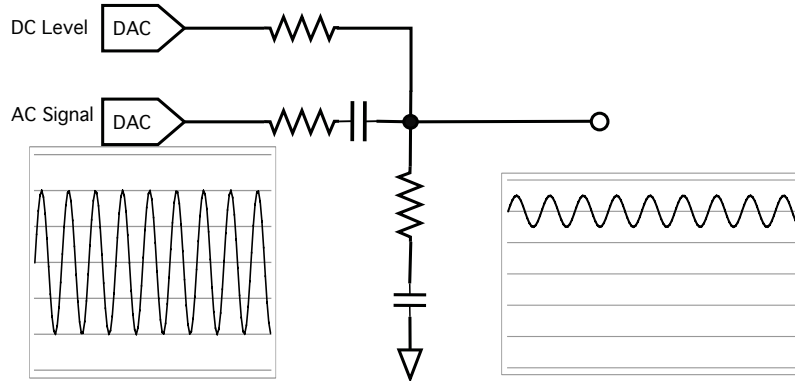


Figure 131. Increasing dynamic range of a DAC by adding the DC component of the signal using analog means.

The above techniques are used throughout the design of the system. These are what allows us to reduce the size and power consumption of the circuitry.

Task 5.7 Drive Electronics Design

This generation design uses off-the shelf integrated circuits and discrete components. To minimize the size, may use advanced fabrication techniques, such as ultra-small resistors and chip-on-board assembly.

As shown above in Figure 124, the operation of the magnetometer consists of many feedback loops. The entire magnetometer consists of the following subsystems:

Cell Heater. The cell must be heated to the proper operating temperature.

VCSEL temperature control. The VCSEL device must be heated to an operating temperature such that the output frequency is close enough for the fine frequency control to operate

VCSEL frequency control. The fine control on the VCSEL frequency is performed by adjusting the current through the device.

Larmor Frequency Loop. This is the actual magnetic field measuring portion of the system. The Larmor resonance must be detected, locked, and stabilized.

Operation

Operation of the sensing system consists of the following major events:

Startup. The temperatures must be brought close to enough to the desired operating point to allow the system to begin operation.

Find the resonance. The system must next scan a wide range of frequencies looking for the Larmor resonance

Lock onto the resonance. Once the resonance is found, the system may then begin to set its desired operating points, and then track the resonance using the fine feedback control mechanisms.

System Block Diagram

The system consists of three boards in total, as shown in Figure 132.

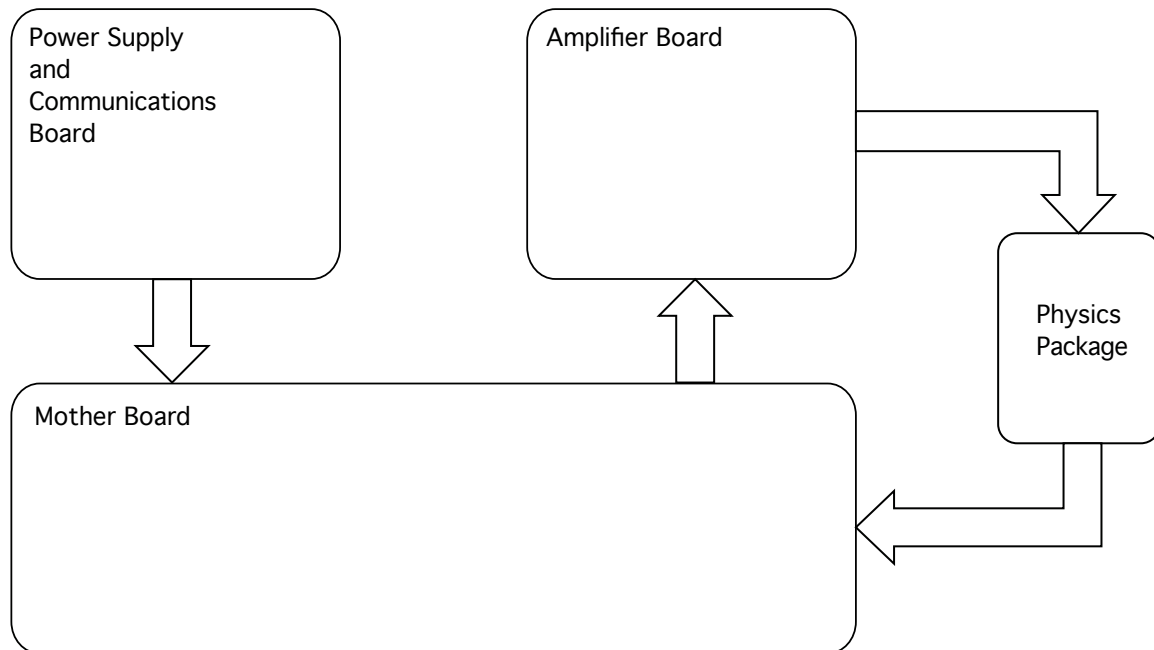


Figure 132. Board-Level Block Diagram.

Task 5.8 Frequency Measuring Electronics Design

The magnetic field output of the system is proportional to the resonance frequency found in the operation of the sensor package. Ultimately, the physics package is a tuned circuit, and the whole point of the electronics is to find the frequency of resonance. The electronics circuitry produces an analog signal at the resonant frequency. This frequency of this signal must be determined. When multiplied by the correct scale factor (3 Hz per nT) the magnetic field is obtained.

When the Larmor signal is generated using analog means, the period of this signal must be determined, which allows for the frequency to be measured. This measurement must be determined to very high accuracy. Since our desired noise levels are on the order of pico-Tesla, on a signal of 50,000 nT, the frequency must be determined to within 0.003 Hz.

The actual design is described below as part of the Final Electronics Design.

Task 5.9 Final Electronics Design

This section describes our work on the final electronics design.

Power supply

Referring to Figure 136, in the upper left corner, Q1 is dual P-channel power MOSFET. It provides protection against inverted power connections, because unless the power is properly applied, the device is turned off. When power is correctly connected, it passes the current with very little voltage drop. It also serves as a power on surge limiter because it is prevented from turning on too quickly by the action of Q2.

The power for the Laser and Cell heaters is run directly from the reverse protected input voltage and not from regulated voltages. This is done for two reasons. The regulator circuits do not have to produce the roughly 2W of power required by the heaters and thus the magnetics can be made much smaller. The AC currents from the heaters are prevented from flowing through the sensitive electronics.

The two supply voltages created in this board are +3.3V and +8.3V. The +8.3V supply is made such that it can never be more than 5V above the +3.3V at any time, including shorts on the +3.3V. This ensures that excess stresses are never placed on some of the components.

The +8.3V supply is made with a buckler running at a frequency well above the Larmor. Both the high frequency and modest difference between the input and output voltages allow for a small sized inductor. Some efficiency is sacrificed on the output of this circuit in order to avoid adding an inductor. A series resistor and a capacitor to ground reduce the noise enough to meet our requirements.

The inductor in the +8.3V supply has a second winding that is used to develop an unregulated isolated supply needed for the communications circuits. Although the V232 is unregulated, in practice, its voltage only varies over a narrow range. Its nominal value will be 8.3V. This supply will be discussed further in the section about communications.

The 3.3V supply is done in two steps. A pair of switched capacitors converts from the +8.3V to and intermediate +4.1V supply, without using inductors. U3 and U4 are serving this purpose. The inductorless converters are forced to run 180 degrees out of phase to each other by U1. This is so that their ripple cancels. All of the ripple current for these components is confined to their local supply voltage.

This +4.1V is then linearly regulated down to the +3.3V supply in the lower left corner of the sheet. This regulator is designed to have a very low output impedance and noise. This means that the +3.3V supply will be very low noise in the important frequency bands.

The power supply section is designed so that it can serve 4 magnetometers. By sharing some sections, the total power consumption of arrays can be reduced by avoiding repeating the overhead for each unit.

Communications and I/O

Please refer to Figure 137. The data is produced in digital form. Several protocol options were considered. USB was rejected because it does not permit the length of cable required. Network methods were rejected for reasons of power consumption. RS-232 has a very high power efficiency because the signaling is done at relatively high impedances and the number of transitions per bit transmitted is almost exactly 0.5.

Because the power wires may be long and may in fact run to a different location than the communications, a large common mode voltage is allowed between the power connections and the communications connections.

The communications is a multi-protocol system. RS-232, RS-422 and RS-485 are all possible with the hardware provided. In the case of RS-485, the termination resistors must be provided at the end units by external resistors. The most common case is the RS-232 case where the negative wire of the transmitter and receiver are connected together externally to the magnetometer.

U10 and U12 are comparators that allow very large common mode voltages. These circuits will function with a common mode as high as 200V.

U10 allows a triggering signal to be brought into the instrument to trigger the cycling. Normally, the signal from U12 serves as both the RS-xxx input and the triggering signal. Logic is provided to select the trigger signal and precondition it before sending it to the interrupt connection of the main CPU.

When operating in concatenated slave mode, the data from the RS-xxx receiver can be routed by logic to the RS-xxx output circuit. This removes the delay of passing the data through a processor from the path of the concatenated data. This is done so that large arrays of magnetometers can be deployed and synchronized. When multiple magnetometers are connected to the same power supply, the concatenation of the 4 local units is done with logic level signals between the units.

The RS-xxx output also uses comparators with a high common mode voltage to bring the signals to the output transistor section.

The output section is a transistor bridge. This design allows us to meet the communications requirements with only needing to make a single isolated supply. Since power consumption is a primary focus of this design, removing the overhead of having two supplies was part of the consideration for this design. The output also needs to be able to operate differentially to be compatible with RS-422 and RS-485.

Motherboard

The main motherboard connections are shown in Figure 138. This diagram shows the interconnections amongst the other schematic pages to follow.

Main CPU

Please refer to Figure 139. The logic for concatenation of multiple units is in this code. When the software sees that it is not the first one in a concatenated string of units, it operates in “slave mode”. Normally the unit operates in “master mode”.

In Master mode, the first character of the data string is transmitted exactly at the end of one measurement period and the start of the next. This means that the master will cause the start bit transition of its data to happen at that time.

In Slave mode, the magnetometer must capture the magnetometer reading when it sees the start bit from the master. It must do this without disturbing the continuation of the measurement process. After the character is received, it can then test it to see that it is the proper character for the triggering of the reading. This means that the slave effectively has two measurements in progress during this brief interval. It has the continuation of the previous reading for the case where this was not the trigger character and the beginnings of a new reading for the case where this was.

When the external trigger is being used, an externally triggered version of the master mode and slave mode are used. The master still transmits the trigger character but the slave does not use this for its triggering action. The trigger character from the master is still available to the data recording device to allow it to correctly assign times to the measurements.

Counting

Please refer to Figure 140. Counting is not really the correct word for this function. It is a more general frequency measurement. The method used takes advantage of counters built into the main CPU IC.

The common high performance method of measurement of frequencies in the 100kHz range is to measure the period of a group of cycles and compute the inverse. The counters are then restarted and the period of the next group of cycles is measured.

Geometrics has for a long time used an improved version of this method where two banks of counters are used and a new measurement is begun at the exact instant when the previous is ended. A further improvement on this method is needed in order to obtain the specified performance.

The circuit shown on the counter section diagram shows the method used for this trading off of counters. The PulseA output is active while the second flip-flop is set and PulseB is active while this flip-flop is cleared. The first flip-flop ensures that the change from one counter to the other

can only happen on a falling edge after a rising edge after the request for change is made. This ensures that there can't be metastable states because of coincidence of the timing of the "GATEREQ" and the "FREQ"

Because the Larmor is generated by a system that operates as a multi-pole filter, there is the expected noise peak near the gain crossover of the servo loop. The noise shaping causes a second peak near 1200Hz. These peaks are well above the frequency band of interest but would be aliased by the sampling nature of the system. For this reason, the period measurements are made at a rate much higher than the reporting rate and then digitally filtered.

Larmor CPU

Please refer to Figure 141. The Larmor CPU contains an ADC and a DAC. This is a digital implementation of a system that performs two main correlation functions and some digital filtering.

The main correlation is between the signal from the photo-detector and an internally generated copy of the modulation waveform. This develops the error signal for the servo. There is a digital filter included that integrates this signal to develop an offset that brings the error exactly to zero. This prevents any offsets in the amplifiers that follow this from creating an offset in the reading. This is part of what makes the measurement absolute

The noise shaping of the numbers being input to the DAC, causes the quantization noise to appear in a band from about 600Hz to 1800Hz, with a noise level of 10uV per sqrt(Hz)

VCO

Please refer to Figure 142. The error signal enters this sheet on the lower left. The two op-amp stages are integrators with resistors in series with the integration capacitors. This places a zero in each section's transfer function. At frequencies below 0.3Hz, the gain of this circuit rises very rapidly with decreasing frequency.

The DAC signal into this section will be at its center point for constant fields or fields that rise at a steady rate over the long term. This allows all of the resolution of the DAC to be available to follow anomalies. A copy of the voltage from the second stage is fed back to the CPU. This is only used in the process of obtaining lock. Once lock is obtained, the servo ignores this and only uses the signal from the quantum physics.

The input to this section is from a DAC that has the noise shaping logic applied to it. This means that there will be a peak in the noise near the Nyquist frequency of this DAC. The pole at 159 Hz partly serves to reduce the amplitude of this before it reaches the VCO.

The upper half of the sheet contains the counter that steps off the phase of the Larmor cycle. At each change in the contents of this counter, the inhibit line of the multiplexers will be taken high.

Without this, the timing of the bits from the counter and the internal decoders of the muxes may cause spikes on the outputs of the muxes.

The test connector allows an external generator to be substituted for the VCO as part of the testing of the system.

DACS

Please refer to Figure 143. The local DACs construct the voltages that the main CPU has control over.

H1 Control

Please refer to Figure 144. The H1 control section scales the H1 drive with resistors and provides the needed amplifiers and high output impedance. The 3 operational amplifiers on the right side of the page are performing this function.

The amplifiers on the left side of the page are making the very small DC current that we feed into the H1 coils to remove the remaining quantum mechanical heading error. Because the current from these produces a small local dipole, the curve of the bias to the field created almost exactly matches that of the remaining heading error. These circuits are driven with DACs so that the exact amount of error to be removed can be automatically calibrated by the software of the system.

Voltage reference

Please refer to Figure 145. The reference voltage does not need to be absolutely accurate. The most important specification for these voltages are the drift and noise values. Since these voltages are used as references for the creation of the H1 drive, the measurement of the photodiode signal and the current into the Laser, any noise in the reference would be able to find its way into the performance of the system.

The references are all developed from a buried zener reference IC. Band gap references are far too noisy to be using in this application. The circuit involving U1402B is the only part of this circuit that is not self explanatory.

C1404 is a tantalum capacitor. These provide large values in a small space at the cost of some leakage current. High K value ceramics can not be used in such circuits because they are far too micro-phonic.

U1402B amplifies the difference between the REF400 signal and the voltage on the C1404 and applies it to C1403. The operation is most obvious if it is assumed that C1404 is extremely large and is at exactly the average voltage of REF400. Observe that this makes the voltage appearing on C1403 101 times whatever noise may be on the REF400 signal. The AC current into C1403 is thus 101 times larger that it would normally be making C1403 appear to be over 10uF.

This view of the circuit operation is valid above about 10Hz. It is thus valid for the band of frequencies that are important to the other circuits.

Photo preamp

Please refer to Figure 146. The first state of the photo-preamplifier is a fairly normal trans-impedance amplifier design. Because this circuit is running on the end of a cable from the sensor, the op-amp needs some protection from RF picked up in the cable and local feedback to prevent oscillation.

The second stage is DC coupled and level shifts the output of the first. The level shifting is needed so that the DC part is at the center of the range of the ADC it is fed to. There is also a 3:1 attenuation of the DC signal. This is to reduce the span to fit within the range of the ADC.

When the Laser is not on the absorption line and the Laser current is set to maximum, the output of the first stage is nominally 7.5V. Under these conditions, the “PHOTODC” signal is very near zero volts. When the absorption line is first encountered, it will be seen as a dip in the voltage on the first stage and a rise away from zero on the second.

The AC component sees a gain of 5. This is used when the system has obtained lock. Since a very small variation in the Laser current is used to keep it centered on the absorption line, the 15:1 advantage of the AC signal over that of the DC signal is needed to ensure high stability.

The second stage provides an added gain of 5. This is an AC coupled signal that is used by the Larmor locking section.

Sensor Driver Board.

Top level schematic is shown in Figure 147.

Laser servo

The laser servo operation is shown in block diagram form in Figure 133. The heater signals are shown in Figure 134 for high and low power heating. The goal is to make the heater circuit efficient, yet have few harmonics which interfere with the noise performance of the entire system. A square wave with a varying duty cycle would be the most efficient. A sin wave with a varying amplitude would have the least harmonics. We have chosen a waveform with the 1st and 3rd harmonics of a fundamental to achieve a compromise

The Laser servo schematic, shown in Figure 148, is a case where having a schematic of the circuit provides almost no insight to its operation. Almost all of the operational details are encoded in the firmware.

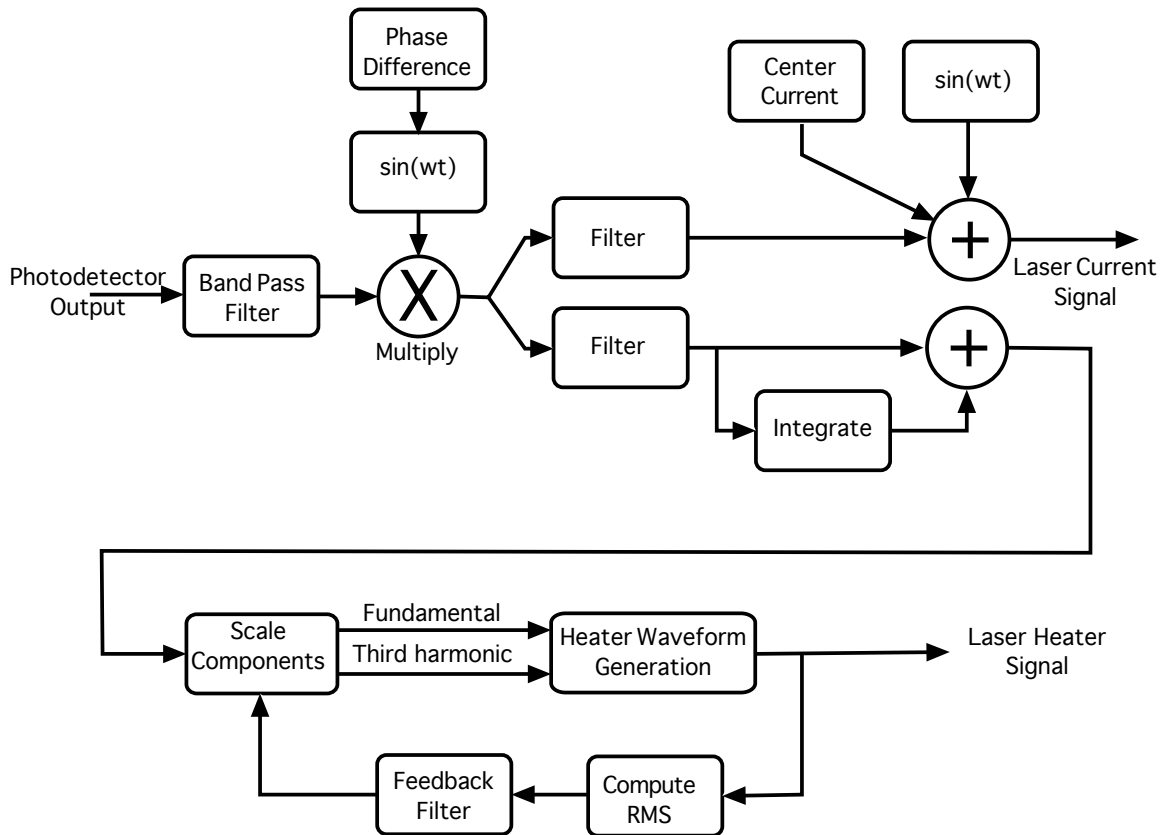


Figure 133. Laser servo block diagram.

In operation, the two heater outputs generate signals with the needed RMS value to generate the amount of heat needed to hold the Laser and cell at the required temperatures. These waveforms are composed of a fundamental and a 3rd harmonic, as show

These waveforms are used so that we can be sure that the heaters do not have any frequencies on them that are near the Larmor or near any of the other operating frequencies.

The heater waveforms have two noise shaping effects applied to them. In the short term, the DAC values have noise shaping to prevent the heaters from containing any current in the zero to 20Hz band. The second level of noise shaping is applied to keep the power to the heaters from having any artifacts on them that may cause cyclic changes in temperature.

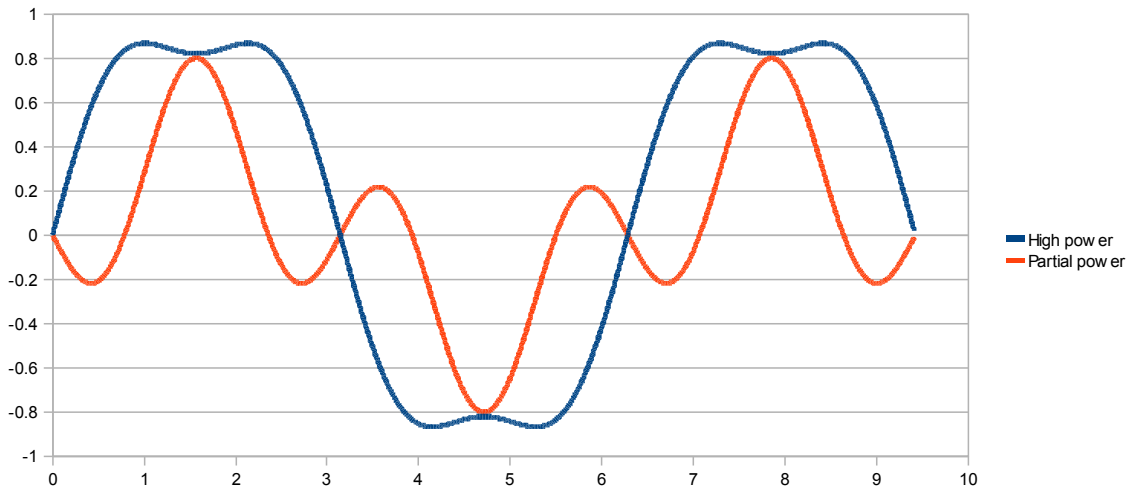


Figure 134. Laser heater waveforms.

The “LaserI” signal has a small sine wave on it. This slightly varies the wavelength of the Laser. This is part of the process that keeps the Laser in the exact center of the line. As the sine wave moves the Laser wavelength over the peak of the line, a signal as shown in Figure 135 is generated.

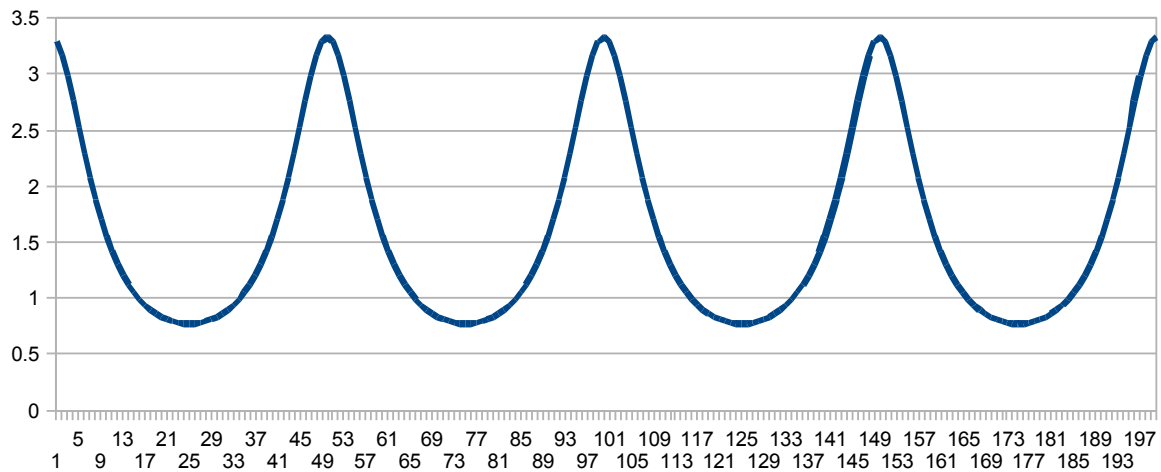


Figure 135. Absorption signal as wavelength is varied.

Once the Laser has been locked onto the line, the amplitude of the modulation of the Laser current is reduced to prevent it from contributing to the system noise. As this is done, the servo's gain is adjusted to maintain stable operation with the reduced signal.

Laser driver

Please refer to Figure 149. In the upper left corner, the Laser current setting from the DAC is combined with a reference voltage. This reduces the span over which the DAC controls the current and thus improves the resolution.

C602 decreases the gain of the current control at frequencies above 2Hz. 1Hz is used when the software is attempting to discover the absorption line. Once the line is found and brought to the center of the span of the DAC, the frequency is increased and thus the span reduced allowing more resolution from the DAC.

C601 ensures that no noise at the Larmor frequency can make its way into the circuit via this path.

U601B implements a constant current circuit by making the voltage drop on R607 proportional to the input voltage. The values are selected so that even in the case of a failed U601, destructive currents are not allowed to flow in the Laser.

U601A implements a high pass filter with an extra zero in its transfer function. The Laser has a thermal time constant near the center of the Larmor band. This zero helps to equalize the amplitude of the Bell-Bloom action over the Larmor band. The detailed matching of the curve is done by the micro processor.

Heater amplifiers

Please refer to Figure 149. This is a moderately high fidelity audio power amplifier that can drive signals to within 0.2 volts of the supply rails and is efficient.

When U301 attempts to pull its output in the positive direction, The current on its positive supply biases Q301 on which is what actually drive the circuit output positive. Q302 works on the negative supply connect to pull the output down.

R303 does two things. One is that it provides a negative feed back by taking the output of the op-amp in the direction that the load is being taken. It also provides a path by which the output of the op-amp can set the output voltage when there is nearly zero load current.

R301 and R302 sets the overall gain of this circuit as 2. By using a low gain here, the op-amp only needs to be one with a modest gain bandwidth specification.

U301 is an op-amp with an unusual topology. It produces very high slew rates and is remains fairly linear for large differential voltages. Because of this it can switch over between Q301 and Q302 and back again very quickly. This allows us to use what is effectively a class C output section and yet have low distortion.

C301 is needed to compensate for the stray capacitances in the circuit. Without it, the circuit can oscillate under some conditions. The actual size of C301 will depend on the layout of the circuit.

B301 is needed to prevent RF from radio stations from getting into the output section of the amplifier. This circuit is driving a cable that for size and weight considerations is not a 100% shielded cable.

Temperature sensor

Please refer to Figure 151. The thermistor used in the sensor is selected for its accuracy at the running temperature. The circuit shown here allows the temperature to be measured using a very small current. During start up in cold conditions, the firmware needs to be able to measure the existing temperature at the sensor. By changing the values on the DACs, the processor and reconfigure this circuit to give an accurate reading at low temperatures.

Sensor assembly:

The Laser assembly thermal isolation allows us to obtain a rise of 310 degrees C per Watt of applied power. The gain and phase shift characteristics of the impulse response, was measured and was found to be acceptable for the intended servo design. The phase only lags by 90 degrees at 0.6Hz, means that we can use a moderately fast servo control to obtain rapid settling at startup.

A nearly flat gain vs frequency curve implies that the bulk of the phase shift is being caused by a transport delay like mechanism. The gain near the 0.5Hz point is important to us because that is the intended servo gain cross over point. The gain at that point will be almost exactly 200 degrees per Watt.

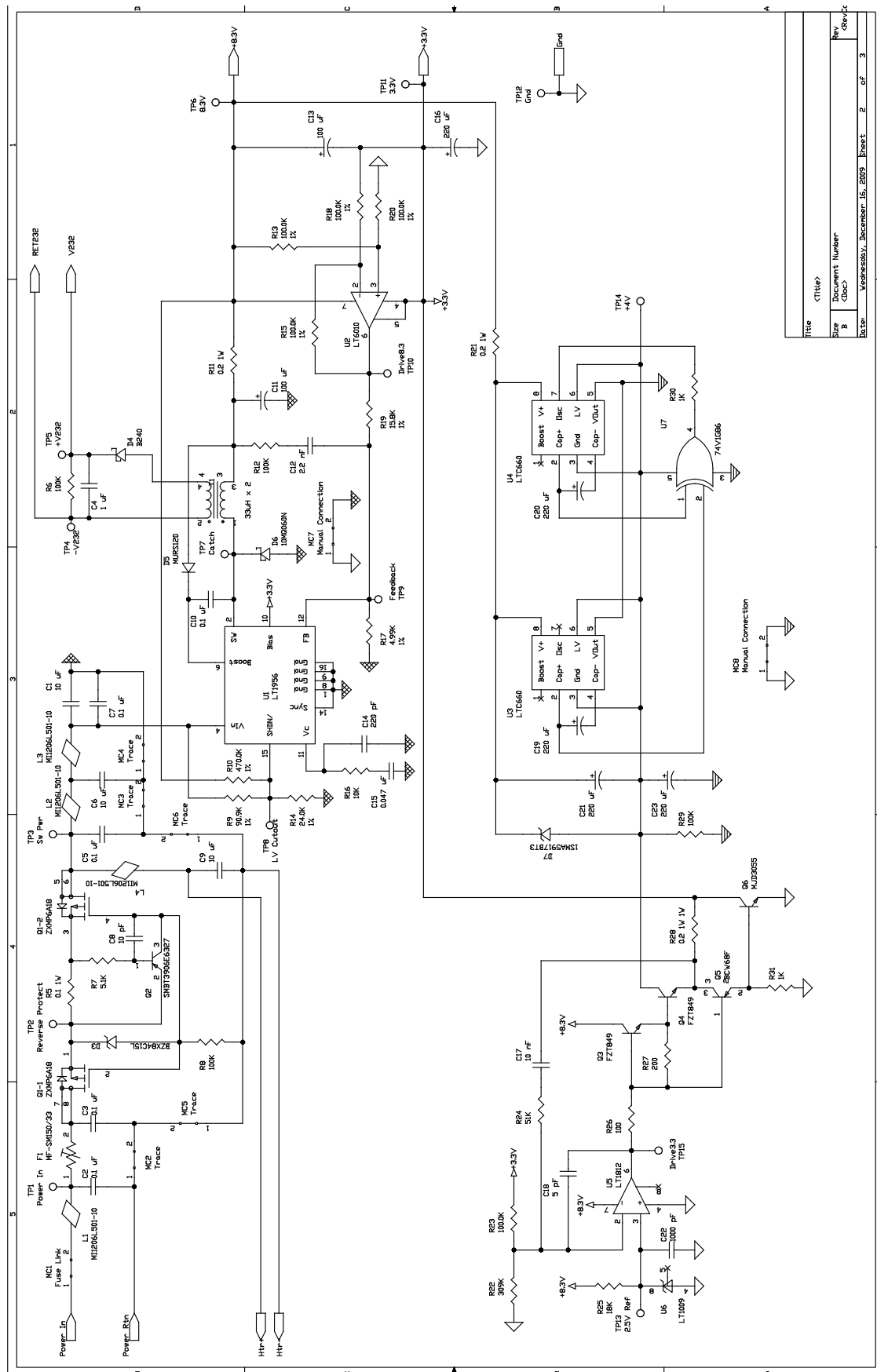
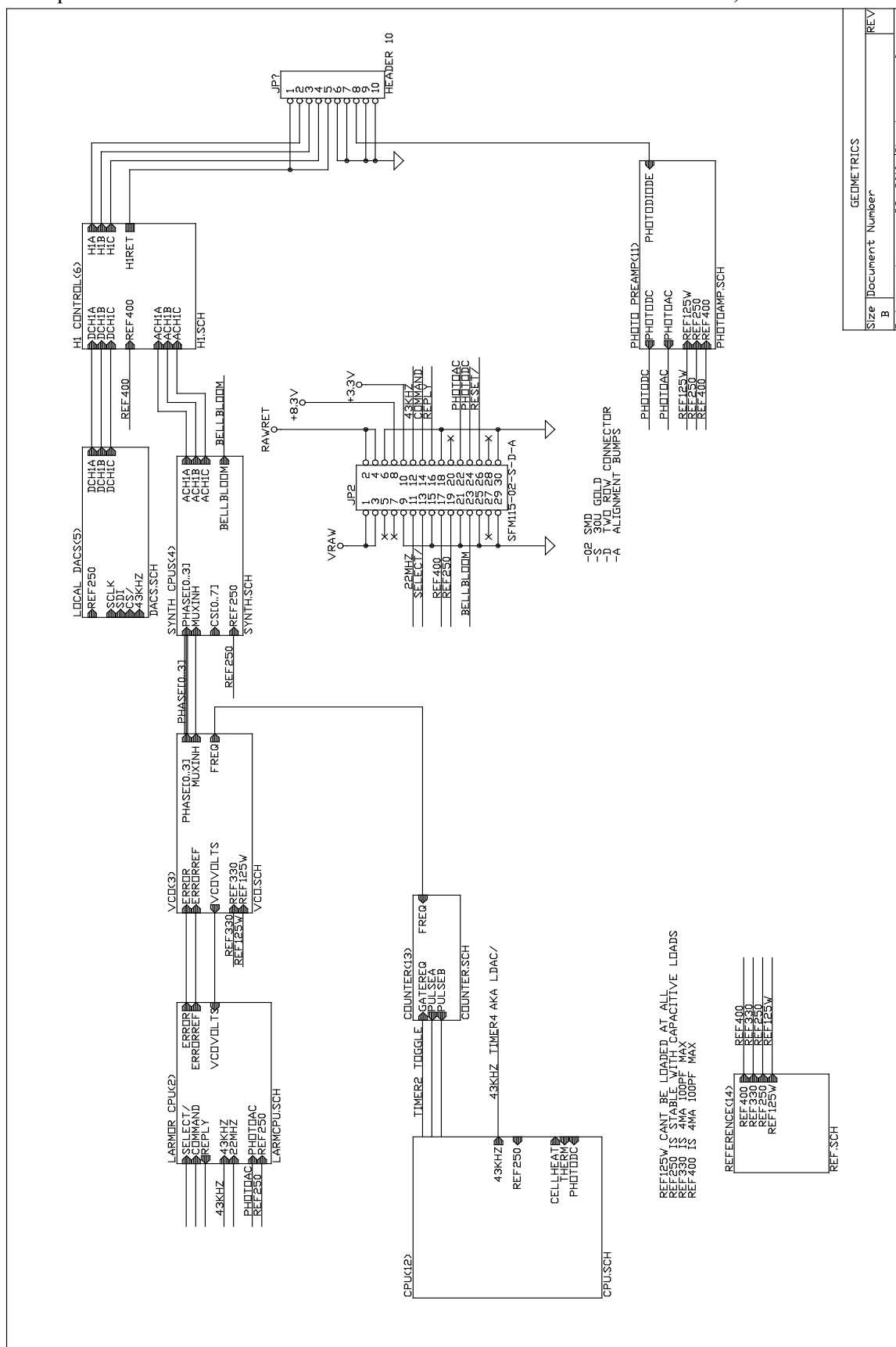


Figure 136. Power Supply Schematic.





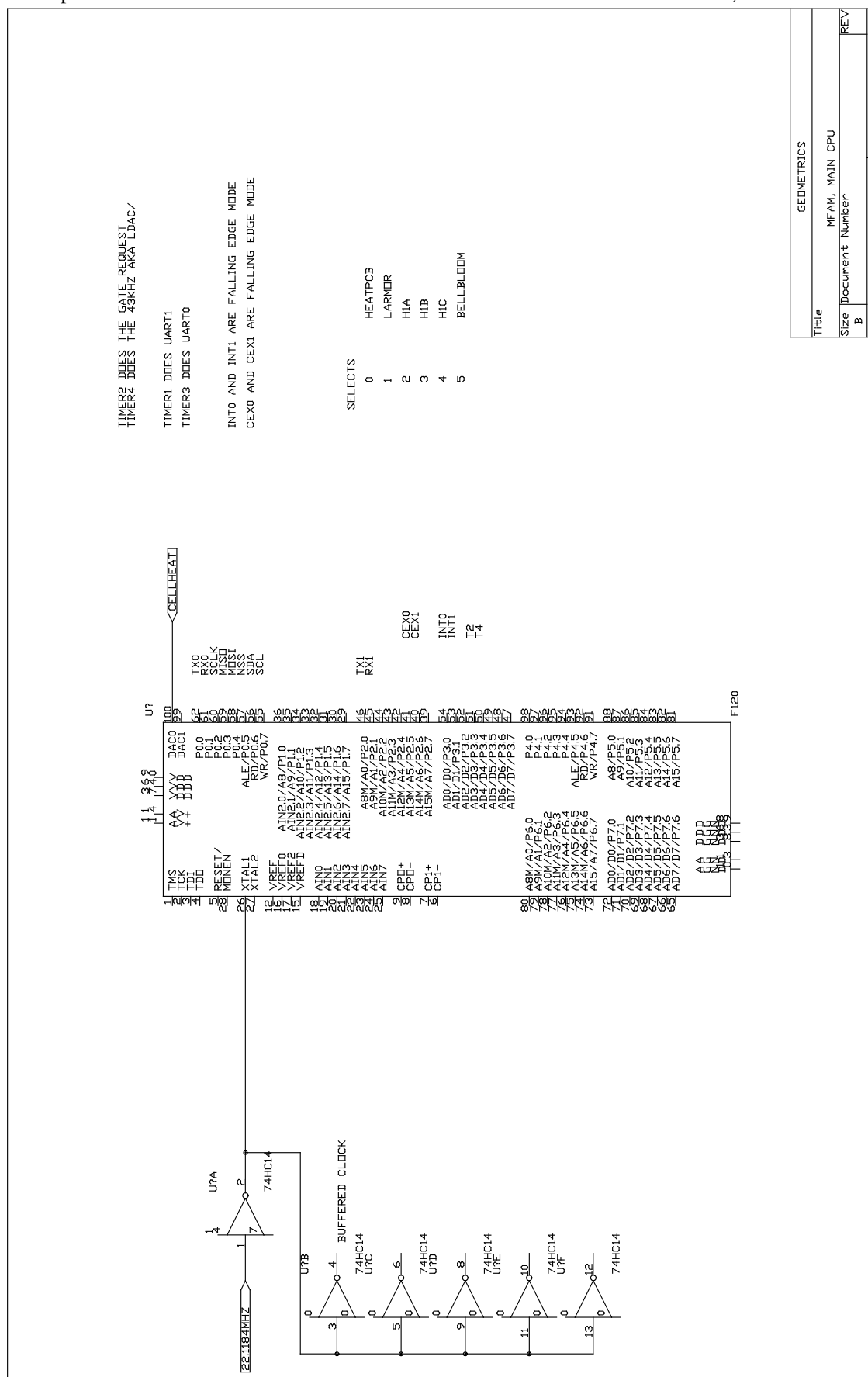


Figure 139. CPU Schematic.

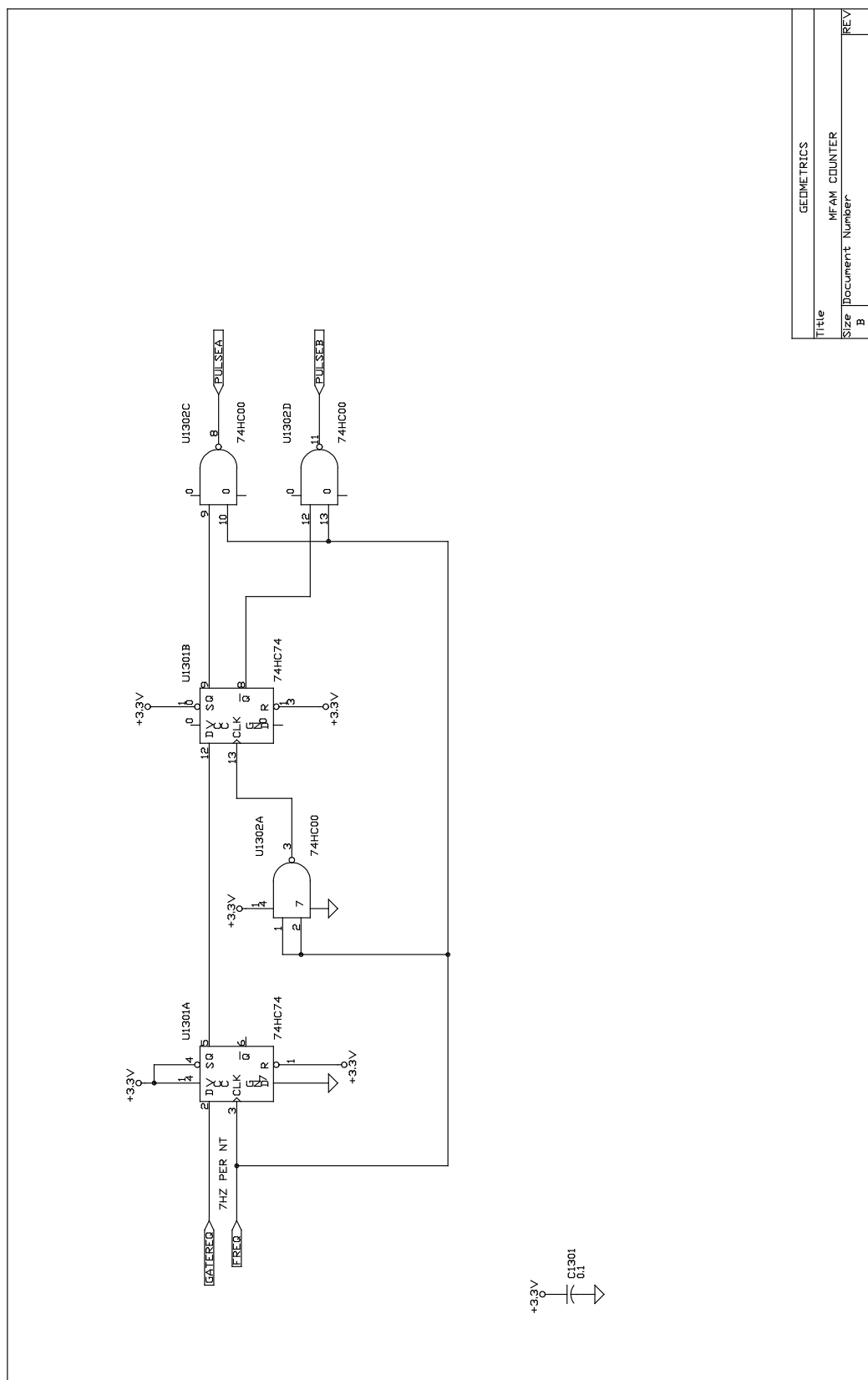


Figure 140. Counter Schematic.



Figure 141. Larmor CPU schematic.

GEOMETRICS	
Title	MFAM, LARMOR CPU
Size	Document Number
B	January 27, 2010 Sheet 2 of 2

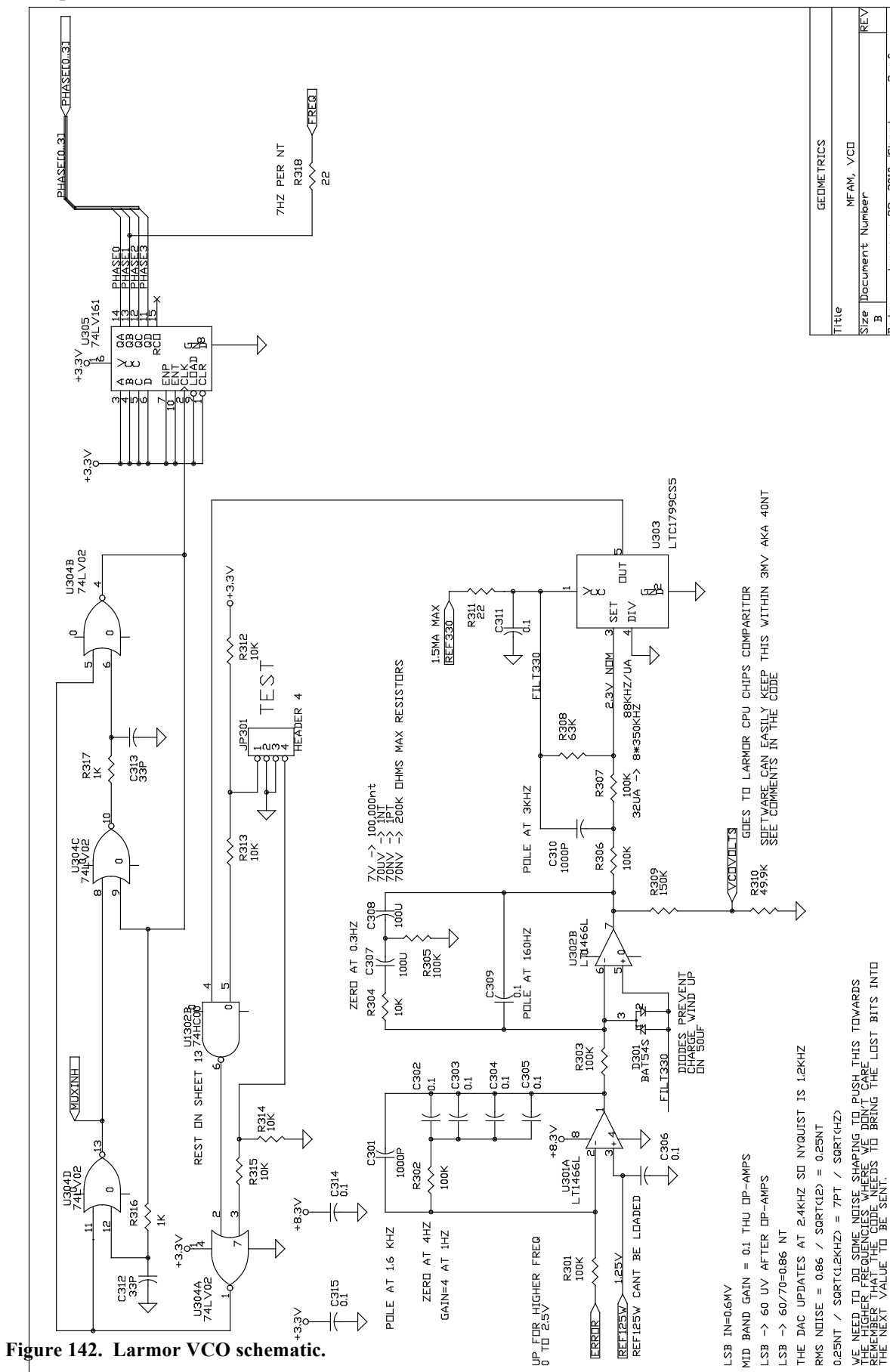


Figure 142. Larmor VCO schematic.

GEOMETRICS	
Title	MFAM, VCO
Size	Document Number
B	REV



147





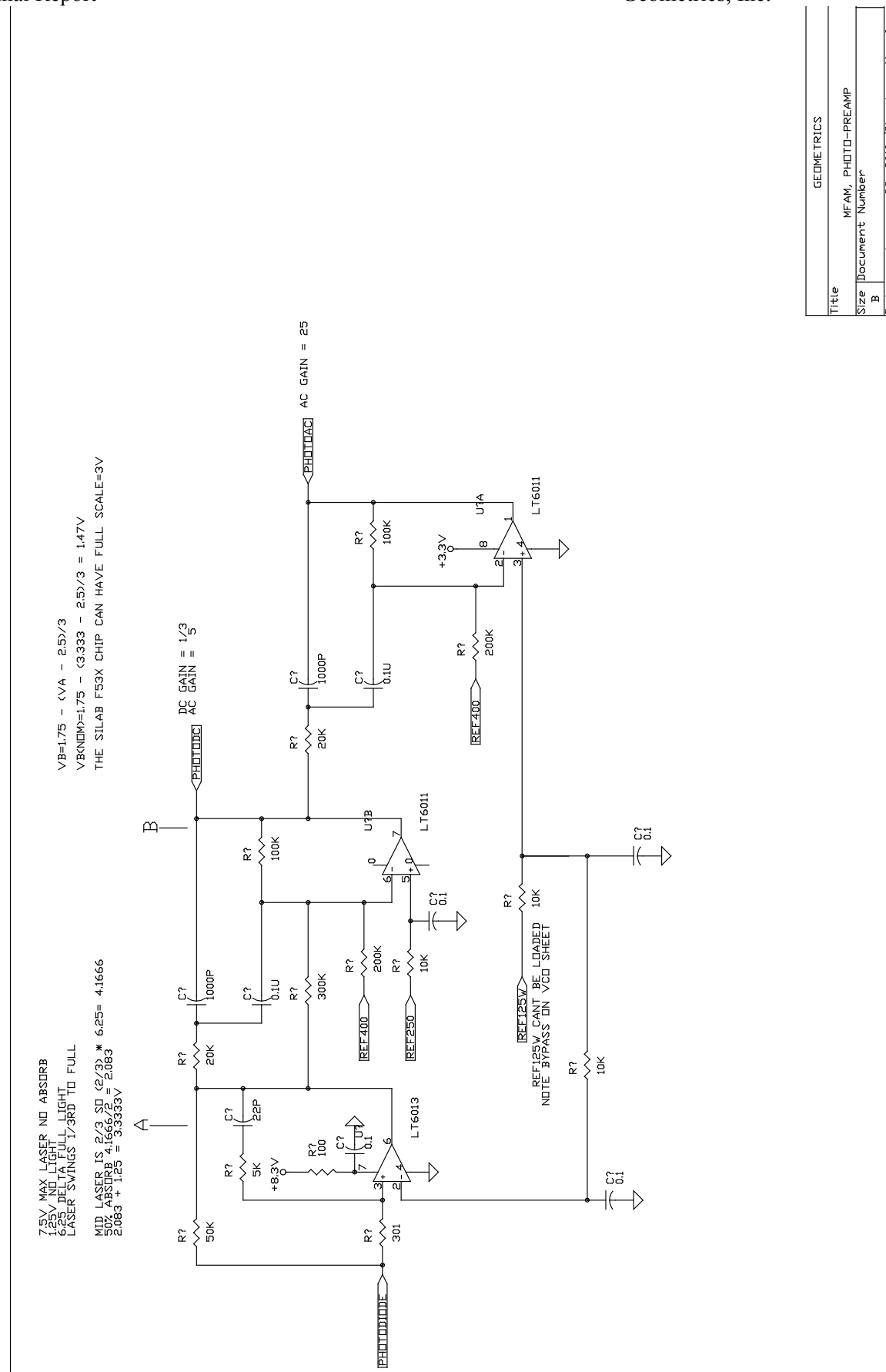


Figure 146. Photo preamplifier schematic.

Title	
MFM, PHOTO-PREAMP	
Document Number	
Size B	

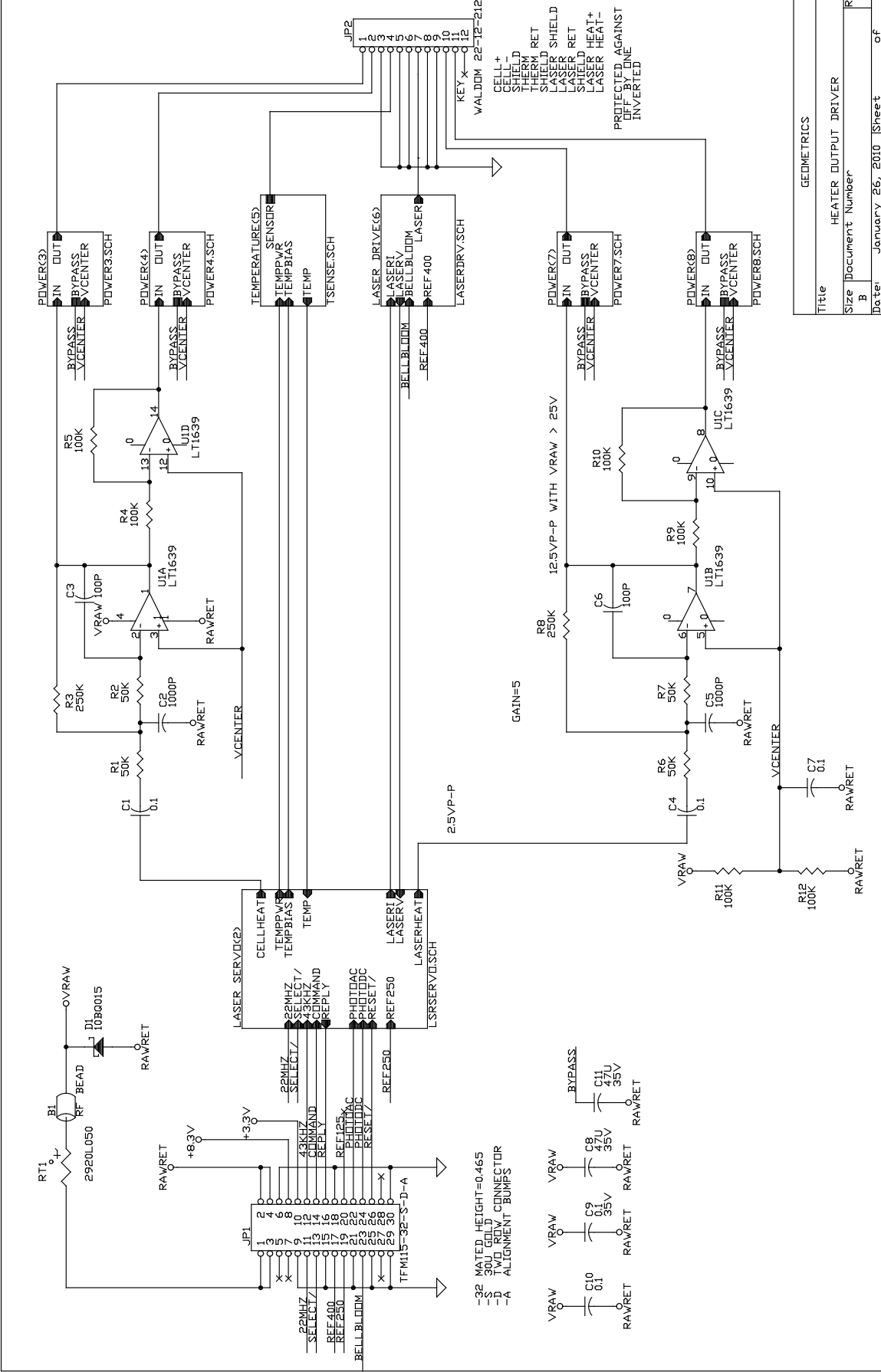


Figure 147. Top-level sensor driver board schematic.

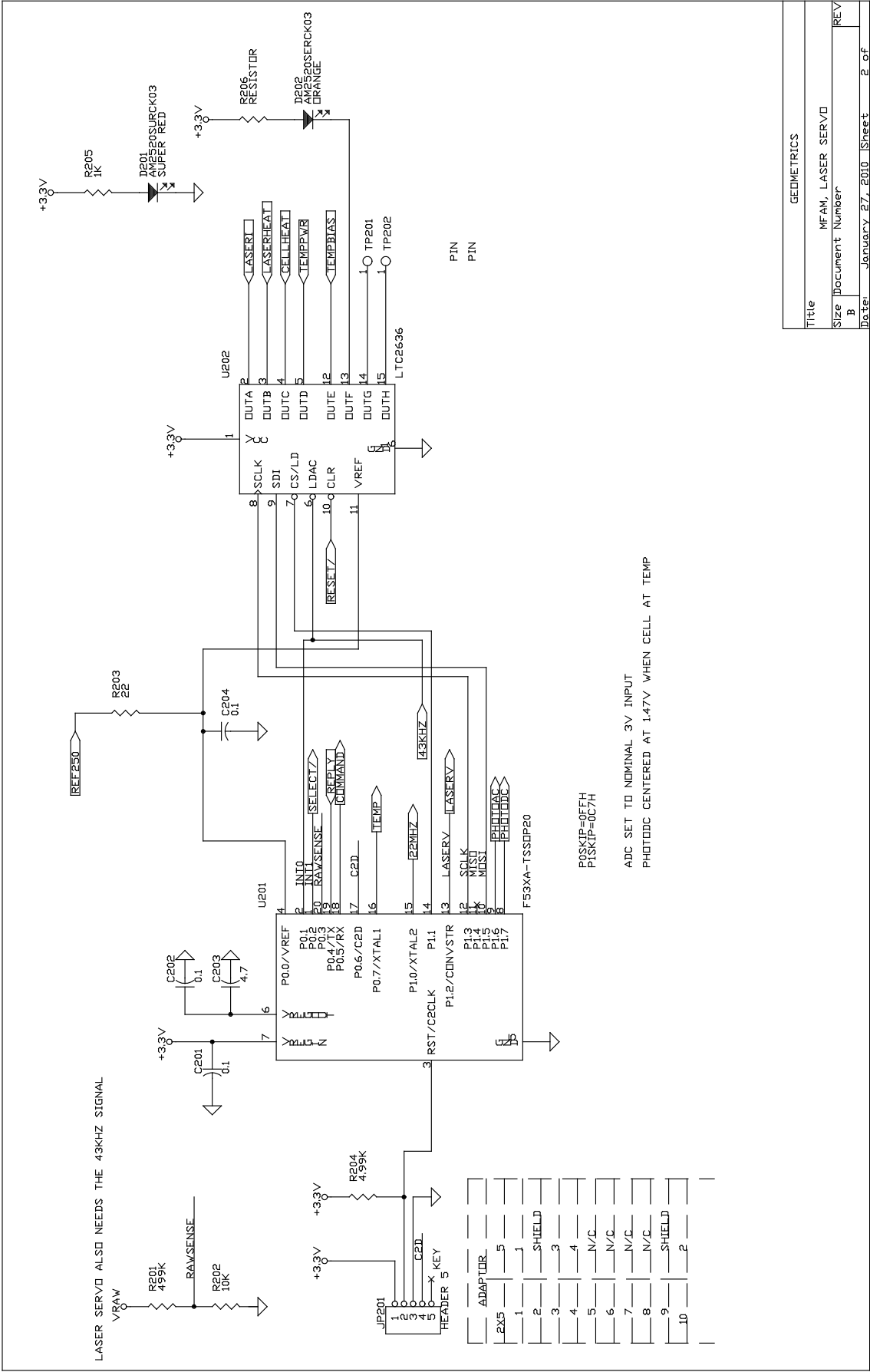
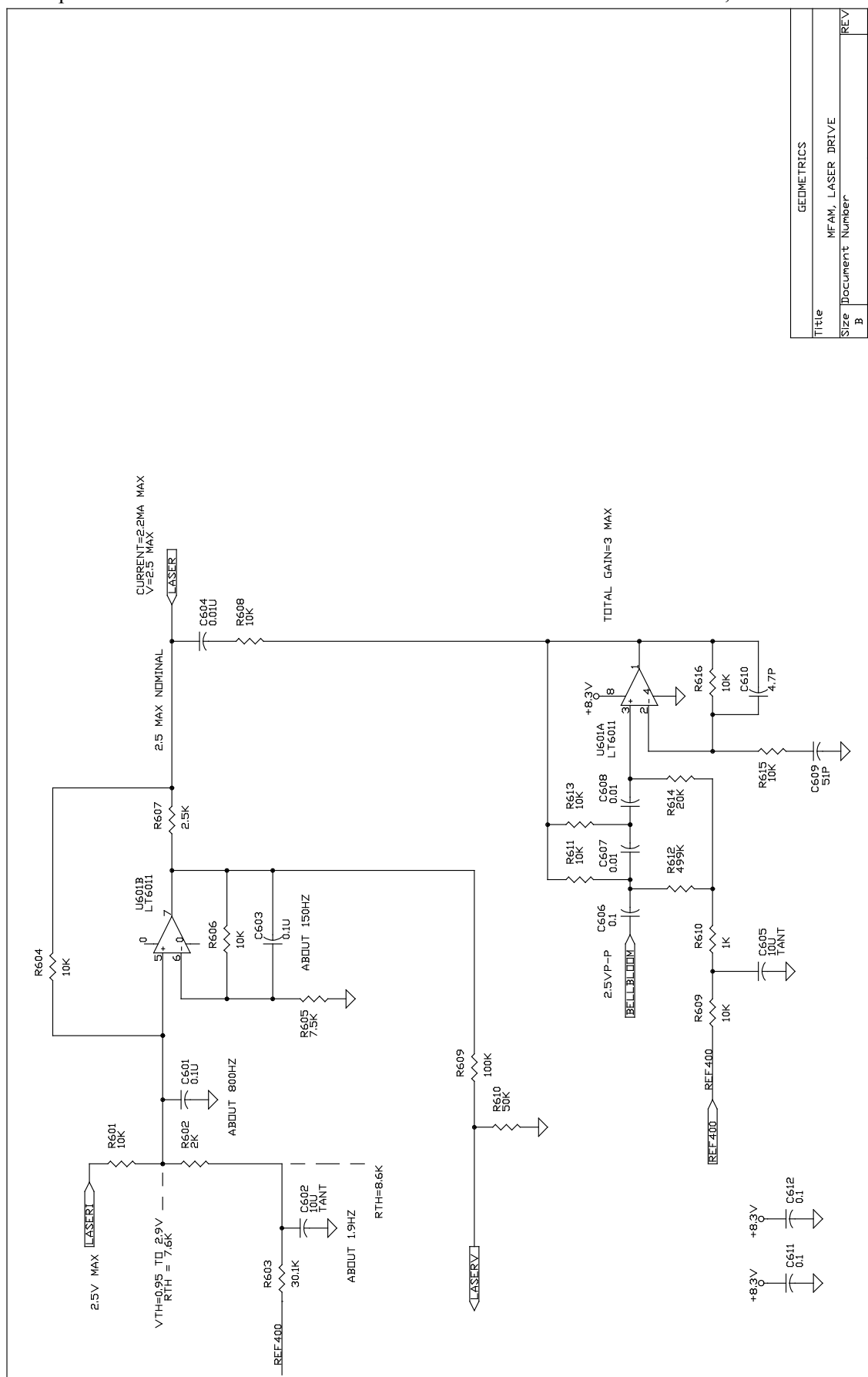


Figure 148. Laser servo schematic.



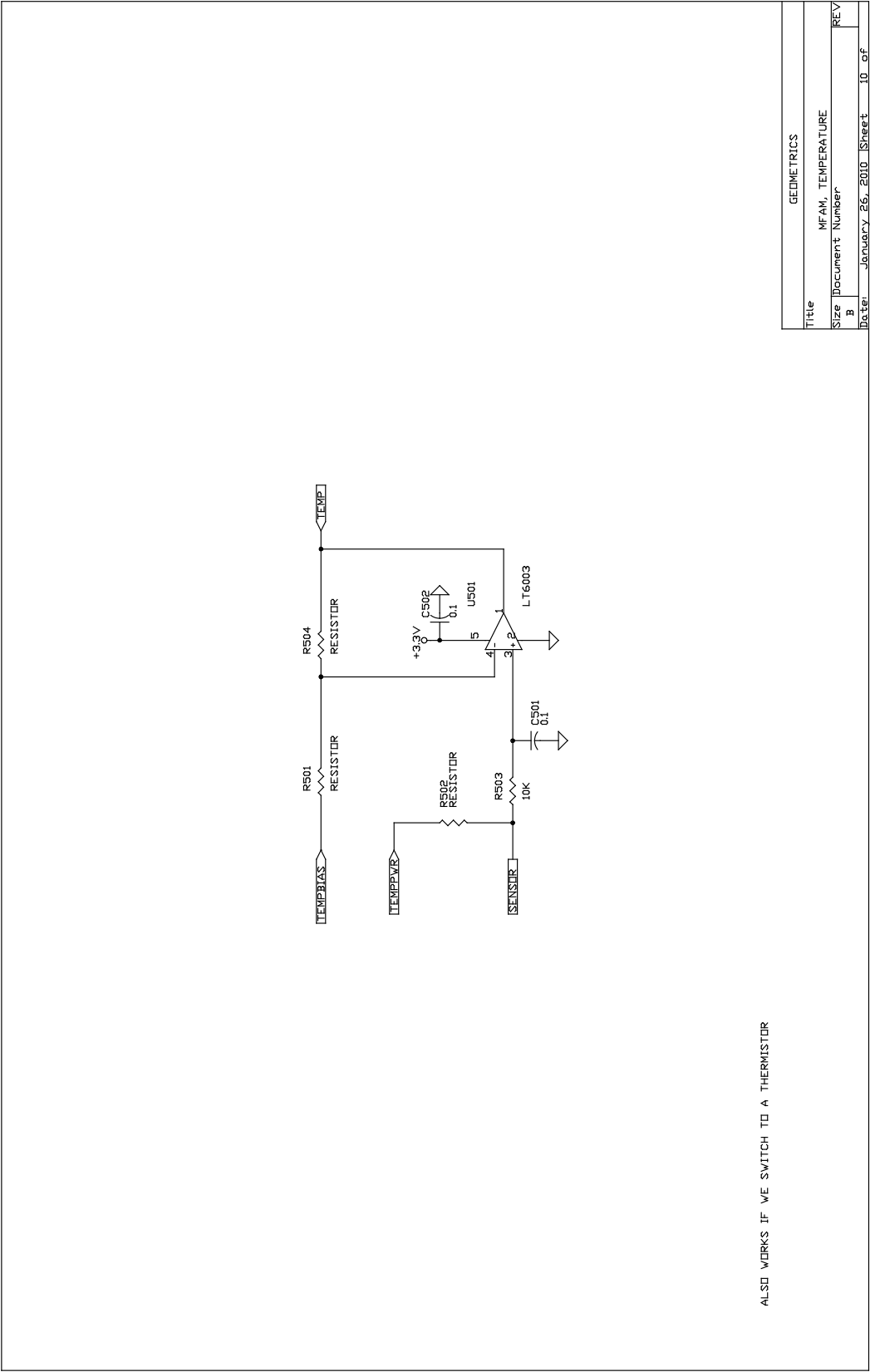


Figure 151. Temperature sensing circuit.

Testing

Task 6.1 Laboratory testing

Figure 152 shows magnetometer signals gathered in an uncontrolled environment in the laboratory. Large amplitude signal variations are due to the movement of a small magnet in the room to change the magnetic field. Smaller noise variations are due to the unshielded environment in the noisy laboratory. Figure 153 shows the spectral response, indicating a noise level of about 60 pT per root Hz.

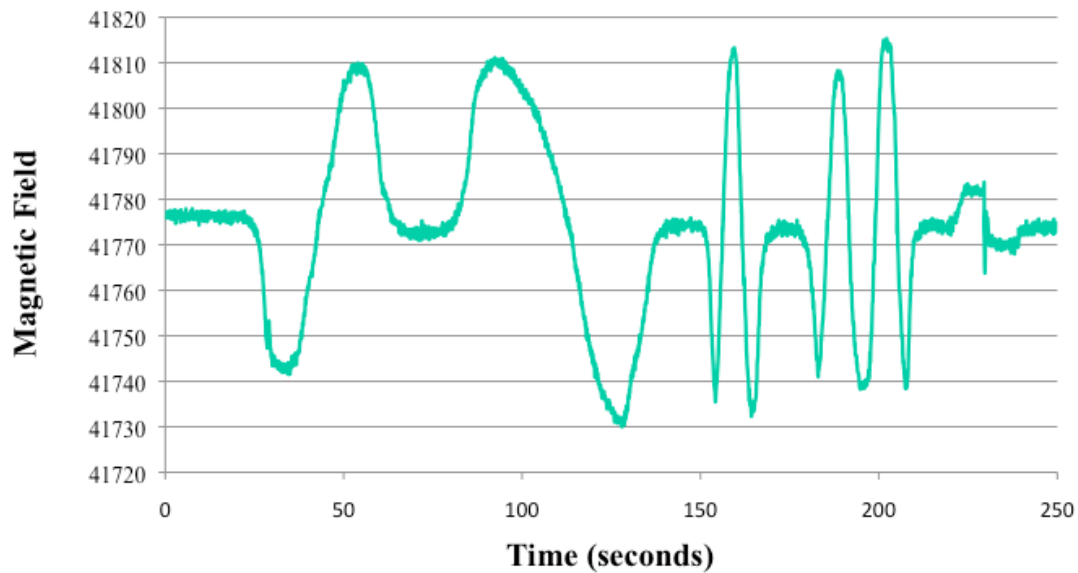


Figure 152. Magnetometer signals gathered in an uncontrolled environment in the laboratory.

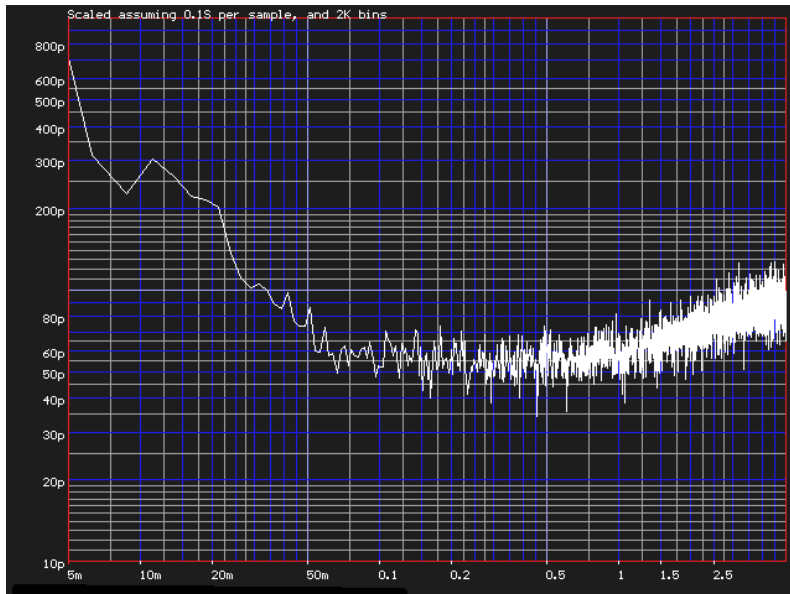


Figure 153. Spectral response of magnetometer with a reference sensor.

Task 6.2 Field testing

In order to prove that the system could operate in uncontrolled conditions, we took it outside to measure the fields of passing vehicles, and to do a small simulated survey with the system in motion. The purpose of this brief test was simply to show that the system was capable of complete operation in an uncontrolled environment. A few results are shown below.

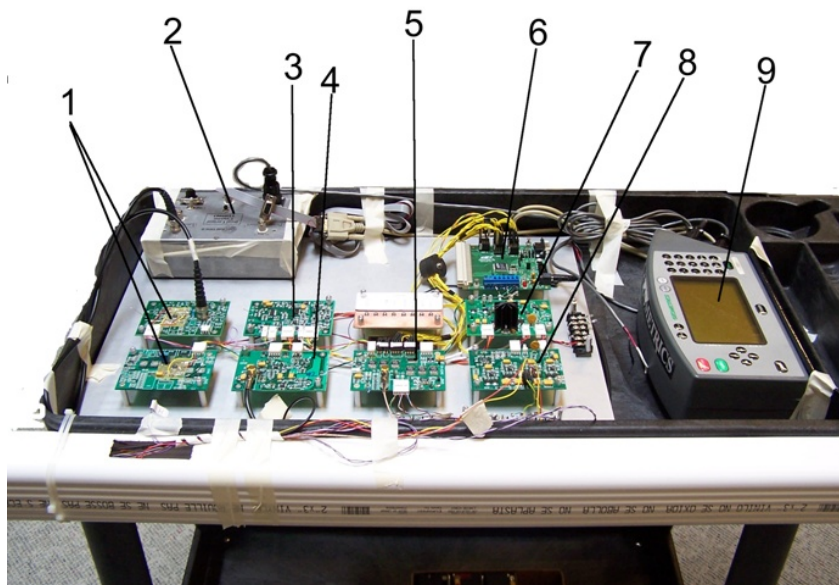


Figure 154. Electronics system mounted on a cart for field testing..



Figure 155. Photographs of the test system.

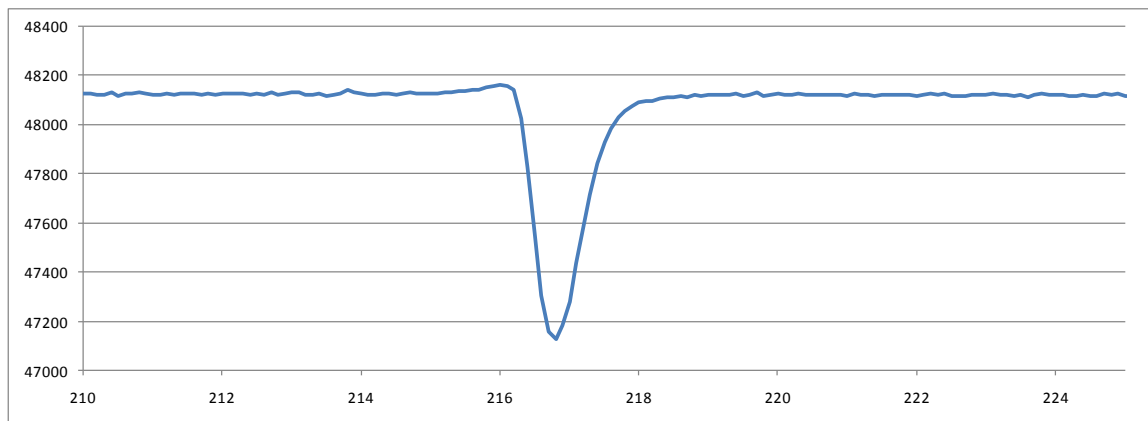


Figure 156. Time series data taken with an automobile passing by at a distance of 10m.

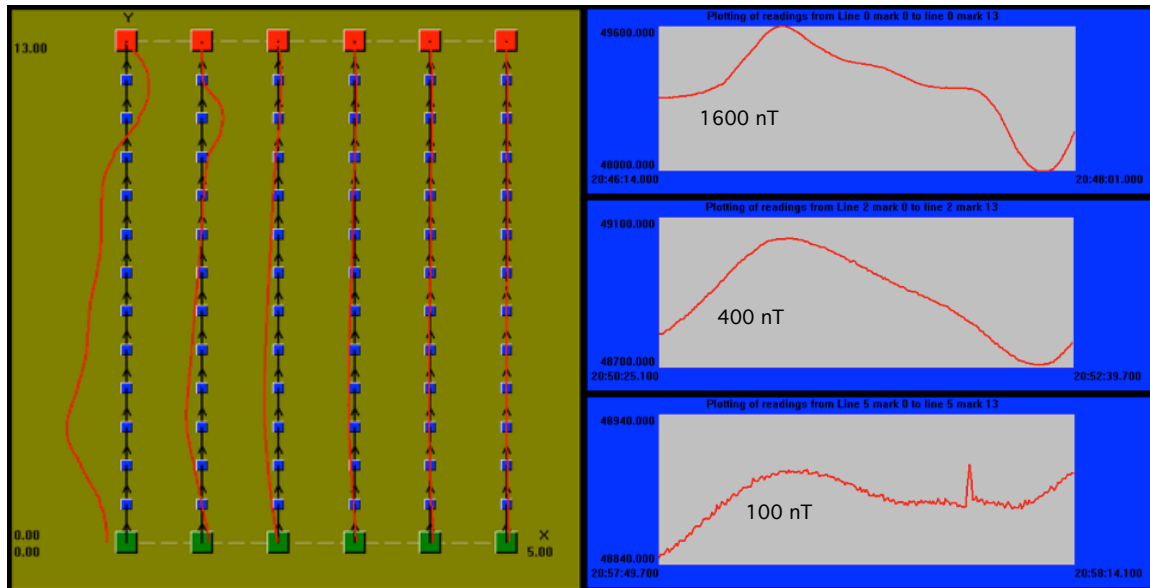


Figure 157. Field data over a small survey grid. Three representative lines are shown.

Concluding Summary

We are extremely pleased with the results of our work on this project. Early on, we had a good understanding of the major issues involved with the physics of the system, and we continued to learn more about the tradeoffs to be made in possible designs of complete systems. We now have the ability to model the performance of a complete magnetometer in significant detail, allowing us to efficiently design a variety of commercial systems. This technology will have a great impact in future commercial products.

In February of 2007, we successfully passed major go/no-go decision points:

- Determine if the laser performance is adequate to meet project sensitivity goals.
- Determine the cost and performance of our chosen cell filling method.
- Determine if the performance of the signal extraction methods will be adequate.

In 2007 we then reached an excellent understanding of the major issues involved in the various cell interrogation methodologies. We understood the tradeoffs to be had, and the performance potential of each method. We then built prototype physics packages implementing the design elements pursued earlier in the project.

In 2008, we furthered our understanding of the quantum effects leading to heading errors, to begin an optimization to reduce those effects. We also implemented the electronics in a form factor suitable for laboratory and field measurements. We showed a performance of 60 pT per root Hz with an actual system, capable of operation without operator intervention. Further improvements in performance and size reductions in the circuitry were then pursued.

In 2009 and 2010, we completed detailed quantum mechanical calculations, including important higher order effects which allow us to model the heading error and sensitivity of various designs of a magnetometer. This is quite valuable, as there are a wide variety of parameters, such as buffer gas pressure, light intensity, temperature, and modulation intensities which can be varied in the design, and the simulation capability allows us to optimize the performance much more efficiently than prototyping each design.

We also have completed a final electronics design, further reducing the size and improving the performance of the electronics with an eye towards operating arrays of sensors.

Our ultimate goal is to transition this technology into commercial products. Toward that goal, we have identified a phased approach:

	First generation	2nd Generation	3rd Generation
Sensor	VCSEL 1 cc hand made cell	VCSEL 1mm cells	Parallel production techniques
Electronics	Discrete analog	Digital	Custom digital
Counter	Separate, discrete	Separate, digital	Integrated
Quantities	100	1000	10,000
Cost Single / array	\$5000 / \$1000	\$1000 / \$200	\$200 / \$50
Market	Existing applications Smaller platforms Improved deployability, reliability	In situ array application	Remote monitoring applications

Table 3. Characteristics of commercial systems. Estimated cost is given for single sensors and for each sensor in an array.

We know the performance potential of these devices from the work that NIST has done in the laboratory, achieving 6 pT per root Hz sensitivity. That work indicated the ultimate performance obtainable from the system, without additional noise added due to the actual electronics required to control the system. In practice, this will not be possible, of course. We have so far achieved better than 30 pT per root Hz sensitivity with small circuit boards portable enough for field usage.

Several factors lead to a lowering of performance with real-world electronics. First of all, the electronics must perform several functions at once. Key functions are the laser frequency control and the signal extraction modulation. These functions will interfere with each other to a certain extent, which will lower performance. Secondly, the electronics must be able to rapidly track changing magnetic fields. NIST's measurement of noise occurs at a constant magnetic field. In changing fields, the feedback loops will add noise as they must servo back towards the equilibrium with finite gains.

We still have several factors at our disposal to design devices that meet our performance goals. First and foremost, is that we may use somewhat larger cells that used by NIST to regain sensitivity lost by the finite performance of the electronics. This will still make a vastly improved sensor, and makes the most sense commercially for the first generation of systems as well.

Table 4 shows a summary of performance characteristics for the two prototypes built in this project, as well as the first and second commercial systems based on those designs. The second commercial system is based on the first prototype sensor with the MEMS-based cell. The first generation commercial system is based upon the 2 cc hand-blown cell in the second prototype.

	Proto 1	Proto 2	Commercial 1	Commercial 2
Physics package size	10 cc	10 cc	10 cc	1 cc
Sensor power consumption	50 mW	400mW	200mW	50mW
Electronics size	30 in ²	15 in ²	15 in ²	5 in ²
Electronics power consumption	5W	2W	2W	0.5W
Cell size	0.001 cc	2 cc	2 cc	0.001 cc
Attainable sensitivity	6 pT / rt Hz	1 pT / rt Hz	1 pT / rt Hz	6 pT / rt Hz
Measured sensitivity	75 pT/ rt Hz	15 pT/ rt Hz	5 pT / rt Hz	10 pT / rt Hz
Heading error	40 nT	30 nT	2 nT	40 nT

Table 4. Summary of performance characteristics.

This has been a very exciting, highly successful project. With the understanding of the design and performance issues gained through this work, we have developed an excellent base from which to design commercial systems. We will be very excited to see the impact of this new technology in the marketplace. The improvement in applications, such as UXO detection, using magnetometers resulting from this work, will be even more exciting.

Appendices

Appendix A: List of Technical Publications

R. Jimenez, W.C. Griffith, Y. Wang, S. Knappe, J. Kitching, K. Smith, and M. Prouty, "Sensitivity Comparison of Mx and Frequency Modulated Bell-Bloom Cs Magnetometers in a Micro-Fabricated Cell," IEEE Transactions on Instrumentation and Measurement, Vol 59, No 2, February 2010.

Prouty, Mark, "Commercialization of Miniature Magnetometers," UXO Forum, Orlando, FL, 2009.

Prouty, Mark, "Advances in Atomic Magnetometers," Military Sensing Symposium, Battlefield Acoustic and Magnetic Sensors, Laurel, MD, 2009.

P. D. D. Schwindt, B. Lindseth, J. Kitching, and L.-A. Liew, "A chip-scale atomic magnetometer with improved sensitivity using the Mx technique," Accepted, Applied Physics Letters, 2006.

P. D. D. Schwindt, L. Hollberg, and J. Kitching, "Self-oscillating Rb magnetometer using non-linear magneto-optic rotation," Review of Scientific Instruments, vol. 76, pp. 126103, 2005.

L.-A. Liew, J. Moreland, and V. Gerginov, "Wafer-level fabrication and filling of cesium-vapor cells for chip-scale atomic devices," proceedings of Eurosensors, Sweden, 2007

D. K. Serkland, K. M. Geiba, G. M. Peakea, R. Lutwak, A. Rashed, M. Varghesec, G. Tepolte, M. Prouty, "VCSELs for Atomic Sensors" Photonics West, Santa Clara, CA, SPIE, 2007.

Prouty, Mark, "Miniature Total Field Magnetometers," Laser Science XXIII, San Jose, CA Sept 2007

Prouty, Mark, "Progress in Chip-Scale Total Field Magnetometers," Battlefield Acoustic and Magnetic Sensors, Laurel, MD, Aug 2007, BC01.

Prouty, Mark, "Miniature Total Field Magnetometers," UXO Forum, Orlando, FL Aug 2007

Prouty, Mark, "A Miniature Total-Field Magnetometer," SERDP-ESTCP Partners Symposium, Washington, DC, 2007.

M. A. Perez, et al., "Rubidium Vapor Cell with Integrated Nonmetallic Multilayer Reflectors," presented at Submitted to 2008 IEEE International Conference on Microelectromechanical systems, 2008.

P. D. D. Schwindt, et al., "A chip-scale atomic magnetometer with improved sensitivity using the Mx technique," Applied Physics Letters, vol. 90, pp. 081102, 2007.

B. Lindseth, P. Schwindt, J. Kitching, D. Fischer, and V. Shusterman, "Non-contact measurement of cardiac electromagnetic field in mice by use of a microfabricated atomic magnetometers," presented at Computers in Cardiology, 2007.

E. Hodby, E. Donley, and J. Kitching, "Differential Atomic Magnetometry Based on a Diverging Laser Beam," Applied Physics Letters, vol. 91, pp. 011109, 2007.